ON THE USE OF DYNAMICALLY SIMILAR EXPERIMENTS TO EVALUATE THE THERMAL PERFORMANCE OF HELIUM-COOLED TUNGSTEN DIVERTORS

A Dissertation
Presented to
The Academic Faculty

By

Brantley H. Mills

In Partial Fulfillment
Of the Requirements for the Degree
Doctor of Philosophy
G. W. Woodruff School of Mechanical Engineering

Georgia Institute of Technology
August 2014

ON THE USE OF DYNAMICALLY SIMILAR EXPERIMENTS TO EVALUATE THE THERMAL PERFORMANCE OF HELIUM-COOLED TUNGSTEN DIVERTORS

Approved By:

Dr. Said I. Abdel-Khalik, Co-Advisor
School of Mechanical Engineering
Georgia Institute of Technology

Dr. Minami Yoda, Co-Advisor
School of Mechanical Engineering
Georgia Institute of Technology

Dr. Nolan Hertel
School of Mechanical Engineering
Georgia Institute of Technology

Dr. Roman Grigoriev
School of Physics
Georgia Institute of Technology

Dr. Mark Tillack
Center for Energy Research
University of California, San Diego

Date Approved: May 30th, 2014

ACKNOWLEDGEMENTS

I would like to thank my advisors, Dr. Abdel-Khalik and Dr. Yoda, for their guidance and support through this long and difficult process. They were both a source of encouragement and inspiration during the most trying times of my research. Without them, none of this would have been possible. I felt extremely privileged to have been a part of their research group, and I have definitely enjoyed my time under their leadership. I would also like to thank the rest of my committee: Dr. Nolan Hertel, Dr. Roman Grigoriev, and Dr. Mark Tillack. Their feedback and contributions were very beneficial to the completion of my dissertation.

My thanks also goes to Dennis Sadowski for all the assistance he provided in designing and fabricating many of the test sections and the helium loop used in this research. His expertise was extremely valuable, and I learned a great deal from him. Thanks also goes to my colleague Dr. Jordan Rader whom I collaborated with frequently over the years. His friendship was very beneficial throughout the process.

In addition, I would like to thank my colleagues Bailey Zhao and Carlos Charry. Bailey was instrumental in helping me finish many of the experiments using the helium loop, and Carlos was very helpful in its construction. I would also like to thank my other friends and colleagues: Necmettin Cevheri, Yaofa Li, Tongran Qin, Ben Chan, Andrew Yee, and Matt Golob.

Finally, I would like to thank my family who has consistently supported me throughout this whole process. My mother, Lisa, my father, Jeff, and my brother, Tyler, have always believed in me, and I wouldn't be where I am today without them. My final thanks goes to Sonia, who has always been a source of encouragement and a wonderful influence on my life.

TABLE OF CONTENTS

LIST OF TABLES

LIST OF FIGURES

NOMENCLATURE

Variable	Definition	Units
Re	Reynolds number	-
Re_p	Prototypical Reynolds number	-
$\overline{Nu}$	Average Nusselt number	-
Nu	Local Nusselt number	-
Pr	Prandtl number	-
κ	Thermal conductivity ratio	-
K_L	Loss coefficient	-
β	Pumping power as a fraction of incident power	-
M	Mach number	-
Π	Non-dimensional group	-
$\dot{m}$	Coolant mass flow rate	kg/s
$\bar{h}$	Average heat transfer coefficient	W/m^2·K
$\overline{h_{eff}}$	Average effective heat transfer coefficient	W/m^2·K
$\overline{h_{act}}$	Average actual heat transfer coefficient	W/m^2·K
k	Thermal conductivity of the coolant	W/m·K
k_s	Thermal conductivity of the test section	W/m·K
ΔP	Pressure drop across the test section	Pa
P_i	Coolant inlet pressure	Pa
P_o	Coolant outlet pressure	Pa
$\overline{T_c}$	Average cooled surface temperature	K
T_{cr}	Extrapolated local cooled surface temperature	K
T_r	Thermocouple temperature measurement	K
$\overline{q''}$	Average heat flux incident on the test section	W/m^2

T_i	Coolant inlet temperature	K
T_o	Coolant outlet temperature	K
$\overline{T_s}$	Average pressure boundary interface temperature	K
ρ_L	Coolant density for the loss coefficients	kg/m^3
$\overline{V}$	Average coolant velocity at the jet	m/s
$\overline{\rho}$	Average coolant density across the test section	kg/m^3
ρ_i	Coolant inlet density	kg/m^3
ρ_o	Coolant outlet density	kg/m^3
μ	Dynamic viscosity of the coolant	Pa-s
$\overline{c_p}$	Average specific heat of the coolant	J/kg·K
A_c	Cooled surface area	m^2
A_h	Heated surface area	m^2
A_t	Cross sectional area of the tile	m^2
A_p	Cooled surface area uncovered by fins	m^2
A_f	Surface area of fins excluding the fin tips	m^2
A_j	Total area of jet holes on the HEMJ jet cartridge	m^2
D_f	Diameter of a pin fin	m
D_j	Jet nozzle diameter for HEMP-like divertor	m
D_o	Central jet diameter on the HEMJ jet cartridge	m
D_h	Hydraulic diameter	m
L_f	Length of a fin	m
δ_{TC}	Distance between cooled surface and thermocouples	m
η	Fin efficiency	-
ε_f	Fin effectiveness	-
γ	Specific heat ratio	-

$\Re$	Specific ideal gas constant	J/kg·K
ρ_R	Coolant density at the Rotameter exit	kg/m^3
Q	Volumetric coolant flow rate	m^3/s
ρ_v	Coolant density entering the Venturi meter	kg/m^3
ΔP_v	Pressure drop across the Venturi meter	Pa
P_v	Coolant pressure entering the Venturi meter	Pa
T_v	Coolant temperature entering the Venturi meter	K
$\overline{q''}_{\max}$	Maximum calculated heat flux on the divertor module	MW/m^2
$\overline{q''}_{tile}$	Maximum calculated heat flux on the tile	MW/m^2
R^2	Coefficient of determination	-

SUMMARY

Making fusion a commercial power source has been a goal of scientists and engineers around the globe for more than sixty years, but a commercial fusion reactor remains elusive to this day. Nevertheless, many scientific and technological breakthroughs have been made during this time, which have brought commercial fusion power closer to a reality than it has ever been. A consortium of several countries, including the United States, are currently constructing ITER, a large fusion research reactor that should, for the first time, produce more power than the amount of input power required to initiate and sustain fusion. However, many technological hurdles still remain before a viable commercial fusion power plant can be constructed, including the development of plasma-facing components with long lifetimes that can survive the harsh environment inside the reactor. Among these components, the divertor, which maintains the purity of the plasma by removing fusion byproducts from the reactor, must be able to accommodate very large incident heat fluxes of at least 10 MW/m^2 during normal operation.

Modular helium-cooled tungsten divertors are one of the leading designs for a commercial fusion reactor. Helium is a desirable coolant because it is chemically inert, compatible with other reactor materials, has a low neutron cross section, and can be used at high temperatures to achieve higher thermodynamic efficiencies. Tungsten is desirable because of its high melting point, high thermal conductivity, low sputtering yield, and low erosion yield. A number of different helium-cooled divertor designs have been proposed including the modular He-cooled divertor concept with pin array (HEMP), the modular He-cooled divertor concept with multiple jet-cooling (HEMJ), and the helium-cooled flat plate (HCFP). These three designs typically operate with helium coolant inlet temperatures of 600 °C and inlet pressures of 10 MPa.

There have been few experiments to evaluate these designs at prototypical conditions because such experiments are both challenging and resource-intensive. An alternative, more economical approach for experimentally evaluating different designs exploits dynamic similarity. Here, geometrically similar mockups of a single divertor module are tested using coolants at lower temperatures and pressures. The correlations for the nondimensional heat transfer coefficient, or Nusselt number Nu, and nondimensional pressure drop, or loss coefficient, from these experiments can then be extrapolated to prototypical conditions to predict the maximum incident heat flux that can be accommodated by the divertor and the coolant pumping power required under the proposed divertor operating conditions. Dynamically similar experiments were therefore performed on an HEMP-like divertor with helium and argon at inlet temperatures close to room temperature, inlet pressures below 1.4 MPa, and incident heat fluxes up to 2 MW/m^2. The results are used to predict the maximum heat flux that the divertor can accommodate, and the pumping power as a fraction of incident thermal power, for a given maximum tungsten temperature. The Nu is assumed to be a function of the nondimensional mass flow rate, or Reynolds number, as well as the thermal conductivity ratio which accounts for variations in the amount of conduction heat transfer through the walls of the divertor module. Numerical simulations of the HCFP divertor, using a commercial CFD software package, are performed to investigate how the thermal conductivity ratio affects predictions for the maximum heat flux obtained in previous studies. Finally, a helium loop is constructed and used to perform dynamically similar experiments on an HEMJ module at inlet temperatures as high as 300 °C, inlet pressures of 10 MPa, and incident heat fluxes as great as 4.9 MW/m^2. The correlations generated from this work can be used in system codes to determine optimal designs and operating conditions for a variety of fusion reactor designs.

CHAPTER 1: INTRODUCTION

1.1 Introduction and Motivation

The world's appetite for energy is perpetually growing, and major advances in energy technology are required to meet the challenges that accompany such growth. According to projections in the 2013 International Energy Outlook produced by the Energy Information Agency [1], worldwide energy consumption is expected to increase by 56% from 2010 to 2040, as illustrated in Figure 1. While continuing improvements in energy efficiency should help to dampen this growth, new sources of energy are also surely necessary to meet the demand, with the greatest needs in increasing electricity generation. However, in an era fraught with concern over the production of greenhouse gases from traditional fossil-fuel sources and the safety of nuclear fission power plants in the wake of the Fukushima Daiichi crisis, new technologies are desired to generate the future's electricity. Of course, other technologies, such as renewables, already exist that address these specific concerns, but like all forms of electricity generation they too have their own shortcomings (*e.g.* intermittency, geographical availability, etc.) that limit their potential contribution to the electrical grid.

While no single technology is able to completely meet the future's energy needs, electricity from fusion offers a promising alternative to many of the conventional methods. Fusion directly addresses many of the deficiencies inherent in other types of electricity generation including greenhouse emissions, safety, and intermittency. Furthermore, fusion provides a means to keep pace with staggering growth for energy consumption with a single station possessing the ability to produce electricity on par with, or exceeding, existing fission power plants.

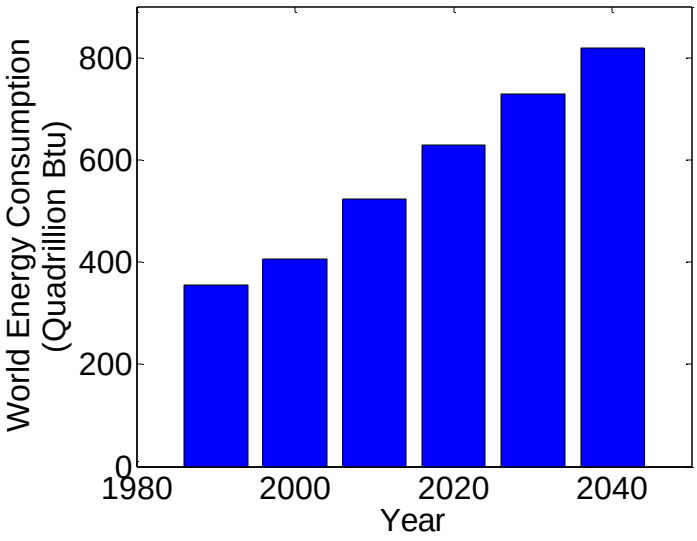

Figure 1. World energy consumption from 1990-2040. Data collected from EIA [1]

Nuclear fusion has long been studied as a potential source of commercial power generation due to the numerous advantages it possesses over current forms of electricity generation. First, greenhouse gases and other hazardous pollutants are not produced in a fusion reactor as the primary byproduct is inert helium. Second, a single fusion plant has the potential to produce large quantities of consistent base load electricity akin to its fission cousins, thus addressing many intermittency problems associated with renewables like wind and solar. However, unlike a fission power plant, the products from a fusion reaction are not radioactive (the reactor itself does become radioactive during its lifetime, but it is significantly less hazardous than waste from fission plants). In addition, the low volume of fuel present inside a fusion reactor is small enough that the risk of a catastrophic runaway reaction is nonexistent. Finally, the most common fuel for a fusion reactor are hydrogen isotopes, which can be harvested or created from naturally occurring, nearly limitless sources, such as the oceans, with proven technology.

Despite these advantages, a working, commercially viable demonstration plant has still eluded scientists and engineers for over 60 years. Nevertheless, a successful demonstration plant could usher in an era of abundant clean energy to meet tomorrow's demands. Thus, significant research continues to be performed on fusion power and fusion related-projects. Many designs for fusion power plants have been proposed and explored over the decades, and two branches have emerged as viable candidates, appropriately named magnetic confinement fusion energy (MFE) and inertial confinement fusion energy (IFE). While both are promising technologies, MFE is the subject of the work herein.

The path to building a commercial MFE reactor is fraught with many challenges that extend beyond the plasma physics. A number of technological hurdles remain primarily centered around the interaction between the hot plasma inside the reactor and the surrounding materials, and this is the focus of a significant amount of active research. The extreme temperatures and radiation inside the vessel severely limit the number of suitable materials that comprise the reactor, and many components inside the reactor also require very long lifetimes to be economical.

Specifically, a particular component of many modern tokamak MFE designs, the divertor, whose function is to remove byproducts of the fusion reaction from the reactor, will be studied. Various divertor designs have been proposed, but this work will focus on the most promising concept at present for future commercial fusion reactors: modular helium-cooled tungsten divertors. A more detailed description of modular helium-cooled tungsten divertors will be provided later in this chapter.

As it is imperative to have a firm understanding of the fundamental concepts in nuclear fusion, the remainder of this chapter will be devoted to introducing the reader to many basic principles and subjects. First, a brief introduction to fusion energy will be

discussed highlighting some of the essential concepts. Next, the basic MFE designs will be introduced including tokamaks and stellarators. Finally, the technologies associated with removing the byproducts of the fusion reaction will be reviewed with emphasis given to the divertor.

1.2 Fusion Energy

In the simplest terms, nuclear fusion is the process by which two lighter nuclei fuse into a single heavier nucleus. If the appropriate light nuclei undergo fusion, a significant amount of energy is released in the process. This is best summarized in the following chart illustrating the binding energy per nucleon of each element shown in Figure 2.

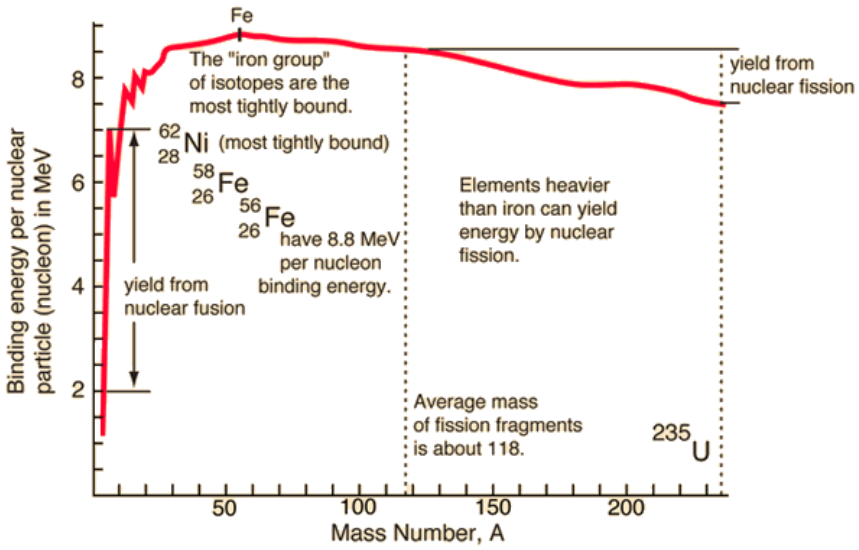

Figure 2. Binding energy per nucleon for each element [2]

For two nuclei that fuse with lower binding energy per nucleon than the resulting fused nucleus, energy will be released. That is, the resulting products of that fusion reaction will have a lower mass than the reactants, and the difference is released as

energy. Typically this occurs for nuclei with atomic numbers less than Fe where the binding energy curves peaks (although Ni-62 has the highest binding energy per nucleon), but fusion can occur in heavier nuclei if energy is added to the reaction. Fusion is the opposite of nuclear fission that is utilized in today's nuclear power plants. In fission, nuclei with atomic numbers greater than Fe can typically be split into two lighter nuclei to release energy. The difference in the binding energy directly correlates to the yield from each respective reaction type. As seen in Figure 2, the yield from fusion reactions with low atomic numbers can significantly exceed the yield from fission reactions. Particularly, the fusion of two hydrogen nuclei into a helium nucleus is of the most interest due to its exceptionally large yield.

For nuclear fusion to occur, the nuclei must be brought within close proximity of one another in order for the strong nuclear force to overcome the electromagnetic repulsion of the positively charged protons. The energy required to bring nuclei close enough is referred to as the Coulomb barrier. This barrier is smallest for hydrogen isotopes with an atomic number of only one, and this fact coupled with the potential energy yield of helium fusion seen in Figure 2 makes them ideally suited for a fusion reactor. Using classical mechanics, the kinetic energy required to exceed the Coulomb barrier is far greater than what is realistically feasible for a reactor, but when factoring in quantum mechanics, a particle's probabilistic ability to tunnel through barriers significantly lowers the energy burden [3].

The sun is the best example of a fusion reactor. Inside of the sun, a complex fusion chain reaction occurs known as the proton-proton chain reaction with a yield of approximately 25 MeV [4]. To initiate and sustain a fusion chain reaction, the sun takes advantage of its immense gravitational force to create large plasma densities at its core. There, nuclei can possess enough thermal energy to overcome the Coulomb barrier

while the gravitational pull maintains confinement of the plasma. However, for a terrestrial nuclear reactor, gravitation confinement of the plasma is not feasible, and an alternative means must be used. As a result, these less effective means of confinement result in plasma densities significantly smaller than stellar reactors requiring larger temperatures in order to achieve a self-sustaining fusion reaction (~100 million K terrestrially versus ~15 million K in the sun [3]). Magnetic and inertial confinement are the two most commonly used techniques.

Each specific fusion reaction requires different temperatures in order to overcome the Coulomb barrier. Obviously, a fusion reaction with a large fusion cross section (reaction probability) at lower energies is desired. Other criteria are also used in selecting a potential candidate reaction such as energy yield and the ability to remove energy from the plasma. A promising example of a reaction is the fusion of deuterium and tritium (D-T), and its reaction equation is as follows:

$$ {}_{1}^{2}D + {}_{1}^{3}T \rightarrow {}_{2}^{4}He + {}_{0}^{1}n + 17.6MeV \quad (1) $$

The D-T reaction requires relatively low average thermal energies for nucleons of ~10 keV [3] with cross sections well above other candidate reactions for energies exceeding 100 keV. This is shown schematically in Figure 3. In addition, the resulting neutrons provide a means to extract energy from the plasma. Neutrons are created with 14.1 MeV of kinetic energy and are unaffected by magnetic fields. Therefore, they can impinge on surrounding surfaces. While this is damaging to the surfaces, the thermal energy imparted by the neutrons as they collide with the surface can then be extracted and used to generate electricity. As for natural deposits of the fuel, deuterium can be found in ocean water using the same technology commonly used to extract heavy water for fission reactors. Tritium is not found in nature due to its short half-life of 12.3 years,

but can be bred from neutron irradiation of the naturally abundant lithium isotopes ${}^{7}_{3}Li$ and ${}^{6}_{3}Li$ [5].

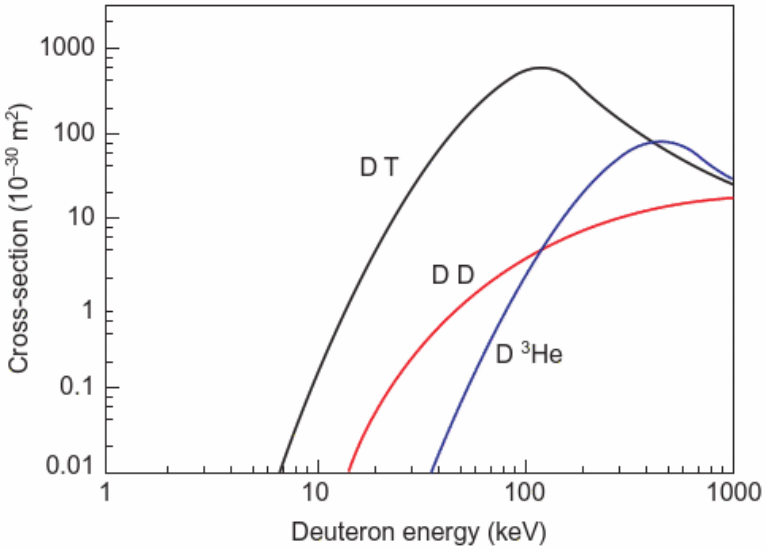

Figure 3. Fusion cross sections as a function of deuterium energy for a deuterium-tritium (DT), deuterium-deuterium (DD), and a deuterium-helium-3 (D^3He) fusion reaction [5]

1.3 Magnetic Confinement Fusion Energy

Numerous designs have been proposed as a means to confine the plasma inside a fusion reactor. As stated earlier, this work focuses on MFE designs as opposed to IFE designs. For MFE reactors, two types have historically been pursued: the stellarator and the tokamak. The stellarator was an American concept first proposed by Lyman Spitzer of Princeton in the early 1950s [5]. While promising as a future design and still actively researched, the stellarator largely fell out of favor when Soviet successes with tokamaks were confirmed by British scientists in 1968 [5]. As a result, most of the recent fusion facilities built since that time have been tokamaks.

Although the stellarator and tokamak share a similar fundamental design using external magnetic coils to confine the plasma, the tokamak features a simpler physical geometry. An example of a tokamak design, ITER, is shown in Figure 4. The plasma is

confined in a D-shaped torus using toroidal and poloidal magnetic fields generated from superconducting magnets and electric currents that encompass the torus. The charged particles in the plasma spiral about the toroidal magnetic field lines that encircle the torus, but the curvature of the torus itself leads to a perpendicular drift of the particles that will ultimately result in the particles striking the walls of the reactors. To correct for this drift, a poloidal magnetic field is added by driving an electric current through the plasma that causes the toroidal field lines to spiral in the torus. This significantly improves the confinement time of the plasma and also acts to 'pinch' the plasma away from the walls of the torus. Poloidal magnets are also commonly used to aid in creating the poloidal field. Typically, the toroidal magnetic field is about 10 times stronger than the poloidal field [5]. For stellarators, the winding of the toroidal magnetic field lines is created by either winding the torus or the toroidal coils themselves.

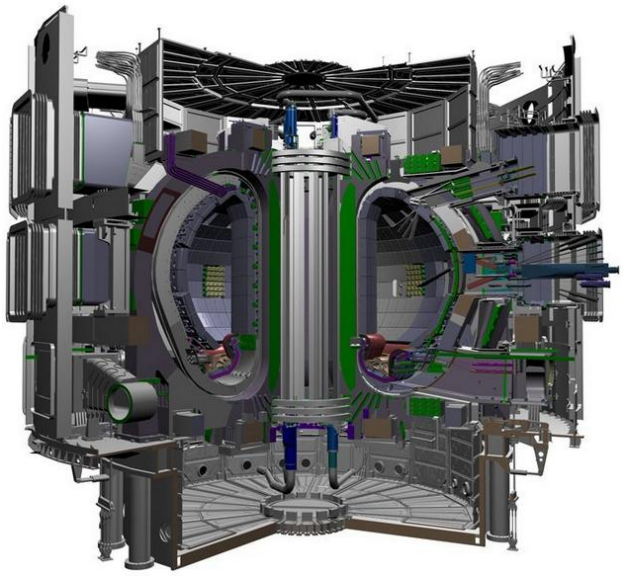

Figure 4. An example of a tokamak fusion reactor design, ITER. Currently under construction in Cadarache, France [6]

In addition to confinement, the plasma must be heated to a high enough temperature to provide the ions and electrons enough energy to fuse, and this is

accomplished by a number of different methods. First, in addition to inducing a poloidal field, the electric current also acts to heat the plasma. However, this is not sufficient to heat the plasma fully as the electrical resistance of the plasma falls with increasing temperature and the plasma heating must be supplemented by other methods [5]. One such method is known as neutral beam injection where neutral deuterium atoms, unaffected by the magnetic fields, are propelled into the plasma at high velocity. Another method is radiofrequency heating where radio waves are emitted into the plasma at a precise frequency that the plasma can absorb. Both of these techniques will be used for ITER [6]. Once the plasma reaches a desired temperature, D-T fusion reactions begin to occur in sufficient numbers where the energy released in the alpha particle (neutrons mostly escape the plasma) is sufficient to maintain the plasma temperature and further fusion reactions. This point is commonly referred to as 'ignition' and is the ideal operating point as no external heating is required [5].

As the fusion reactions begin, 14.1 MeV neutrons, unaffected by the magnetic field, bombard the walls of the torus depositing their energy as they slow. This thermal energy is then removed with a coolant to drive turbines and ultimately to generate electricity. The neutron bombardment is also potentially used as a means to breed tritium from lithium, and future commercial reactors are designed to incorporate liquid lithium near the walls (in conjunction with Be or Pb as a neutron multiplier). The helium that is created inside the plasma by the fusion reaction must also be removed after it imparts its energy to the plasma since it will not undergo fusion and hinders further D-T reactions. The removal of the helium 'ash' is then accomplished by altering the outer magnetic field lines such that particles can be removed from the plasma using either limiters or divertors.

1.4 Divertors

In MFE reactors, helium and other impurities (eroded particles from the walls of the vessel or other gaseous atoms) must be removed from the plasma such that the fusion reaction is not hindered and ignition can occur. The two most common devices to perform this function are divertors and limiters. Both devices are positioned inside the vacuum chamber such that the outer most layers of the confined plasma, referred to as the scrape-off-layer (SOL), impinge on an actively cooled surface. This is shown in Figure 5. As a result, heat fluxes can reach extraordinarily high values on these surfaces, of $O(10\ \mathrm{MW/m^2})$. Historically, limiters have been used on older MFE reactors as the primary means to remove helium and impurities from the plasma primarily due to their smaller size and simplicity; however, limiters typically resulted in considerable impurities sputtered into the plasma volume [3]. As shown in Figure 5, limiters extend up to the separatrix that divides closed plasma volume from the SOL such that any sputtered or eroded ions are injected directly into the plasma volume. On the other hand, divertors are positioned away from the closed magnetic field lines where sputtered ions must travel a distance before reaching the closed plasma volume. Furthermore, the discovery of the high-confinement regime (referred to as H-mode) with divertors in the ASDEX experiment which effectively doubles the total plasma confinement time, led to the mass adoption of divertors in modern tokamaks [3]. When discussing divertors and limiters, it is important to emphasize that these terms include the impingement surfaces as well as required components necessary to cool and structurally house the surfaces.

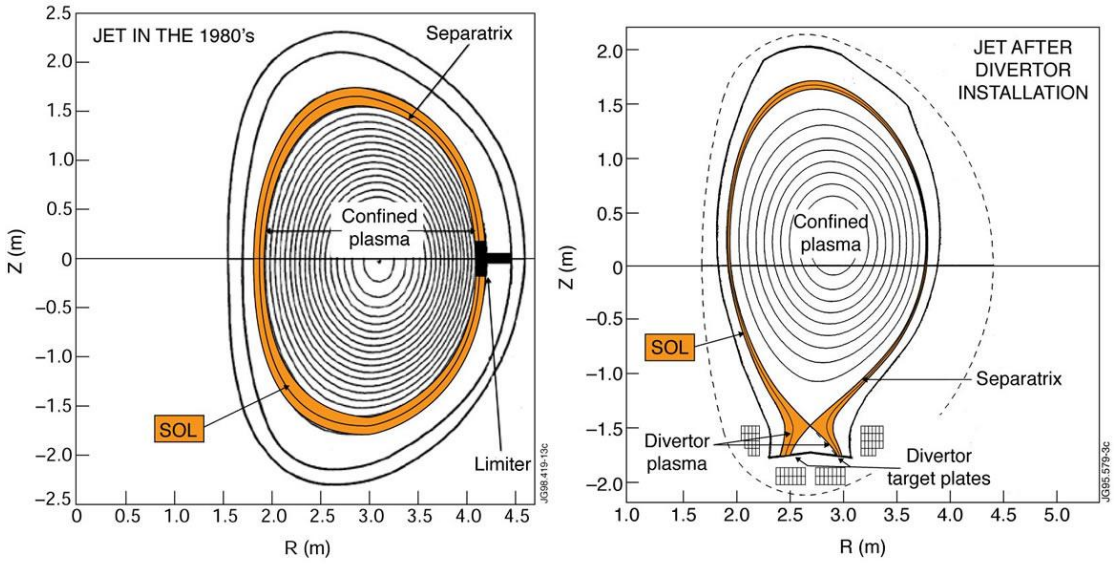

Figure 5. A schematic of the different magnetic field lines using a limiter (left) and a divertor (right) [7]

In using a divertor inside a fusion reactor, the outer magnetic field lines are altered such that the SOL resides in open magnetic field lines that directly impinge on the divertor's plasma facing surface or target plates. That is, particles that drift across the separatrix (the boundary separating the SOL from the confined plasma) are immediately directed to the target plates. In this manner, particles will collide with the target plate and become embedded in the material or scattered at significantly cooler temperatures to the surrounding region (but still outside of the separatrix in H-mode). The cooler ions recombine with electrons, and vacuum pumps can then be used to remove the neutral gas of hydrogen isotopes, helium, and other impurities to desired levels [8]. A more detailed depiction of the magnetic field lines for a divertor configuration is shown in Figure 6.

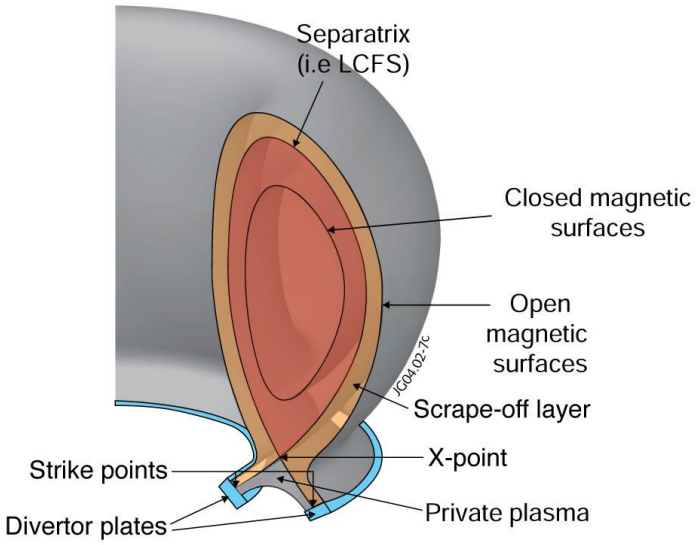

Figure 6. Cutaway of the plasma in a reactor vessel with a divertor configuration [7]

Heat fluxes parallel to field lines in the SOL can exceed 500 MW/m^2 and must be reduced to acceptable levels before impinging on the target plates of the divertor [9]. The values commonly cited and used as design criteria for thermal performance are 10 MW/m^2 for steady-state conditions [3,8,9] and 20 MW/m^2 for transient events [9]. The reduction in the heat flux is accomplished by a number of methods including but not limited to: altering the orientation of the target plates, distributing the heat flux over a large area, and using the cooler gas surrounding the target plates for preliminary collisions to decrease the kinetic energy of the incident particles [9]. Despite these methods, true steady-state heat fluxes for commercial sized reactors have not been experimentally measured, and transient heat fluxes could well exceed 10 MW/m^2 for short durations during off-normal events such as edge localized modes (ELMs). Such events are avoided or minimized as it would likely result in significant erosion or melting of the target plates.

Divertor designs can vary significantly based upon their material composition, coolant, and geometry. Divertors can also be designed to exist at the top and bottom of

a reactor vessel to improve performance. Such designs have been implemented in the DIII-D divertor, as well as in a number of ARIES studies. The extreme conditions at the divertor target plates have narrowed the range of possible wall materials down significantly. Any divertor material must be able to withstand extremely high temperatures and irradiation without significant activation or degradation of its material properties. In addition, materials with low atomic numbers are desired since any eroded particles (sputtering, chemical erosion, etc.) will reduce plasma temperatures through Bremsstrahlung radiation. The larger the atomic number of the impurities, the more significant the contribution is to radiation losses (losses are proportional to the atomic number squared, Z^2) [3,5].

The two most commonly cited materials are carbon fiber composites (CFCs) and tungsten. CFCs are advantageous primarily due to their good thermal and mechanical properties, inability to melt at high temperatures, and low atomic number. However, one of the most serious concerns about using CFCs is their chemical affinity to hydrogen isotopes, especially tritium (referred to as chemical erosion). Chemical erosion of carbon based surfaces by tritium will subsequently redeposit in other locations inside the vessel as hydrocarbons or contaminate the plasma with carbon. Tritium deposition also presents a challenge in maintaining a sufficient tritium inventory in the plasma since tritium is limited in supply [9]. Newer, larger MFE reactors, such as ITER, specify very low tritium retention rates on the plasma facing surfaces of approximately 0.1% of the total injected tritium during normal operation [9]. Such targets have yet to be achieved experimentally [9]. As an alternative material, tungsten has been proposed for the first wall as it possesses excellent thermo-mechanical properties with lower erosion rates for a longer expected lifetime [6]. Its high atomic number requires that the impurity concentrations in the plasma must not exceed 10^{-4} for ignition, but high sputtering

thresholds mitigate this concern [9]. However, the use of tungsten requires minimal occurrences of large heat flux transients in the plasma (*e.g.* ELMs) that could result in surface melting or sublimation which contaminate the plasma [3]. Despite this concern, tungsten is viewed as an extremely viable first wall material for divertors in future commercial fusion reactors [3]. In fact, ITER, which had originally proposed to test both a CFC and a tungsten divertor, has recently discarded its CFC divertor in favor of a tungsten design [6].

For the divertor coolant, helium cooling is generally regarded as a more viable solution than water in commercial reactors for several reasons. First, He possesses a very high thermal conductivity among gas coolants and has been widely studied as a high heat flux coolant. Second, as it is desired to use the same coolant throughout the reactor for simplicity, helium is more compatible in areas where materials such as Li, Be, or Pb are present (for tritium breeding). Furthermore, helium does not undergo a phase change which allows for cooling at higher temperatures. Since a significant fraction of the total thermal energy output of the reactor is imparted on the divertor surface (~10-15% [10,11,12]), it is critical to extract that energy for electricity production and high temperature helium is more thermodynamically efficient. Finally, large neutron fluences are expected in commercial reactors significantly larger than those encountered in fission reactors, and helium has very low neutron cross sections.

Divertors for large commercial reactors will likely be divided into smaller units that will be able to be removed from the vessel as needed to repair damage that may occur during operation. Since the reactor itself will be radioactive due to the neutron bombardment of its surfaces and the deposition of tritium on surfaces, remote handling will be required [5]. The ITER divertor has been segmented into a series of 54 removable cassettes as shown in Figure 7.

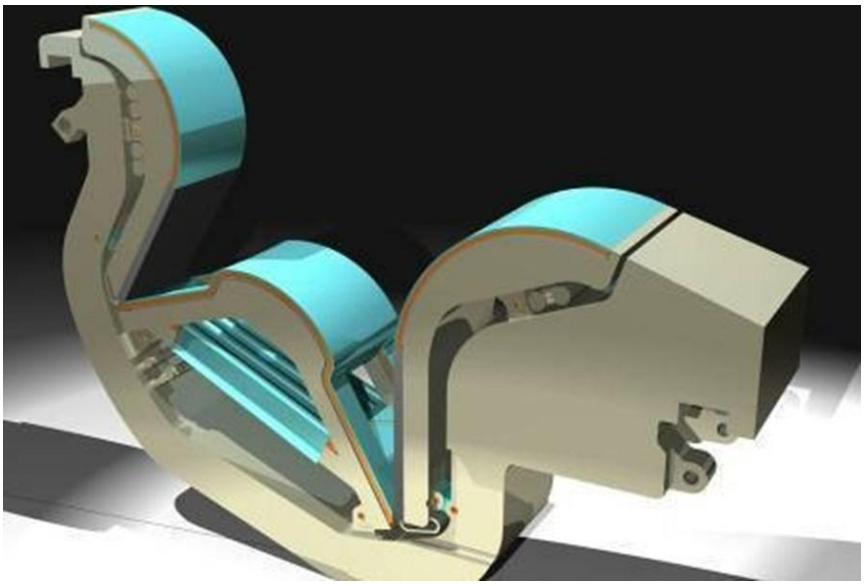

Figure 7. An ITER divertor cassette [6]

Large temperature gradients inside divertors also pose a structural risk due to the significant resultant thermal stresses. While the divertor target plate is not a structural element, other components that contain the coolant or support the divertor must be ductile and capable of withstanding the thermal stresses without failure during both steady-state operation and transients. To mitigate these problems, many commercial fusion divertor designs have resorted to modular designs [3], which typically require thousands of modular units to completely cover the divertor surface with an area $O(100\ m^2)$.

In short, modular helium-cooled tungsten divertors are some of the most promising divertor designs for future commercial fusion reactors and are therefore the subject of the research herein. This research will focus on the thermal performance of three specific designs: the modular He-cooled divertor concept with pin array (HEMP), the modular He-cooled divertor concept with multiple-jet-cooling (HEMJ), and the helium-cooled flat plate (HCFP), and will complement and extend the existing work that has been presented in the literature. Dynamically similar experiments are performed to

evaluate each design, and the results are extrapolated to determine the thermal performance under prototypical conditions. From these extrapolations, generalized maximum heat flux correlations based upon experimental data can be developed and used within system codes to aid in finding optimal designs and operating conditions for future commercial fusion reactors.

The experimental procedure is as follows. First, experiments are conducted on mock-ups of the divertor designs using air, helium, and argon as a coolant at low temperatures and pressures. Then, temperatures measured with thermocouples embedded in these mock-ups, or test sections, are used to calculate Nusselt number correlations over a range of Reynolds numbers. By taking advantage of dynamic similarity, the Nusselt number correlations are used to predict the maximum heat flux a design can endure using prototypical materials and coolant pressures and temperatures. The measured pressure drop across the test section is used to generate loss coefficient correlations that can also predict the prototypical pressure drop.

Numerical simulations of the experiments using a commercially available computational fluid dynamics (CFD) software package, ANSYS FLUENT® 14.0, are performed to evaluate the capability of the software to accurately model the divertor. The simulations are also used to investigate several important assumptions in the creation of the Nusselt number correlations. Finally, a helium loop is constructed that circulates helium at temperatures and pressures near prototypical conditions under incident heat fluxes of approximately half the prototypical values. This loop is used to conduct further dynamically similar experiments at nearly prototypical heat fluxes and elevated inlet temperatures to enhance confidence in the extrapolations that were developed at lower incident heat fluxes and at lower coolant temperatures and pressures. The construction

of this helium loop will also support future divertor research beyond the scope of this thesis.

The remainder of this thesis is divided as follows. Chapter 2 consists of a literature review of this topic focusing on: various heat transfer enhancements used to achieve high cooling performance, current modular helium-cooled tungsten divertor designs, existing experimental facilities and helium loops, and previous CFD simulations and the corresponding turbulence and heat transfer models utilized within. Chapter 3 presents dynamically similar experiments of a HEMP-like divertor with and without fins conducted at low pressure and low temperature using helium and argon as coolants. Chapter 4 describes CFD simulations of the experiments in Chapter 3 and of previous dynamically similar experiments on the HCFP divertor using ANSYS FLUENT® 14.0. Chapter 5 extrapolates the results presented in Chapters 3 and 4 to prototypical conditions for both the HEMP-like divertor with and without fins and the HCFP divertor. Chapter 6 details the helium loop and presents dynamically similar experiments on the HEMJ divertor performed with the helium loop at temperatures, pressures, and incident heat fluxes closer to prototypical conditions. Finally, Chapter 7 summarizes the conclusions of this thesis and makes recommendations for future work.

CHAPTER 2: LITERATURE REVIEW

The technology required to actively cool heat fluxes of 10 MW/m^2 is not a simple matter, and the divertor designs that have been devised thus far utilize many advanced concepts. The cooling requirements alone present a challenge and are further complicated by the restriction of materials and coolants due to the high neutron fluences inside a fusion reactor. However, scientists and engineers from many different countries have managed to propose several possible solutions each at varying stages of development. Some of the most popular designs being actively researched include modular helium-cooled tungsten divertors for the variety of advantages they hold over alternative candidates as described in Chapter 1. Accordingly, these divertor designs are the subject of this work.

Of the modular helium-cooled tungsten divertors that have been proposed, this work will focus on three designs: the He-cooled modular divertor with multiple-jet cooling (HEMJ), the He-cooled modular divertor design with integrated pin array (HEMP), and the He-cooled flat plate divertor (HCFP). The HEMJ and HEMP designs are commonly referred to as ‘finger-type’ divertors, while the HCFP is appropriately called a ‘plate-type’ divertor. In the following sections each of the designs will be discussed further in addition to briefly addressing one other candidate. Recently, research has also been performed on the integration of the HCFP and HEMJ designs to take advantage of the favorable characteristics of each and this integrated design will also be included.

It has been clear from the early stages of divertor development that in order to cool up to 10 MW/m^2 on the divertor surface using helium, it would be necessary to incorporate additional techniques to enhance the thermal performance including: cooling fins, jet impingement, porous media, etc. Each modular helium-cooled tungsten divertor uses one or more of these techniques to achieve the required heat transfer coefficients.

Information regarding the advantages and disadvantages each of these heat transfer techniques will be discussed further in Section 2.1. Experimental facilities that have been constructed to test these divertor designs at or near prototypical conditions will also be included together with their capabilities and limitations. Finally, relevant numerical simulations that have been performed using commercial CFD codes will be reviewed, with emphasis on the relevant turbulence models that have shown promise for helium-cooled divertors.

2.1 Heat Transfer Enhancements

2.1.1 Cooling Fins

Cooling fins, sometimes referred to as extended surfaces, have long been used as a means to enhance the heat transfer in gas cooling applications. A cooling fin is simply an extension of an otherwise level surface that increases the surface area over which convection occurs. They can take many shapes such as an array pins or ridges or as more complex designs as depicted in Figure 8. Cooling fins find use in many everyday objects including electronics and radiators and can be machined directly into, or attached to, the appropriate surface.

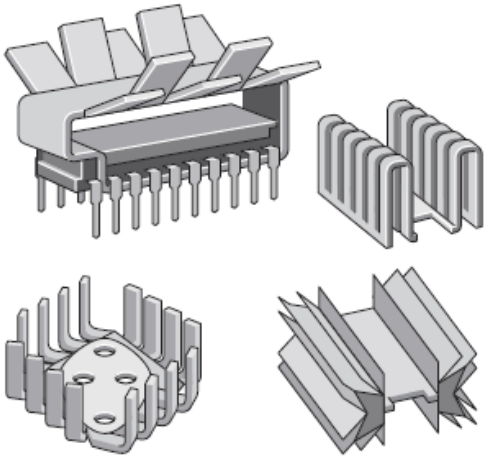

Figure 8. Examples of some complex fin designs. [13]

As described in these references [13,14,15], the temperatures along the length of the fin decrease from the base fin temperature depending on the fin material and the coolant. Ideally, a fin would have an infinite thermal conductivity to maximize the temperature difference between the coolant and the surface for as large an area as possible, so fins are typically made of highly conductive materials to maintain as high a temperature difference as possible. The length of the fin would also ideally be infinite, but as the temperature decreases along the length of the fin, the value of this additional area is reduced. In addition, there are often practical considerations that limit the size of fins such as the clearance between the surface and other components.

A useful metric for characterizing the thermal performance of cooling fins is the fin effectiveness ε_f. As stated in Incropera and DeWitt [15], ε_f is the ratio of the fin heat transfer rate q_f to the heat transfer rate that would exist without the fin. This is given as follows:

$$\varepsilon_f = \frac{q_f}{hA_c\left(T_c - T_\infty\right)} \tag{2}$$

where h is the heat transfer coefficient, A_c is the area of the cooled surface without fins, T_c is the cooled surface temperature, and T_∞ is the ambient coolant temperature. As a rule of thumb, it is desirable to have a fin effectiveness greater than or equal to 2 [15], while a fin effectiveness less than one indicates that the fin is acting as insulation and hindering heat transfer [13].

To evaluate the fin effectiveness, it is critical to define the tip condition of the fins. For the purposes herein, it is useful to evaluate fins with adiabatic fins tips with constant cross sectional areas along its length. For fins of this type, an 1D analytical solution for fin heat transfer rate is defined as follows [15]:

$$q_f = \sqrt{hPk_f A_f}\left(T_c - T_\infty\right)\tanh\sqrt{\frac{hP}{k_f A_f}}L \tag{3}$$

where P is the perimeter of the fin cross section, k_f is the thermal conductivity of the fin, A_f is the cross sectional area of the fin, and L_f is the length of the fin. Substituting into the fin effectiveness equation ultimately gives:

$$\varepsilon_f = \frac{k_f}{h}\alpha \tanh(\alpha L_f) \quad \textit{where} \quad \alpha = \sqrt{\frac{hP}{k_f A_f}} \tag{4}$$

Another useful metric for assessing the performance of cooling fins is the fin efficiency η. The fin efficiency is a measure of the actual heat transfer rate from the fin compared to the maximum amount of heat that could be transferred to the coolant assuming the fin was entirely at the base temperature or at an infinite length. A value of one indicates that the maximum amount of heat is being transferred from the additional area while a value of zero indicates that there is none. Again, for adiabatic fins tips (the most relevant in this work), the fin efficiency is as follows:

$$\eta = \frac{\tanh(\alpha L_f)}{\alpha L_f} \tag{5}$$

Based on this equation for the fin efficiency, it is important to notice that as the heat transfer coefficient increases, the fin efficiency decreases. That is, the better the fluid is able to cool, the less of the extended area of the fin will be at the higher base temperature, and so there is less benefit in having larger surface area. This is largely why fins are used in gas cooling, as opposed to liquid cooling, since gas cooling usually has lower heat transfer coefficients [15]. While helium is a gas, its high thermal conductivity usually gives relatively high heat transfer coefficients compared with other gasses. Therefore, it is critical to evaluate the benefit of using fins with helium-cooling so that it may be accurately weighed against the additional cost of manufacturing the fins and resulting pressure drop. Combining fins with other techniques to increase the heat transfer coefficient such as jet impingement may further reduce the benefit, if any,

although jet impingement has been combined with cooling fins in air cooling applications [16].

Determining the appropriate length for a fin can be done by comparing the ratio of heat transfer from a finite fin with an adiabatic fin tip to an infinitely long fin under the same conditions [13]. This ratio will simplify to:

$$\frac{q_{f,L}}{q_{f,\inf}} = \tanh\left(\alpha L_f\right) \tag{6}$$

The closer this ratio is to one, the closer to the maximum amount of heat that can be extracted from the fin for a given α. For $\alpha L_f = 2.5$, already 99% of the heat is transferred, compared with that for an infinitely long fin. Further increases in length are therefore not justified.

In addition to increasing the surface area of a cooled surface, cooling fins also help promote turbulence and mixing in the coolant. However, the arrangement of the fins will of course affect the benefit from mixing. For example, in an array of pin fins in cross flow, which can be approximated by tube banks, staggering successive rows of fins will improve the heat transfer coefficient [15]. Typically, the heat transfer coefficient can be improved until approximately the fifth row, at which point adding further rows will not affect the turbulence. Furthermore, additional rows are not beneficial since the temperature of the coolant is progressively heated as it passes from one row to the next thereby decreasing the temperature difference between the coolant and the fin.

Hermsmeyer and Malang [17] were the first to propose the use of pin fins in helium-cooled tungsten divertors specifying fins with a diameter of 1 mm, pitch of 1.2 mm, and height of 2 mm in a hexagonal array as having the best performance. Other more complicated pin fin arrangements were later proposed for the HEMP design

(discussed in Section 2.2.2) by Diegle et al. [18] to increase the heat transfer coefficient. These designs were later integrated with jet impingement for further improvement.

2.1.2 Jet Impingement

An effective method to improve the heat transfer across a surface involves the use of impinging jets. An impinging jet is simply the acceleration of a fluid through a constriction in the flow area directed onto an opposing surface which is used to improve heating or cooling characteristics of the flow. The jet usually emerges either from a round exit, or a high aspect-ratio rectangular exit, known as a slot. Very high heat transfer coefficients can be achieved with jet impingement since thin thermal and hydrodynamic boundary layers are formed on the impingement surface [14]. Jet impingement is common in materials processing applications including the tempering of glass and the annealing of metals, and it is frequently used in the cooling of heated components [15].

A jet can be divided up into four distinct regions as described in the following references and depicted in Figure 9 [14,15]. As the fluid leaves through the nozzle exit of diameter D or width W, a nearly uniform velocity profile can be used to characterize the flow, which dissipates as the flow moves axially. This region with the nearly uniform velocity profile is referred to as the potential core. As the potential core dissipates axially, the flow forms the free jet region where the velocity profile broadens and becomes distinctly non-uniform with a maximum at the center. For submerged jets that discharge into the same ambient medium, this broadening is more exaggerated. As the flow moves closer to the surface in the stagnation or impingement region, it begins to decelerate axially and accelerate along the cross-stream direction. These regions of the flow with a velocity component along the cross-stream direction are known as the wall jet region, where the flow's momentum decays to zero as it moves away from the jet.

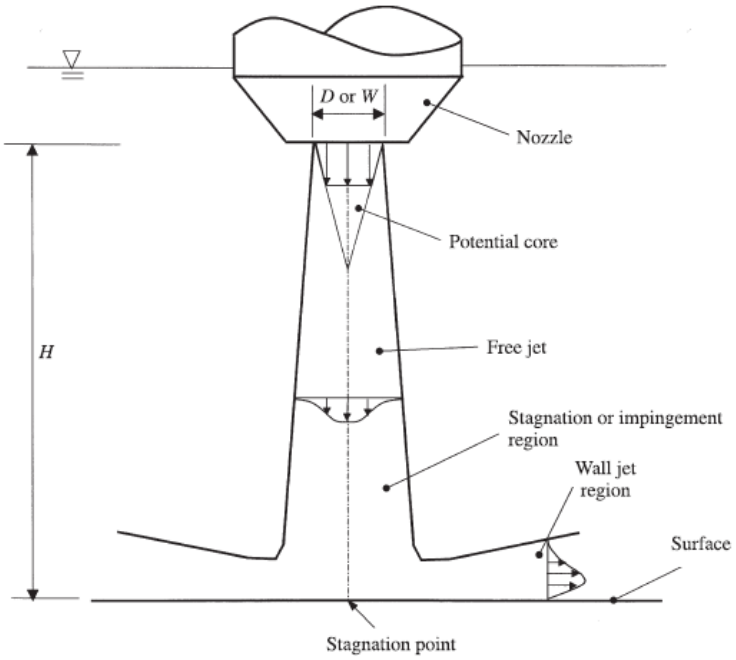

Figure 9. Diagram of submerged jet impingement of a single round jet or slot [14]

As one might expect, the thermal performance of jet impingement cooling described by the Nusselt number, typically improves with increasing jet velocity or Reynolds number, although the distance between the nozzle exit and the surface also plays an important role in the Nusselt number and shape of the profile [19]. A useful non-dimensional parameter used to evaluate relative distances is H/D_h where H is the jet to wall spacing and D_h is the hydraulic diameter of the nozzle exit. For $H/D_h \geq 5$, the Nusselt number profile along the surface of the profile is bell-shaped, with a maximum in the center near the stagnation point. As H/D_h decreases to values less than 5, a characteristic secondary peak in the Nusselt number profile may be observed after the maximum found at the centerline; the Nusselt number at this secondary peak may even exceed the centerline value. This second local peak tends to move closer to the centerline as H/D_h decreases [20]. The second peak has been attributed to a sharp rise in turbulence as the flow transitions from the radially accelerating stagnation region

to the decelerating wall jet region [19]. Some studies examining local Nusselt number profiles have even observed a third peak for specific jet conditions [21].

As observed in Figure 10a, for confined submerged circular jets, the stagnation Nusselt number (centerline local Nusselt number) has been experimentally observed to decrease with increasing H/D_h as a result of entrainment of the flow back into the free jet region [21], and this entrainment of higher-temperature air degrades the thermal performance. Other experimental studies (Figure 10b) have, however, observed that the stagnation Nusselt number remains roughly constant for $H/D_h < 5$ [22]. These differing observations have been attributed to the different types of confinement in the wall jet region of the flow: two dimensional flow [21], *vs.* three-dimensional radial flow [22]. Such results suggest that jet impingement heat transfer is complex and that the geometry of the jet and its neighboring jets have a major effect on the thermal performance.

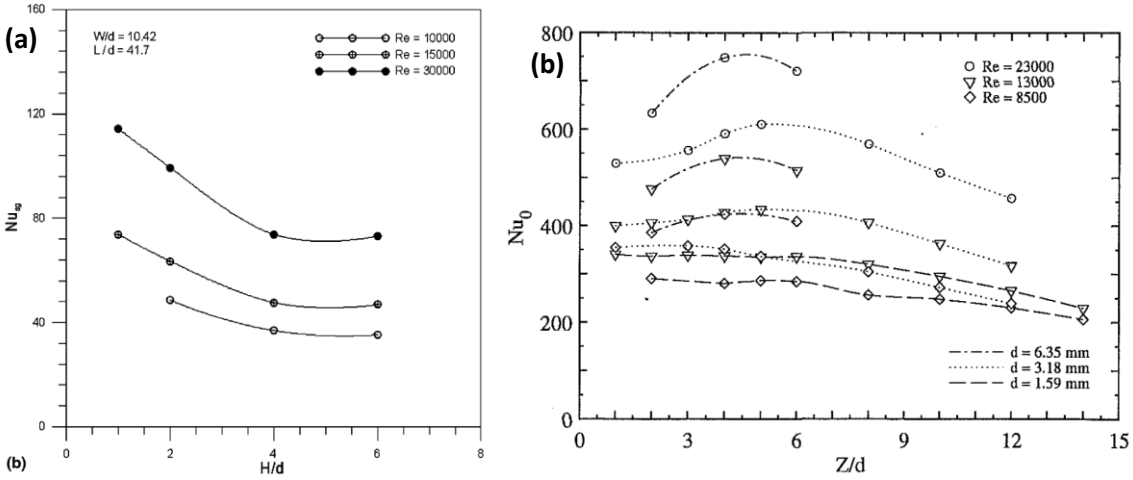

Figure 10. Stagnation Nusselt number against H/D_h (*i.e.* Z/D_h) for various Reynolds numbers in [21] (a) and [22] (b)

For jet impingement heat transfer, average Nusselt numbers $\overline{Nu}$ are commonly defined to be a function of the Reynolds number Re, the Prandtl number Pr, the area ratio between the nozzle and the impingement region A_r, and H/D_h. For dynamically similar experiments, $\overline{Nu}$ can be simplified as shown below:

$$\overline{Nu} = f\left(Re, Pr\right) \tag{7}$$

where

$$\overline{Nu} = \frac{\bar{h} D_h}{k} \tag{8}$$

$$Re = \frac{\rho V_e D_h}{\mu} \tag{9}$$

and ρ, V_e, and μ are the density, velocity of the fluid at the nozzle exit, and dynamic viscosity of the fluid, respectively [15]. Average heat transfer coefficients $\bar{h}$ are defined as:

$$\bar{h} = \frac{\overline{q''}}{(\overline{T_c} - T_e)} \tag{10}$$

where $\overline{q''}$ is the average heat flux through the surface, $\overline{T_c}$ is the average temperature of the surface, and T_e is the temperature of the fluid leaving the nozzle.

For cooling applications, jets are typically found in arrays of multiple slots or holes. The use of multiple jets can increase the cooled surface area but will typically complicate the dynamics of the flow and appropriate layout of the nozzles is required to effectively cool this larger area. Typical arrangements for round and slot jet arrays are depicted in Figure 11.

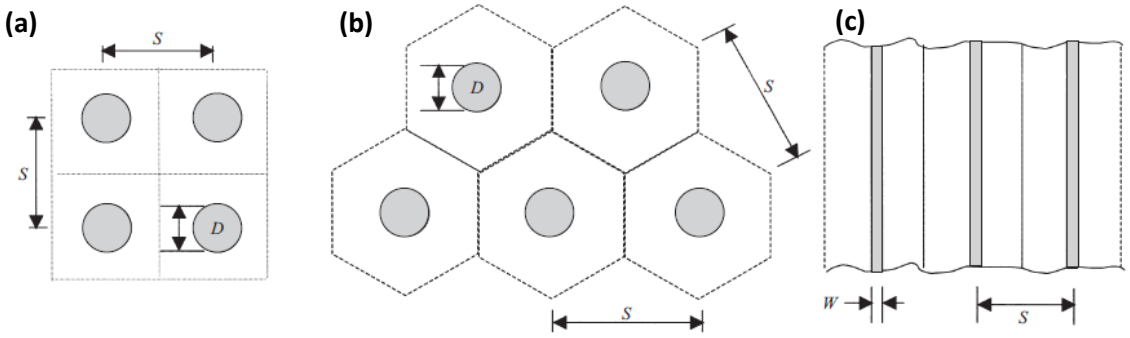

Figure 11. Jet array configurations for (a) in-line round jets, (b) staggered round jets, (c) and slot jets [14]

The dynamics of jet arrays has been studied both experimentally and numerically by a number of researchers [19,23,24,25] and guidelines and correlations have been developed based on this body of work. Critical to the performance of multiple jet arrays is the spacing between jets relative to the height of the jets. For a fixed jet height, as the jets move closer together, there is interference that occurs between the free jet and stagnation regions of adjacent jets. This interference, depicted in Figure 12a, is believed to weaken the jet strength and degrade the performance [23]. As the jets move further apart, a jet fountain can occur where the bifurcating streams of each jet recirculate back up into the free jet region of each respective jet, depicted in Figure 12b. This can also reduce the performance as higher-temperature fluid is re-entrained into the primary jet streams [23]. Fountains were observed experimentally in the well-known work of Saripalli [25].

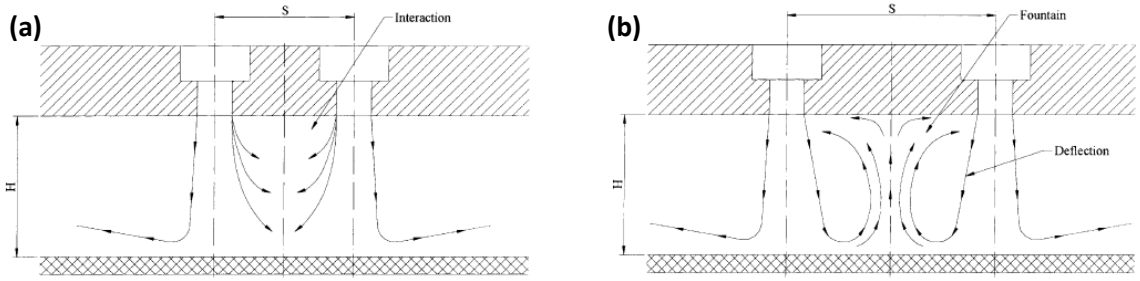

Figure 12. Schematic of two adjacent jets showing the effect of jet spacing on the profiles for jet interference before impingement (a) and jet fountains (b) [23]

For arrays of staggered circular jets where fountains occur between jets, the stagnation Nusselt number will be reduced and may be lower than the secondary peak that occurs at the transition between the stagnation region and the wall jet region [23]. As the spacing between jets increases further, high-temperature gas can escape (*i.e.*, there is no formation of fountains) and the Nusselt number values increase and form a bell shaped profile [23]. As the spacing between jets increases even further, the Nusselt numbers will eventually decrease, because each individual jet will no longer be able to

adequately cool its portion of the heated surface. This suggests that there is an optimal jet spacing for a given array of jets. Also, for a given height, this optimal spacing appears to be independent of the Reynolds number [23]. The optimal spacing will, however, depend on the jet to wall spacing because the conditions under which fountains will form depend on this parameter [23].

In addition to the geometrical arrangement of jet arrays, the venting of spent coolant from the system is imperative to the overall heat transfer from the impingement surface [15]. For an array of jets, coolant is typically not designed to flow normal to the impingement surface between the jets to exhaust. In such cases, spent coolant is often forced to re-entrain back in the free jet region of each respective jet reducing the performance. The analysis is further complicated by the shape of the cooled surface. For concave surfaces, such as those most likely encountered in helium-cooled divertors like the HEMJ (discussed in Section 2.2.1), the exhaust is more likely to become re-entrained in the jet flow region and jets near the axis of the divertor (at the center of the array) do not have means to exhaust the coolant [26]. However, both the distance between the nozzle and the surface and the diameter of the surface to the jet diameter play a strong role in the behavior of the jet.

Most modular helium-cooled tungsten divertor designs utilize jet impingement as a means to improve heat transfer coefficients including, but not limited to, the HEMJ, HEMP, and HCFP modules. These designs are discussed in more detail in the next sections. Typically, most designs are limited to small nozzle to surface distances $H/D_h < 2$, which is outside the range of most of the Nusselt number correlations that have been developed (*i.e.* Martin [19]). Although a few correlations that are valid at low jet to wall spacings exist [20], it is unclear if they are valid in the confined geometries typical of divertors, much less, for the complex jet arrays, concave surfaces, and high jet

Reynolds numbers typical of divertors. Each specific divertor design must therefore be experimentally and numerically analyzed.

2.1.3 Porous Media

Another method to improve the thermal performance of divertors involves the use of porous media. An insert made of a porous medium, such as a metallic foam, acts in a manner similar to cooling fins in that it significantly increases the cooled surface area over which cooling occurs. In addition, it aids in conduction heat transfer perpendicular to the surface. The porous medium itself can take many forms such as a bed of small spheres or an irregular foam, and it is typically composed of a highly conductive material such as a metal to improve conduction through the material. The complex nature of the flow through a porous medium (particularly irregular medias) makes it difficult, if not practically impossible, to develop analytical correlations. Empirical correlations based on experimental databases are therefore usually relied upon for more complex geometries.

While not studied in this work, porous media inserts have been proposed as a means to increase heat transfer coefficients for several helium-cooled divertors for more than a decade [27]. As such, it deserves special mention since it frequently appears in divertor research, and using porous media with helium cooling has been cited as a means to cool very high heat fluxes up to 40 MW/m^2 [28]. One of the earliest candidates for a helium-cooled divertor was a concept using either small packed spheres or a metallic foam [27], as shown Figure 13.

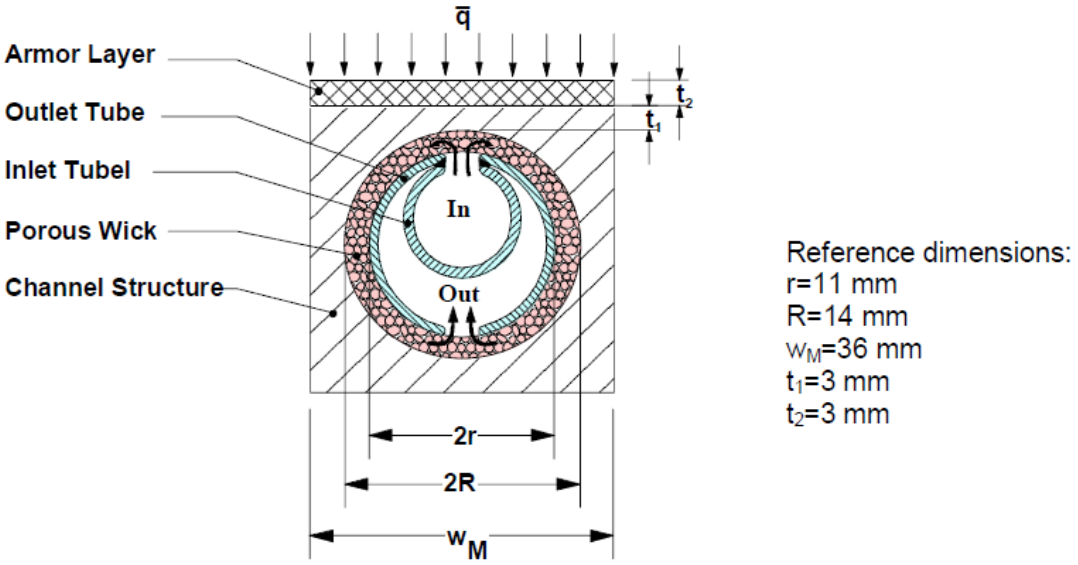

Figure 13. Cross section of the porous media concept [27]

As with cooling fins, the presence of the porous medium increases the pressure drop. For divertors, this is a critical parameter that affects the overall efficiency of the plant since an increase in pressure drop will increase the power required to pump the coolant at a desired flow rate. The Darcy flow model can be used to estimate the pressure drop ΔP in a given direction through a porous medium in terms of knowing the volume averaged velocity $\overline{u_{pm}}$ as shown below:

$$-\Delta P = \frac{\overline{u_{pm}}\mu}{K} \tag{11}$$

where μ is the dynamic viscosity and K is a proportionality factor called the permeability of the porous media that is determined experimentally or analytically for simple geometries [14]. Gayton et al. [29] investigated the use of porous media in the HCFP divertor design (Section 2.2.3) using Ultramet molybdenum foam with an 88% porosity in the jet impingement region. For the best configuration tested, they reported that there was considerable improvement in the HTC of 52% at the cost of an increase in pressure drop of approximately 87%.

2.2 Modular Helium-Cooled Tungsten Divertor Designs

Several modular helium-cooled tungsten divertor designs will be discussed in this section emphasizing those designs considered in this work. Most designs have undergone significant revisions since their original conception, and these changes will be addressed where relevant; however, several aspects (*e.g.* the alloys, coolant temperature operating window, and geometric dimensions) remain the topic of active research and may well change in the near future.

2.2.1 HEMJ

The most widely researched and developed design to date is the modular He-cooled divertor concept with multiple-jet-cooling (HEMJ). This design was first conceived in 2005 [10] as an alternative 'finger-type' to existing designs such as the modular He-cooled divertor concept with pin array (HEMP) and the modular He-cooled divertor concept with slot array (HEMS). Both the HEMP and HEMS designs are discussed later. Finger-type designs, such as the HEMJ, derive their name from a single module's cylindrical shape, which is oriented perpendicular to the plasma. Hexagonal or square tiles of pure tungsten are brazed to each module to form the actual plasma-facing surface.

An HEMJ module is depicted in Figure 14. In this design, He at approximately 600 °C and 10 MPa flows axially through a cylindrical steel jet cartridge and is then accelerated through an array of holes as jets to impinge on the underside of the plasma facing surface. The helium flows radially outward, then through the annulus between the jet cartridge and the thimble, exiting the module at ~700 °C. In the early designs, it was estimated that flow rates of about 6.8 g/s would be required to cool ~12 MW/m^2 [30,31]. The thimble is made of W-1%La_2O_3 (WL10) and is brazed to a ODS Eurofer steel

structure that connects the module to a manifold. The WL10 thimble has a 15 mm OD and a thickness of 1 mm. A hexagonal 18 mm flat-to-flat pure tungsten tile is then brazed to the top of the WL10 thimble that acts as the plasma facing surface. A significant amount of this tungsten tile is expected to be lost (*i.e.*, sputtering, melting, sublimation) during the lifetime of module.

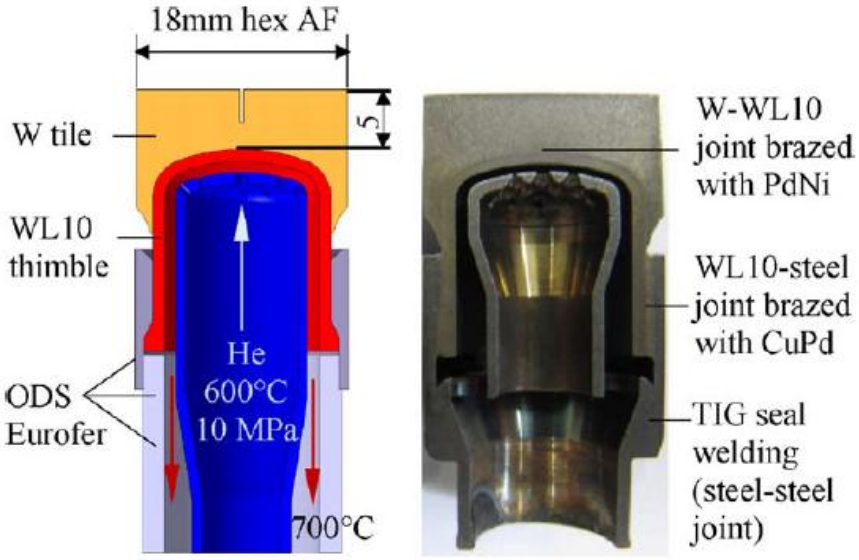

Figure 14. Cross section of the HEMJ module (left) and constructed HEMJ module (right) [32]

Each individual module is combined with 8 others to form a 9-finger module that uses a common inlet and outlet for helium. Several of these 9-finger modules are attached to a long hexagonal manifold to form a ‘stripe-unit’. Finally, each stripe unit is aligned with other units to form the target plate for the divertor [33,34]. Each of these stages of the assembly is depicted in Figure 15.

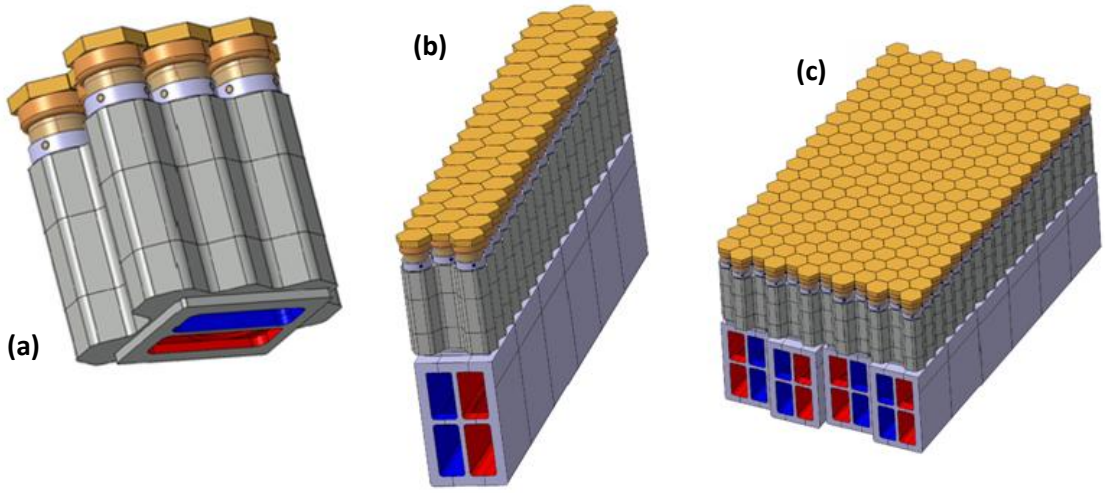

Figure 15. The three stages of the HEMJ assembly to form the target plate: the 9-finger module (a), the stripe-unit (b), and the target plate (c). [33]

Perhaps the greatest disadvantage of the HEMJ design is that a large number of modules are required to completely cover the divertor surface. It is estimated that as many as 500,000 individual modules [35,36,37] may be required to completely cover a plasma-facing surface with an area $O(100\ m^2)$. This large number of units, and more importantly, the difficulties in evenly distributing helium over that many units, presents an enormous design challenge for future commercial fusion power plants and reducing this complexity is an area of active research [32].

The HEMJ design, unlike most other divertor designs, has been studied in a number of experiments. The first experiments were performed at the Gas Puffing Facility (GPF) by Forschungszentrum Karlsruhe (FZK) in 2004-2005 using the 'reverse heat-flux method' (this method is detailed in Section 2.3.1) [30,38]. The highlights of the experimental results showed that for a nominal flow rate or 6.8 g/s, the 'J1a' variant of the HEMJ design could accommodate an incident heat flux of 12.5 MW/m^2 without exceeding the operating temperature limits. These results were also consistent with numerical simulations of the design using FLUENT® that showed the maximum thimble

temperature would not exceed 1300 °C, the specified recrystallization temperature for WL10 [11]. Moreover, the HEMJ design has been experimentally studied at prototypical conditions, specifically in high heat flux experiments performed on mockups from 2006 to 2008[34,39,40]. The Efremov Institute and the Karlsruhe Institute of Technology (KIT), formerly FZK, used a combined helium loop and 60 kW, 27 keV electron-beam facility to simulate the steady-state performance of the HEMJ with 600 °C He at 10 MPa for heat fluxes of 5-14 MW/m^2 (Section 2.3.4). These experiments were the first experiments performed at prototypical conditions (*i.e.* ~600 °C, 10 MPa, and 10 MW/m^2) for a modular helium-cooled tungsten divertor. Several variations of the HEMJ design were tested in this set of experiments with different brazing materials and dimensions. The experiments were also conducted at various flow rates for different cycles of heat loads (one of the mockups survived 1114 cycles). The results of these experiments indicated that the HEMJ design could accommodate heat fluxes >10 MW/m^2 albeit at higher mass flow rates of ~13 g/s and lower inlet temperatures <550 °C to avoid damage (due to joining of the various tungsten and steel components). A 9-finger unit was also tested for short durations with flow rates varying between 20 g/s and 100 g/s. Pressure drop was consistent with a single module, and the temperature distribution over the surface of the nine-finger unit was shown to be uniform. In 2010, more tests were conducted on six HEMJ modules, which all successfully survived over 200 heating cycles without significant damage [32].

Crosatti et al. [41] conducted experiments on an HEMJ module to evaluate the thermal performance for various Reynolds numbers utilizing dynamic similarity. The experiments were conducted with room temperature air at inlet pressures <1.4 MPa flowing through a brass module. A cartridge heater providing incident heat fluxes as great as 1 MW/m^2 was used as the heat source. The experimental results were

compared with predictions from numerical simulations performed in FLUENT® 6.2. The Nusselt numbers at various Reynolds numbers estimated from cooled surface temperatures measured with embedded thermocouples were in good agreement with the numerical predictions, but the discrepancies in pressure drops obtained at various Reynolds numbers were as great as ~12%, with the experimental measurements consistently higher than the numerical predictions.

Rader et al. [42] performed further experiments on the same module, developing generalized design curves that could be integrated into system codes used in optimization of fusion reactors. Again taking advantage of dynamic similarity, the experiments were conducted with room temperature air, helium, or argon at inlet pressures <1.4 MPa flowing through a brass or steel module. The module was heated with an oxy-acetylene torch to create incident heat fluxes as great as 3 MW/m^2. Nusselt numbers were again calculated from cooled surface temperatures measured with embedded thermocouples. Correlations for the Nusselt number and pressure loss coefficient, based upon measurements of pressure drop through the test section, were generated. These correlations were then extrapolated to prototypical conditions and generalized design curves were generated showing the maximum heat flux the design could accommodate for various Reynolds numbers without exceeding different maximum tungsten alloy temperatures $\overline{T_s}$ and pumping powers, quantified as the fraction of the incident thermal power β. The maximum incident heat flux the design could accommodate was plotted for $\overline{T_s} = 1100$, 1200, and 1300 °C (where tungsten alloys typically approach their recrystallization temperature) and $\beta = 5$, 10, 15, and 20%. This chart is depicted in Figure 16.

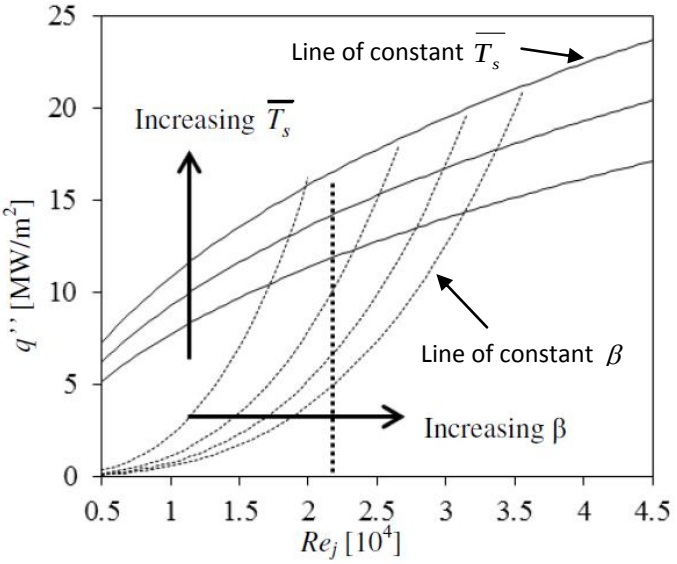

Figure 16. Prototypical design curves for the HEMJ for maximum alloy temperatures $\overline{T_s}$ = 1100, 1200, and 1300 °C and β = 5, 10, 15, and 20%. Dashed vertical line indicates Reynolds number of 2.14×10^4 for 6.8 g/s [42]

The results in Figure 16 were created from experiments using various coolants and test section material combinations. Although there are minor differences in the HEMJ design used by Rader and those specified in the original HEMJ design (*e.g.* a wall thickness of 2 mm, *vs.* the 1 mm specified in the original design), the results are largely in agreement with those from the gas puffing experiments performed at KIT with a maximum heat flux on the tile of 11.4 MW/m^2 for 1300 °C maximum alloy temperature. To further confirm the validity of the correlation, however, experiments must be performed under conditions closer to the prototypical values, specifically at higher incident heat fluxes and coolant inlet temperatures and pressures, which is the subject of this thesis.

2.2.2 HEMP/HEMS

The earliest modular tungsten helium-cooled finger-type divertor design was the helium-cooled modular divertor concept with integrated pin array (HEMP) by Diegele et

al. in 2003 [18]. One of the most important motivations in developing a finger-type divertor is to minimize thermal stresses to accommodate higher heat fluxes [37]. In addition, the divertor can achieve very high heat transfer coefficients with enhancements if appropriate while ensuring that the total coolant pumping power is less than 10% of the incident power. For the HEMP design, this was accomplished using an array of pin fins on the cooled surface to enhance heat transfer. The design underwent many modifications over several years [43] before being largely abandoned in favor of the geometrically simpler HEMJ design. However, the need for higher heat transfer coefficients has renewed interest in this design and also in the use of fin arrays in general.

A single HEMP module is depicted in Figure 17. In the original design, helium enters the annulus created by the thimble with an ID of 12 mm and an OD of 14 mm and tube with an ID of 5 mm and an OD of 5.6 mm at 600 °C and 10 MPa. After reaching the cooled surface, the helium then flows across an array of pin fins affixed to the surface before being redirected out the inner tube at a temperature of approximately 700 °C. The thimble is made of WL10 and the tube is made of ODS Eurofer steel. A square 5 mm thick pure tungsten tile brazed onto the top of the thimble which, forming the plasma facing surface. The WL10 thimble is then brazed to an ODS Eurofer steel manifold.

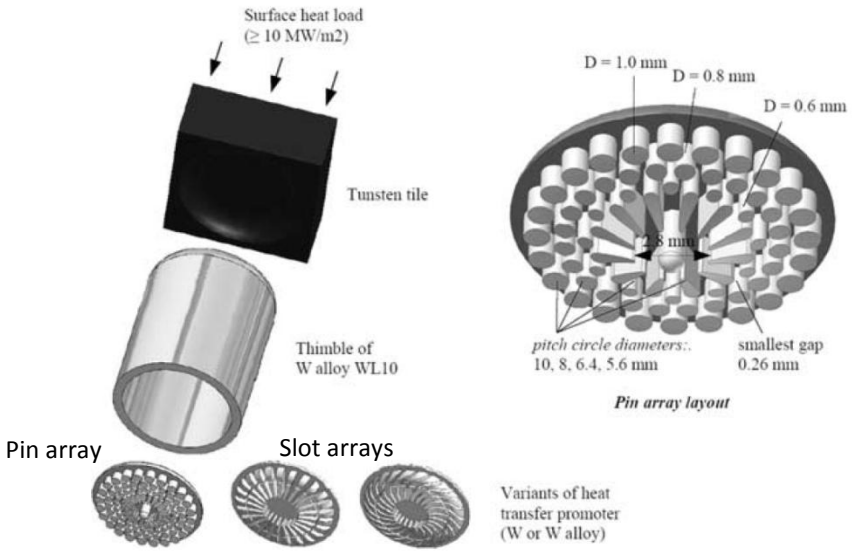

Figure 17. HEMP module depicting tile, thimble, and three different cooling arrays (left). The primary pin fin array in more detail (right) [43]

The use of a pin array to enhance heat transfer coefficients in helium-cooled divertors was conceived in early iterations of the HCFP design (referred to as the 'modified slot concept') [17], but it was adopted for finger-type designs with the emergence of the HEMP. As seen in Figure 17, the pin array in the original design was supposed to be fabricated separately from the thimble. However, the fin array can be machined directly into the thimble's cooled surface using electro-discharge machining (EDM) although early attempts to achieve this in WL10 were unsuccessful, as shown in Figure 18. It is unclear, however, whether it is practical to fabricate such fin arrays using EDM in hundreds of thousands of tungsten alloy modules. Another cooling array also depicted in Figure 17 is the slot array. The use of the slot array with this design is commonly referred to as the HEMS design (helium-cooled modular divertor concept with integrated slot array). Using a slot array in lieu of a pin-fin array would simplify the machining of the cooled surface. The HEMS design was experimentally tested at

prototypical conditions in conjunction with the HEMJ design at incident heat fluxes of 9 MW/m^2, and successfully accommodated 100 heating cycles [39].

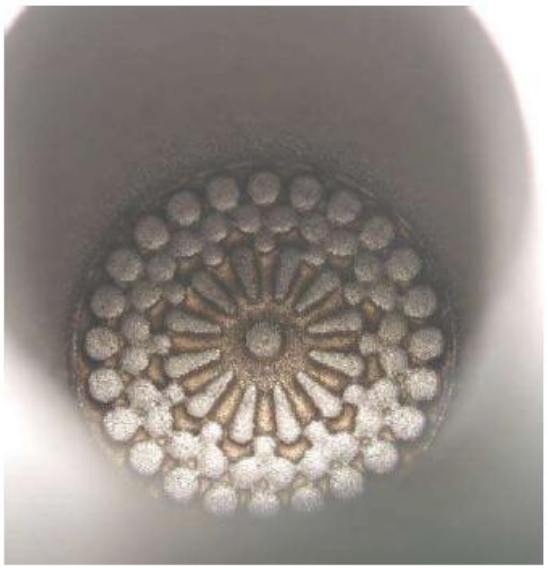

Figure 18. Failed pin array structure in WL10 after EDM [44]

While the original design specified helium flow entering through the annulus, later iterations reversed the direction of the flow [33], similar to that in the HEMJ, to exploit the additional advantage of an impinging flow. As such, the end of the tube became a contraction ending in a smaller orifice to create a jet at the expense of increased pressure drop.

2.2.3 HCFP

The helium-cooled flat plate (HCFP) design originated from the 'modified slot concept' developed by Hermsmeyer and Malang in 2002 [17] as an alternative to the leading helium-cooled porous media design. This design was created to increase the maximum sustainable steady-state heat flux to 10 MW/m^2 by shortening the conduction paths from the surface to the coolant and reducing thermal stress (*i.e.* temperature gradients). Although originally not a modular design, this feature was integrated in later

iterations [35]. The ‘flat plate’ moniker derives from the rectangular shape of the cross section where the plasma facing surface forms a flat surface with adjacent units. Divertors of this type are also commonly referred to as ‘plate-type’ divertors. The latest iterations of the design are depicted in Figure 19.

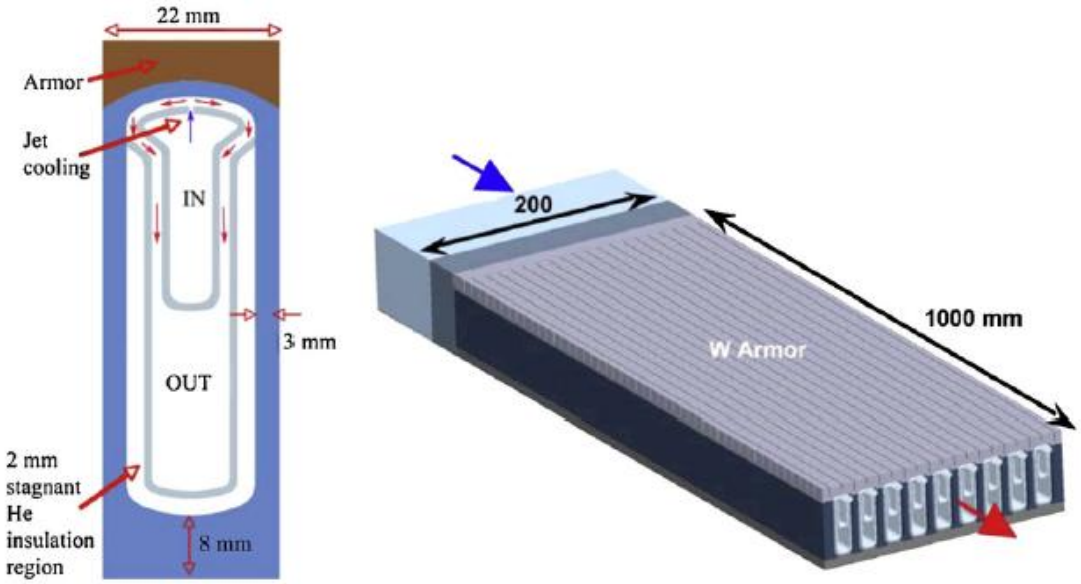

Figure 19. A cross section of a single HCFP channel (left) and a solid model of a HCFP module consisting of 9 channels in parallel [36]

In this design, helium at 10 MPa and 600 °C enters a channel and flows longitudinally through an upper enclosed manifold. The flow is then accelerated vertically through a narrow 0.5-2 mm slot that runs the length of the upper manifold to impinge on and cool the underside of the plasma facing surface. Finally, the flow is then directed outward through the gap created between the upper and lower manifolds where it is ultimately removed through the lower manifold. The upper manifold is tapered such that the flow through the slot is uniform along its length as shown in Figure 20. A small region of stagnant He at the bottom of the lower manifold insulates the divertor from the surrounding structure.

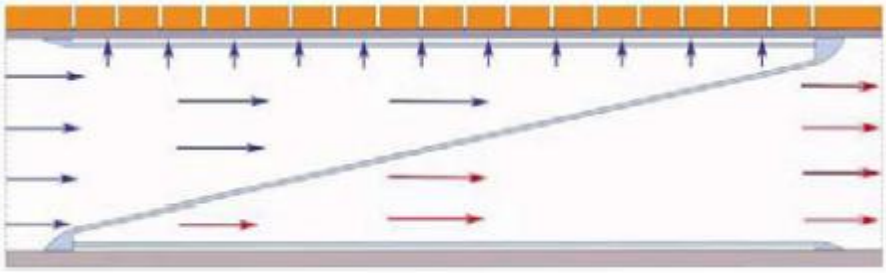

Figure 20. Schematic of the HCFP depicting the tapered channel to encourage uniform flow through the slot along its length [35]

Numerical simulations suggest that this design could accommodate peak heat fluxes of approximately 10 MW/m^2 while keeping pumping power less than 10% of thermal power [35] with some estimates putting the maximum peak heat flux as low as 8 MW/m^2 [36,37]. Dynamically similar experiments performed by Hageman et al. [45] using air at room temperature and an inlet pressure of <700 kPa on a brass HCFP module have indicated that a HCFP at prototypical conditions can endure peak heat fluxes up to 14 MW/m^2 and up to 18 MW/m^2 with an array of cylindrical pin fins attached to the cooled surface that span the entire gap between the jet exit and the cooled surface for prototypical jet Reynolds numbers of 3.3×10^4. The experiments also showed that this maximum heat flux was unaffected by slot width (2 mm *vs.* 0.5 mm). Gayton et al. [29] also performed dynamically similar experiments using molybdenum open-cell foam (Ultramet) of 88% porosity or 65 pores per inch between the slot jet and the cooled surface to enhance heat transfer; this modification did increase the heat transfer coefficient by 52%, but at a significant cost in pressure drop of 87%. Again, further studies are required to determine if these dynamically similar predictions are valid for different combinations of coolant and test sections materials (primarily helium with a WL10 cartridge), as discussed further in Chapter 4 and Chapter 5**.**

The principal advantage of this design is its geometric simplicity and its ability to cover large areas of the divertor region in the reactor. Approximately 750 modules [36,35,37] would be required to cover the divertor surface with an area $O(100\ m^2)$ compared to several hundred thousand for finger type divertors.

2.2.4 Other Designs

Several other modular helium-cooled tungsten divertors have been proposed that are in varying stages of development. Perhaps the most developed of these concepts is the ARIES T-Tube divertor concept [37,46] developed as part of the ARIES-CS study. Although originally proposed for a stellarator type reactor, the design criteria are the same for tokamaks. A T-Tube module is depicted in Figure 21. In this design, helium at 600 °C and 10 MPa enters the central channel which ends in the center of a 100-150 mm long perpendicular tube made of a tungsten alloy with a 0.5 mm slot along its length. The flow accelerates through the slot, cools the inside surface of a larger 15 mm diameter tungsten alloy tube, and exits azimuthally around the inner tube before leaving through channels parallel to the incoming helium. Pure tungsten armor sits atop the outer tungsten alloy tube, and serves as the plasma facing surface. An estimated 110,000 modules would be required to cover a divertor with an area of $O(100\ m^2)$ [36,35,37].

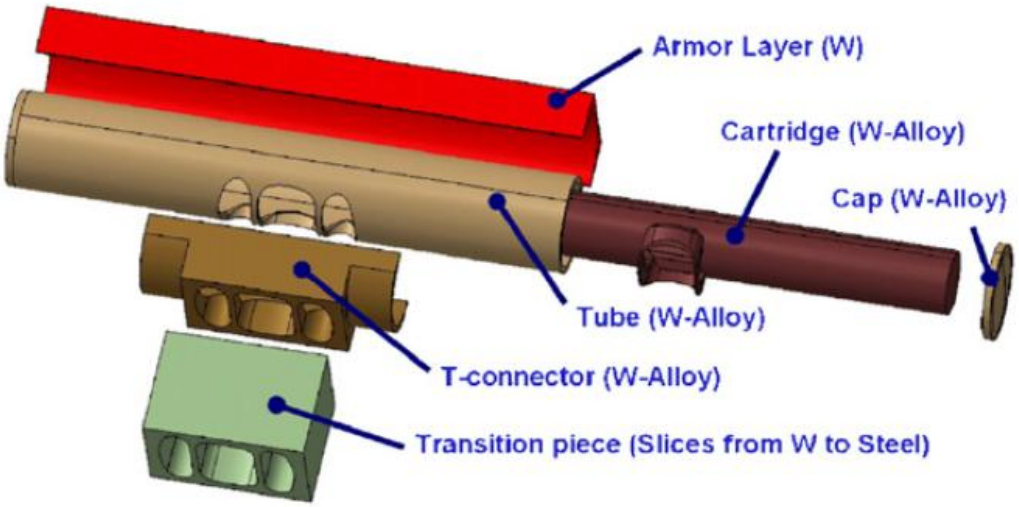

Figure 21. Solid model of the T-Tube divertor concept [47]

To the author's knowledge, the only experiments performed on the T-Tube design are the dynamically similar studies performed by Crosatti et al. [48,49]. These experiments were performed using air at room temperature and inlet pressures <500 kPa through brass test sections. Incident heat fluxes as great as 0.85 MW/m^2 were obtained using electrical heater cartridges embedded in a tapered copper heater block. Numerical simulations performed with FLUENT® were validated with surface temperature measurements obtained in the experiments using thermocouples embedded near the cooled surface of the test section, and used to calculate Nusselt numbers as a function of Reynolds number. These validated numerical simulations were then used to predict the performance of the T-tube divertor at prototypical conditions.

A thorough thermo-mechanical analysis of the T-Tube design was performed at FZK by Ihli et al. [47] using FLUENT®. The results of these simulations indicated that the design could accommodate heat fluxes of 10 MW/m^2 while maintaining a maximum alloy temperature of <1300 °C. Furthermore, simulations performed with ANSYS Workbench® showed that the maximum thermal stress was less than the maximum of 370 MPa

specified for the tungsten alloy. Although this design has been shown numerically to be able to withstand heat fluxes of 10 MW/m^2, it is unclear if it is possible to further increase its thermal performance [37].

While the precise steady-state heat flux profile incident upon the plasma-facing surface in future reactors is unknown at present, a common approximation is to use a Gaussian profile with a peak of 10 MW/m^2 [37,47]. Some experimental measurements have been made in other reactors using thermocouples, Langmuir probe arrays, and infra-red cameras that show that this is a reasonable assumption [9]. Given that sections of the plasma-facing surface will not be subject to the maximum heat flux of 10 MW/m^2, it may be feasible to use other designs with reduced thermal performance in these areas that are simpler to manufacture and less expensive. This would greatly reduce the cost of the divertor. Designs of this type are often referred to as 'integrated designs.'

Such an integrated design combines the HEMJ and HCFP designs depicted in Figure 22 [36,37]. Here HEMJ-like modules, integrated into the HCFP manifold cools the parts of the plasma-facing surface of the divertor receiving >6-8 MW/m^2, while the traditional HCFP design is used in areas where the heat flux <6-8 MW/m^2. This integrated approach would use helium at temperatures and pressures similar to the HCFP and HEMJ designs (~600-700 °C and 10 MPa), but would change the manifolding and dimensions for each HEMJ module. Each HEMJ module would have 18 mm OD as opposed to the 15 mm OD in the original design. With these changes, ~87,820 HEMJ modules would be required compared to the original estimate of 500,000.

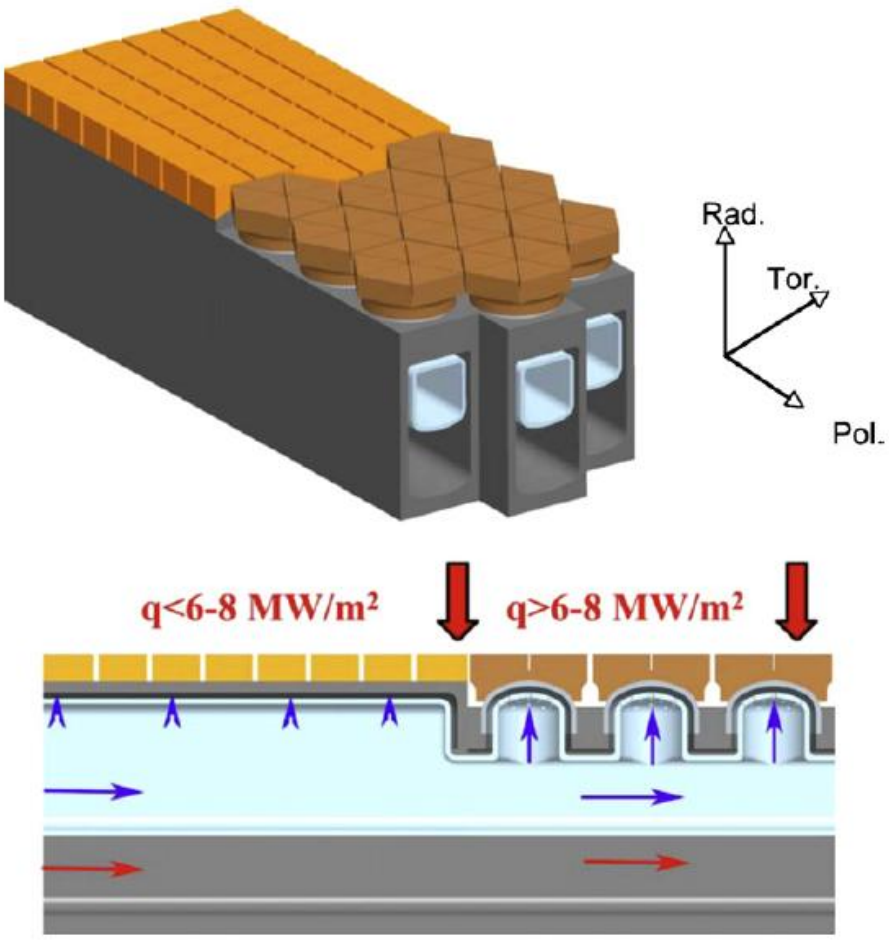

Figure 22. Integrated HCFP and HEMJ design [36]

2.3 Helium Loops

A number of experimental facilities have been constructed to test the performance of helium-cooled components for fusion research. This section briefly describes four of these helium loops in Europe, Russia, and the United States focusing on those that have been used for divertor research.

Helium is by nature difficult to contain, and building and maintaining loops using helium at prototypical conditions for divertors (~600-700 °C and 10 MPa) presents many

challenges. In addition to these conditions, providing the expected incident steady-state heat flux of 10 MW/m^2 on the test section significantly increases complexity and cost. Electron beams or plasma arc jets have been successfully used to supply incident heat fluxes of 10 MW/m^2, but typically require a large capital investment. As a result, few helium loops are capable of operating at prototypical conditions.

2.3.1 Gas Puffing Facility

One of the first facilities created primarily for testing modular helium-cooled tungsten divertors at near prototypical conditions was the Gas Puffing Facility (GPF) operated in partnership between Forschungszentrum Karlsruhe (FZK, now KIT) and the Efremov Institute [38,30]. This loop was in operation from 2003 to 2005. Unlike, traditional loops, the GPF was designed to run in pulses and could not sustain steady operation as its name suggests. However, during a pulse, which typically lasted ~100 s in later loop modifications, the loop could achieve 5-15 g/s of helium. The ultimate objective of the GPF was to compare the thermal performance of different designs and validate CFD simulations. The loop tested several early HEMJ modules and an HEMS module.

The first iteration of the GPF, referred to as GPF1, was used to measure pressure drops in different designs. This facility was modified to the GPF2 in order to evaluate the thermal performance. A diagram of the GPF2 is depicted in Figure 23. In this loop, source tanks at 16 MPa released helium through a regulator providing a steady 10 MPa to the test section. The pressure drop through the test section was then measured during each pulse. Helium is heated to the appropriate temperatures just before the test section and is cooled just after returning to the source tanks at room temperature. The compressor is used to recharge the source tanks to 16 MPa before performing the next pulse.

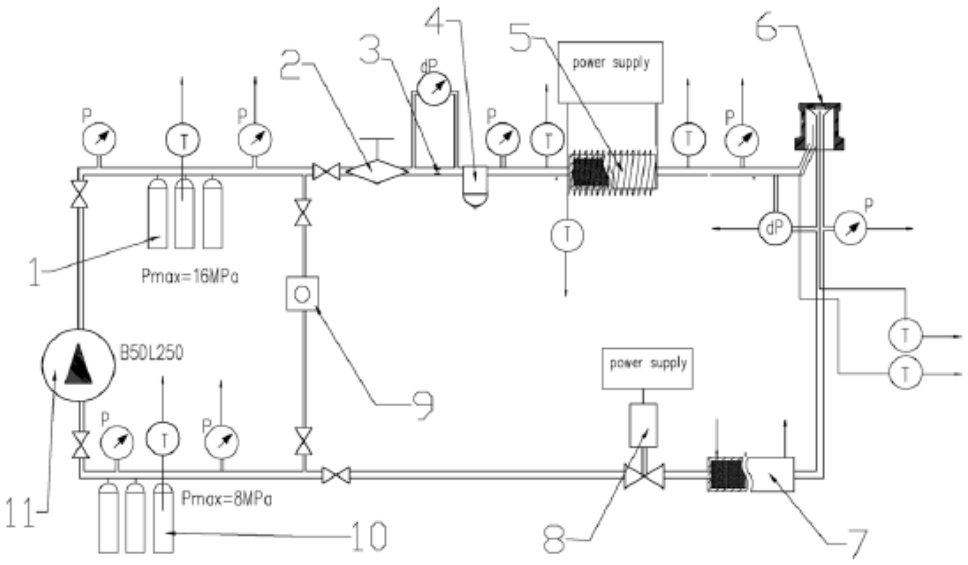

Figure 23. GPF2 schematic: 1) source tanks, 2) pressure regulator, 3) orifice meter, 5) heater, 6) test section, 7) cooler, 9) vacuum pump, 10) receiving tanks, 11) compressor [38]

One of the most novel aspects of the GPF2, is the use of the reverse heating method to measure the thermal performance. Instead of heating the test section, hot helium at ~650 °C that was heated just before the test section was cooled in the test section by a thin film of water at ~20 °C over the surface of the divertor module. Then computed HTCs and measured pressure drops were plotted for various flow rates to estimate the steady-state thermal performance of the various designs. The heater and cooler were constructed of 4 mm steel balls wrapped in either a NiCr resistor jacket for heating or a water jacket for cooling. Brass test sections were used with similar thermal conductivities to that of tungsten at prototypical conditions.

2.3.2 Sandia HeFL

A closed helium loop was constructed at Sandia National Laboratories as part of its high heat flux test facility called the Plasma Materials Test Facility (PMTF) [28]. The PMTF performs research on a variety of helium and water cooled high heat flux

components including heat exchangers, gyrotrons, microwave amplifiers, and other components with a particular focus on fusion related research. As a heat source for the facility, the Electron Beam-1200 KW System or EB-1200 is used which provides up to 1.2 MW of beam power and has achieved record heat fluxes of 140 MW/m^2 for water and 40 MW/m^2 for helium [28]. The facility underwent significant modification in the late 2000s to upgrade to the EB-1200 from the previous EB-60.

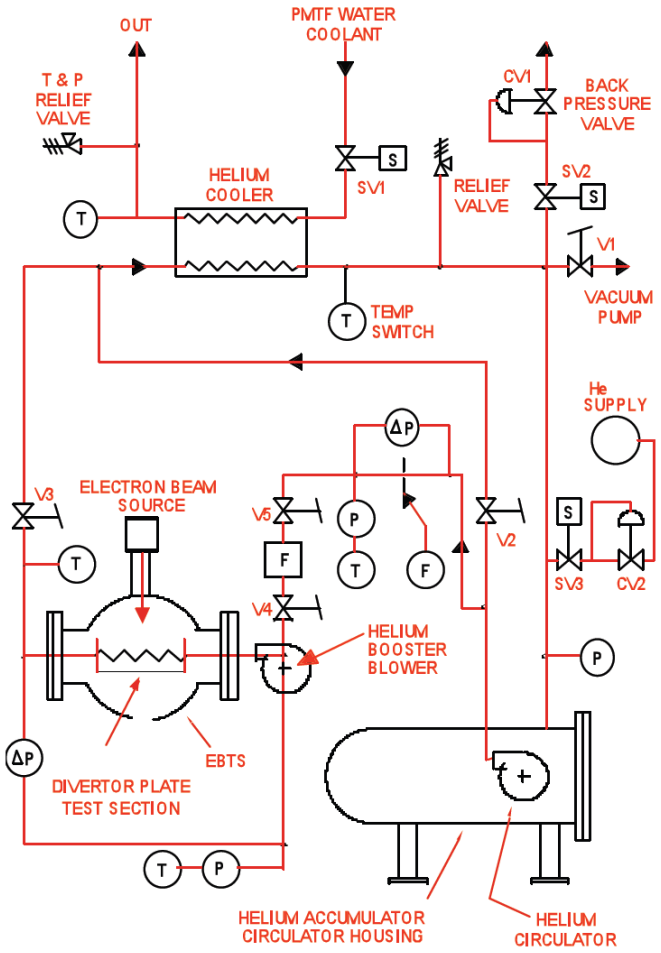

Figure 24. Diagram of the PMTF HeFL before upgrade [50]

The helium loop itself is capable of providing flow rates up to 100 g/s at pressures up to 4 MPa and temperatures up to 300 °C. The maximum pressure drop for steady flow is 55 kPa at 4 MPa. Although not designed specifically for testing modular

divertor designs, it has been used previously to test porous metal divertor modules indicating possible concerns for flow instabilities in helium-cooled divertors [51].

2.3.3 HEBLO

KIT also owns and operates a closed helium loop called the Helium Blanket Test Loop (HEBLO) that has been used to research various helium related first wall components including divertors [3,44,52,53]. The loop operates at 8 MPa with a helium flow rate up to 120 g/s. The maximum helium temperature is 430 °C with 60 kW of helium heating power. The loop was modified in 2004 to work with early mock-ups of finger-type divertors including the HEMJ, HEMS, and the HEMP. Surface heating is available up to 3 kW using an electric heater.

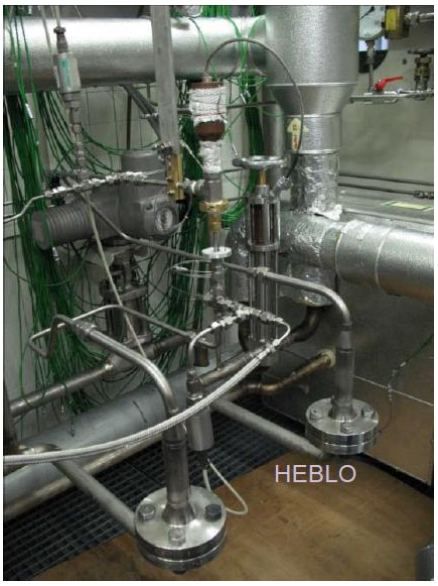

Figure 25. Image of HEBLO using brass HEMJ test section fabricated at Georgia Tech [3] used in Crosatti et al. [41] and Weathers et al. [54]

Most of the divertor experiments that were performed using HEBLO were used for early experimental verification of CFD simulations. In partnership with Georgia Tech, a brass HEMJ test section developed for the experiments conducted by Crosatti et al. [41] and Weathers et al. [54] was used to validate an ANSYS CFX® model with very

good agreement, giving heat transfer coefficients within 5% in all cases. However, further experimental divertor research was largely relocated to the combined helium loop and electron beam test facility at the Efremov Institute.

2.3.4 Efremov and KIT EB and Loop

The experimental facility at the Efremov Institute in partnership with KIT has a helium loop and electron beam that are capable of testing helium-cooled divertor modules at prototypical conditions [39,40]. A schematic and picture of the facility is depicted in Figure 26. This facility was designed as a successor to the GPF to ultimately provide the experimental evidence that individual modules and 9-unit modules could adequately cool 10 MW/m^2 without failure. In addition, it provides the capability to provide cyclic loading to the modules to document fatigue in the design. This facility conducted experiments on prototypical HEMJ mockups between 2006 and 2010.

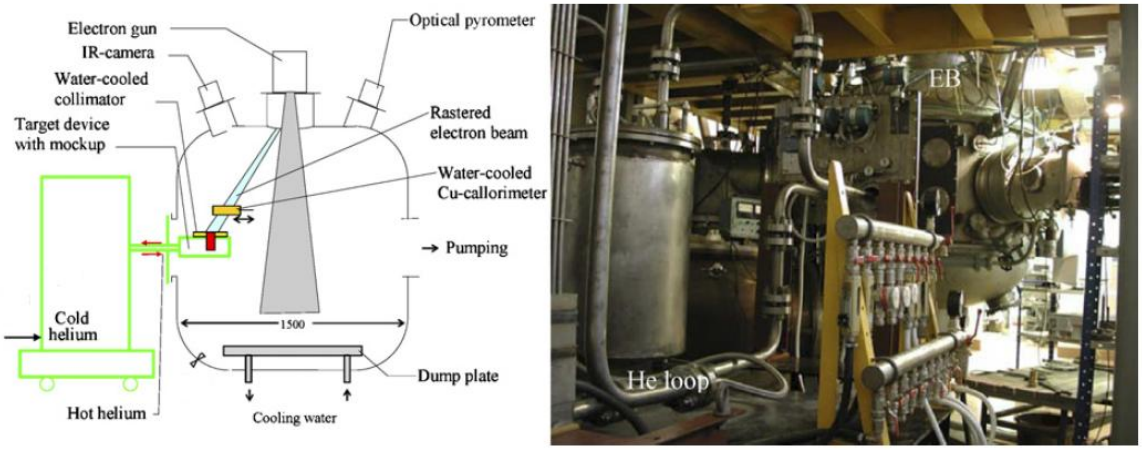

Figure 26. The Efremov and KIT Electron Beam and Helium Loop [40]

The helium loop was capable of providing ~5-15 g/s of helium at inlet conditions of 600 °C and 10 MPa in steady-state operation. In addition, with the electron beam, heat fluxes as high as 15 MW/m^2 could be tested. This loop mostly examined HEMJ

designs (with the exception of one HEMS design) fabricated using different manufacturing and bonding techniques.

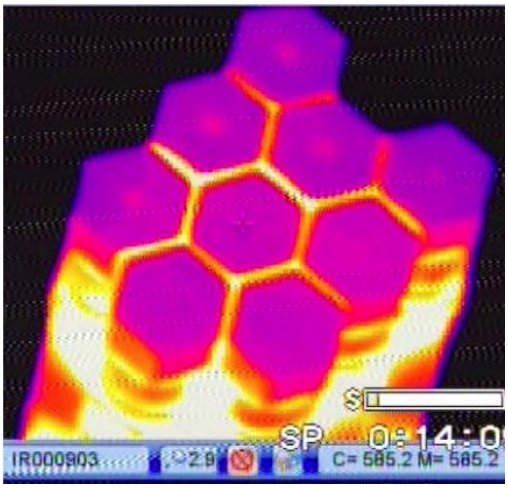

Figure 27. Infrared image of a 9-finger HEMJ module during test in the helium loop at 600 °C [39]

2.4 Numerical Simulations

Due to the extreme conditions under which divertors operate, performing experiments at prototypical conditions is both challenging and resource-intensive. The few experiments that have been conducted at these conditions are therefore for specific, well-developed geometries. Conducting dynamically similar experiments, as is the case for this work, can reduce resource and time requirements, but evaluating small changes in the geometry often requires the fabrication of new test sections. A faster, more economical alternative for evaluating different divertor designs involves the use of numerical simulations. Given the current availability of powerful commercial computational fluid dynamics (CFD) codes such as ANSYS FLUENT®, most numerical simulations are now performed with commercial CFD codes with appropriate validation by experimental measurements.

Although the exponential growth in computing power over the last 25 years has made it possible to perform direct numerical simulations (DNS) of the 3-D Navier-Stokes equations, even for turbulent flows, these simulations are still limited to basic geometries and relatively low Reynolds numbers, typically of $O(10^4)$ at most. In the complex geometries typical of helium-cooled divertors, it is therefore still necessary to use turbulence models to solve the governing equations. Hence, the choice of turbulence model is critical in accurately simulating the thermal-hydraulics of a divertor. Studies to determine the appropriate models for different helium-cooled divertors typically compare the predictions from different turbulence models with experimental measurements, when available. Therefore, experiments are not only useful in evaluating a specific divertor design, they also gather the data required to validate numerical models that can then be used to evaluate how modifying the existing design, or the operating conditions for the design, affect the thermal-hydraulic performance of the divertor.

The CFD simulations in this work use the commercial software package ANSYS FLUENT® to evaluate the turbulence models that, according to previous studies, have the best agreement with experimental measurements for similar geometries. The next sections summarize the relevant numerical work previously performed on helium-cooled tungsten divertors using commercial CFD packages and the turbulence models used in these studies.

2.4.1 Previous Work

An early comparison between different CFD commercial software packages was performed at FZK on one of the HEMJ designs (HEMJ1a) [44]. The packages evaluated included: Star-CD®, ANSYS Flotran®, FLUENT® and Cosmos®. The predictions for maximum thimble temperature from all of these commercial CFD packages, when used with the appropriate turbulence models, agreed within ~70 °C (with the exception of the

Cosmos package). The authors of the study therefore concluded, based on these numerical predictions, that this design did not exceed the material temperature limits, but also recommended that experimental studies be performed to validate these predictions. A parametric study on the geometry was also performed using FLUENT® (now ANSYS FLUENT®) with the realizable k-ε turbulence model at heat fluxes of 8-15 MW/m^2, mass flow rates of 5.3-15.5 g/s, and coolant inlet pressures of 10-14 MPa (only at a mass flow rate of 6.8 g/s). The results indicated that, the design could cool 12 MW/m^2 at a mass flow rate of 6.8 g/s, while the maximum tungsten alloy temperature remained below the recrystallization temperature of 1300 °C. Finally, the effect of varying the width of the gap between the jet exits and the cooled surface and the jet hole diameters was also investigated; the results indicated that the hole diameter had a strong effect, but the gap width had little effect, upon the pressure drop. The heat transfer coefficient, however, depended on both parameters.

Koncar et al. [55] used ANSYS CFX® 11.0 to develop a 3-D numerical model to study the optimal diameter and distributions of the jet holes in the cartridge of the HEMJ design. Two mass flow rates, namely 6.8 g/s and 13.5 g/s and eight different nozzle configurations, including the reference design, were examined in this study. The numerical model, a 30° 'wedge' of the HEMJ with periodic boundary conditions, consisted of a hexagonal mesh with 400,000 elements (Figure 28). The simulations were validated using the maximum tile temperature measurements from the high heat flux experiments performed at Efremov [32], and good agreement was found between the simulations and the experimental measurements at a heat flux of 10 MW/m^2 using the SST k-ω turbulence model (Figure 28). This study suggested that a jet array of nozzles, all with the same exit diameter of 0.62 mm, gave the lowest tile temperatures. This model was refined further in 2012 [56] by including a more accurate profile of the

incident heat flux, radiative losses (since the Efremov experiments were performed on an uninsulated test section in a vacuum), and more accurate correlations of how the material properties depended upon temperature, and this improved model gave predictions that were in better agreement.

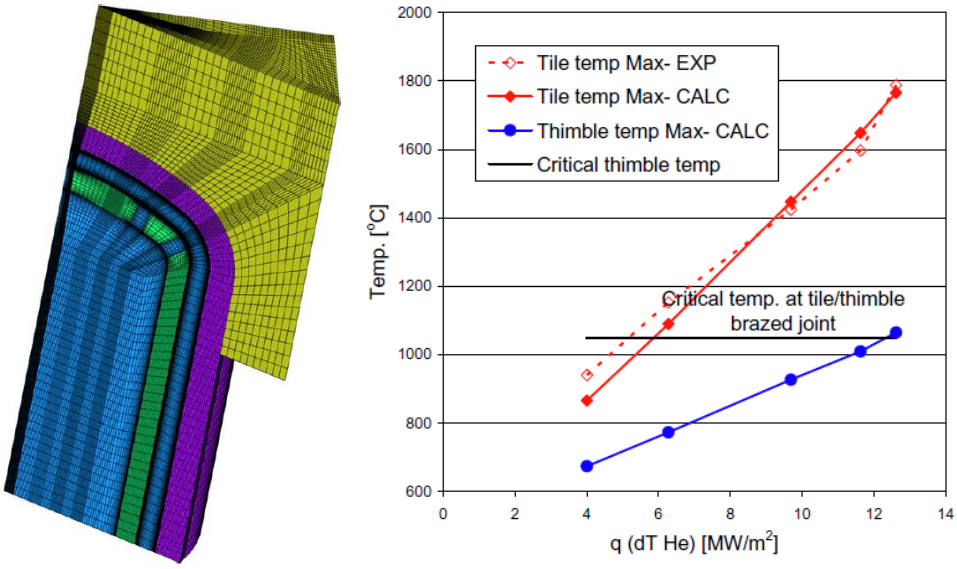

Figure 28. Hexagonal mesh of the 30° section of the HEMJ used in Koncar et al. (left) and the maximum tile temperature compared between experiments and the simulations (right) [55]

Several numerical models using FLUENT® or ANSYS FLUENT® have been developed at Georgia Tech since 2007 of the T-Tube, HCFP, HEMJ, and a variation of the HEMP and validated against dynamically similar experiments using air as a coolant. Crosatti et al. created 3D models of two different dynamically similar T-Tube experiments conducted in 2007 [48] and 2009 [49]. Both models consisted of a hexagonal mesh with ~1×10^6 cells with a finer spatial resolution near the walls to resolve the boundary layer. The models also took advantage of symmetry using a half model [48] and a quarter model [49] as appropriate. The standard k-ε turbulence model was used, and found to give results that were nearly identical to those obtained using the more computationally intensive RNG k-ε model. The temperatures predicted by the

simulations agreed with the experimental measurements, at least within their uncertainty, and pressure drop was also accurate for Reynolds numbers >1.9×10^4.

Weathers et al. [54] and Crosatti et al. [41] also developed a numerical model of the HEMJ in FLUENT® that was validated by measurements from dynamically similar experiments. This 3-D half model (limited to half symmetry by the manifold), depicted in Figure 29, consists of ~1.4×10^6 tetragonal/hybrid cells with a finer mesh in the jet impingement region. The simulations again used the standard k-ε model with standard wall functions. These simulations also gave temperature predictions that agreed with the experimental measurements from embedded thermocouples within experimental uncertainty.

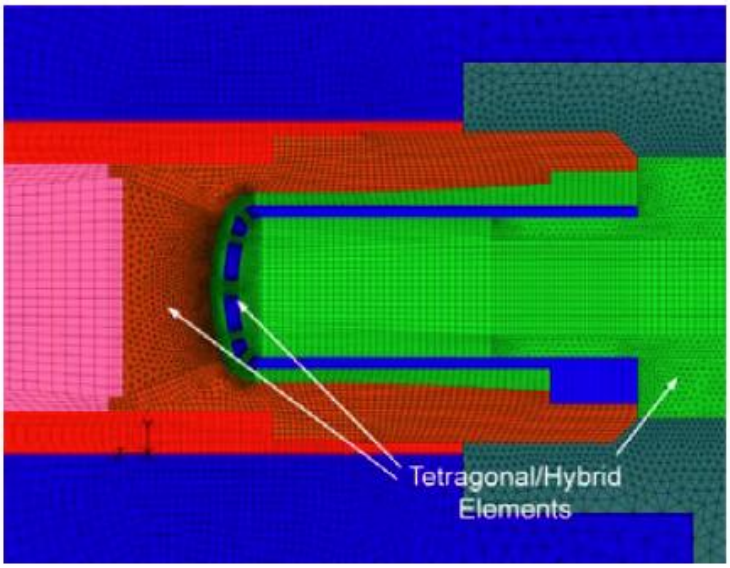

Figure 29. HEMJ mesh on the symmetry face illustrating the tetragonal/hybrid unstructured grid used in Crosatti et al. [41]

Gayton [57] created a 3-D half model of the HCFP geometry using FLUENT® that was also validated using dynamically similar experiments using air. This model differs from the HEMJ geometry primarily in the number of cells required to model the entire geometry, and a total of 1.67×10^6 mixed quadrilateral and hexahedral cells were used

with a minimum node spacing of 0.25 mm in the impingement region. The model used both the standard k-ε model with standard wall functions and the Spalart-Allmaras model; the Spalart-Allmaras model was found to give the best agreement with a 5% overestimation of the heat transfer coefficient. Numerical simulations of the prototypical HCFP module were also been performed by Wang et al. [35] using ANSYS CFX® on a narrow slice of a module using the standard k-ε model with wall enhancement; these simulations reported that the design could accommodate heat fluxes of 10 MW/m^2.

Rader [58] simulated a 2D numerical model of a HEMP-like geometry without cooling fins (also studied in this thesis) using ANSYS FLUENT® and compared the predictions obtained with different turbulence models. The model was validated using a set dynamically similar experiments performed with air [59]. The model consisted of a uniform quadrilateral grid for a total of ~7×10^5 cells with dimensions of 25 μm, and only a radial slice of the HEMJ was modeled because of its axisymmetric geometry. The turbulence models examined included: standard k-ε (SKE), RNG k-ε (RNGKE), realizable k-ε (RKE), and Spalart-Allmaras (SA); the k-ε models used FLUENT's enhanced wall treatment. The model which gave predictions that most closely matched the embedded thermocouple measurements varied with the flow direction in the divertor. For flow entering the central tube and using jet impingement, the predictions using the Spalart-Allmaras model provided the best agreement with the experimental measurements. For flow entering the annulus with no jet impingement, the realizable k-ε model gave temperature predictions that were the closest to those measured by the thermocouples. These results are summarized for two reference experiments in Figure 30.

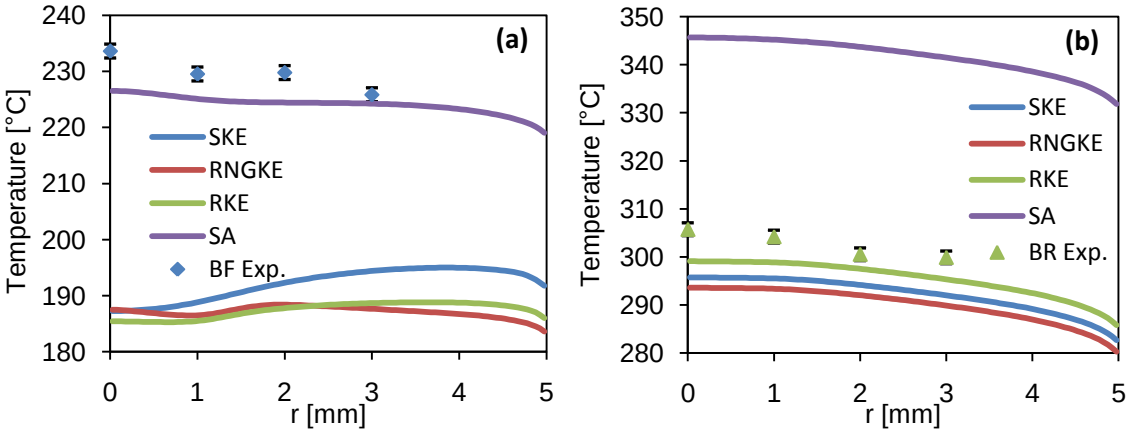

Figure 30. Comparison of different turbulence models against temperature measurements for an HEMP divertor without fins when the coolant enters the central tube (a) and the annulus (b) [58]

2.4.2 Turbulence Models and Heat Transfer

A number of semi-empirical turbulence models have been developed to address the closure problem of turbulence, where there are significantly more unknowns than governing equations. This section focuses on the models available in ANSYS FLUENT® that have been used to model divertors, including the Spalart-Allmaras and various k-ε models.

The basic governing equations for a turbulent flow are the Reynolds-Averaged Navier-Stokes (RANS) equations. As turbulence is inherently an unsteady phenomenon, characterized by stochastic fluctuations about a well-defined time average, the instantaneous values of the flow parameters in the Navier-Stokes equations can be written as the sum of a time average (*e.g.* $\overline{u_i}$ for the velocity) and fluctuations (*e.g.* u_i'). Rewriting the 3-D Navier-Stokes equations using parameters that are decomposed into their time-averaged and fluctuation values, then taking a time average of the result, gives the RANS equations as shown below in Cartesian index notation (where quantities without bars now denote the time-averaged values excluding the last term):

$$\frac{\partial \rho}{\partial t} + \frac{\partial}{\partial x_i}(\rho u_i) = 0$$

$$\frac{\partial}{\partial t}(\rho u_i) + \frac{\partial}{\partial x_j}(\rho u_i u_j) = -\frac{\partial p}{\partial x_i} + \frac{\partial}{\partial x_j}\left[\mu\left(\frac{\partial u_i}{\partial x_j} + \frac{\partial u_j}{\partial x_i} - \frac{2}{3}\delta_{ij}\frac{\partial u_i}{\partial x_j}\right)\right] + \frac{\partial}{\partial x_j}\left(-\rho\overline{u_i' u_j'}\right) \quad (12)$$

The RANS equations are similar to the 3-D Navier-Stokes equations except for an additional term involving a second order tensor, the Reynolds stresses $-\rho\overline{u_i' u_j'}$. The Reynolds stresses introduce six additional unknowns (six as opposed to nine because it is a symmetric tensor) to the problem. There are therefore a total of ten unknowns (the Reynolds stresses, the velocity, and the pressure), and four equations (Continuity and RANS) for a turbulent flow. Thus, there are six more unknowns than there are governing equations, which requires more equations to solve or 'close.' Appropriately, this is often referred to as the turbulence closure problem.

Both the Spalart-Allmaras and k-ε models use the application of the Boussinesq hypothesis [60] using an eddy viscosity μ_t to write the Reynolds stresses in terms of the mean velocity gradients shown below in Cartesian index notation:

$$-\rho\overline{u_i' u_j'} = \mu_t\left(\frac{\partial u_i}{\partial x_j} + \frac{\partial u_j}{\partial x_i}\right) - \frac{2}{3}\left(\rho k + \mu_t\frac{\partial u_k}{\partial x_k}\right)\delta_{ij} \quad (13)$$

where k is the turbulent kinetic energy. This assumption reduces the number of unknowns from six to two; however, it also assumes that μ_t is a scalar. More complex models such as the Reynolds stress model (also provided in ANSYS FLUENT®) solve a transport equation instead for each of the six independent terms in the Reynolds stress tensor, which of course requires significantly longer computation times [61].

The Spalart-Allmaras (SA) model closes the RANS equations by introducing only one additional transport equation for the turbulent eddy viscosity ν_t (where $\nu_t = \mu_t/\rho$) and by eliminating the second term on the right-hand side of Eq. 13 since this term is

negligible for thin shear flows [62]. Therefore, the transport equation for the SA model is as follows:

$$\frac{D\rho\tilde{\nu}}{Dt} = G_{\nu} + \frac{1}{\sigma_{\tilde{\nu}}}\left[\frac{\partial}{\partial x_j}\left(\left(\mu + \rho\tilde{\nu}\right)\frac{\partial\tilde{\nu}}{\partial x_j}\right) + C_{b2}\rho\left(\frac{\partial\tilde{\nu}}{\partial x_j}\right)^2\right] - Y_{\nu} + S_{\tilde{\nu}} \tag{14}$$

where G_{ν} is the production of the turbulent viscosity, Y_{ν} is the destruction of the turbulent viscosity, $S_{\tilde{\nu}}$ is a source term, and C_{b2} and $\sigma_{\tilde{\nu}}$ are constants. In total, the SA model uses a total of twelve constants estimated from experimental data to close the problem. After solving, the working variable $\tilde{\nu}$ can then be related to the turbulent eddy viscosity ν_t by the following relations:

$$\nu_t = \tilde{\nu} f_{\nu 1}, \qquad f_{\nu 1} = \frac{\left(\tilde{\nu}/\nu\right)^3}{\left(\tilde{\nu}/\nu\right)^3 + C_{\nu 1}^3} \tag{15}$$

where ν is the molecular viscosity and $C_{\nu 1}$ is another model constant.

The advantages of the SA model include its simplicity since it introduces only one additional transport equation, its numerical stability, and its ability to accurately simulate flows even at moderate spatial and temporal resolutions [62]. The model is widely used for turbulent wall-bounded flows and boundary layers subject to adverse pressure gradients [61]. ANSYS FLUENT® has modified the SA model to feature its enhanced wall treatment (discussed below) where previously very fine spatial resolutions near walls were required [61].

Three k-ε (KE) models are discussed here: standard k-ε (SKE) [63], re-normalized group k-ε (RNGKE) [64], and realizable k-ε (RKE) [65]. All three of these models solve two coupled transport equations for the turbulent kinetic energy k and the turbulent dissipation rate ε, but the exact form of these transport equations differs between each model. For the SKE model the equations are as follows:

$$\frac{D\rho k}{Dt} = \frac{\partial}{\partial x_j}\left(\left(\mu + \frac{\mu_t}{\sigma_k}\right)\frac{\partial k}{\partial x_j}\right) + G_k - \rho\varepsilon - Y_M + S_k \tag{16}$$

$$\frac{D\rho\varepsilon}{Dt} = \frac{\partial}{\partial x_j}\left(\left(\mu + \frac{\mu_t}{\sigma_\varepsilon}\right)\frac{\partial \varepsilon}{\partial x_j}\right) + C_1\frac{\varepsilon}{k}\left(G_k\right) - C_2\rho\frac{\varepsilon^2}{k} + S_\varepsilon \tag{17}$$

where G_k is the production of turbulence kinetic energy from velocity gradients and buoyancy, Y_M is the dissipation of the turbulence kinetic energy due to the effect of compressibility (proposed by Sarkar and Lakshmanan [66] for compressible flows), C_1 and C_2 are constants, and σ_k and σ_ε are turbulent Prandtl numbers for k and ε, respectively. Then, μ_t is related to k and ε by:

$$\mu_t = C_\mu \rho \frac{k^2}{\varepsilon} \tag{18}$$

where C_μ is an empirically determined constant.

The RNGKE and RKE models were developed to improve upon issues with the SKE model in flows with a high mean shear rate or large separation region where SKE significantly overpredicts μ_t [65]. The models differ from the SKE model primarily in the transport equation for ε and the definition of μ_t. For brevity, the transport equations for each model are not included and can be found in the references for each model. In general, the RKE model gives more accurate results for separated flows and flows with complex secondary flow features [61].

Critical to the performance of these turbulence models is how the models treat near-wall flow. ANSYS FLUENT® provides several options when applicable in the KE models to model near-wall behavior including: standard wall functions, scalable wall functions, non-equilibrium wall functions, and enhanced wall treatment. Of these, standard wall functions and enhanced wall treatment are used here. Near the solid wall interface, there are regions of the flow where viscous effects predominate over the turbulent effects [67]. One approach to model the flow in this region, when the spatial

resolution is not sufficiently fine, is to use wall functions. Wall functions are semi-empirical formulas that are used to that blend the viscosity-affected region near the wall with the fully turbulent region in the flow [61]. A value commonly identified to determine the need to use wall functions is the dimensionless wall-normal coordinate y^+ defined as:

$$y^+ = \frac{yV_f}{\nu} \tag{19}$$

where y is distance normal to the wall, $V_f = \sqrt{\tau_w / \rho}$ is the friction velocity, τ_w is the wall sheer stress, ρ is the coolant density, and ν is the coolant kinematic viscosity.

The standard wall functions, based upon the work of Launder and Spalding [67], were developed specifically for relatively coarse spatial resolution along the walls so that the viscous effects are negligible compared with turbulent effects [67]. These functions, defined in the manual for this software [61], therefore tend to break down as y^+ decreases, where viscous effects become more significant. The enhanced wall treatment in ANSYS FLUENT® is instead a combination of near-wall modeling (when the mesh is sufficiently fine enough to resolve the viscous sublayer (*i.e.* $y^+ \approx 1$)) with the use of wall functions. This approach combines the work of several researchers [68,69,70,71,72,73] and is unique to ANSYS FLUENT®. The details of how each model is blended to create the enhanced wall treatment are best described in the manual for this software [61]. The advantage of this enhanced wall treatment is that it allows for flexibility in the spatial resolution of mesh along all the walls of the model, reducing the computation time while still providing more accurate boundary layer modeling as required. Note that the SA model has been modified in FLUENT® to use the enhanced wall treatment.

The inclusion of heat transfer in the numerical models of divertors is critical, and ANSYS FLUENT® models heat transfer in both the solid divertor materials and the coolant. For the coolant, the energy equation is solved in the following form:

$$\frac{\partial}{\partial t}(\rho E)+\frac{\partial}{\partial x_i}\left[u_i(\rho E+P)\right]=\frac{\partial}{\partial x_j}\left(k_{eff}\frac{\partial T}{\partial x_j}+u_i\tau_{ij}^{eff}\right)+S_h \tag{20}$$

where E is the total energy, ρ, P, and T are the density, pressure, and temperature of the coolant, respectively, $k_{eff}=k+k_t$ is the effective thermal conductivity, k is the thermal conductivity of the coolant, k_t is the turbulent thermal conductivity (determined by the turbulence model), τ_{ij}^{eff} is the stress tensor, and S_h is a source term. The first two terms on the right represent the contributions to the total energy from conduction and viscous heating, respectively. For compressible flows, such as those encountered in this work, viscous heat can't be neglected [61]. The total energy is defined as:

$$E=h-\frac{P}{\rho}+\frac{u^2}{2} \tag{21}$$

where h is the enthalpy of the coolant.

For the SA, SKE, and RKE turbulence models, k_t is simply defined as:

$$k_t=\frac{c_P\mu_t}{Pr_t} \tag{22}$$

where c_P is the specific heat of the coolant, and Pr_t is the turbulent Prandtl number set to a constant value of 0.85. The RNGKE model follows a different approach to define k_{eff} as:

$$k_{eff}=ac_P\mu_{eff} \tag{23}$$

where μ_{eff} is the effective viscosity (the sum of the laminar and turbulent viscosities) and a is defined as:

$$\left|\frac{a-1.3929}{a_0-1.3929}\right|^{0.6321}\left|\frac{a+2.3929}{a_0+2.3929}\right|^{0.3679}=\frac{\mu}{\mu_{eff}} \tag{24}$$

where

$$a_0 = \frac{k}{\mu c_P} \tag{25}$$

Finally, heat transfer in the solid material is derived by the energy equation of the following form (for a stationary solid):

$$\frac{\partial}{\partial t}\left(\rho_s h\right) = \nabla \cdot \left(k_s \nabla T\right) + S_h \tag{26}$$

where ρ_s is the density of the solid, h is the enthalpy, k_s is the thermal conductivity of the solid, and S_h is a source term. For the purposes of this work, all solids are modeled as isotropic.

CHAPTER 3: HEMP-LIKE DIVERTOR DYNAMICALLY SIMILAR EXPERIMENTS

A set of dynamically similar experiments using air as a coolant were performed on an HEMP-like divertor with and without fins to evaluate the thermal performance at prototypical conditions [74]. The experiments were used to generate curves for the maximum heat flux as a function of Reynolds numbers for three different maximum tungsten alloy temperatures. In order to verify that these experiments are indeed dynamically similar, additional experiments were performed on the same geometry using helium and argon as coolants. The experimental setup and the results of these experiments for all three coolants are described in this chapter.

3.1 Experimental Setup

3.1.1 Divertor Test Section Assembly

The test section used to simulate the HEMP-like divertor with and without fins consists of an inner tube of OD 8 mm and ID 5.8 mm centered within a cylindrical outer shell of OD 12 mm and ID 10 mm. The inner tube has a 3 mm thick endcap with a 2 mm diameter port in the center, and the outer shell has either a 6 mm or 10 mm thick endcap. The inner tube is positioned such that there is a 2 mm axial gap between the end of the inner tube and outer shell endcap. The inner tube is constructed of C36000 brass alloy; two different outer shells constructed of C36000 brass alloy and AISI 1018 carbon steel were used. The outer shell is bolted at a flange to a 25.4 mm concentric brass cylinder that serves as the manifold, which in turn is attached to an insulating polyetherimide annular cylinder that centers the inner tube and prevents any leakage of coolant using rubber gaskets. The entire assembly and a cross section of the test section are depicted in Figure 31.

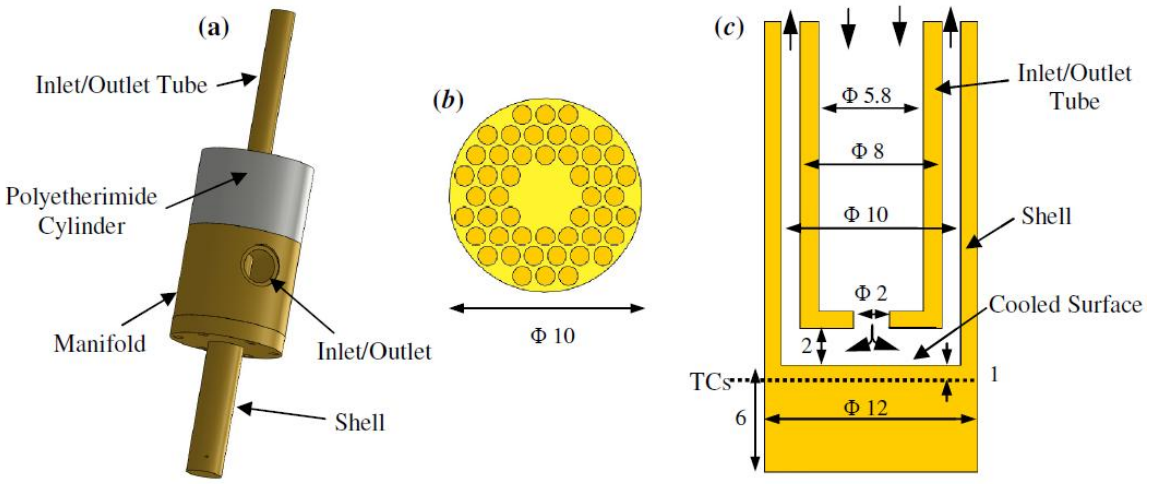

Figure 31. A solid model of the test module used in the experiments (a), a diagram of the pin fin array (b), and a cross section of the finger without fins (c). All dimensions in mm

Three HEMP-like outer shells were constructed for the once-through experiments. One is constructed of AISI 1010 carbon steel, and two are made from C36000 brass alloy. The endcap of the steel shell has a thickness of 10 mm, while that of the brass shells is 6 mm in thickness. This difference in the dimension of the endcap is due to the lower thermal conductivity of steel (~50 W/m·K) versus brass (~120 W/m·K); increasing the thickness of the steel endcap provides more material for the heat to diffuse through to reduce any effects from a non-uniform incident heat flux. A hexagonal array of cylindrical pin fins is machined into the inner surface of the endcap of one of the two brass shells, as shown in Figure 31b. The pin fins are 2 mm in length and 1 mm in diameter with a 1.2 mm pitch, and the tips of the fins contact the endcap of the inner tube. However, the pin fins do not make perfect contact with the inner tube endcap due to machining imperfections.

The test section can be configured such that the coolant can flow in two directions, referred to here as ‘forward flow’ and ‘reverse flow’. In forward flow, coolant flows through the inner tube where it is accelerated through the port and impinges upon the inner surface of the endcap on the shell or ‘cooled surface’. The coolant then flows

radially outward before turning 90° and flowing out the annulus created by the shell and the tube. In reverse flow, the coolant flows in the opposite direction. Both flow directions utilize cross flow over the fin array when available, but forward flow also uses jet impingement cooling. Using the two different flow directions and the two different types of shells, four configurations can be tested: forward flow without fins (BF), forward flow with fins (FF), reverse flow without fins (BR), and reverse flow with fins (FR). While there are differences in the geometry, the BF configuration is similar to an HEMJ configuration (albeit with only a single round jet as opposed to an array of jets) and the FF and FR configurations are HEMP-like configurations. Since the geometry without fins is dimensionally similar to the HEMP divertor (same shell and tube diameters, flat cooled surface, etc.), it will be simply be referenced here as an HEMP-like divertor without fins to differentiate it from the HEMJ divertor discussed later in this work.

Temperatures inside the shell are measured by four type-E thermocouple probes with a sheath diameter of 0.81 mm embedded in the test section endcap at radial distances of 0 mm, 1 mm, 2 mm, and 3 mm from the centerline. The probes are spaced by 90 degrees and are all 1 mm from the cooled surface. As a result, the thermocouple measurements are extrapolated to cooled surface values assuming 1D conduction through 1 mm of the shell material. The thermocouples are held in place by force fitting between the holes and the probes. Although thermocouples were also embedded 1 mm from the heated surface to try to measure the incident heat flux assuming one dimensional conduction between the thermocouples axially, these temperature data were not reproducible. It is impractical given the nonuniform heat source (discussed in the next section) to accurately measure the temperature this close to the heated surface since even slight changes in the position of the flame can give different results. A cross section of the thermocouple layout is depicted in Figure 32.

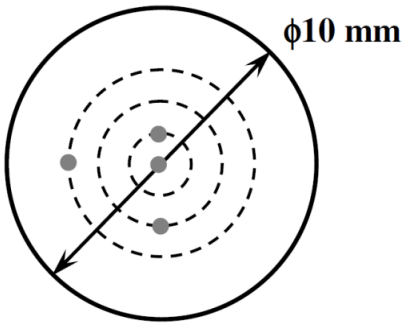

Figure 32. Cross section of the HEMP shell cooled surface depicting the thermocouple arrangement. Grey circles depict location of the thermocouple junctions

3.1.2 Flow Loop

The test section in the 'once-through' experimental setup is cooled using air, helium, or argon vented by a fume hood. Air is provided from the building compressed-air line at pressures up to nearly 700 kPa. Helium and argon are supplied from as many as five interconnected 300 ft^3 compressed gas cylinders. Two pressure regulators in series are used to limit the maximum pressure from the gas cylinders to ~1.4 MPa. A Rotameter (Brooks 1110) is used to measure the volumetric flow rate and ultimately the mass flow rate of the coolant entering the test section. A static pressure transducer is located at the exit of the Rotameter to calculate the coolant density (Omega PX302-2KGV or Omega PX302-300AV; two pressure transducers are listed as the system was modified for helium and argon experiments to allow for higher pressures). More details about using a Rotameter to calculate the mass flow rate are provided in Appendix D.

The pressure is measured at the inlet to the test section using a static pressure transducer (Omega PX302-300AV or Omega PX180-060GV), and the pressure drop across the test section is measured from the inlet to the outlet by a differential pressure transducer (Omega PX26-100DV or Omega PX26-30DV). The coolant temperatures at the inlet and the outlet of the test section are measured using type-E thermocouple probes.

An oxy-acetylene flame, which impinged directly on the outer surface of the shell endcap or 'heated surface,' is used as the heat source, providing heat fluxes up to 2 MW/m^2. Oxy-acetylene is chosen due to its very high flame temperature. Although this torch is in theory capable of providing heat fluxes much greater than 2 MW/m^2, most of the heat is lost to the surroundings, as opposed to being transferred to the heated surface. The relatively small heated surface area of 113.1 mm^2 on the HEMP test section also makes it difficult to concentrate large flames on the surface. Experiments on an HEMJ test section with a heated surface area of 227.0 mm^2 achieved heat fluxes up to 3 MW/m^2 with the same torch [42].

The entire test section assembly is insulated by a combination of pipe foam, rock wool, and Marinite® blocks. A 12 mm hole is drilled through a series of the Marinite® so that the shell fit inside the blocks, which are bolted to a Unistrut® structure that supports the test section assembly. Pipe foam is used to cover any instrumentation lines and piping leading to and from the assembly. Finally, rock wool is inserted into any gaps or crevices that are not adequately covered by the Marinite® blocks or the pipe foam.

A small ceramic 'sleeve' (Figure 33) is used to shield the thermocouples and insulation from the flame. The last 0.5 mm of the shell endcap is inserted inside the flanged end of the sleeve, resting on a 1 mm thick lip (the inside diameter of the sleeve was 10 mm). The sleeve flange is clamped to the shell in the last Marinite® block. A machinable ceramic is chosen for the sleeve material because it could be machined precisely to the required dimensions and can withstand the high temperatures produced by the flame without melting. The sleeve also has a low thermal conductivity, and therefore did not remove much heat by conduction from the test section. Moreover, the heat conducted by the sleeve will be transferred to the outer shell of the test section, since the sleeve only contacts the shell. While the sleeve protects the thermocouples

from the flame, it also reduces the stability of the flame. The oxy-acetylene flame, which is several centimeters in length, must be positioned very close to the test section surface to provide sufficient heat flux. As the flame enters the sleeve, the flame reflected off the heated surface must escape without extinguishing itself, which requires impinging the flame on the surface at a slightly off-normal angle.

Figure 33. Ceramic sleeve used to shield the thermocouples and insulation from the flame

3.2 Experimental Procedure

Experiments are conducted by setting the flow rate through the test section at the desired value, then applying the oxy-acetylene torch to the heated surface until a steady-state condition is achieved. Only steady-state conditions, defined to be the condition where the inlet temperature T_i and the outlet temperature T_o vary by less than 1 °C over a 5 min period with no heating or cooling trend observed, were studied in this work. Typically, T_i and T_o vary by no more than 0.5 °C. Fluctuations in the oxy-acetylene flame can produce variations in the embedded thermocouple readings as great as ~5 °C, so all experimental data is averaged over a 200 s interval to obtain steady-state values for temperatures and pressures.

The range of flow rates selected for experiments on this divertor geometry is based upon the Reynolds number Re at the 2 mm diameter port calculated as follows:

$$Re = \frac{\rho V D_j}{\mu} = \frac{\dot{m} D_j}{A_j \mu} = \frac{4\dot{m}}{\pi D_j \mu} \tag{27}$$

where $\dot{m}$ is the mass flow rate of the coolant through the port, μ is the dynamic viscosity, D_j is the port diameter, and A_j is the area of the port. For forward flow μ is evaluated at the inlet temperature, and for reverse flow μ is evaluated at the outlet temperature. The evaluation of material properties is discussed in more detail in Appendix B. The prototypical Reynolds number Re_p for this geometry is determined to be $Re_p =$ 7.6×10^4 and $Re_p =$ 7.0×10^4 for forward flow and reverse flow, respectively. This is well within the range for this experimental apparatus 8.0×10^3 $< Re <$ 1.6×10^5. The Reynolds number, and ultimately $\dot{m}$, are controlled by varying the inlet pressure or by closing a needle valve at the exit of the test section.

It takes several minutes for each experiment to reach steady-state. Previous work using cartridge heaters in a copper concentrator as the heat source took hours to reach steady-state because of the large time constant of the concentrator [53,75]. Using an oxy-acetylene torch greatly decreased this time, which made it possible to conduct several experiments at various flow rates with a single run without turning off the torch.

The thermal power incident on the heated surface of the shell is determined by an energy balance using the inlet and outlet temperature of the coolant. The average incident heat flux $\overline{q''}$ is then calculated by dividing the calculated incident thermal power by the cross sectional area of the shell $A_h = 113.1$ mm^2:

$$\overline{q''} = \frac{\dot{m}\overline{c_p}\left(T_o - T_i\right)}{A_h} \tag{28}$$

where $\dot{m} = \rho Q$ is the mass flow rate, ρ is the coolant density at the Rotameter, Q is the volumetric flow rate measured by the Rotameter (see Appendix D), and $\overline{c_p}$ is the specific heat evaluated at the average coolant temperature. Admittedly, the average incident heat flux determined in this manner does not account for heat losses; however, it is assumed that these losses are small because the test section and piping are well-

insulated. For a single divertor module in an array, radial losses to a neighboring module would be negligible since these modules would share a similar heat flux load and would be at similar temperatures. Modeling the boundaries of the test section to be adiabatic is therefore a reasonable assumption.

The actual profile of the heat flux incident on a single module in an actual divertor is unknown at present, depending on the location of the module within the array. However, the incident heat flux can be approximated as uniform since each module covers a very small portion of the divertor surface. In the experiments performed here, an oxy-acetylene flame is used to provide the incident heat flux, which is not uniform, although Eq. 28 is given in terms of an average incident heat flux. However, the shell tip (with thicknesses of 6 mm in the brass shell and 10 mm in the steel shell) helps to even out any spatial variations in the incident heat flux via conduction. To verify that using a flame as the heat source gives results consistent with using a uniform heat flux, Rader performed simulations using ANSYS FLUENT® 14.0 on this geometry [58]. He found that the difference between using a uniform incident heat flux and an incident heat flux profile that was a Gaussian function with peaking factors as great as 4 (with the same total thermal power input) was negligible for both the steel and brass shells.

The temperature at the cooled surface at radial locations corresponding to the embedded thermocouples T_{cr} is determined by extrapolating the embedded thermocouples readings T_r (where r corresponds to the radial distance from the centerline, *i.e.* 0, 1, 2, and 3 mm) to the cooled surface assuming one-dimensional conduction.

$$T_{cr} = \frac{\overline{q''}\delta_{TC}}{k_s} + T_r \tag{29}$$

where $\delta_{TC} = 1$ mm is the distance to the cooled surface, and k_s is the thermal conductivity of the shell evaluated at the average temperature between the two values (this requires iteration). Next, an area-weighted average is calculated of the four thermocouple readings to estimate the average cooled surface temperature $\overline{T_c}$:

$$\overline{T_c} = \frac{1}{100} T_{c0} + \frac{8}{100} T_{c1} + \frac{15}{100} T_{c2} + \frac{76}{100} T_{c3} \tag{30}$$

Finally, an average heat transfer coefficient $\bar{h}$ is computed for the shell without fins as follows:

$$\bar{h} = \frac{\overline{q''}}{(\overline{T_c} - T_i)} \frac{A_h}{A_c} \tag{31}$$

where $A_c = 78.5$ mm^2. The area ratio between the heated surface and the cooled surface assumes that all of the heat entering the test section will be removed by convection at the cooled surface. In reality, some heat is conducted through the side walls of the divertor shell, but this is initially assumed to be negligible. This assumption is reexamined later. For the geometry with fins, $\bar{h}$ needs to account for the temperature variation along the fins. The surface of the fins is not at the uniform temperature $\overline{T_c}$ and, will decrease from $\overline{T_c}$ along the length of the fins. To account for this variation, the fin efficiency η is computed and used to adjust the area ratio of the average heat transfer coefficient:

$$\bar{h} = \frac{A_h}{(A_p + \eta A_f)} \frac{\overline{q''}}{(\overline{T_c} - T_i)} \tag{32}$$

where $A_p = 40.8$ mm^2 is the area of the cooled surface not covered by the fins, and $A_f = 302$ mm^2 is the surface area of the fins excluding the tips. The fin efficiency is derived from a one-dimensional model assuming that the temperature only varies along the length of the fin and the fin tip is an adiabatic boundary, as discussed in Section 2.1.1. An adiabatic boundary condition is used here since there will be a thin layer of

stagnant coolant (a poor thermal conductor) between the fin tip and the tube because of the lack of perfect contact from machining imperfections and misalignment. The fin efficiency is taken from Eq. 5 and simplified for pin fins below:

$$\eta = \frac{\tanh\left(\alpha L_f\right)}{\alpha L_f} \quad \text{where} \quad \alpha = L_f \sqrt{\frac{4\bar{h}}{k_f D_f}} \tag{33}$$

where $L_f = 2$ mm is the length of the fins, k_f is the thermal conductivity of the fins evaluated at $\overline{T_c}$, and $D_f = 1$ mm is the diameter of a fin. Note that η decreases as $\bar{h}$ increases. Solving for η also requires an iterative solution since η and $\bar{h}$ depend upon one another.

Evaluating $\bar{h}$ using Eq. 31 for the cases with fins gives a metric for evaluating the value of an array of fins compared to a surface without fins because both geometries are based off the same cooled surface area. As a result, $\bar{h}$ in Eq. 31 is commonly referred to as the 'effective' heat transfer coefficient $\overline{h_{eff}}$ [59]. By contrast, $\bar{h}$ in Eq. 32 is referred to as the 'actual' heat transfer coefficient $\overline{h_{act}}$. Note that for cases without fins, $\overline{h_{act}} = \overline{h_{eff}}$. Unless otherwise specified, $\bar{h}$ refers here to $\overline{h_{act}}$. Finally, the average Nusselt number $\overline{Nu}$ is computed as follows:

$$\overline{Nu} = \frac{\bar{h} D_j}{k} \tag{34}$$

where k is the thermal conductivity of the coolant evaluated at the average coolant temperature $\left(T_i + T_o\right)/2$. As in most heat transfer applications, $\overline{Nu}$ should be a function of both Re and the Prandtl number Pr (*i.e.* $\overline{Nu} = f\left(Re, Pr\right)$). However, for the three coolants considered here, Pr varies between 0.66 and 0.71, and typically $\overline{Nu}$ is proportional to $Pr^{0.4}$. As a result, the effect of Pr has been ignored in these studies. So the performance of the divertor under prototypical conditions is estimated based on a correlation of the form $\overline{Nu} = f\left(Re\right)$.

Loss coefficients K_L are computed for each case as follows:

$$K_L = \frac{\Delta P}{\frac{1}{2}\rho_L \overline{V}^2} \tag{35}$$

where ΔP is the measured pressure drop, ρ_L is the coolant density, and $\overline{V}$ is the average coolant velocity at the jet. Most of the pressure drop occurs as the coolant is accelerated through the port either before or after it is heated depending on the direction of flow (*i.e.* forward or reverse flow), based on numerical simulations [44,58]. In forward flow, the coolant is unheated as it passes through the port and ρ_L is evaluated by the ideal gas law using the outlet pressure and the inlet temperature. In reverse flow, ρ_L is evaluated using the outlet pressure and the outlet temperature. Loss coefficients are typically evaluated instead based on the *total* pressure, but since the velocity of the coolant at the location of the pressure measurements is very small, static pressure measurements for ΔP can be used instead. As a hydraulic parameter, K_L is only a function or Re, and like $\overline{Nu}$, a correlation for K_L can be used to predict the pressure drop of the divertor module at prototypical conditions.

3.3 Results

A total of 40 steady-state experiments were performed using the brass test sections with and without fins and either helium or argon as a coolant: 20 forward flow experiments and 20 reverse flow experiments. Of these 20 experiments, 6 were performed with helium and without fins, 6 with helium and fins, 4 with argon and without fins, and 4 with argon and fins. The Reynolds number Re for these studies varied from 1.5×10^4 to 1.2×10^5, spanning the prototypical value $Re_p = 7.6\times10^4$ and $Re_p = 7.0\times10^4$ for forward flow and reverse flow, respectively. These experiments were compared to a series of experiments performed on the same geometry using air as a coolant [59,74].

The average effective heat transfer coefficient $\overline{h_{eff}}$ is plotted in Figure 34 for all three coolants. Details regarding the calculation of the experimental uncertainty are given in Appendix C.

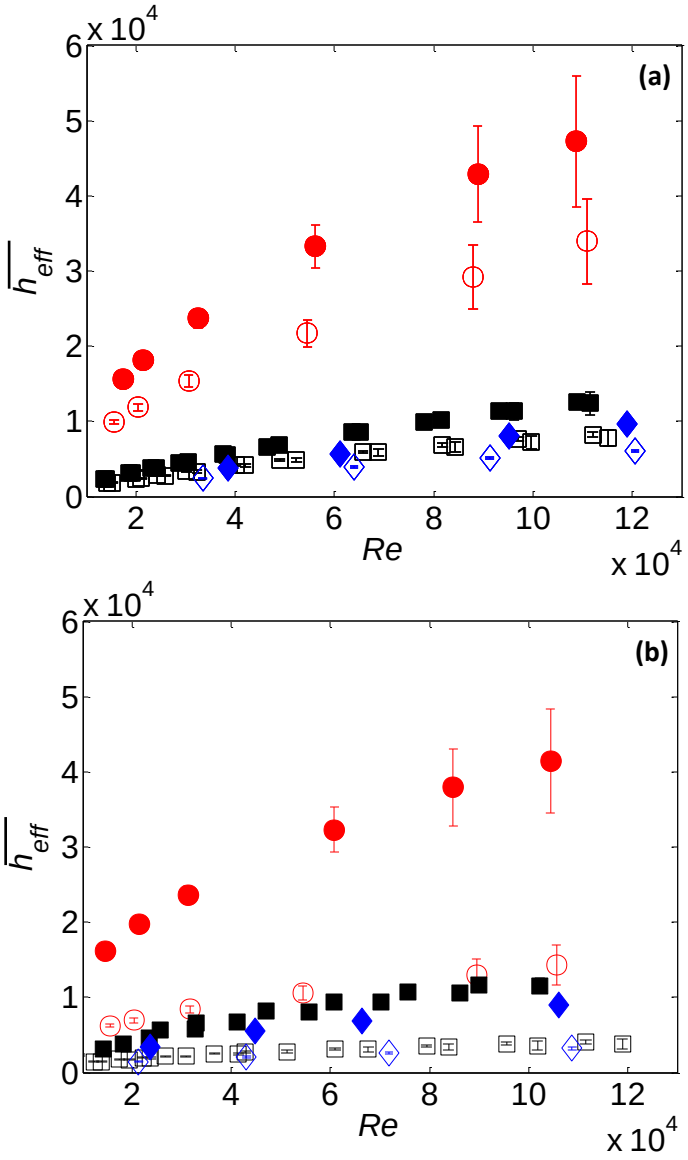

Figure 34. Average effective heat transfer coefficients for air (■), He (●), and Ar (♦) in forward flow (a) and reverse flow (b). Open symbols indicate bare experiments and closed symbols indicate finned experiments

Several conclusions can be drawn from Figure 34. First, helium, as expected, produces the largest effective heat transfer coefficients, due to its high thermal

conductivity. Second, fins significantly enhance cooling for all coolants when compared to their respective bare geometries over this range of Re. However, this advantage may not necessarily be valid at prototypical conditions based on these results because the fin efficiency may be different at prototypical pressures and temperatures. Third, the enhancement of $\overline{h_{eff}}$ due to fins is significantly more pronounced in reverse flow, which is likely due to the absence of jet impingement cooling in these cases. Also, $\overline{h_{eff}}$ for reverse flow without fins is less than that for its forward flow counterpart, presumably also due to the absence of jet impingement cooling. Finally, $\overline{h_{eff}}$ for configurations with fins is within experimental uncertainty of one another suggesting that any benefit from jet impingement is small for cases with fins.

Before calculating $\overline{Nu}$, the actual heat transfer coefficient $\overline{h_{act}}$ must be calculated for the cases with fins (recall that for the cases without fins: $\overline{h_{act}} = \overline{h_{eff}}$). The results for $\overline{h_{act}}$ are plotted in Figure 35.

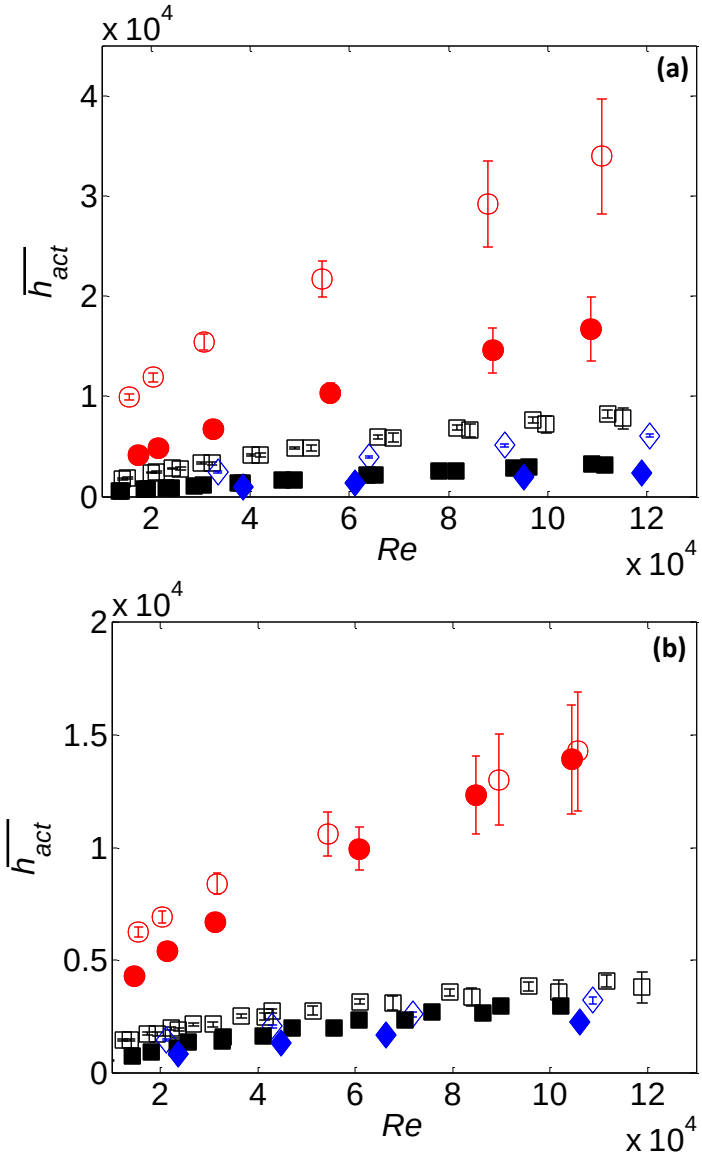

Figure 35. Average actual heat transfer coefficients for air (■), He (●), and Ar (♦) in forward flow (a) and reverse flow (b). Open symbols indicate bare experiments and closed symbols indicate finned experiments

Comparing $\overline{h_{act}}$ between the corresponding cases without and with fins can be misleading because of the difference in their cooled surface areas (the cases with fins have about 4.5 times the cooled surface area of the cases without fins). We therefore compare $\overline{h_{eff}}$ to determine the value of the fins in terms of enhancing thermal performance. In Figure 35, $\overline{h_{act}}$ in all the cases with fins is less than $\overline{h_{act}}$ for the

corresponding cases without fins. This is simply because the average surface temperatures along the length of the fins is less than that for the cases without the fins, although this decrease is partially offset by the increase in cooled surface area due to the fins.

Figure 36 shows $\overline{Nu}(Re)$ for each coolant and flow configuration.

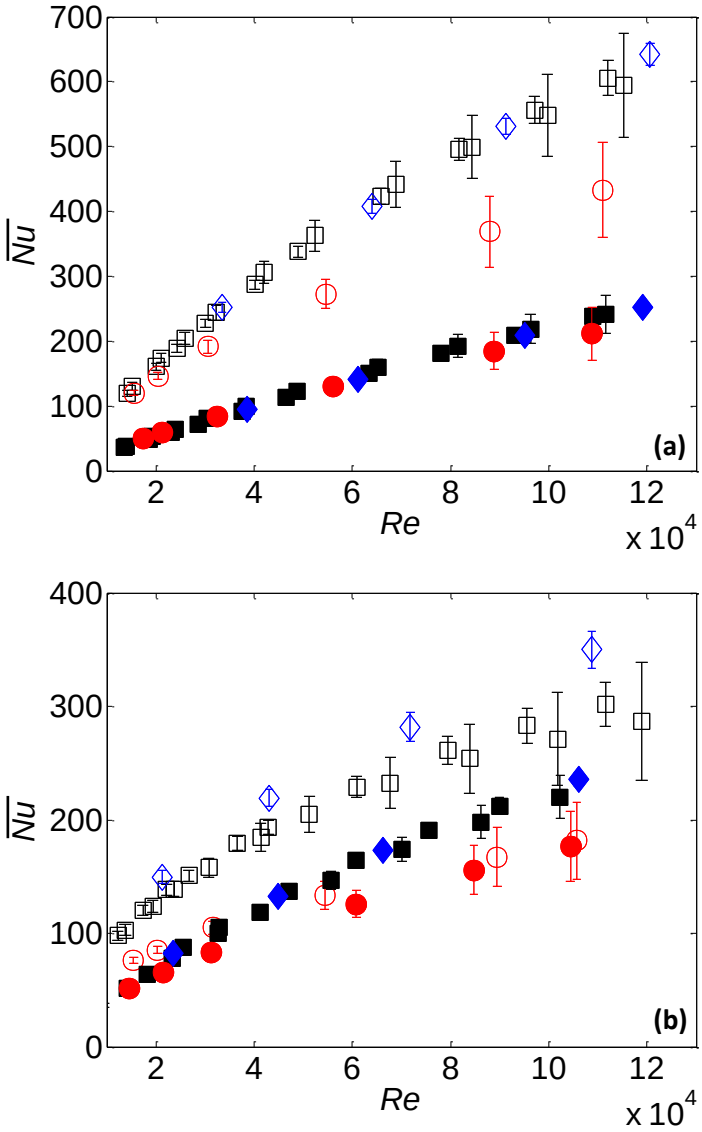

Figure 36. Average Nusselt numbers for air (■), He (●), and Ar (♦) in forward flow (a) and reverse flow (b). Open symbols indicate bare experiments and closed symbols indicate finned experiments

Similar to the heat transfer coefficients shown in Figure 35, $\overline{Nu}$ is lower for cases with fins compared to cases without fins; however, this does not account for the larger cooled surface area of the cases with fins. The $\overline{Nu}$ values calculated for each coolant, which should account for this enhanced surface area, should therefore be the same for the cases with and without fins for a given coolant, but Figure 36 shows that this is not the case for all flow configurations except for forward flow with fins (FF). For forward flow, the $\overline{Nu}$ values without fins for He are well below those for air and Ar. Conversely, the $\overline{Nu}$ values with fins for all three coolants are in reasonably good agreement. For reverse flow, the $\overline{Nu}$ results for He with and without fins are significantly below the values for air and Ar. Furthermore, the reverse flow without fins (BR) results for air and Ar also differ. These results clearly show that these experiments are not dynamically similar, and that $\overline{Nu}$ must depend on additional dimensionless groups beyond Re.

As mentioned previously, the mass flow rate in these experiments was controlled by varying the inlet pressure to the test section, with inlet pressures as high as 1.4 MPa for the He experiments. The maximum inlet pressure for the air and Ar experiments was much lower, about 400 kPa. It was initially assumed that compressibility effects were negligible for all three coolants. Although this had already been confirmed for experiments conducted with air [59], sixteen more experiments were conducted with Ar at higher constant inlet pressures $P_i \approx 1.4$ MPa (eight in forward flow and eight in reverse flow) to confirm this assumption for He and Ar. These experiments are referred to 'high inlet pressure experiments,' while the previous experiments are referred to as 'variable inlet pressure experiments.' Experiments with He at higher inlet pressure were not practical as the necessary pressures to reach the desired relevant differences in Mach number M were too large for this experimental setup, which was already at its

maximum inlet pressure of 1.4 MPa. The Mach number at the port (the location of maximum velocity), for a uniform velocity profile, is:

$$M = \frac{1}{\sqrt{\gamma \Re T_i}} \frac{4\dot{m}}{\rho_L \pi D^2} \tag{36}$$

where γ is the specific heat ratio and $\Re$ is the specific ideal-gas constant. The results are depicted in Figure 37 for He and Ar for both forward and reverse flow along with high inlet pressure experiments performed with air ($P_i \approx 700$ kPa) [59,74].

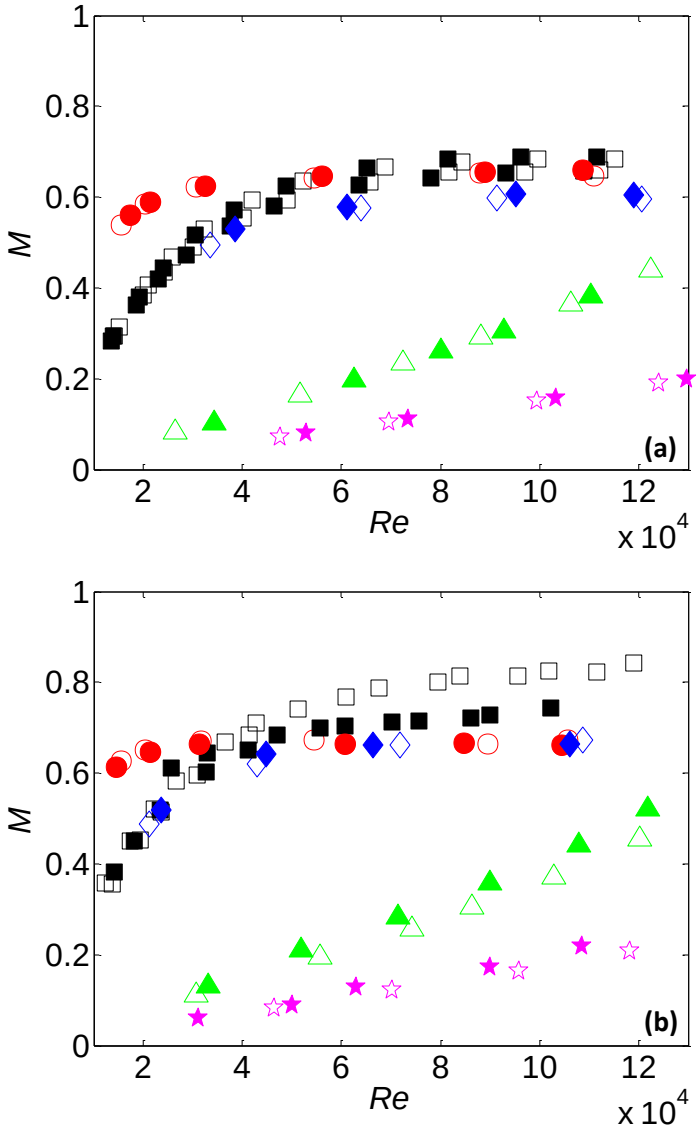

Figure 37. Mach numbers for air (■), He (●), Ar (♦), high pressure air (▲), and high pressure argon (★) in forward flow (a) and reverse flow (b). Open symbols indicate bare experiments and closed symbols indicate finned experiments

For the variable inlet pressure experiments, M varied from approximately 0.3 to 0.7 for forward flow and 0.3 to 0.85 for reverse flow. Compressibility effects should therefore be significant at the upper end of this range. Conversely, M was significantly lower for the high inlet pressure experiments: a maximum of 0.5 for air and 0.2 for Ar. High inlet pressure experiments with Ar were at low enough Mach numbers so that the

flow could be considered to be incompressible. By comparing $\overline{Nu}$ values from the variable inlet pressure experiments with those from the high inlet pressure experiments, it can be determined if compressibility is significant, as shown in Figure 38.

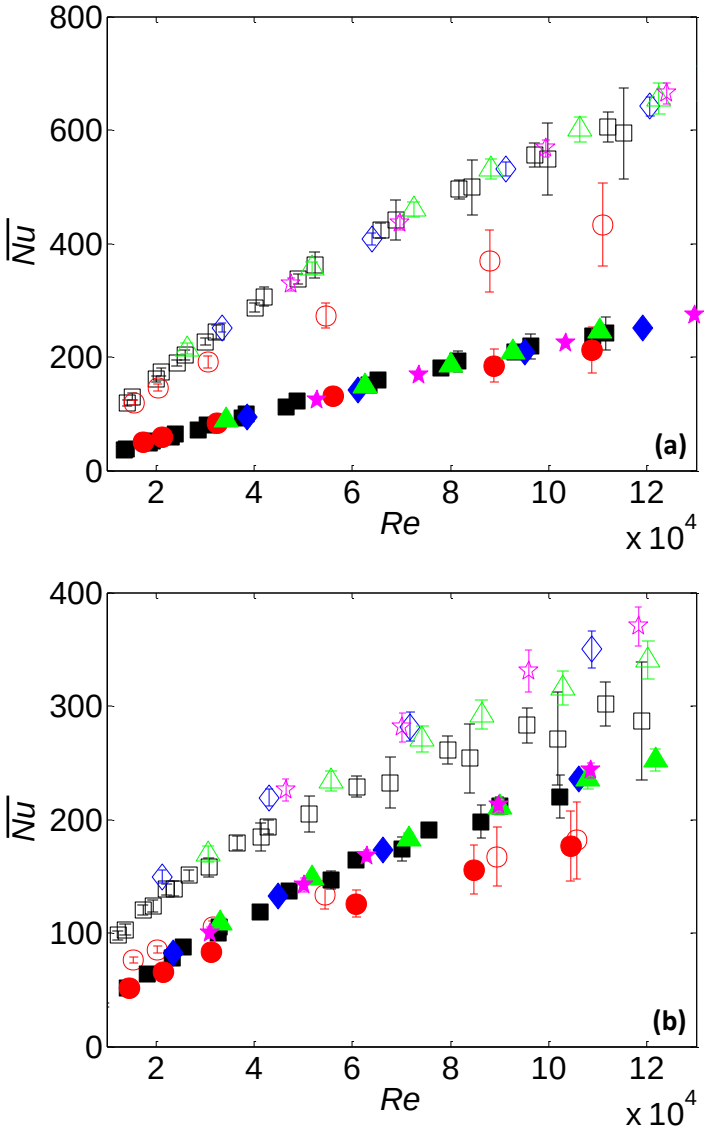

Figure 38. Average Nusselt numbers for air (■), He (●), Ar (♦), high pressure air (▲), and high pressure argon (★) in forward flow (a) and reverse flow (b). Open symbols indicate bare experiments and closed symbols indicate finned experiments

Figure 38 shows that the $\overline{Nu}$ values obtained from high inlet pressure experiments agree with those from variable inlet pressure experiments. Therefore,

compressibility effects are judged to be negligible. To further study the discrepancy in $\overline{Nu}$ shown in Figure 36, numerical simulations of these experiments have been performed using a commercial CFD code, as will be detailed in Chapter 4.

The loss coefficient K_L, computed for each steady-state experiment using Eq. 35, is plotted in Figure 39 as a function of Re. The results are in good agreement for all four flow configurations (for a given configuration), all three coolants, and all inlet pressures. Some discrepancy is admittedly observed at low Re (particularly for cases with fins), in part because experimental error is significant at low Re since the measured pressure drops for these cases are comparable to the measurement uncertainty of the differential pressure transducer. Regardless, these Re are much less than Re_p for both flow directions. As expected, the cases with fins have a larger pressure drop than their respective cases without fins. The highest pressure drops are also observed for the FR cases, and this is consistent with the observation that most of the pressure drop occurs at the port. In reverse flow, the coolant is heated before passing through the port, so there should be a larger loss across the port because viscosity increases with temperature. However, the cases without fins show approximately the same K_L at higher Re for both forward and reverse flow.

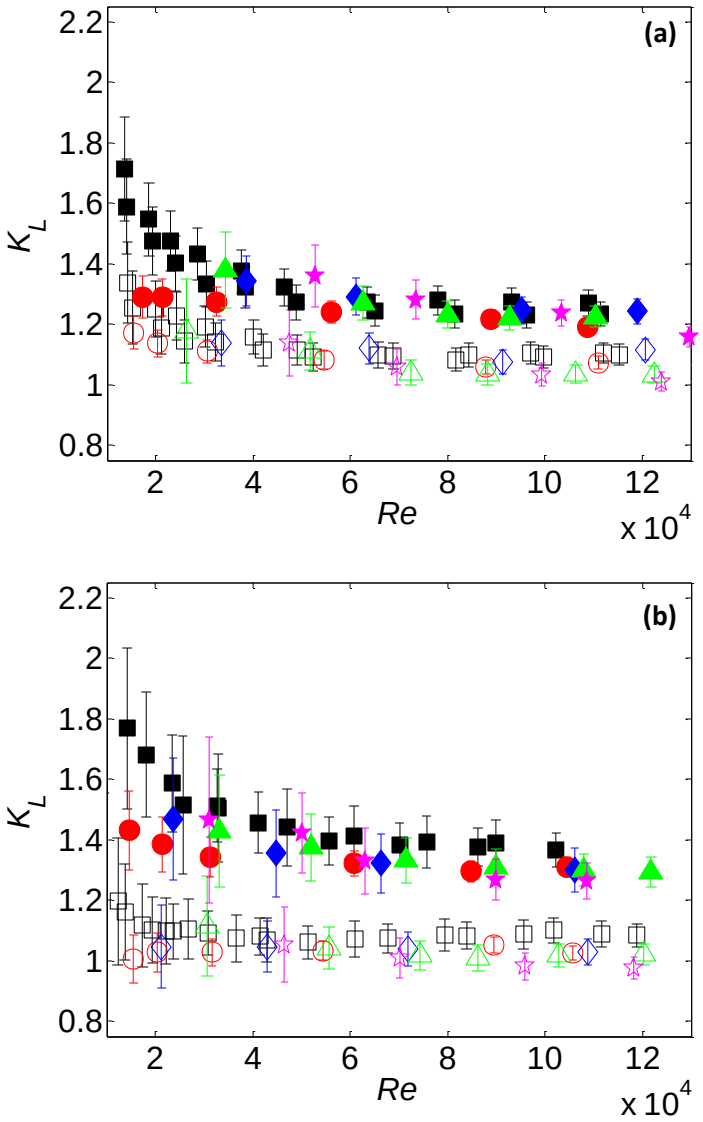

Figure 39. Loss coefficients for air (■), He (●), Ar (♦), high pressure air (▲), and high pressure argon (★) in forward flow (a) and reverse flow (b). Open symbols indicate bare experiments and closed symbols indicate finned experiments

These data were used to develop correlations for the loss coefficient as a function of Re that can be used to predict the prototypical pressure drop through the divertor for each flow configuration. The form of the correlations was chosen to be a power law with a constant offset; in all cases the coefficient of determination R^2

exceeded 0.98. These correlations, generated using the built-in fitting function in MATLAB® 2008b, are given below:

$$\begin{aligned} K_L &= 8.495\times10^{4}\,Re^{-1.337}+1.056 \quad \text{(BF)} \\ K_L &= 6.965\times10^{4}\,Re^{-1.268}+1.208 \quad \text{(FF)} \\ K_L &= 6.690\times10^{6}\,Re^{-1.904}+1.045 \quad \text{(BR)} \\ K_L &= 5.712\times10^{4}\,Re^{-1.243}+1.294 \quad \text{(FR)} \end{aligned} \tag{37}$$

The procedure for using these correlations to estimate prototypical pressure drop is discussed further in Chapter 5.

In summary, a series of experiments with He and Ar on a brass HEMP-like test section with and without fins were performed, and used to develop correlations for $\overline{Nu}$ and K_L, as both a function of Re. Discrepancies in $\overline{Nu}$ were found for different coolants. These discrepancies are not due to compressibility effects. To explain the discrepancies, CFD simulations of the experiments are performed using ANSYS FLUENT® 14.0, and the models and results are discussed in depth in the next chapter.

CHAPTER 4: NUMERICAL MODELING

4.1 Numerical Modeling of HEMP-like Divertors

A numerical model was constructed to further investigate the disparity in the $\overline{Nu}$ values calculated from dynamically similar experiments of the HEMP-like module with and without fins using different coolants. Given that the experiments can only measure a limited set of temperatures and the overall pressure drop, simulations with this numerical model, validated by the available experimental data, make it possible to determine thermal transport parameters that are not accessible in the experiments. In addition, this experimentally validated model can be used in subsequent studies to investigate how changes in the divertor geometry and operating conditions affect its thermal-hydraulic performance. Building upon previous experience (*cf.* Section 2.4.1), this numerical model is built using FLUENT® in ANSYS Workbench® 14.0 and solves the continuity equations for mass, momentum, and energy in the coolant, and conduction heat transfer through the shell and tube. Both a 2D axisymmetric model and a 3D model including the shell and tube of the HEMP-like geometry without fins (*i.e.* bare; BF/BR flow configurations) were created. The 3D model consisted of a 30° wedge of the shell and tube. The 3D model was mainly used to validate the results obtained with the 2D model and determine which turbulence models give the best match to the experimental data. Only 2D simulations were performed of the experiments with the steel shell, discussed in Chapter 5, as the 3D model was ultimately shown to be redundant and significantly more computationally intensive.

Simulations were performed using data gathered from experimental measurements from each steady-state experiment as boundary conditions. The model was then validated by comparing $\bar{h}$ and ΔP to experimentally calculated values.

Previous work using the FLUENT® solver to model dynamically similar HEMP-like divertor experiments using air was able to predict $\bar{h}$ values that were within ±10% of experimental values for relevant Re [58]. These simulations are, however, intended to also duplicate experiments conducted with helium and argon. Previous simulations of this geometry have been unable to predict pressure drop values ΔP consistent with experimental measurements, with discrepancies between the numerical and experimental values of ΔP of 20-40% depending on the Re and the configuration [58]. A geometrical modification, described next, has been included in the model to improve the numerical predictions of pressure drop.

Simulations performed by Rader [58] indicated that a significant fraction of the overall pressure drop occurs at the port entrance as the coolant is accelerated into a jet. As a result, it is important to accurately model the port geometry. When fabricating the tube, the port on the tube endcap was machined with a 45° chamfer on the inside to remove burrs from the drilling process. This chamfer was not included in the numerical model used for the original simulations. Measurements were obtained for this chamfer indicating the chamfer extended 1.0 ± 0.5 mm into the 3 mm tube endcap, and this design modification was applied to the geometry for subsequent simulations.

4.1.1 2D Model

The 2D axisymmetric model, shown in Figure 40, consisted of 50 mm of the brass shell, and 42 mm of the tube, closest to their respective endcaps. All solid boundaries are chosen to be adiabatic with the exception of the heated surface. Although the ceramic sleeve conceals 1 mm of the heated surface radius, it is ignored in this model since small non-uniformities in the incident heat flux have been shown to have a negligible effect on the results [58]. Instead, the incident heat flux is assumed to be a uniform heat flux calculated from experiments using Eq. 28. Given the large

temperature variations in these simulations, temperature dependent properties are used for both the solid materials and the coolants. Material properties were compiled from several sources, as detailed in Appendix B.

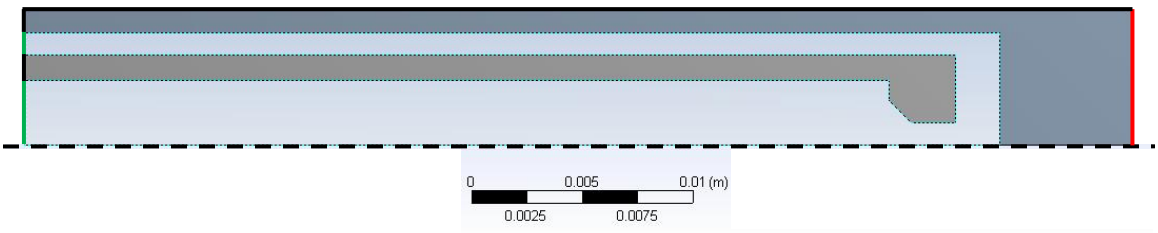

Figure 40. 2D axisymmetric model used in the CFD analysis. Solid black lines indicate adiabatic boundary conditions, red line indicates heat flux boundary condition, green lines indicates coolant boundary conditions (mass flow inlet or pressure outlet depending on the direction of flow), dashed black line indicates axis

The turbulence model was chosen based on previous work by Rader [58]. After a study of the various turbulence models available in ANSYS FLUENT®, Rader found that the Spalart-Allmaras (SA) model gave results for the forward flow configurations using air that provided the best agreement with the corresponding experimental measurements. For reverse flow experiments using air, the realizable k-ε (RKE) turbulence model with enhanced wall treatment gave predictions that were the closest to the experimental results.

A mass flow inlet and pressure outlet coolant boundary conditions are defined and taken from experimental measurements of $\dot{m}$, T_i, T_o, P_i, and P_o. Only T_i and P_o are required, and T_o and P_i are defined in the event of any recirculating flow at the boundaries (which only occurs briefly in the initial iterations). For the SA model, the parameter $\tilde{\nu}$ (related to the turbulent eddy viscosity) must also be defined at the boundaries according to the following equation [61]:

$$\tilde{\nu} = \sqrt{\frac{3}{2}} V_{avg} I l \tag{38}$$

where V_{avg} is the average velocity of the inlet, I is the turbulence intensity, and l is the turbulence length scale all defined as:

$$V_{avg} = \frac{\dot{m}}{\rho_i A_i} \tag{39}$$

$$I = 0.16\left(Re_i\right)^{-1/8} \tag{40}$$

$$l = 0.07L \tag{41}$$

where the inlet area $A_i = 26.4$ mm^2 and 28.3 mm^2 for forward flow and reverse flow, respectively, ρ_i is the density at the inlet to be determined by the ideal gas law, and Re_i is the Reynolds number using the hydraulic diameter of the inlet (5.8 mm) and the outlet (2 mm) for forward flow and reverse flow, respectively.

For the *RKE* model, the turbulent kinetic energy k_t and the turbulent dissipation rate ε are determined for the flow boundary conditions using the following equations [61]:

$$k_t = \frac{3}{2}\left(V_{avg} I\right)^2 = \frac{\tilde{\nu}^2}{l^2} \tag{42}$$

$$\varepsilon = C_\mu^{3/4} \frac{k_t^{3/2}}{l} \tag{43}$$

where C_μ is an empirical constant set equal to 0.09.

The mesh is comprised of approximately 5×10^5 quadrilateral cells ~25 μm on each side and is depicted in Figure 41. This mesh size is determined from a series of convergence studies using models with mesh sizes ranging from 15 μm up to 300 μm, all representing an experimental reference case, referred to here as Reference Case #1 or RC1. RC1 is a BF experiment using a brass shell with helium with a Reynolds number close to Re_p. Specific details for the reference cases are given in Appendix A. One of the most important parameters in these simulations is the average cooled surface

temperature $\overline{T_c}$ since this is in the general location of the largest temperature gradients. $\overline{T_c}$ is then compared to the experimentally calculated values, and the results of the mesh convergence analysis are depicted in Figure 42. As the mesh size decreases, the numerical predictions of $\overline{T_c}$ approach a value that is within 3 °C of the experimentally calculated values for mesh sizes ranging from 25 μm to 100 μm, suggesting that the mesh has already converged at 100 μm. A conservative mesh size of 25 μm was ultimately selected because 2D simulations at even this small mesh size were computationally efficient (*i.e.* convergence was achieved within approximately 3 hours) to ensure a converged mesh at all Re studied here. This model consisted of about 486,000 cells.

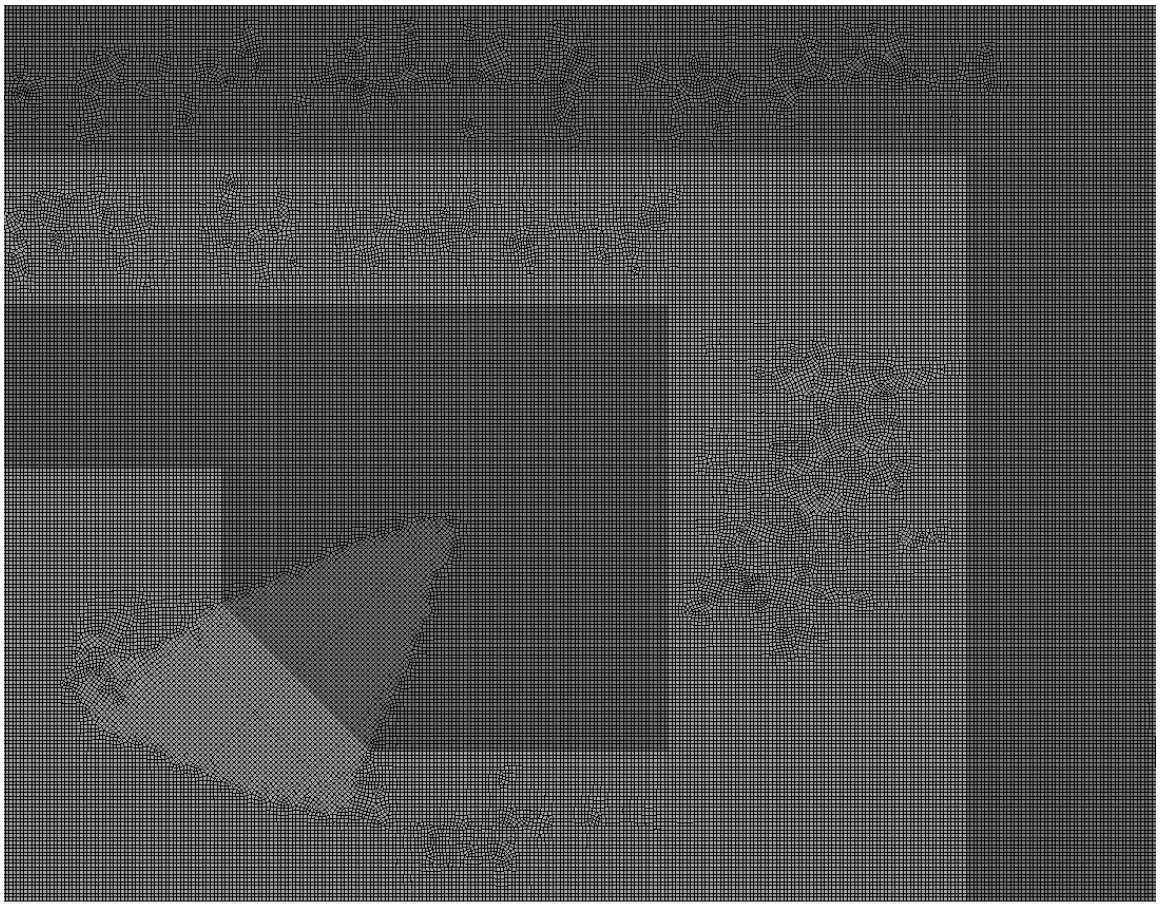

Figure 41. Quadrilateral mesh in the impingement region generated for the 2D simulations.

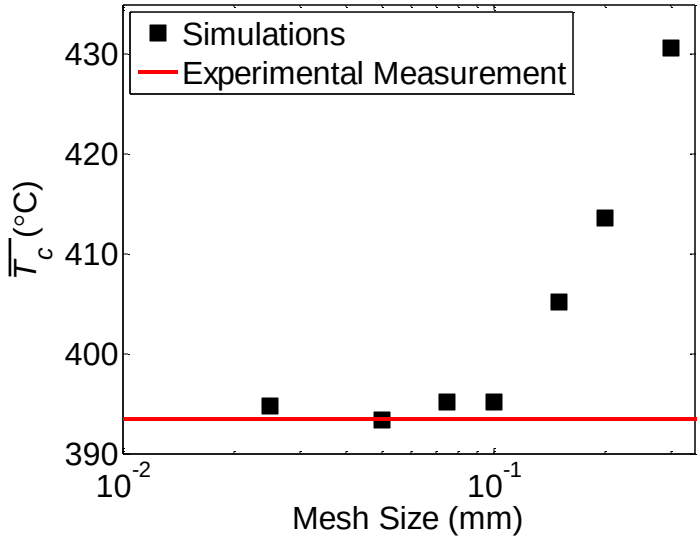

Figure 42. 2D forward flow mesh convergence analysis compared to experimental measurements in RC1

4.1.2 3D Model

Like the 2D model, the 3D model, shown in Figure 43, consisted of a 30° wedge of the 50 mm section of the brass shell and the 42 mm section of the tube next to their respective endcaps. All the outer boundaries are adiabatic with the exception of the heated surface. Symmetry boundary conditions are used for the 'sides' of the wedge. Non-uniformities in the heated surface from the flame and the ceramic sleeve are also ignored and an experimental average uniform heat flux calculated with Eq. 28 is used as the heat flux incident upon the heated surface. The temperature-dependent properties used for both the coolant and the solid materials are identical to those used for the 2D model as described in Appendix B.

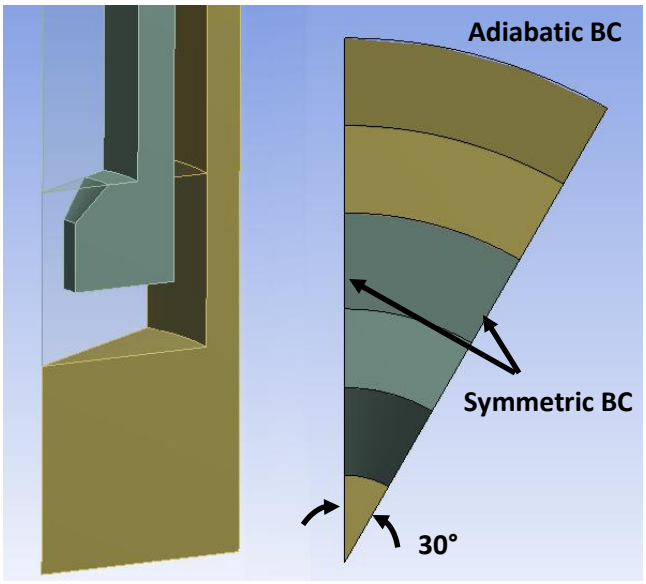

Figure 43. 3D 30° numerical model used for the numerical analysis without fins (left). Cross section of the model illustrating the boundary conditions (right)

Similar to the 2D simulations, all inlet and outlet coolant boundary conditions are identical to those measured in the experiments. Previous 3D numerical work for air suggested the RKE model with enhanced wall treatment provides results that most closely match the experimental measurements for forward and reverse flow; however, the numerical predictions here using the RKE model over predicted the heat transfer coefficients by approximately 5-30% over those obtained in the experiments [58]. Nonetheless, the RKE model was selected here. The turbulence parameters, k_t and ε, at the boundaries were defined using the equations given above.

The number of cells in the mesh was constrained by limitations on the maximum RAM available for the PC used for these simulations. Given the much larger number of cells required for the 3D model, a variable mesh was implemented with the most refined cells concentrated in the gap between the end of the tube and the cooled surface. In the gap, 50 μm tetrahedral cells are used in the coolant and the cell size expands at a predefined growth rate from this location, resulting in a mesh consisting of approximately

3.7×10^6 cells. As in the 2D simulations, reference case RC1 was used to evaluate the mesh convergence by comparing numerical predictions of $\overline{T_c}$ as the mesh size decreases with experimental results. The results of the mesh convergence study are shown in Figure 44. Overall, the mesh size has a very small effect on the final result, and the numerical predictions, although 8 °C less than the experimental results for even the finest mesh, appear to have converged for the two smallest mesh sizes. The larger of these two mesh sizes, 50 μm, was therefore used in the 3D simulations.

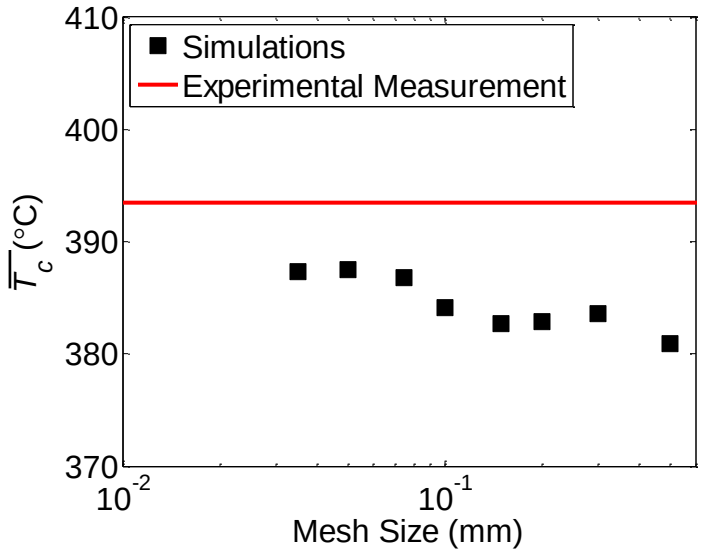

Figure 44. 3D bare forward flow mesh convergence analysis compared to experimental measurements in RC1

4.2 Results

4.2.1 2D Results

Each numerical simulation was compared to the corresponding experimental results for $\bar{h}$ and ΔP to validate the model over the full range of Re. In each simulation, numerically determined values for $\overline{T_c}$ are used to calculate $\bar{h}$ using Eq. 31. Then $\bar{h}$ is plotted versus $\dot{m}$ (*i.e.*, the dimensional form of Re) and compared with experimental values given in Figure 34. The comparison is shown in Figure 45.

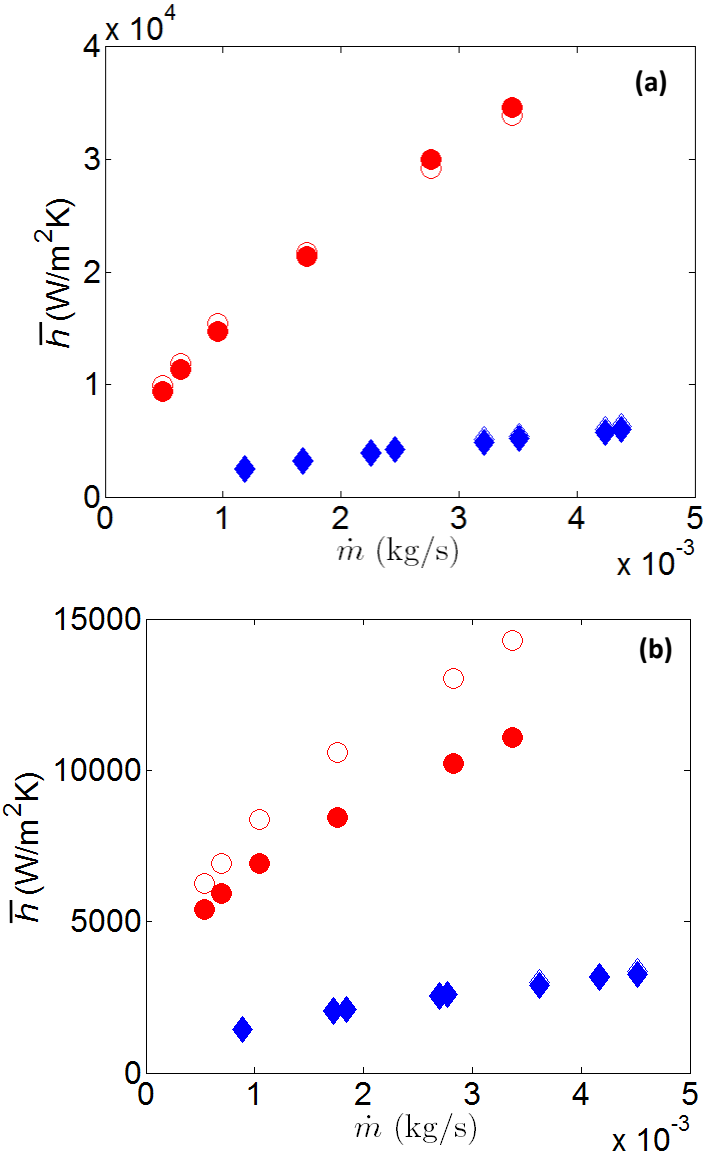

Figure 45. Numerically determined values (closed symbols) for $\overline{h}$ compared to experimental values (open symbols) for He (●) and Ar (♦) in forward flow (a) and reverse flow (b)

Alternatively, the discrepancy between the numerical predictions and the experimental results can be plotted as a percent difference, as in Figure 46. Except for the reverse flow cases with He, the numerical predictions are within approximately ±5% of the experimental values for $\overline{h}$, giving confidence that these models accurately

simulate the experiments. For further validation, the discrepancy between the numerical predictions and experimental measurements of ΔP is given in Figure 47.

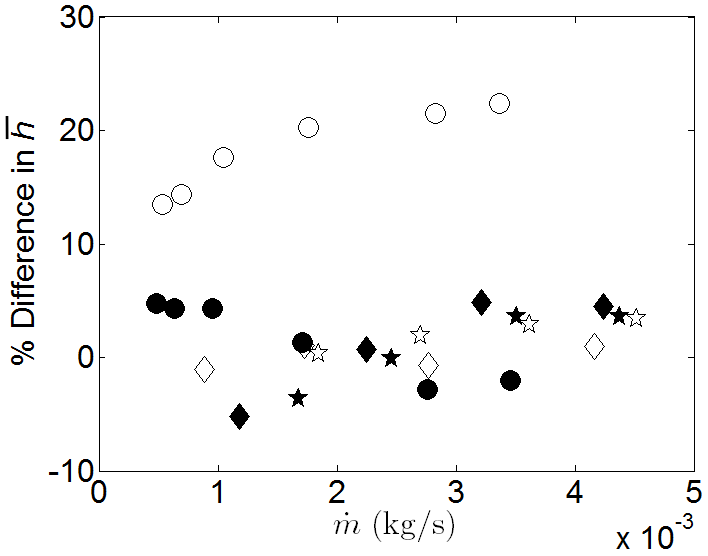

Figure 46. Percent difference in $\overline{h}$ from 2-D numerical simulations versus experimental values. Includes cases with He (●), Ar (♦), and high pressure Ar (★) for forward flow (closed symbols) and reverse flow (open symbols)

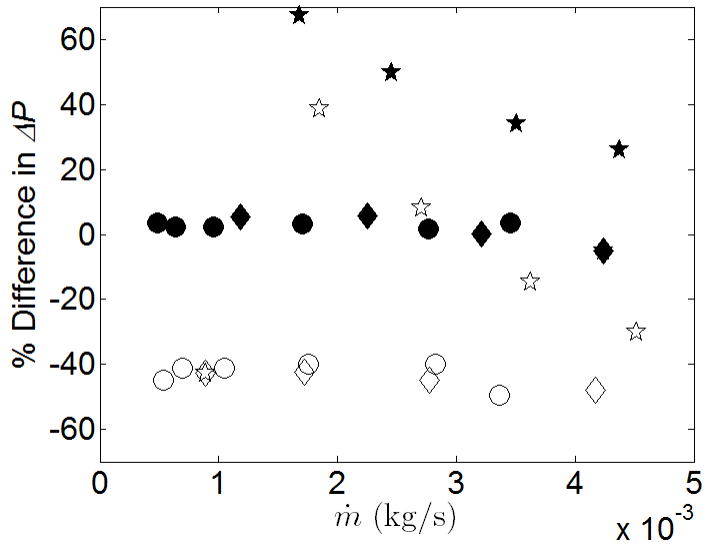

Figure 47. Percent difference in ΔP from 2-D numerical simulations versus experimental values. Includes cases with He (●), Ar (♦), and high pressure Ar (★) for forward flow (closed symbols) and reverse flow (open symbols)

The numerical predictions of ΔP for the forward flow cases with variable inlet pressure are in good agreement with the experimental data, but reverse flow cases differ by as much as ~40% from the experimental measurements. Nevertheless, given that the discrepancy between the numerical simulations and experimental measurements of Rader [58] showed deviation of ~40% for both the forward and reverse flow cases with air, those results suggest that adding the 45° chamfer to the port significantly improved the accuracy of ΔP for the forward flow cases. The reverse flow cases appear, however, to be unaffected by this modification.

The numerical predictions for $\bar{h}$ and ΔP using the SA turbulence model are in good agreement with the experimental values for the forward flow cases. Predictions for the reverse flow cases with He for $\bar{h}$ differ from the experimental values by 10-20%, and those for ΔP differ by approximately 70% for both He and Ar. Two additional turbulence models available in ANSYS FLUENT®, the SA and standard k-epsilon (SKE) models, were therefore explored for these reverse flow cases in an attempt to improve upon the results with helium. Neither of these two models gave results that were a noticeable improvement over those obtained with the RKE model. All of this suggests that there is considerable room for improvement in these numerical models. Ideally, the same turbulence model would be used for each flow direction; however, this might require that a different mesh is used for each flow direction. Nevertheless, the numerical predictions for the forward flow cases can be used with reasonable confidence to study the discrepancies between the experimental results for different coolants.

To better understand the discrepancy in $\overline{Nu}$ values for different coolants shown in Figure 36a, a radial profile of local Nusselt number $Nu(r)$ was calculated along the cooled surface for simulations performed with air, He, and Ar, all at approximately the same $Re \approx 5\times10^4$ for four reference cases RC1-RC4. The values for air were calculated

from the simulations performed by Rader (RC2-RC3) [58]. The radial cooled surface temperature profiles $T_c(r)$ and cooled surface heat flux profiles $q''(r)$ from these simulations were extracted from the simulations and used in the following equation to calculate $Nu(r)$:

$$Nu(r) = \frac{q''(r)D_j}{[T_c(r) - T_i]k} \tag{44}$$

The local Nusselt number is graphed in Figure 48. As one would expect of dynamically similar experiments, $Nu(r)$ is similar over all four cases for air, He, and Ar. The small differences in $Nu(r)$ can be explained by inaccuracies in the turbulence models, variations in Re ($47500 < Re < 54500$), and the use of an average thermal conductivity for the coolant k. Nevertheless, the average values calculated from $Nu(r)$ in Figure 48 are all significantly lower than those presented in Figure 36a for $Re \approx 5\times10^5$ (open symbols). Given that $\bar{h}$ values from the simulations and the experiments were in good agreement for the forward flow cases (Figure 46a), this result suggests that a significant fraction of the heat incident on the HEMP-like divertor is not removed at the cooled surface as was originally assumed in Eq. 31. This heat must instead be conducted through the side walls of the divertor before it is ultimately removed by convection from the inner surface of the side walls. This conduction through the side walls of course reduces the heat transfer coefficient at the cooled surface, and the relative importance of this effect will presumably vary with the coolant, which explains the discrepancy in $\overline{Nu}$ among air, He, and Ar.

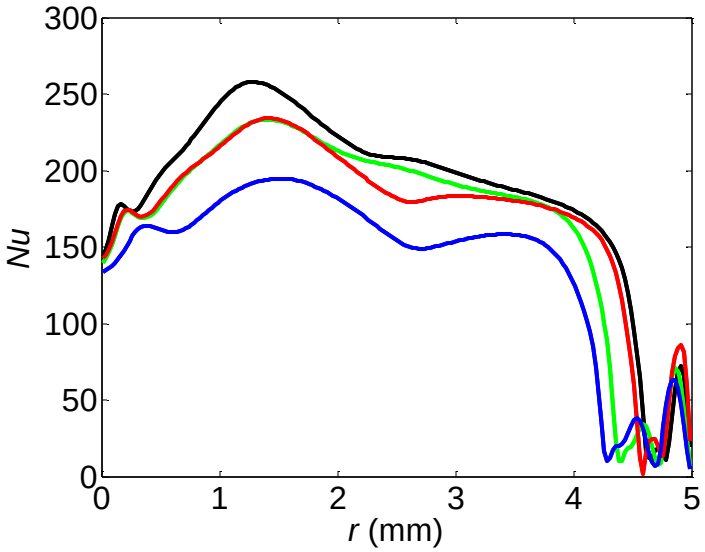

Figure 48. Numerically determined local Nu profile at $Re \approx 5\times10^4$ for helium (red, RC1), air (black, RC2) [58], high-pressure air (green, RC3) [58], and high pressure argon (blue, RC4)

The fraction of heat that is removed at the cooled surface is plotted as a function of Re for the various coolants for both forward and reverse flow cases in Figure 49. From these figures it is immediately clear that the fraction of heat incident on the module, which is being removed by the cooled surface, is well below 100%, and that it varies strongly depending on the coolant with a weak dependence on Re. For simulations performed with air [58], the fraction of heat convected to the coolant at the cooled surface is 35-45% for forward flow and 10-15% for reverse flow. For He, it varies from 45% to 65% in forward flow and from 20% to 35% in reverse flow. Finally for Ar, it ranges from 33% to 40% in forward flow and from 9% to 11% in reverse flow. As expected, the inlet pressure does not affect the fraction of heat convected away at the cooled surface. Although the HEMP-like design was not intended to be used without a fin array, the low fractions of heat being removed by convection at the cooled surface suggest there is significant room for improvement in the design.

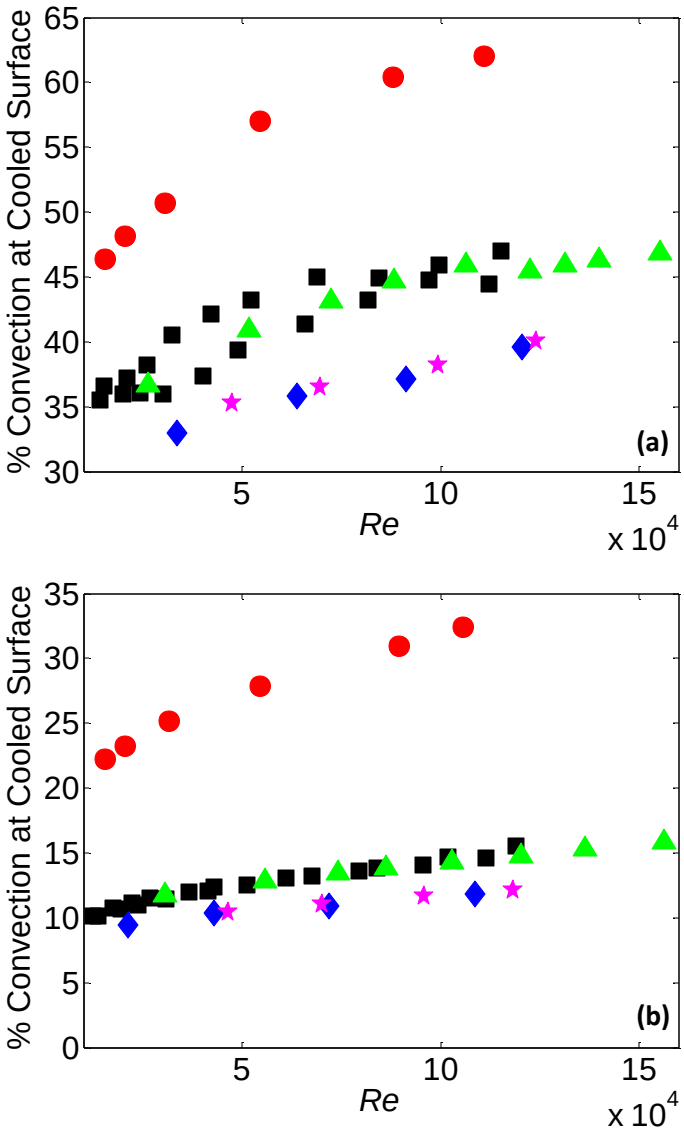

Figure 49. Fraction of the total incident heat that is convected away at the cooled surface for air (■), He (●), Ar (♦), high pressure air (▲), and high pressure argon (★) for forward flow (a) and reverse flow (b)

The fraction of heat removed by convection at the cooled surface from the simulations can be used to calculate a true average heat flux at the cooled surface. However, the resulting $\overline{Nu}(Re)$ correlation cannot be used to estimate the prototypical performance for a tungsten divertor since the fraction of heat that would be conducted through the walls cannot be accurately estimated without further simulations, and further

experiments to validate these simulations. Dimensional analysis is instead used to consider the fraction of heat flux that is conducted through the walls of a divertor, and as will be discussed in Chapter 5.

4.2.2 3D Results

Each steady-state experiment was also simulated using the 3D model, and the results were evaluated by comparing the numerical predictions and experimental values of $\overline{h}$ and ΔP. The $\overline{T_c}$ values from the simulations were again used to calculate $\overline{h}$ using Eq. 31, and the discrepancy between the numerical predictions and the experimental values is plotted in Figure 50.

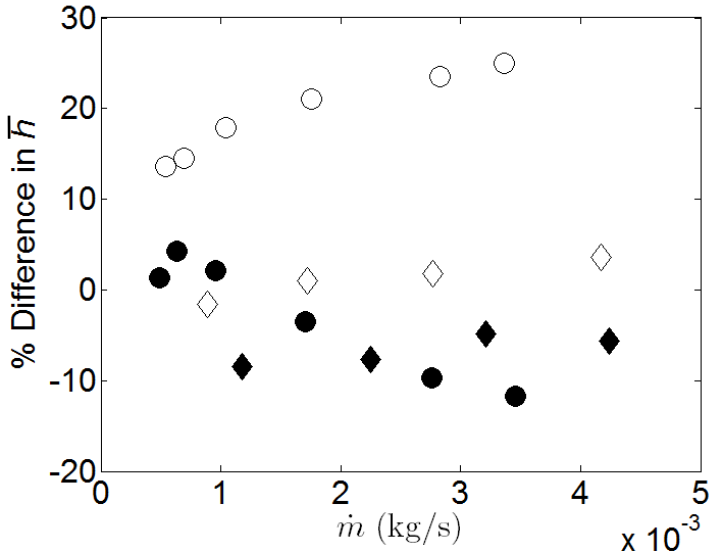

Figure 50. Percent difference in $\overline{h}$ from 3D numerical simulations versus experimental values. Includes cases with He (●) and Ar (♦) for forward flow (closed symbols) and reverse flow (open symbols)

Similar to the 2D simulations, the 3D simulations do a good job of predicting $\overline{h}$ for all of the flow configurations except for reverse flow with helium. The discrepancy in $\overline{h}$ between the simulations and the experiments is as large as 10% in some cases at higher Re, compared with a maximum deviation in the 2D simulations of approximately

5%. However, the 2D and 3D models can be considered to be in reasonable agreement given that they employ different meshes. The discrepancy in ΔP between the simulations and the experiments is shown in Figure 51.

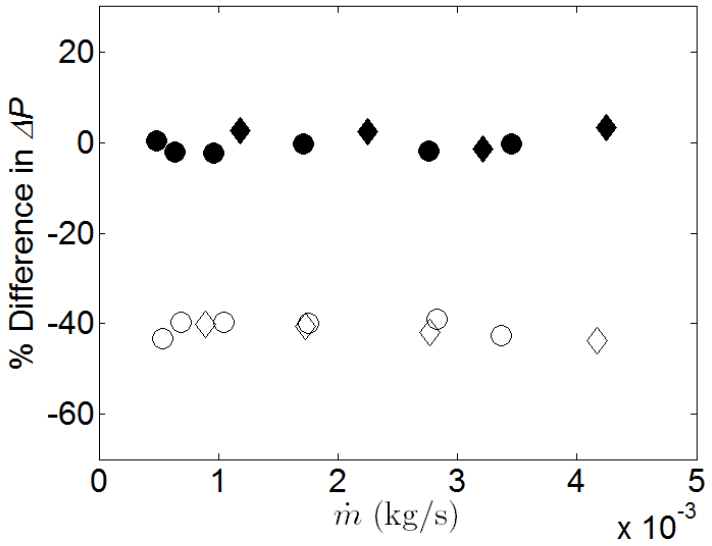

Figure 51. Percent difference in ΔP from 3D numerical simulations versus experimental values. Includes cases with He (●) and Ar (♦) for forward flow (closed symbols) and reverse flow (open symbols)

For the forward flow cases, the numerical and experimental values of ΔP are again in very good agreement with the experiments. However, in reverse flow cases, the discrepancy between the simulations and the experiments is about 40%. This indicates that including the chamfer in the 3D model did not improve the predictions for ΔP for reverse flow, as was the case for the 2D simulations, and the discrepancy is comparable to that found in the original simulations by Rader [58] using air. Nevertheless, using the RKE turbulence model with FLUENT's enhanced wall treatment in 3D simulations gives results that are in good agreement with the experiments in forward flow.

4.3 Numerical Modeling of HCFP Divertors

As discussed in Section 2.2.3, dynamically similar experiments were performed by Hageman et al. [45] on a brass HCFP module using air at room temperature and pressures up to 700 kPa. Correlations for $\overline{Nu}$ as a function of Re were developed based on temperature data from embedded thermocouples which measured temperatures near the cooled surface. The correlations were then used to predict the maximum heat flux an HCFP module could accommodate with and without an array of cylindrical pin fins. HCFP modules with slot widths of 2 mm and 0.5 mm were studied to investigate whether slot width had a significant effect on performance. For $Re_p = 3.3\times10^4$, these studies determined that the prototypical HCFP module could accommodate steady-state heat fluxes up to 14 MW/m^2 and 18 MW/m^2 without and with fins, respectively.

As discussed in Chapter 3 for the HEMP-like divertor, the results of the experiments in Hageman et al. should be confirmed by performing dynamically similar experiments using He and Ar. However, the mass flow rates required to perform dynamically similar experiments on the HCFP module using these coolants is impractical due to excessive costs with the experimental setup used in Chapter 3. Therefore, as an alternative to performing these experiments with He and Ar at room temperature and low pressures, a numerical model was created in ANSYS FLUENT® and validated with the air experiments. Simulations were then performed with He and Ar as coolants. Obviously, a numerical model using He at prototypical temperatures and pressures can also be created to directly predict the thermal performance, but simulations at room temperature and low pressures are first required to validate the model with experimental data. Furthermore, these simulations can also determine whether a significant fraction of heat is also conducted through the divertor walls in a divertor design other than the HEMP-like divertor. Only the HCFP geometry with a 2 mm wide slot without fins was

simulated because the number of elements that would be required to accurately model the flow between the fins was prohibitively large, and slot widths of 0.5 mm did not show any improvement in the thermal performance.

4.3.1 HCFP Model

Figure 52 shows the HCFP test section used in the dynamically similar experiments and the 3D half model that was used in the simulations. The HCFP test section, which is significantly larger than the HEMP-like test section, requires larger cells. All outer boundaries, except for the symmetry plane and the heated surface, were modeled as adiabatic. The test section was heated in the experiments using a copper heater block with three embedded cylindrical cartridge heaters. The heat flux incident on the heated surface was given in the simulations as a uniform profile whose value was taken to be the thermal power, determined again from a control volume energy balance on the coolant divided by the area footprint of the copper heater block $A_{hb} = 1.753\times10^{-3}$ m^2. Given the relatively large size and high thermal conductivity of the copper heater block, conduction within the heater block should ensure that the incident heat flux is essentially uniform. The test section consists of an outer shell of C36000 brass alloy surrounding an inner aluminum cartridge. Temperature dependent properties were used for brass alloy shell and coolants in these simulations (the aluminum cartridge did not have a large enough temperature variation in the simulations to warrant temperature dependent properties); further details are given in Appendix B.

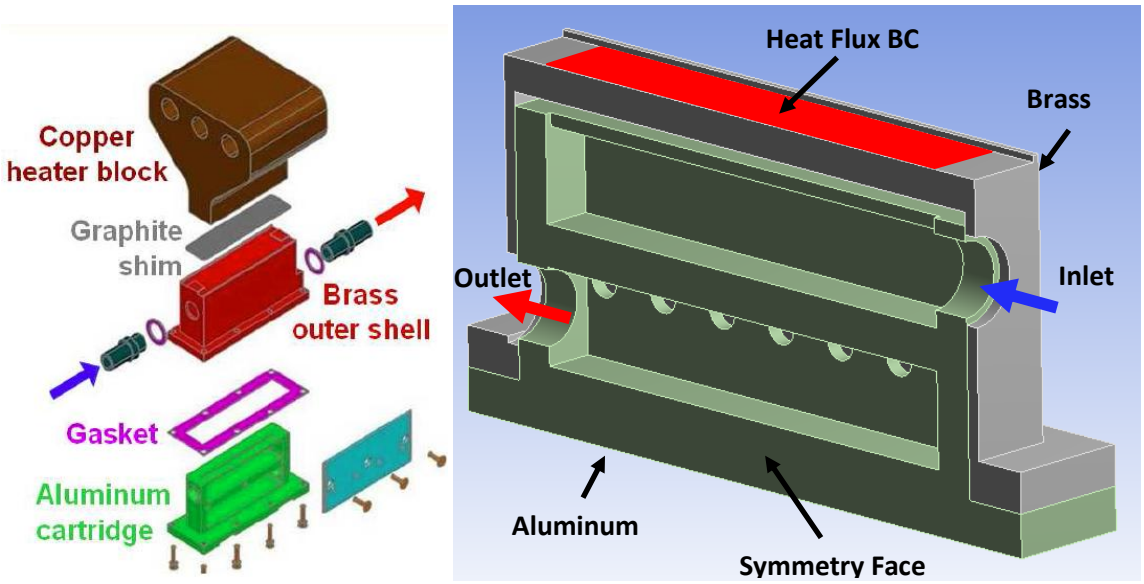

Figure 52. Solid model of the dynamically similar experimental setup used in Hageman et al. [45] (left) and the numerical 3D half model used to simulate the test section (right). The heat flux boundary condition is highlighted in red and all other solid boundaries are adiabatic

The turbulence model used in these simulations was the standard k-ε (SKE) model with standard wall functions. Given the large size of this test section, it is impractical to perform these simulations with as fine a mesh as that used in the HEMP-like simulations, and so the mesh resolution is much greater than a wall unit. Standard wall functions were therefore used here in conjunction with the SKE model.

The mass flow inlet and pressure outlet coolant boundary conditions were taken from experiments performed at different Re. As in the HEMP-like models, $\dot{m}$, T_i, T_o, P_i, and P_o are defined; however, T_i and P_o are fixed, and T_o and P_i are defined in the event of any recirculating flow at the boundaries (which only occurs briefly in the initial iterations). The turbulence parameters at the boundaries, k_t and ε, were defined using Eqs. 42 and 43.

The mesh consists of approximately 3.85×10^6 hexahedral and tetrahedral cells of varying sizes, where the smallest cells of about 0.25 mm are placed along the cooled

surface. The size of the cells increases from the cooled surface in the jet impingement region to 0.75 mm in the coolant, and increase further in the solid to a maximum cell size of 1.5 mm in the outer shell of the test section. This range of cell sizes was determined from a series of simulations of the same steady-state experiment, Reference Case #5 (RC5) with different mesh sizes. Predicted values of the average cooled surface temperature $\overline{T_c}$ along the midline of the test section (near the embedded thermocouples) were again compared for different meshes; Figure 52 shows $\overline{T_c}$ as a function of the total number of cells on the cooled surface compared with the experimental values. Since the cooled surface temperature monotonically deceases to the experimental value, the mesh with the largest number of cells on the cooled surface, ~3.3×10^4, or 3.85×10^6 cells total, was used in these simulations. Unfortunately, using a mesh with an even larger number of cells was impractical with the computational resources available.

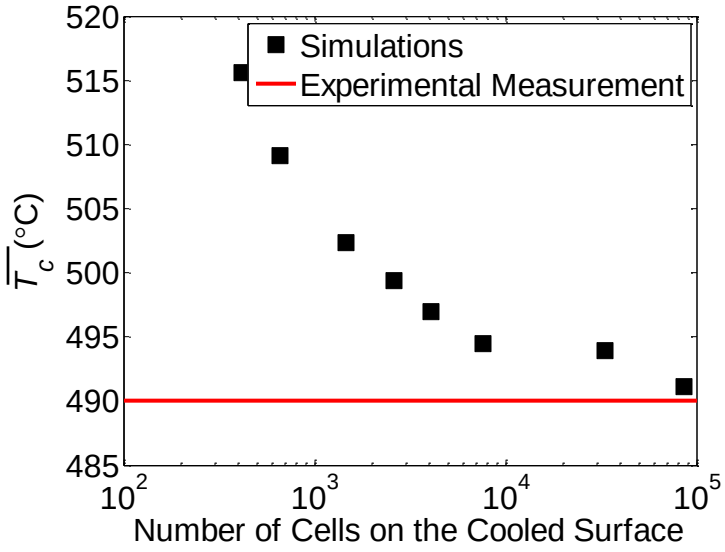

Figure 53. Average cooled surface temperature along the test section midline in the simulations and experiment (RC5) versus the total number of cells on the cooled surface

4.3.2 Results

Hageman et al. [45] carried out dynamically similar experiments performed at three approximate Re of 12700, 33000, and 47,000, compared to a Re_p of approximately 3.3×10^4. One experiment at each Re was simulated here. The data from Hageman et al. are used to compute an average Nusselt number $\overline{Nu}$ using a procedure similar to that described in Section 3.2 for the HEMP-like divertor.

The average incident heat flux is calculated using Eq. 28 where the area of the heated surface for the HCFP $A_h = 2.206\times10^{-3}$ m^3. Then, the five thermocouples embedded 0 mm, 4.1 mm, 4.1 mm, 8.2 mm and 8.2 mm from the plane of symmetry are extrapolated to values at the cooled surface assuming one-dimensional conduction using Eq. 29. Next, an area-weighted average cooled surface temperature $\overline{T_c}$ is calculated as follows:

$$\overline{T_c} = \left(T_{c0} + T_{c4.1} + T_{c4.1} + T_{c8.2} + T_{c8.2}\right)/5 \tag{45}$$

An average heat transfer coefficient is computed using Eq. 31 for an HCFP cooled surface area $A_c = 1.853\times10^{-3}$ m^3. Finally, an average Nusselt number $\overline{Nu}$ is computed for each experiment using Eq. 34 and the $\overline{T_c}$ from Eq. 45. The experimentally determined $\overline{Nu}$ is then compared to the $\overline{Nu}$ calculated from the simulations, and the difference between these two values is used to estimate the numerical error. The percent difference between the numerical and experimental values is shown for the three Re in Figure 54.

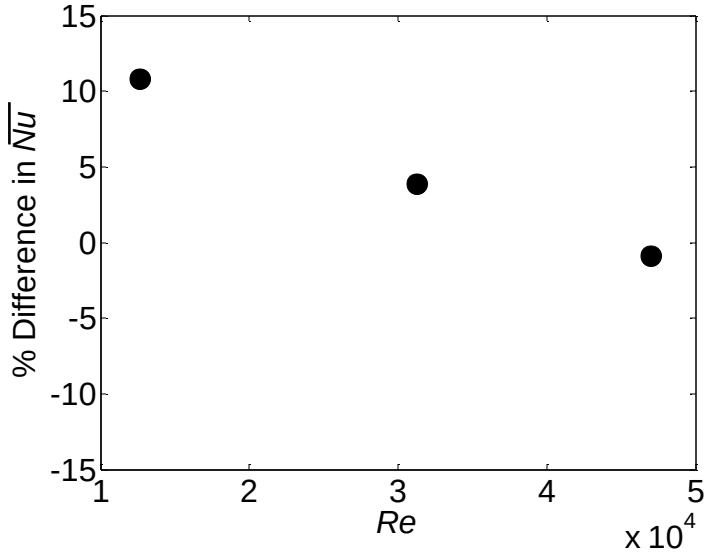

Figure 54. Percent difference in $\overline{Nu}$ between the experiments and the numerical simulations of the HCFP module using air as a coolant

Figure 54 shows that the simulations and the experiments are in reasonable agreement, with a maximum difference of ~11% at the lowest Re. Therefore, the numerical model can be used to estimate $\overline{Nu}$ values for the coolant He. Furthermore, since the simulations of the HEMP-like module showed that the deviations in $\overline{Nu}$ between different coolants were due to differences in the fraction of heat conducted through the walls of the divertor, simulations were performed for three different test section materials with very different k_s values. These three materials were a stainless steel alloy, a fictitious high-conductivity material, and a fictitious low-conductivity material. The five different coolant/test section material configurations simulated here are summarized in Table 1.

Table 1. HCFP configurations simulated in the numerical model. Details for the material properties are found in Appendix B.

Configuration	Coolant	Test Section Material	k_s (W/m·K)
1	Air	Brass	~140
2	He	Brass	~140
3	Air	Stainless Steel	~20
4	Air	High Conductivity	~185
5	Air	Low Conductivity	~9

Figure 55 shows the numerical results for $\overline{Nu}$ obtained at the three Re using the same coolant boundary conditions as in the three original simulations with air and the appropriate mass flow rates for helium.

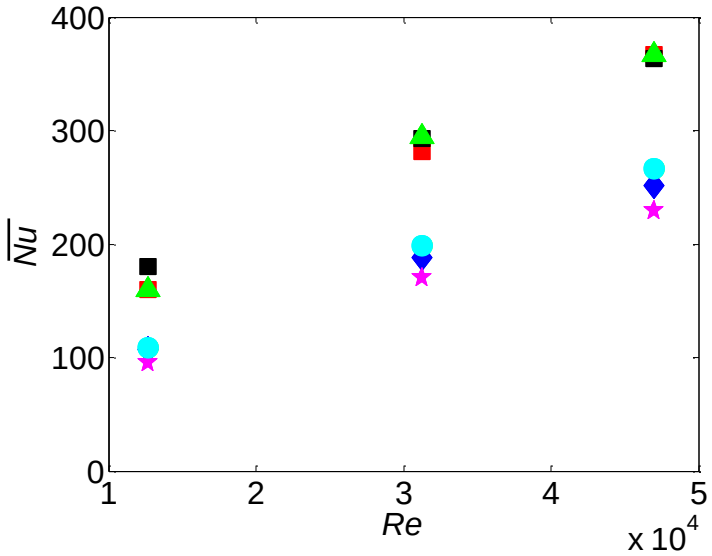

Figure 55. $\overline{Nu}$ for each Re experimentally tested in Hageman et al. for the five different coolant/test section material configurations listed in Table 1: experiments (■) [45], conf. 1 (■), conf. 2 (●), conf. 3 (♦), conf. 4 (▲), and conf. 5 (★).

As observed for the HEMP-like divertor, $\overline{Nu}$ depends on the coolant, with He giving lower $\overline{Nu}$ than air. This again suggests that less heat is being conducted through the walls of the divertor in experiments with He (*cf.* Figure 49). Furthermore, reducing

the thermal conductivity of the test section material has the same effect, with more heat convected away at the cooled surface. Dimensional analysis will also be used for the HCFP geometry to account for conduction through the walls of the divertor, as will again be discussed in Chapter 5.

CHAPTER 5: PROTOTYPICAL PERFORMANCE

5.1 Effect of Thermal Conductivity Ratio

It is initially assumed in Eq. 31 that all of the incident heat flux on the test section is removed at the cooled surface via convection. However, as shown in Chapter 4, a significant fraction of the incident heat flux is instead conducted through the walls of the divertor. This heat is of course ultimately removed by convection as the coolant flows over the side walls of the divertor, but this is not included in the current dimensional analysis of $\overline{Nu}$. A new dimensional analysis was therefore performed to obtain a revised simple and experimentally based correlation for the $\overline{Nu}$, as detailed next.

The average heat transfer coefficient $\bar{h}$ was originally assumed to depend upon D_j, ρ, $\overline{V}$, μ, $\overline{c_p}$, and k. The problem therefore involves seven variables and four basic dimensions: mass M, length L, time T, and temperature Θ. From Buckingham's Pi Theorem, three unique non-dimensional groups, or Π terms, are sufficient to completely describe this problem, and the Π terms used here are namely, $\overline{Nu}$, Re, and Pr. However, since the Pr values for the three coolants considered in this problem are comparable, ranging from ~0.66 to 0.71, and most correlations for turbulent heat transfer scale as $Pr^{0.4}$ we assume that the dependence of $\overline{Nu}$ on Pr is negligible. Hence, $\overline{Nu}$ only depends upon the Re.

However, given that conduction through the divertor walls is non-negligible, $\bar{h}$ must also depend upon an additional parameter, namely the thermal conductivity of the divertor material k_s. By the Buckingham Pi Theorem, the problem then requires four Π terms, whose derivation is briefly summarized below.

First, the variables are expressed in terms of their basic dimensions:

$$\begin{aligned} \bar{h} &= MT^{-3}\Theta^{-1} & \mu &= ML^{-1}T^{-1} \\ D_j &= L & \overline{c_p} &= L^2T^{-2}\Theta^{-1} \\ \rho &= ML^{-3} & k &= MLT^{-3}\Theta^{-1} \\ \bar{V} &= LT^{-1} & k_s &= MLT^{-3}\Theta^{-1} \end{aligned} \tag{46}$$

Then, using the Method of Repeating Variables, the four repeating variables, which contain all the basic dimensions, are chosen to be D_j, $\bar{V}$, μ, and k. Each of the four remaining variables is then combined with these four repeating variables to create four dimensionless groups. For the group involving $\bar{h}$:

$$\Pi_1 = \bar{h}D_j{}^a\bar{V}^b\mu_i{}^c k^d = \left(MT^{-3}\Theta^{-1}\right)(L)^a\left(LT^{-1}\right)^b\left(ML^{-1}T^{-1}\right)^c\left(MLT^{-3}\Theta^{-1}\right)^d \tag{47}$$

$$\begin{aligned} &1+c+d=0 \quad (M) \\ &a+b-c+d=0 \quad (L) \\ &-3-b-c-3d=0 \quad (T) \\ &-1-d=0 \quad (\Theta) \\ &a=1 \quad b=0 \quad c=0 \quad d=-1 \end{aligned} \tag{48}$$

$$\Pi_1 = \frac{\bar{h}D_j}{k} = \overline{Nu} \tag{49}$$

Repeating this process to determine Π terms that involve ρ, $\overline{c_p}$, and k_s gives the dimensionless groups Re, Pr, and κ respectively:

$$\Pi_2 = \frac{\rho\bar{V}D_j}{\mu_i} = Re \tag{50}$$

$$\Pi_3 = \frac{\overline{c_p}\mu_i}{k} = Pr \tag{51}$$

$$\Pi_4 = \frac{k_s}{k} = \kappa \tag{52}$$

Finally, the dimensional analysis gives:

$$\overline{Nu} = f\left(Re, Pr, \kappa\right) \approx f\left(Re, \kappa\right) \tag{53}$$

In this dimensional analysis, the only new dimensionless group involving the thermal conductivity of the divertor material k_s, κ, is simply the ratio of the thermal

conductivity of the solid to that of the coolant. Of course, this analysis does not yield a unique set of dimensionless groups. It is convenient, however, to use the dimensionless groups that are commonly used in heat transfer, namely $\overline{Nu}$, Re and Pr. The range of κ produced from the experimental data is summarized in Table 2:

Table 2. Approximate experimental thermal conductivity values for different coolants. Temperature dependent thermal conductivities are given which account for the different values in the same test section material

Test Section Material	Coolant	k_s (W/m·K)	k (mW/m·K)	κ (-)
Brass (C36000)	Ar	136	19	7200
Brass (C36000)	Air	140	28	5000
Brass (C36000)	He	125	158	800

Physically speaking, κ characterizes the relative contributions of conduction and convection observed in Figure 36. In heat transfer, the Biot number Bi is usually used instead in problems where both convection and conduction are relevant

$$Bi = \frac{\bar{h} L_c}{k_s} \tag{54}$$

where L_c is a characteristic length, assumed to be the diameter of the cooled surface $D_c = 10$ mm. Here, κ is used instead of the more common Bi because κ, unlike the Biot number, is independent of $\bar{h}$. Since $\overline{Nu}$ is also a function of $\bar{h}$, using Bi in a correlation for $\overline{Nu}$ would require an iterative solution. Using κ instead may, however, still require an iterative solution because the thermal conductivities of the solid and the coolant are functions of temperature, as detailed in the following sections.

Nevertheless, based on this dimensional analysis, the experimental data from Figure 38 are curve-fit to a power-law function of the form:

$$\overline{Nu} = C \cdot Re^a \cdot \kappa^b \tag{55}$$

where a, b, and C are all constants which are determined using multiple linear regression in MATLAB 2008b. Since the results for FF suggest that $\overline{Nu}$ is essentially independent of κ, the $\overline{Nu}$ correlation for this case is curve-fit to a power-law function that only involves Re. The thermal conductivity of the coolant k is evaluated at the average of the inlet and outlet coolant temperatures $(T_i + T_o)/2$, and the thermal conductivity of the shell k_s is evaluated at the average cooled surface temperature $\overline{T_c}$. The resulting correlations for each flow configuration are as follows:

$$\begin{aligned} \overline{Nu} &= 0.0348 Re^{0.7534} \kappa^{0.1182} \quad \text{(BF)} \\ \overline{Nu} &= 0.0113 Re^{0.8574} \quad \text{(FF)} \\ \overline{Nu} &= 0.0789 Re^{0.5194} \kappa^{0.2629} \quad \text{(BR)} \\ \overline{Nu} &= 0.0196 Re^{0.7429} \kappa^{0.0944} \quad \text{(FR)} \end{aligned} \tag{56}$$

where these correlations, based upon the data in Table 2, are valid for:

$$\begin{bmatrix} 1\times10^4 \le Re \le 1.3\times10^5 \\ Pr \approx 0.7 \\ 800 \le \kappa \le 7200 \end{bmatrix} \tag{57}$$

Figure 56 (forward flow) and Figure 57 (reverse flow) compare the experimental data with their respective correlations (solid lines), as well as ±10% uncertainty bands (dashed lines).

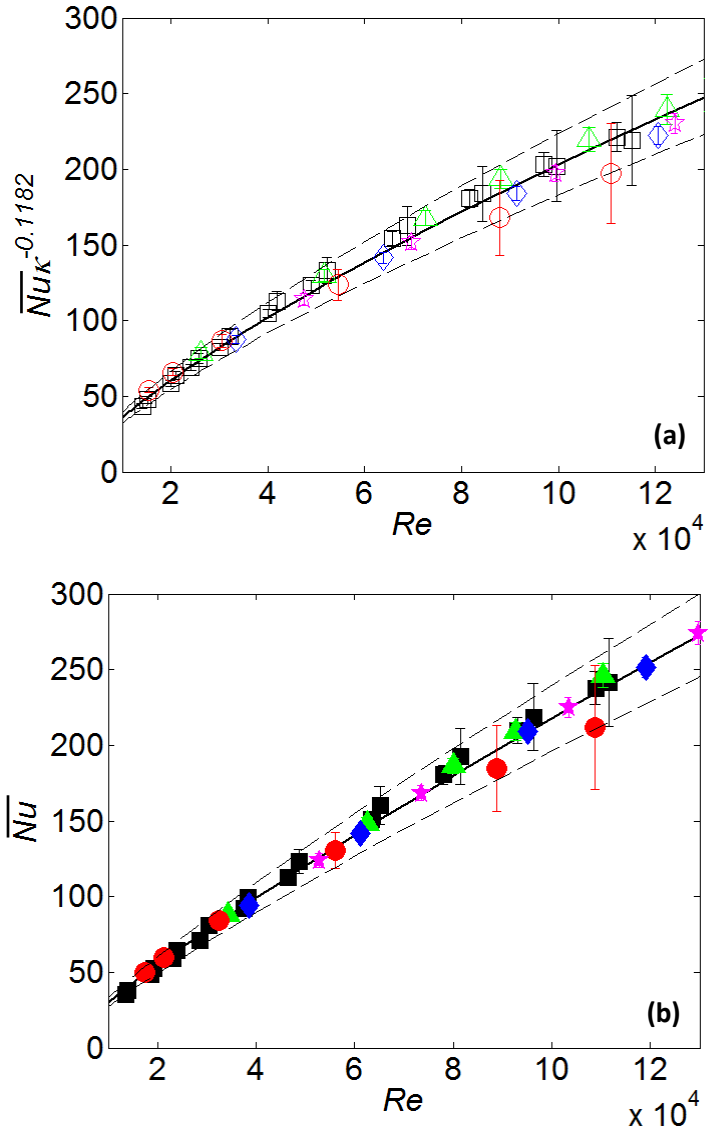

Figure 56. Average Nusselt number correlation using the thermal conductivity ratio for air (■), He (●), Ar (♦), high pressure air (▲), and high pressure argon (★) in BF (a) and FF (b). Dashed lines indicate ±10% deviation from the correlation

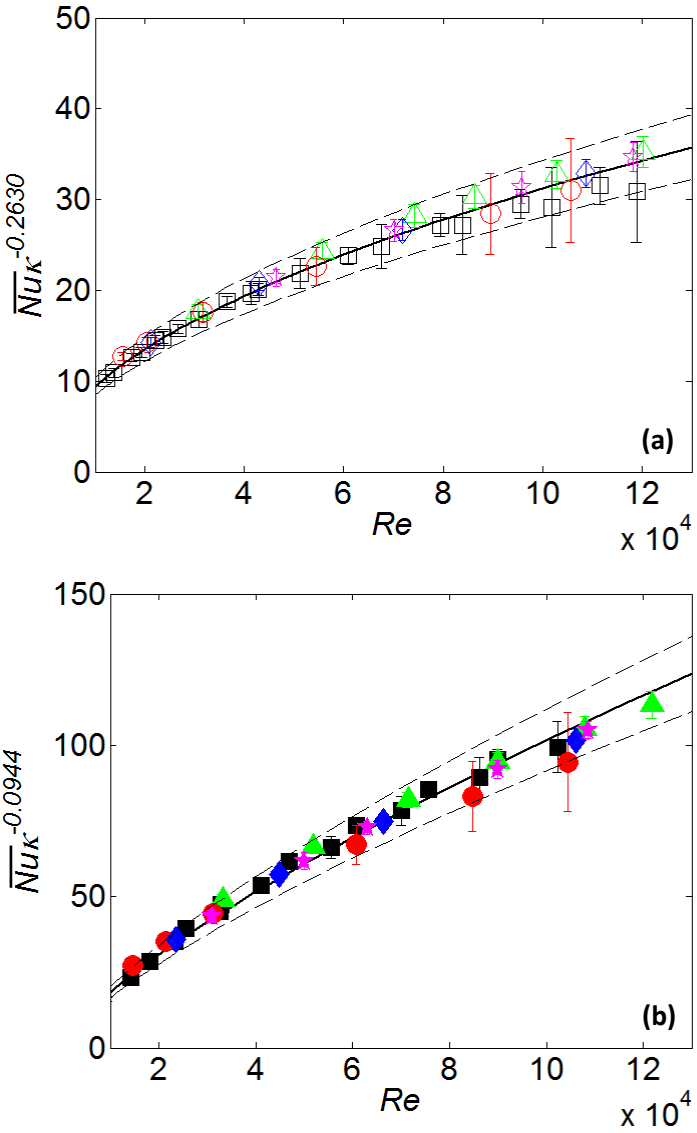

Figure 57. Average Nusselt number correlation using the thermal conductivity ratio for air (■), He (●), Ar (♦), high pressure air (▲), and high pressure argon (★) in BR (a) and FR (b). Dashed lines indicate ±10% deviation from the correlation

The experimental measurements are within ±10% of the correlations of Eq. 56, suggesting that these correlations can be used with reasonable confidence to predict the thermal performance of these divertor configurations at prototypical operating conditions. Typically, heat transfer correlations for turbulent internal flows have $\overline{Nu} \propto Re^n$ where

$n \approx 0.8$. This relationship appears in the correlations here for $\overline{Nu}$ if they are expressed in terms of Bi instead of κ. Dividing $\overline{Nu}$ by κ yields:

$$\frac{\overline{Nu}}{\kappa} = \frac{\bar{h}D_j}{k}\frac{k}{k_s} = Bi\frac{D_j}{L_c} = CBi \tag{58}$$

where C is a constant. Then, the FR correlation given in Eq. 56 can be rewritten:

$$\frac{\overline{Nu}}{\kappa^{0.0944}} = 0.0196Re^{0.7429} = CBi^{0.0944}\overline{Nu}^{0.9056} \tag{59}$$

$$\overline{Nu}^{0.9056} = CRe^{0.7429}Bi^{-0.0944} \tag{60}$$

Finally, $\overline{Nu}$ can be written in terms of Re and Bi as:

$$\overline{Nu} = CRe^{0.8203}Bi^{-0.1042} \tag{61}$$

and we see that the Nusselt number depends on the Reynolds number raised to an exponent that is approximately 0.8. Similarly, rewriting $\overline{Nu}$ in terms of Re and Bi gives $\overline{Nu} \propto Re^{0.854}$ for the BF case and $Re^{0.741}$ for the BR case. Finally, for FF, where $\overline{Nu}$ is essentially independent of κ (or Bi), $\overline{Nu} \propto Re^{0.857}$. So, in all four flow configurations, the dependence of $\overline{Nu}$ upon Re is consistent with that expected for turbulent internal flow if the data is fit with alternative dimensionless groups, and the variations in n are likely due to experimental uncertainty and the choice of "characteristic" properties (*e.g.* evaluating properties at inlet, *vs.* average coolant, temperatures).

5.2 Steel Test Section

Before using the correlations of Eq. 56 to predict the prototypical performance, the value of κ at prototypical conditions must be estimated and compared with the bounds given in Eq. 57. The HEMP divertor design specified a shell of the tungsten alloy WL10. For a divertor temperature of ~1000 °C and an average He coolant temperature of ~650 °C, the thermal conductivities of the solid and coolant are ~116 W/(m·K) and

0.354 W/(m·K), respectively, giving a prototypical thermal conductivity ratio $\kappa_p \approx$ 340. This is unfortunately below the range of validity of the correlations; therefore, the correlations must be verified at lower κ values.

5.2.1 Steel Experiments

The simplest way to achieve lower κ values in the experiments is to decrease the thermal conductivity of the shell k_s. Moreover, since the previous experiments only varied the thermal conductivity of the coolant k, using a test section made from a different material also provides confidence that correlations based on κ are valid for changes in the thermal conductivities of the coolant or the shell. The steel test section previously described in Section 3.1.1 was therefore used for further experiments. Since results from a single flow configuration obtained with a different test section should be sufficient to prove that the correlations are valid at lower κ, only the BF configuration was examined.

AISI 1018 carbon steel was chosen as the shell material due to its relatively low thermal conductivity and the availability of k_s data over a range of temperatures. In experiments with helium, $\kappa \approx 330$, based on $k = 0.161$ W/(m·K) at 40 °C and $k_s = 52.9$ W/(m·K) at 250 °C, a value slightly lower than that expected at prototypical conditions. Materials with even smaller k_s could, in theory, be used with other coolants, such as air, to achieve $\kappa = 340$, but this was considered to be impractical because non-uniformities within the flame used to heat the shell can become significant for shells made of materials with very low thermal conductivities. To minimize nonuniformities in the heat flux incident upon the cooled surface of the shell the shell endcap length (*i.e.*, the dimension between the heated outer and cooled inner surfaces) was increased to 10 mm.

Experiments were conducted using the same procedure given in Section 3.2. A total of 22 steady-state experiments were performed: 13 experiments using air, 5 experiments using helium, and 4 experiments using argon, giving three values of $\kappa \approx$ 370, 2000, and 3000 for helium, air, and argon, respectively. Nusselt numbers $\overline{Nu}$ and κ were calculated for each experiment; these results, along with those from previous BF experiments and the BF correlation of Eq. 56, are all plotted in Figure 58.

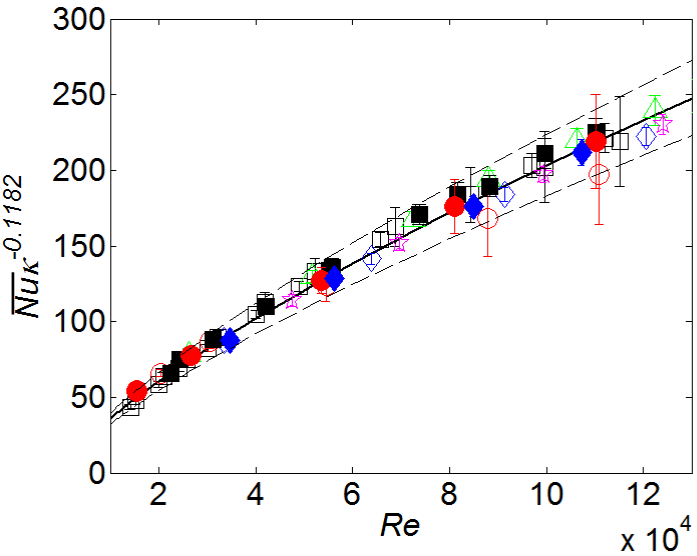

Figure 58. Average Nusselt number correlation using the thermal conductivity ratio for air (■), He (●), Ar (♦), high pressure air (▲), and high pressure argon (★) using the steel shell in BF configuration (closed symbols). Open symbols indicate experiments using a brass shell. Dashed lines indicate ±10% deviation from the correlation

The results for $\overline{Nu}$ using the steel shell are in excellent agreement with the previous BF results for all three coolants providing added confidence in the validity of this correlation approach. Finally, the loss coefficient K_L was computed for each experiment using Eq. 35, and these data, along with those from the previous experiments, are shown in Figure 59. As expected, K_L is independent of k_s and κ.

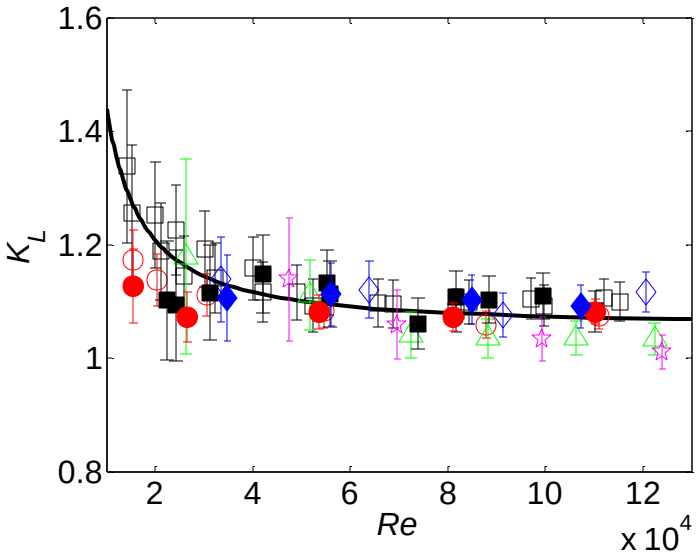

Figure 59. Loss coefficients for air (■), He (●), Ar (♦), high pressure air (▲), and high pressure argon (★) using the steel shell in BF configuration (closed symbols). Open symbols indicate experiments using a brass shell

In summary, it is experimentally confirmed that the correlations of Eq. 56 are valid at lower values of κ, and that these correlations can be extended to κ_p for the BF case. Although the actual value of κ achieved in these experiments with helium (~370) is slightly greater than the expected prototypical value of ~340, the difference is small enough that the correlation can be used with some confidence at prototypical values. Furthermore, while this correlation was only experimentally verified for the BF correlation at lower κ, it can be assumed that the corresponding correlations of Eq. 56 for the other three flow configurations (*i.e.*, FF, BR and FR) can also be extended to prototypical conditions. The bounds over which the correlations of Eq. 56 are valid were therefore extended to:

$$\begin{bmatrix} 1\times10^4 \le Re \le 1.3\times10^5 \\ Pr \approx 0.7 \\ 370 \le \kappa \le 7200 \end{bmatrix} \tag{62}$$

Finally, the experimentally derived correlations for $\overline{Nu}$ and K_L given in Eq. 56 and Eq. 37, respectively, can be used to predict the prototypical performance of the four flow configurations. Additional numerical simulations were performed, however, to confirm that κ accurately characterizes the relative contributions of convection and conduction in the steel test section.

5.2.2 Numerical Simulations of the Steel Test Module

The 2D axisymmetric numerical model given in Section 4.1.1 was used to simulate the experiments performed with the AISI 1018 steel test section. Earlier numerical studies showed that the results obtained with a 2D model were sufficient, and a 3D model was redundant. Two small modifications to the model were required, namely, changing the test section material to steel, and increasing the length of the shell endcap from 6 mm to 10 mm. The model also included the chamfer on the inside surface of the port. The model, when meshed with a quadrilateral grid using 25 μm cells, consisted of approximately 5×10^5 cells. The Spalart-Allmaras turbulence model was used in the simulations, and all the boundary conditions were identical to those used for the simulations of the brass test section, as described in Chapter 4.

The model was first validated by comparing experimentally determined and numerically predicted values of $\bar{h}$ and ΔP. For each simulation, the values of $\overline{T_c}$ from the simulations were used in Eq. 31 to calculate $\bar{h}$. The difference (in percent) between $\bar{h}$ between the experiments and the simulations is plotted as a function of $\dot{m}$ in Figure 60.

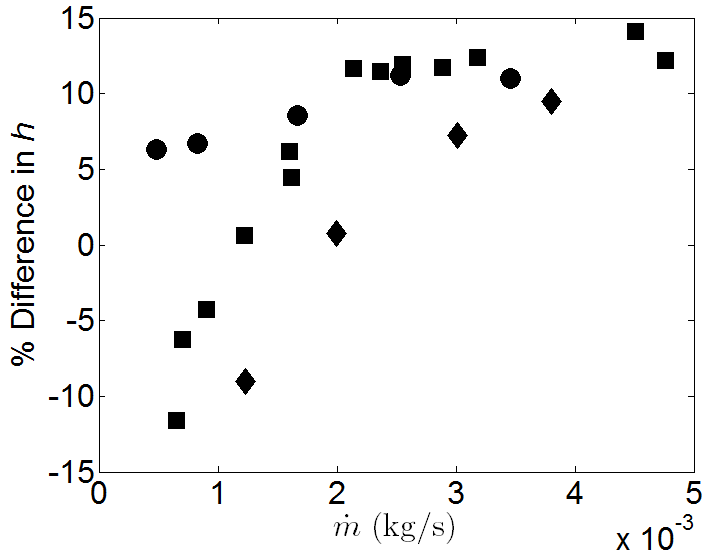

Figure 60. Percent difference in $\overline{h}$ between experiments and simulations using the steel shell for air (■), He (●), and Ar (▲)

The average heat transfer coefficient calculated from the simulations is in all cases within 14% of that obtained in the experiments. At moderate $\dot{m}$, the simulations underestimate $\overline{h}$ by approximately 11%. This discrepancy is slightly higher than that for the brass test section, perhaps because the thermal conductivity of this steel as a function of temperature is not as well-characterized as that of the brass. Nonetheless, the numerical simulations were considered in reasonable agreement with the results from both the brass and steel shell experiments. The difference in ΔP values (again, in percent) between the simulations and the experiments is shown in Figure 61. The simulations give pressure drop values within 7% of the experiments, similar to what was observed for simulations of the forward flow cases using the brass test section.

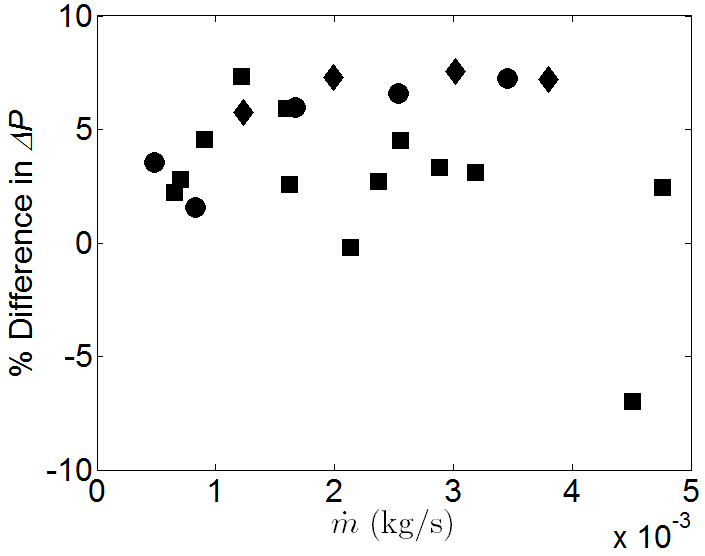

Figure 61. Percent difference in ΔP between experiments and simulations using the steel shell for air (■), He (●), and Ar (▲)

Since only the BF configuration was experimentally studied using a steel shell, the validity of models with different test section materials and tip lengths cannot be determined here for the other three flow configurations. For the BF configuration with a steel shell, however, the SA turbulence model predicts values of $\overline{h}$ and ΔP within 11% and 7%, respectively, at moderate Re. The numerical model is also used to estimate the fraction of the of total incident heat removed by convection at the cooled surface, versus that removed by conduction through the walls of the divertor, as shown in Figure 62. As was the case for the brass shell, the fraction of heat convected away at the cooled surface of the steel shell is much less than 100%, as was originally assumed in Eq. 31. Furthermore, κ is inversely proportional to the fraction of heat convected away at the cooled surface, demonstrating that κ can be used to characterize the relative contributions of convection, *vs.* conduction. For a value of κ near its prototypical value of ~340 (steel shell with helium) in the BF configuration, 53% to 68% of the incident heat is removed by convection at the cooled surface, and this fraction increases with Re.

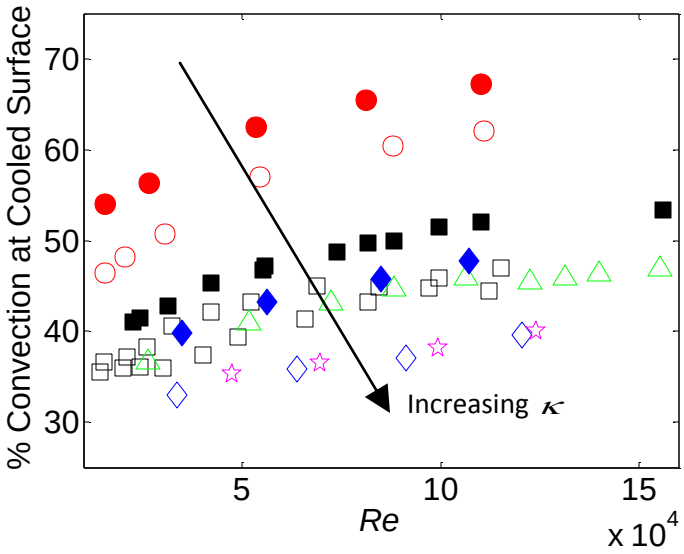

Figure 62. Percentage of the total incident heat that is convected away at the cooled surface for air (■), He (●), Ar (♦), high pressure air (▲), and high pressure argon (★) for a steel test section (closed symbols) and a brass test section (open symbols) in the BF flow configuration

5.3 Prototypical Thermal Performance

5.3.1 HEMP-like Divertor

One of the objectives of this research is to determine, using experimentally based correlations, whether this helium-cooled HEMP-like divertor design can accommodate an expected average incident heat flux of 10 MW/m^2 during normal operation while staying within material temperature limits. To do so, the experimentally determined $\overline{Nu}$ correlations of Eq. 56 are used, while the K_L correlations of Eq. 37 are used to estimate the coolant pumping power at prototypical conditions. It is important to emphasize that this analysis only considers the thermal-hydraulic limitations of the divertor design and does not account for failures due to thermal stresses. Furthermore, the correlations developed thus far are only applicable for divertors of the same geometry.

The prototypical operating conditions for the HEMP-like divertor studied here, which are close to those for the HEMP module, are summarized in Table 3. The average pressure boundary interface temperature $\overline{T_s}$ (*i.e.*, the temperature at the interface between the tile and shell) is where the temperature will be a maximum in the tungsten alloy pressure boundary. As discussed in Chapter 2, the prototypical materials and material temperature limits have yet to be finalized, so this analysis evaluates several temperatures.

Table 3. Prototypical operating conditions for the HEMP-like divertor

Reynolds Number (Re_p)	7.6×10^4 / 7.0×10^4 (Forward/Reverse flow)
Mass Flow Rate ($\dot{m}$)	3.3 g/s
Inlet Pressure (P_i)	10 MPa
Inlet Temperature (T_i)	600-700 °C
Shell Material	WL10
Interface Temperature ($\overline{T_s}$)	1100-1300 °C

For a given Re, the appropriate $\overline{Nu}$ correlation of Eq. 56 is used. Computing $\overline{Nu}$ requires that κ is known, which requires thermal conductivity values at the appropriate temperatures. As noted previously, the thermal conductivity of the solid k_s is evaluated at the average cooled surface temperature $\overline{T_c}$ and the thermal conductivity of the coolant k is evaluated at the average of T_i and T_o. Since, $\overline{T_c}$ and T_o are not initially known, the calculation begins with an estimated value, and these temperatures are then recalculated at each iteration until they converge. Next, an average heat transfer coefficient is computed as follows:

$$\bar{h} = \frac{\overline{Nu}k}{D_j} \tag{63}$$

where k is the thermal conductivity of the He evaluated at the average temperature $(T_i + T_o)/2$. At this point, the outlet temperature T_o is still unknown, so its value is set to that for the initial estimate. Then, the maximum heat flux that can be accommodated by the divertor at the pressure boundary interface $\overline{q''}_{\max}$ for a given maximum pressure boundary interface temperature $\overline{T_s}$ is determined by:

$$\overline{q''}_{\max} = \frac{\overline{T_s} - T_i}{R_T} \tag{64}$$

where the thermal resistance:

$$R_T = \frac{A_h}{A_c \overline{h_{eff}}} + \frac{\delta_s}{k_s} \tag{65}$$

and $\delta_s = 1$ mm is the thickness of the pressure boundary, k_s is the thermal conductivity of the pressure boundary (or shell material) evaluated at the average of $\overline{T_c}$ and the maximum tungsten alloy temperature $\overline{T_s}$. The values of $\overline{T_c}$ and T_o must then be compared to the original estimates. The average cooled surface temperature:

$$\overline{T_c} = \frac{\overline{q''}_{\max}}{\overline{h_{eff}}} + T_i \tag{66}$$

while the outlet temperature:

$$T_o = \frac{\overline{q''}_{\max}}{\dot{m}\overline{c_p}} + T_i \tag{67}$$

These new values for $\overline{T_c}$ and T_o are used to recompute $\overline{q''}_{\max}$ until all the values converge in an iterative process. The specified maximum tungsten alloy temperature is an average value so the calculated $\overline{q''}_{\max}$ could produce peak values larger than the specified maximum temperature limit. However, if the heat flux on a single divertor module is roughly uniform, conduction, if significant, will “smooth” out the temperature

profiles, making them nearly uniform. Typically, a maximum of five iterations are required to achieve convergence within 0.01%.

The pumping power is then determined and given in terms of β, pumping power as a fraction of the total incident thermal power. In general, β should not exceed 10% [36]. Using the correlations of Eq. 37 for the appropriate flow configuration, the loss coefficient K_L is determined, and then used to estimate the pressure drop ΔP as follows:

$$\Delta P = K_L \frac{1}{2} \rho_L \overline{V}^2 \tag{68}$$

Since ρ_L depends on the outlet pressure P_o, this also requires an iterative solution where $P_o = P_i - \Delta P$. The pumping power $\dot{W}$ is then calculated from the converged value of ΔP:

$$\dot{W} = \frac{\dot{m} \Delta P}{\overline{\rho}} \tag{69}$$

where $\overline{\rho} = \left(\rho_i + \rho_o\right)/2$ is an average of the coolant densities at the inlet and outlet. Then, $\overline{q''}_{\max}$ is computed for a range of β values (5, 10, 15, and 20%):

$$\overline{q''}_{\max} = \frac{\dot{W}}{\beta A_h} \tag{70}$$

Finally, the maximum heat flux that can be accommodated by the divertor is calculated over a range of Re below and above Re_p, as shown in Figure 63, for the prototypical conditions given in Table 3 with $T_i = 600$ °C.

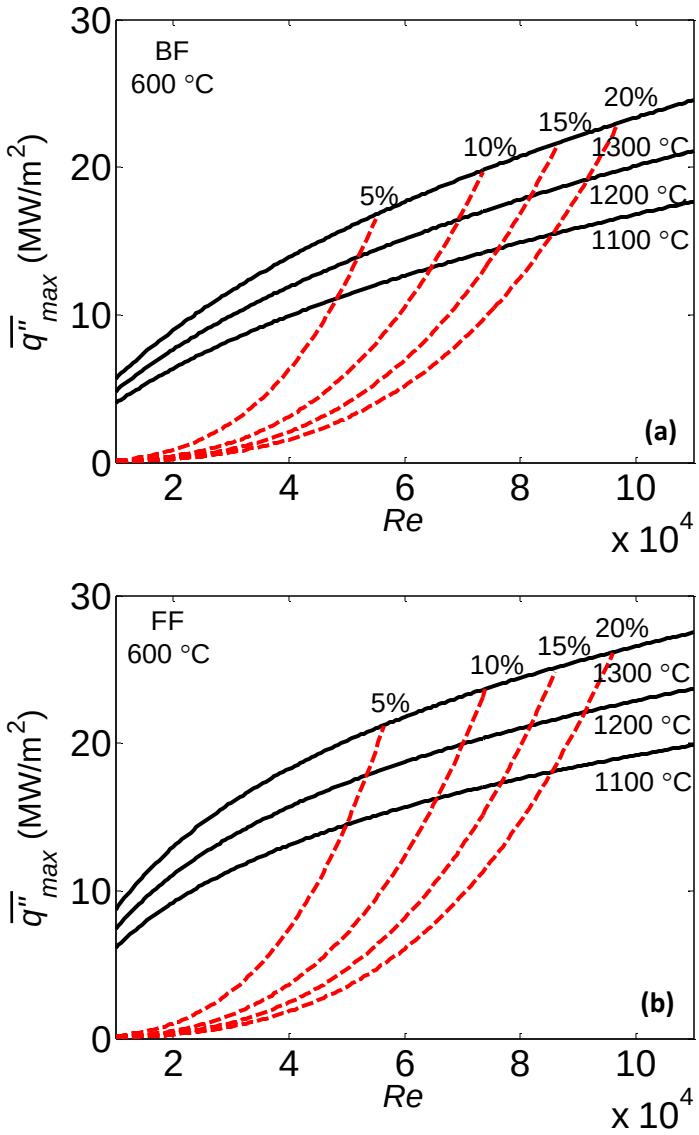

Figure 63. Maximum heat flux for the HEMP-like divertor for each of the four flow configurations (a-d) at $T_i = 600$ °C for $\overline{T_s} = 1100$, 1200, and 1300 °C (solid black lines) and $\beta = 5$, 10, 15, and 20% (red dashed lines)

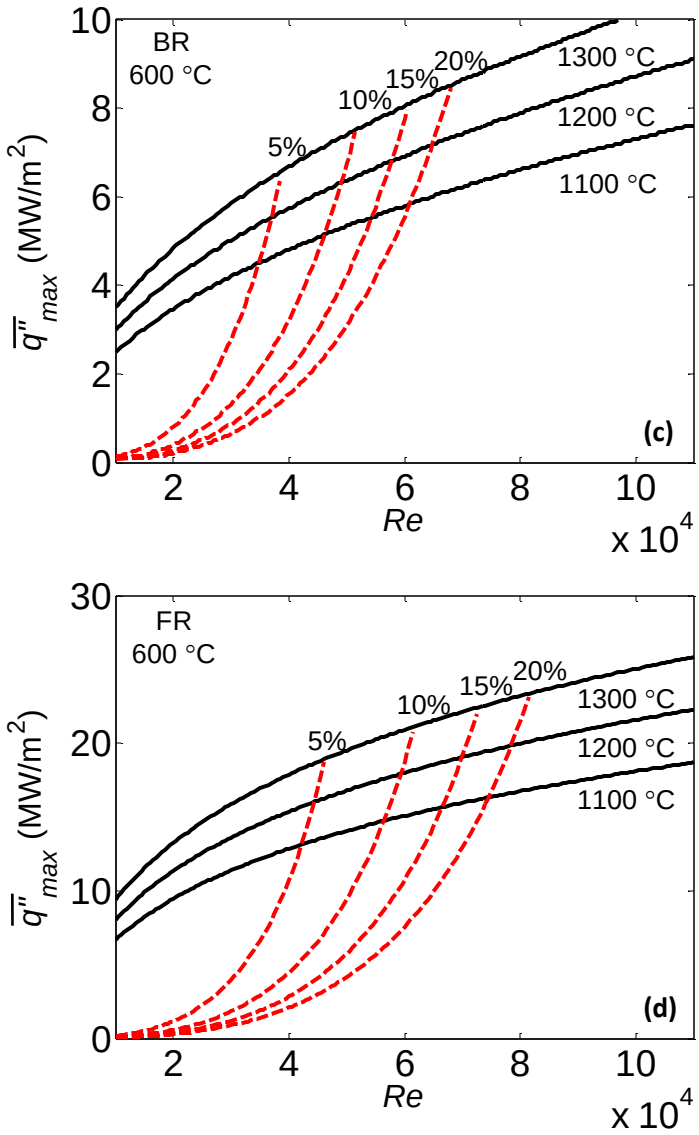

Figure 63 Continued. Maximum heat flux for the HEMP-like divertor for each of the four flow configurations (a-d) at $T_i = 600$ °C for $\overline{T_s} = 1100$, 1200, and 1300 °C (solid black lines) and $\beta = 5$, 10, 15, and 20% (red dashed lines)

As expected, the maximum heat flux the divertor can accommodate $\overline{q''}_{\max}$ given in Figure 63 increases with increasing Re for a given $\overline{T_s}$; however, the pumping power as a fraction of incident thermal power β also increases demonstrating the trade offs in the thermal-hydraulic performance. The maximum heat flux values are based on the cross-sectional area of the shell A_h, but a single module will need to cool a pure

tungsten tile with an area greater than A_h. To account for the larger tile area, $\overline{q''}_{\max}$ needs to be rescaled by the ratio of the tile area A_t to A_h. Since, the tile area was not explicitly defined for this design, $\overline{q''}_{\max}$ is multiplied by the area ratio for the HEMP design, $A_h/A_t = 0.71$, to give the maximum heat flux that can be sustained on the tile $\overline{q''}_{tile}$. For the BF configuration (Figure 63a), $\overline{q''}_{\max} = 17.3$ MW/m^2 and $\overline{q''}_{tile} = 12.3$ MW/m^2 at Re_p for $\overline{T_s} = 1200$ °C, for example. The maximum heat flux values for the four flow configurations are summarized in Table 4. Smaller tiles could, however be used (albeit at the expense of more modules) to increase $\overline{q''}_{tile}$ if required.

Table 4. Thermal performance of the HEMP-like divertor at Re_p and $T_i = 600$ °C

Configuration	$\overline{T_s}$ (°C)	$\overline{q''}_{\max}$ (MW/m^2)	β (%)	$\overline{q''}_{tile}$ (MW/m^2)
BF	1100	14.4	15	10.2
	1200	17.3	13	12.3
	1300	20.2	11	14.3
FF	1100	17.2	15	12.2
	1200	20.6	13	14.6
	1300	23.9	12	17.0
BR	1100	6.2	>20	4.4
	1200	7.5	>20	5.3
	1300	8.7	>20	6.2
FR	1100	16.0	18	11.4
	1200	19.0	15	13.5
	1300	22.1	14	15.7

Three of the four flow configurations, namely the BF, FF and FR cases, are all able to withstand heat fluxes of at least 10 MW/m^2 on the tungsten tile. Of these three configurations, the FF case has the best overall performance, accommodating a heat flux exceeding 17 MW/m^2 on the tile at $\overline{T_s} = 1300$ °C followed by the FR configuration, which has a slightly lower $\overline{q''}_{tile}$ and larger β at Re_p. Both reverse-flow configurations

therefore appear to be inferior to their corresponding forward-flow cases. Finally, all these configurations have β values that exceed 10% (a value often used as cutoff for economical performance). The fourth configuration, the BR (Figure 63c) case, has the worst performance, as was already evident in Figure 38b, and can only accommodate 6.2 MW/m^2 even at a maximum cooled surface temperature $\overline{T_s} = 1300$ °C. This is hardly surprising, since this configuration has neither jet impingement nor fins. In addition, it has the largest values of β. As a result, the BR configuration is only included here for completeness.

The correlations for the $\overline{Nu}$ number in Eq. 56 that were used to predict the prototypical performance fit all of the experimental data within ±10%. Therefore, the uncertainty in the results presented in Figure 63 and Table 4 is approximately ±10% plus the contributions to the uncertainty from the material properties in the extrapolations. However, the uncertainty in the material properties, especially due to long-term exposure to high-fluence neutrons is not well-quantified and is not included in this analysis. Contributions from radiative heat transfer from the cooled surface are also excluded in the preceding figures since simple calculations show that, even in the best circumstances, the fraction of total heat radiated from the cooled surface is minor compared to the total heat removed by convection and conduction. Excluding contributions from radiative heat transfer from the cooled surface also makes extrapolations from the correlations conservative for added confidence in the maximum heat flux each configuration can accommodate.

In addition to evaluating prototypical operating conditions for various geometries, the correlations developed from Figure 63 can be integrated into system codes and used to evaluate the thermal-hydraulic performance of the divertor over a variety of operating conditions. These systems codes can then be used to optimize the operating conditions

for the design, considering the tradeoffs at a system level, well beyond the thermal-hydraulic issues considered here. Obviously, a wide variety of issues beyond thermal hydraulics and thermal stresses, such as the cost of electricity, neutronics, manufacturing and assembly costs, must all be considered in the final design.

As discussed previously, the material temperature limits (and even the specific tungsten alloy) are not yet finalized for this design. Recent work suggests that the minimum tungsten alloy temperature based on the ductile-to-brittle transition temperature should be increased to 700 °C. Figure 64 was therefore generated with this higher inlet temperature $T_i = 700$ °C to determine how increasing T_i degraded the overall thermal performance for the same pressure boundary temperature limits. The maximum heat flux values for the four flow configurations are summarized in Table 5.

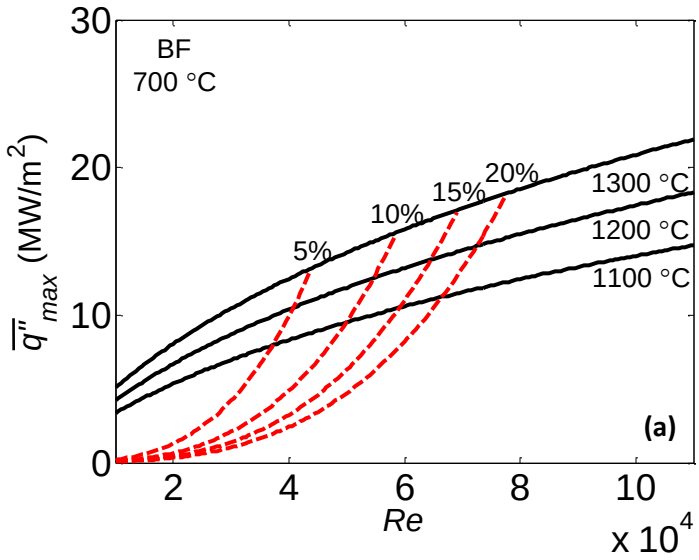

Figure 64. Maximum heat flux for the HEMP-like divertor for each of the four flow configurations (a-d) at $T_i = 700$ °C for $\overline{T_s} = 1100$, 1200, and 1300 °C (solid black lines) and $\beta = 5$, 10, 15, and 20% (red dashed lines)

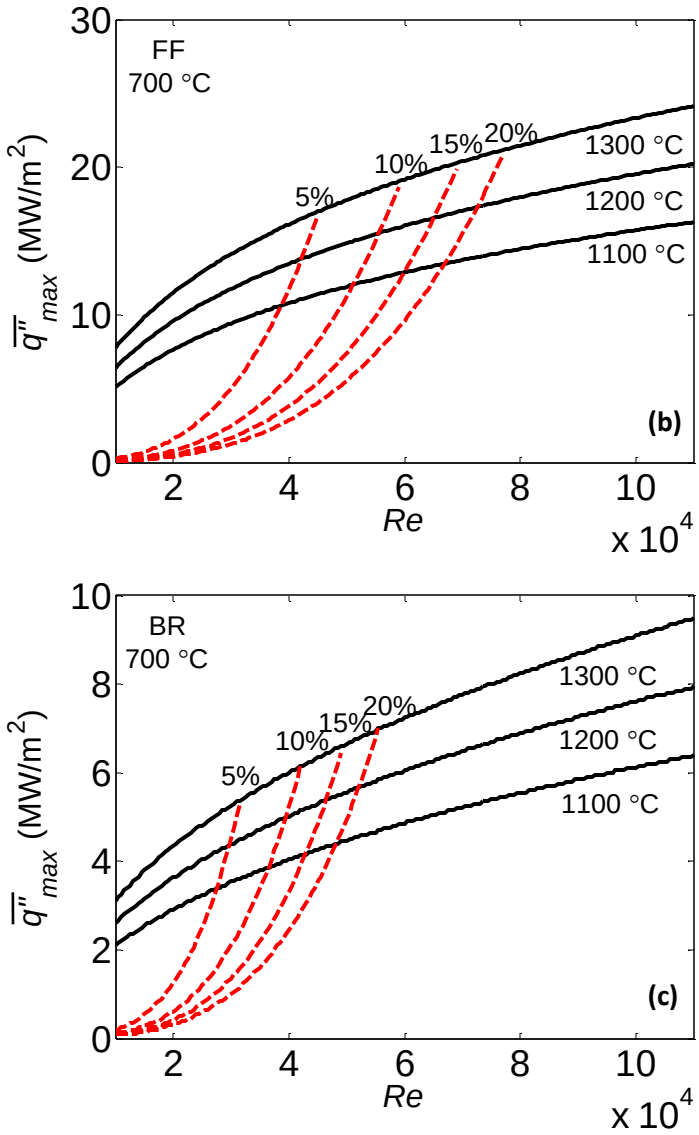

Figure 64 Continued. Maximum heat flux for the HEMP-like divertor for each of the four flow configurations (a-d) at $T_i = 700$ °C for $\overline{T_s} = 1100$, 1200, and 1300 °C (solid black lines) and $\beta = 5$, 10, 15, and 20% (red dashed lines)

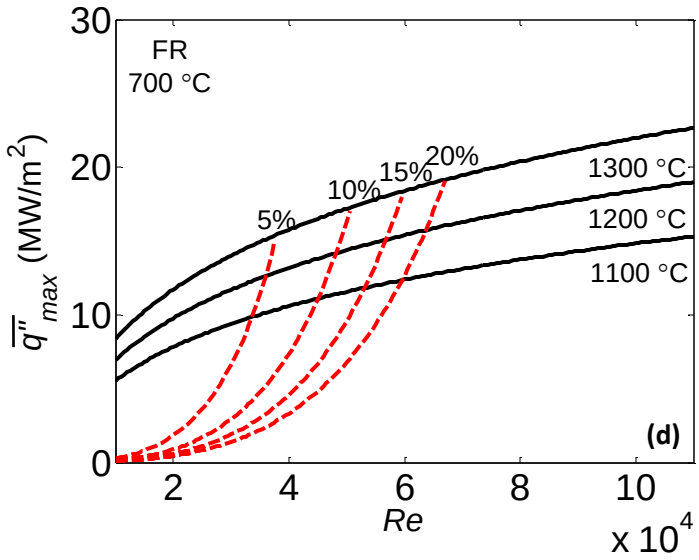

Figure 64 Continued. Maximum heat flux for the HEMP-like divertor for each of the four flow configurations (a-d) at $T_i = 700$ °C for $\overline{T_s} = 1100$, 1200, and 1300 °C (solid black lines) and $\beta = 5$, 10, 15, and 20% (red dashed lines)

Table 5. Thermal performance of the finger-type divertor at Re_p and $T_i = 700$ °C

Configuration	$\overline{T_s}$ (°C)	$\overline{q''}_{max}$ (MW/m^2)	β (%)	$\overline{q''}_{tile}$ (MW/m^2)
BF	1100	12.1	30	8.6
	1200	15.1	22	10.7
	1300	18.0	20	12.8
FF	1100	14.2	30	10.1
	1200	17.6	24	12.5
	1300	21.1	20	15.0
BR	1100	5.2	>40	3.7
	1200	6.5	>40	4.6
	1300	7.8	>40	5.5
FR	1100	13.1	32	9.3
	1200	16.3	27	11.6
	1300	19.4	22	13.8

As expected, there is a significant decrease in $\overline{q''}_{\max}$ at this higher T_i. Nevertheless, the FF configuration can accommodate at least 10 MW/m^2 incident on the tile, and the FR and BF cases can also do so for $\overline{T_s} \geq 1200$ °C, at Re_p for $A_h / A_t = 0.71$. As seen earlier, the reverse-flow configurations appear to be inferior to their corresponding forward-flow cases. For the forward-flow cases, adding an array of pin fins to the cooled surface (FF) increases $\overline{q''}_{\max}$ by ~17-18%, but this also increases the fabrication cost and complexity of the modules. Perhaps the most noticeable effect of increasing T_i is the significant increase in β for all configurations at a given Re_p and $\overline{T_c}$. This increase is due to several factors. First, the relative decrease in $\overline{q''}_{\max}$ reduces β since $\beta \propto 1/\overline{q''}_{\max}$. Next, to keep Re_p constant as T_i increases requires increasing the mass flow rate $\dot{m}$ by 8% to account for the resultant increase in inlet viscosity μ_i (4.528×10^{-5} Pa·s at 700 °C, *vs.* 4.194×10^{-5} Pa·s at 600 °C) since $Re_p \propto \dot{m}/\mu_i$. Furthermore, increasing the temperature reduces $\bar{\rho}$ by approximately 10%. A 10% decrease in ρ_L will also increase ΔP by about 11% since $\Delta P \propto \rho_L \overline{V}^2$ and $\overline{V} \propto 1/\rho_L$. In brief, $\dot{m}$ increases by 8%, $\bar{\rho}$ decreases by 10%, and ΔP increases by 11%. The pumping power then increases by 33% for an equivalent Re_p based only on these effects, as shown below:

$$\dot{W} = \frac{\dot{m}\Delta P}{\bar{\rho}} = \frac{(1.08)(1.11)}{0.9} = 1.33 \tag{71}$$

Finally, a 10% decrease in ρ_L due to the increase in temperature results in a further decrease in ΔP since ρ_L is defined by the outlet pressure P_o. For a fixed inlet pressure $P_i =$ 10 MPa, ΔP will further increase (compared with an inlet temperature of 600 °C) because $\Delta P = P_i - P_o$. In summary, all of these factors contribute to a significant increase in β when T_i increases from 600 °C to 700 °C. Moreover, these effects will

become worse if it is necessary to further increase the minimum operating temperature for the divertor materials (*i.e.* increase the coolant inlet temperature).

5.3.2 HCFP Divertor

Following the previous analysis for the HEMP-like divertor, this analysis can be extended to the numerical simulations of the HCFP divertor performed in Chapter 4. Figure 55 showed that $\overline{Nu}$ at a given Re depends on the test section material or coolant used in the simulations. The conditions for the five different configurations simulated are summarized in Table 6, along with the thermal conductivity ratio κ derived earlier in this chapter.

Table 6. HCFP configurations simulated in the numerical model including the thermal conductivity ratios for each

Configuration	Test Section Material	Coolant	k_s (W/m·K)	k (mW/m·K)	κ (-)
1	Brass	Air	~140	28	~5000
2	Brass	He	~140	158	~770
3	Stainless Steel	Air	~20	28	~750
4	High Conductivity	Air	~185	28	~7000
5	Low Conductivity	Air	~9	28	~330

The thermal conductivity ratios range from 330 to 7000, closely matching the values experimentally tested for the HEMP-like divertor. Since the prototypical values for κ are expected to be ~340 for an average helium coolant temperature of 650 °C and a WL10 tungsten alloy temperature of ~1000 °C, the prototypical values are within the range of the simulations. Since $\overline{Nu}$ decreases with κ at a given Re (Figure 55), as is also the case for the HEMP-like divertor (Figure 36), $\overline{Nu}$ is also fit to a power-law function of the form given in Eq. 55 using multiple linear regression in MATLAB® 2008b. The thermal conductivity of the coolant k is again evaluated at the average of the inlet

and outlet of the coolants $(T_i + T_o)/2$, while the thermal conductivity of the shell k_s is evaluated at the average cooled surface temperature $\overline{T_c}$. The resulting correlation is as follows:

$$\overline{Nu} = 0.095 Re^{0.616} \kappa^{0.191} \tag{72}$$

which is valid for:

$$\begin{bmatrix} 1.2\times10^4 \le Re \le 4.7\times10^4 \\ Pr \approx 0.7 \\ 330 \le \kappa \le 7000 \end{bmatrix} \tag{73}$$

Figure 65 compares the experimental results and the numerical predictions with this correlation (solid lines) and ±10% uncertainty bands (dashed lines).

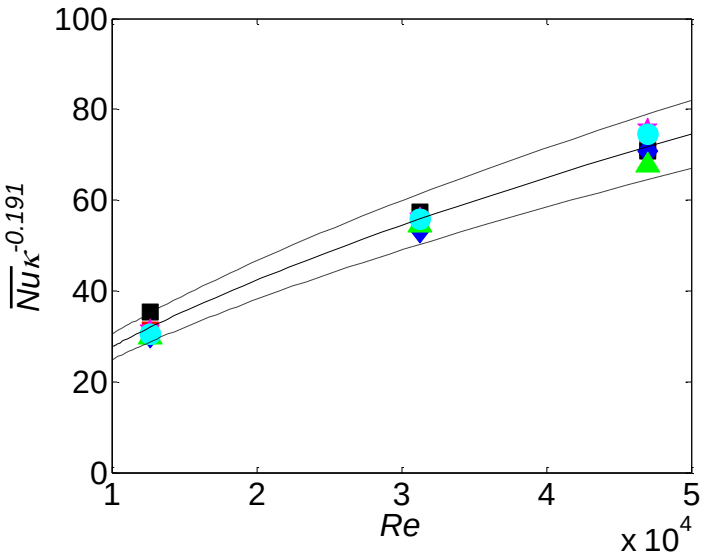

Figure 65. $\overline{Nu}$ correlation using the thermal conductivity ratio for configurations listed in Table 6: experiments (■) [45], conf. 1 (■), conf. 2 (●), conf. 3 (♦), conf. 4 (▲), and conf. 5 (★). Dashed lines indicate ±10% deviation from the correlation

The experiments and simulations are in good agreement with the correlation, within 10% in all cases. This correlation can therefore be used with reasonable confidence to predict the prototypical performance of the HCFP. Unlike the HEMP-like analysis performed above, note that only one thermal conductivity ratio was

experimentally studied, and performing further experiments using different test section materials (and hence different values of κ) to confirm this correlation would be valuable.

To evaluate the pressure drop through the HCFP module at prototypical pressures and temperatures, a correlation for the loss coefficient in the HCFP module was also developed using the experimental data of Hageman et al. [45]. The pressure drop data from the experiments performed with this particular HCFP geometry were converted to pressure loss coefficients K_L using Eq. 35. Since it was shown that the test section material and the coolant have no bearing on K_L, the correlation for K_L was based only on these experimental data, and found to be:

$$K_L = 0.0275 \cdot Re^{0.605} \tag{74}$$

The prototypical operating conditions for the HCFP divertor, which are very similar to those for the HEMP-like divertor, are given in Table 7. Three average pressure boundary interface temperatures $\overline{T_s}$ (*i.e.*, maximum alloy temperature) and two inlet temperatures were again considered.

Table 7. Prototypical operating conditions for the HCFP divertor

Reynolds Number (Re_p)	3.3×10^4
Inlet Pressure (P_i)	10 MPa
Inlet Temperature (T_i)	600-700 ºC
Divertor Material	WL10
Interface Temperature ($\overline{T_s}$)	1100-1300 ºC

The maximum heat flux that can be accommodated by the HCFP-like design was predicted using the same procedure as that used for the HEMP-like divertor. For a given Re, $\overline{Nu}$ is calculated from Eq. 72 and used to calculate an average heat transfer coefficient $\bar{h}$ using Eq. 63. Then $\overline{q''}_{\max}$ is calculated from Eqs. 64 and 65 where the thickness of the pressure boundary $\delta_s = 2$ mm. $\overline{T_c}$ and T_o are then calculated using Eqs.

66 and 67 respectively and this calculation is repeated until $\overline{q''}_{\max}$, $\overline{T_c}$ and T_o all converge with an error less than 0.01%.

Similarly, the procedure for determining the maximum heat flux the design can sustain for a given value of β (pumping power as a fraction of total incident thermal power) is similar to that used for the HEMP-like divertor. For a given Re, ΔP is calculated with Eq. 68, and then used in Eq. 69 to calculate the pumping power. Finally, Eq. 70 is used to determine $\overline{q''}_{\max}$. Figure 66 shows the maximum heat flux for the HCFP divertor over a range of Re spanning Re_p for inlet temperatures of 600 °C and 700 °C

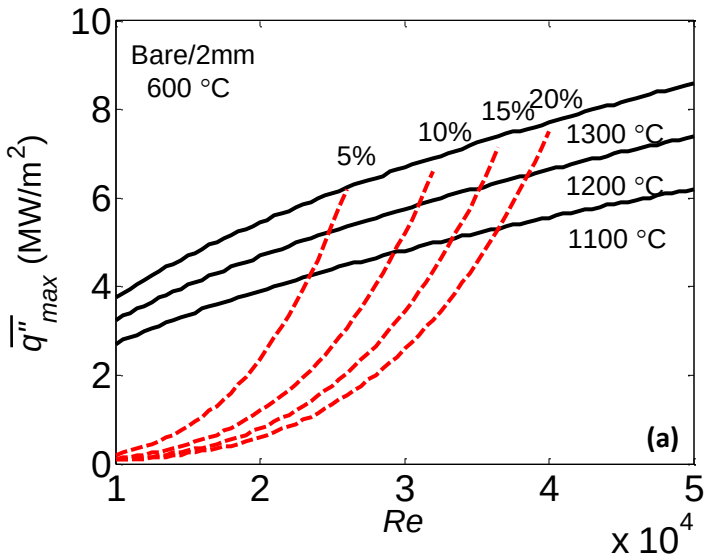

Figure 66. Maximum heat flux for the HCFP divertor for $T_i = 600$ °C (a) and 700 °C (b) for $\overline{T_s} = 1100$, 1200, and 1300 °C (solid black lines) and $\beta = 5$, 10, 15, and 20% (red dashed lines)

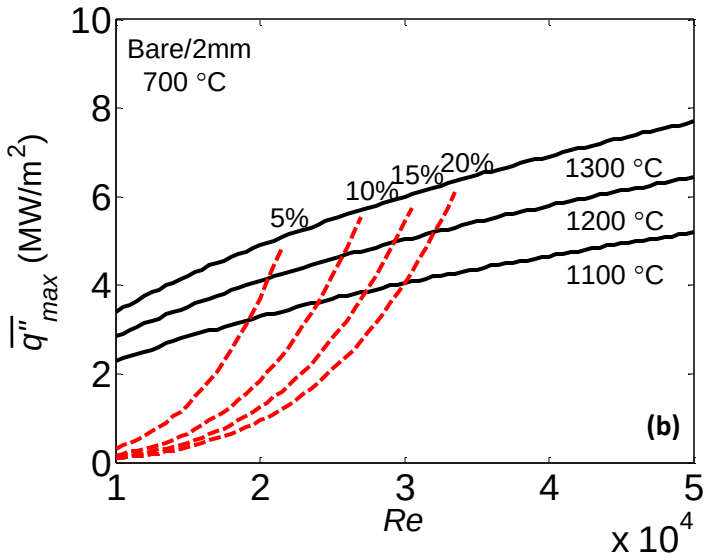

Figure 66 Continued. Maximum heat flux for the HCFP divertor for $T_i = 600$ °C (a) and 700 °C (b) for $\overline{T_s} = 1100$, 1200, and 1300 °C (solid black lines) and $\beta = 5$, 10, 15, and 20% (red dashed lines)

Since the tile area A_t is the same as the heated surface area A_h in the HCFP divertor, the maximum heat fluxes plotted in Figure 66 are the maximum heat fluxes incident upon the tile that can be accommodated by this design. Clearly, the HCFP design cannot withstand heat flux values >10 MW/m^2; indeed, recent studies of a more advanced HCFP geometry also indicate that the maximum heat flux is closer to 8 MW/m^2 [36,37]. At Re_p, $\overline{T_s} = 1300$ °C and $\overline{T_i} = 600$ °C, these results suggest that $\overline{q''}_{\max}$ will be slightly less, about 7.0 MW/m^2. This discrepancy may be due to differences in the HCFP divertor designs studied, as shown in Figure 19 and Figure 52. The final results from these studies are summarized in Table 8.

Table 8. Thermal performance of the HCFP divertor at Re_p

T_i (°C)	$\overline{T_s}$ (°C)	$\overline{q''}_{\max}$ (MW/m^2)	β (%)
600	1100	5.0	14
	1200	6.0	13
	1300	7.0	11
700	1100	4.3	25
	1200	5.3	22
	1300	6.3	19

These predictions of the maximum heat flux for the HEMP-like divertor and the HCFP divertor can also be integrated into system codes and used to find optimal configurations for each respective geometry. However, given that these correlations are all based on dynamically similar experiments (and simulations for the HCFP) using air, He, or Ar at room temperature and low pressure (<1.4 MPa), these correlations should be verified by experiments at temperatures and pressures closer to prototypical values.

Finally, all of the experiments described to this point were performed at heat fluxes of ~2 MW/m^2 or less, *vs.* a prototypical value of 10 MW/m^2. Experiments at higher incident heat fluxes are therefore needed to verify that these results are also valid at prototypical heat fluxes. Such experiments are only practical with helium, and so a new helium loop was designed and constructed in order to perform experiments at higher temperatures, prototypical pressures, and higher heat fluxes. This is discussed in the next chapter.

CHAPTER 6: HELIUM TEST LOOP

The preceding chapters presented a series of dynamically similar experiments on the HEMP-like divertor with and without fins that were used to develop correlations for the Nusselt number and loss coefficient for a range of operating conditions and temperature constraints. These correlations were then used to predict the thermal performance of the divertor at prototypical conditions in terms of the maximum heat flux that can be accommodated by the design and the pumping power as a fraction of incident thermal power for a given coolant flow rate. The results of this analysis are depicted as generalized maximum heat flux charts shown in Figure 63 and Figure 64. These charts, which present results for a number of different constraints (*e.g.* inlet temperatures, maximum tungsten alloy pressure boundary temperatures) can then be used in system codes that optimize the overall plant performance.

The results for experiments using He and Ar as a coolant demonstrate that these correlations depend on the thermal conductivity ratio κ as well as the dimensionless coolant mass flow rate, characterized by Re. This ratio characterizes the fraction of the incident heat flux that is removed via convection, *vs.* conduction, through the divertor. Predictions from numerical simulations using ANSYS FLUENT® for different coolants and test section materials were used in addition to experimental data using air for the HCFP geometry to revise previous correlations for maximum heat flux and include their dependence upon κ.

The experiments on the HEMP-like geometry with and without fins described in the previous chapters were all performed with different coolants at room temperature and at inlet pressures <1.4 MPa, with a maximum incident heat flux of 2 MW/m^2. Obviously, these experimental conditions are quite different from the prototypical conditions specified for modular helium-cooled tungsten divertor designs (*i.e.*, inlet

temperature of ~600 °C, inlet pressure of 10 MPa, and incident steady-state heat flux of 10 MW/m^2). Additional experiments were therefore performed using He at elevated inlet temperatures and prototypical pressures to provide additional validation of these correlations. To do so, a helium loop was designed and constructed to give longer run times than those possible with the previous once-through setup based on a bank of compressed-helium cylinders so that steady-state conditions could be achieved at higher inlet temperatures and at higher incident heat flux values. The helium loop was also designed to perform experiments at the prototypical inlet pressure of 10 MPa. Finally, a new heat source, namely an induction heater, has been used to achieve higher heat fluxes, as great as 4.9 MW/m^2, than those possible with the oxy-acetylene torch.

Test sections modeling the HEMJ divertor were fabricated from the tungsten alloy MT-185 (97% W, 2% Ni, and 1% Fe) and studied in this helium loop. Steady-state experiments were conducted for inlet temperatures ranging from room temperature (~27 °C) up to 300 °C, inlet pressures of ~10 MPa, and heat fluxes as great as 4.9 MW/m^2 over a range of Re. Average Nusselt numbers and loss coefficients were again calculated for each experiment, and used to develop correlations for $\overline{Nu}$ and K_L. These updated correlations are then used to generate generalized maximum heat flux charts for the HEMJ design under various constraints using a procedure similar to that described in the previous chapter.

6.1 Experimental Setup

6.1.1 Helium Loop

Figure 67 shows a schematic of the Georgia Tech helium loop. This loop is capable of providing a maximum helium mass flow rate of 10 g/s at a maximum inlet temperature of 400 °C and inlet pressures between 7.5 MPa and 10.3 MPa. Before

starting the loop, the entire loop and test section are evacuated by a vacuum pump, and charged with helium supplied from 41.4 MPa source tanks. To reduce contamination in the helium loop, the loop is evacuated and refilled with helium to above atmospheric pressure at least three times before filling to 10 MPa. A reciprocating compressor is used to drive the helium through the loop.

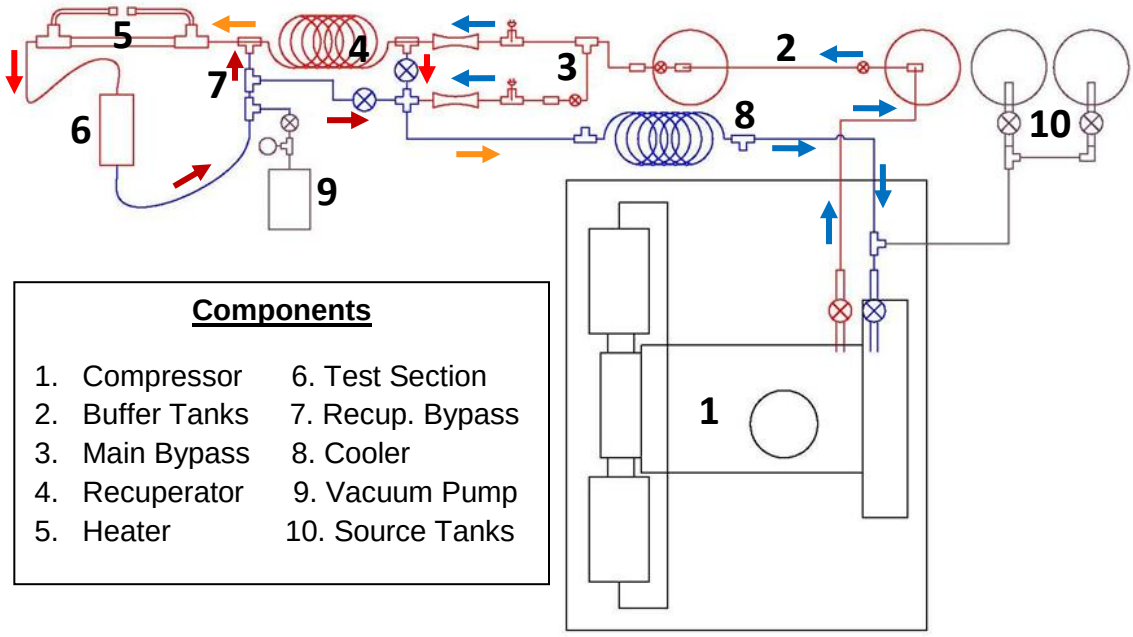

Figure 67. Schematic of the helium loop indicating many of the key components. Red lines indicate piping leading to the test section and blue lines indicate piping leading away from the test section. Arrows indicate the direction of flow for the helium

Helium leaves the compressor at ~10 MPa and nearly room temperature, then passes through two 300 ft^3 compressed gas cylinders (the “buffer tanks” in Figure 68), entering via a vertical tube at the top of the cylinder, exiting the tube at and impinging on the bottom of the cylinder, and finally exiting through the top of the cylinder through a tee via the annulus between the tube and the opening at the top of the cylinder. The buffer tanks should help reduce the pulsations from the reciprocating compressor and also increase the helium inventory in the loop, helping to reduce the effect of small leaks

(which are difficult to avoid in a helium loop). A static pressure transducer (OMEGA PX309-2KGI) measures the pressure, and a type-K thermocouple probe measures the temperature, of the helium after it exits the buffer tanks and passes through a 140 μm inline filter.

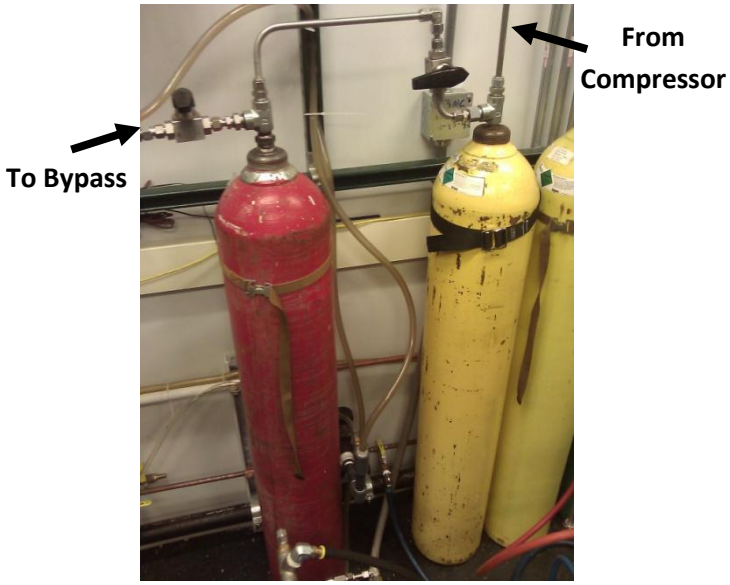

Figure 68. The two buffer tanks in series used in the helium loop. Helium flows from right to left in the photo

Some of the helium is then diverted through the main bypass to regulate the flow rate to the test section. The rest of the helium goes through the main line, and the mass flow rate through this line, which is also the mass flow rate through the test section, is determined from measurements with a Venturi meter (Lambda Square V50-10) and differential pressure transducer (Rosemount 1151DP4E22). The helium then enters a coil-in-coil heat exchanger that serves as a recuperator, where the heated helium exiting the test section through the outer coil heats the room-temperature helium passing through the inner coil as it flows in the opposite direction. This preheated helium then is heated further when it flows over two 2000 W cylindrical cartridge heaters (OMEGA CIR-5121/240V) powered by a 240 V variable autotransformer and mounted within a 1 in

(25.4 mm) ID pipe (Figure 69). The heated helium then flows through flexible steel hosing to the HEMJ test section.

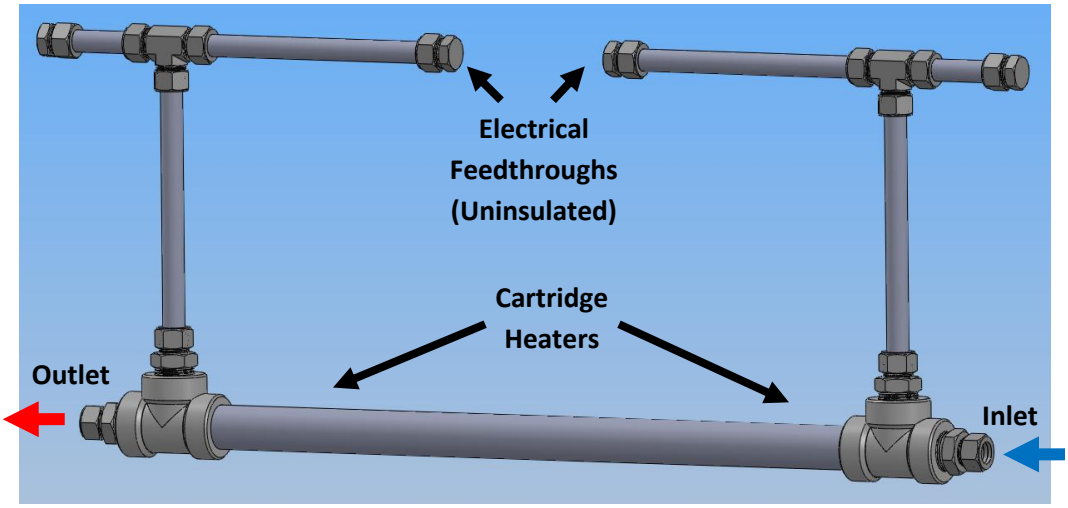

Figure 69. Solid model of the heater used in helium loop

The hot helium then exits the test section, and either flows through the outer coil of the recuperator to preheat the incoming room-temperature helium or through the recuperator bypass for experiments conducted with the coolant at room temperature. The actual flow path is controlled by a needle valve in each flow path (Swagelok SS-3NBS4). The helium exiting the recuperator or recuperator bypass combines with that passing through the main bypass, and then passes through a second coil-in-coil heat exchanger that acts as the cooler. Water at room temperature in the outer coil cools the helium down to room temperature before it returns to the compressor to be circulated again through the loop.

The main bypass line (Figure 70) includes a 7 μm inline filter and a needle valve (Swagelok SS-1RS4) to regulate the flow. A bypass is necessary to control the mass flow rate as the mass flow rate produced by the reciprocating compressor cannot be adjusted. The mass flow rate through the bypass is calculated using the readings from a

Venturi meter (Lambda Square V50-10) and a differential pressure transducer (Rosemount 1151DP4S22).

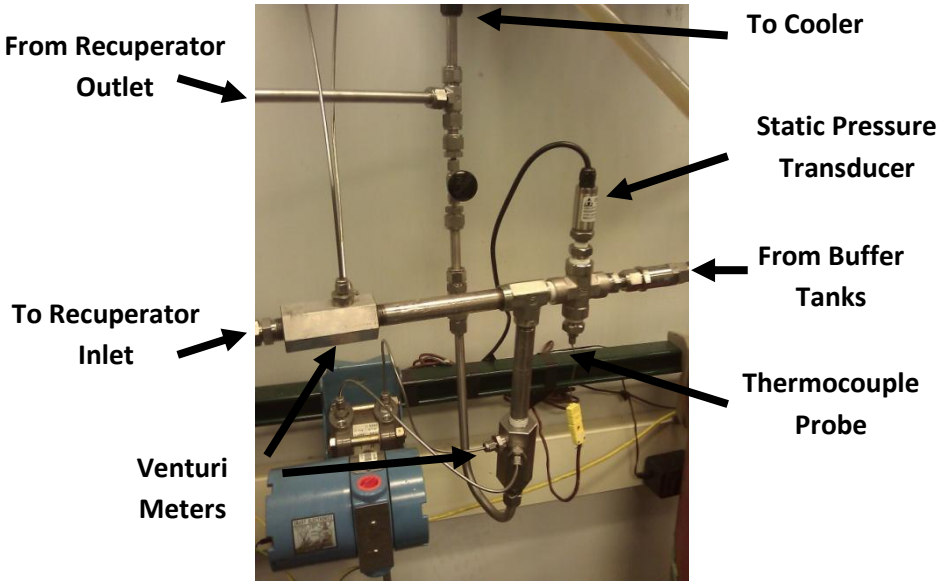

Figure 70. Bypass used to divert helium away from the test section

The piping for the loop is 0.5 in (12.7 mm) 304 stainless steel tubing with a wall thickness of 0.035 in (0.889 mm) rated to a maximum pressure of 13.6 MPa at ~400 °C, and Swagelok compression fittings are used for all connections. The recuperator is heavily insulated with large blocks of rock wool enclosed within stainless steel sheeting (Figure 71), while the tubing between the recuperator and the test section is wrapped in rock wool surrounded by an outer layer of corrugated aluminum sheeting. The heater (Figure 69) is encased in two layers of 1 in (25.4 mm) thick Duraboard® blocks except for the tubing housing the Conax® electrical feedthroughs for the cartridge heaters, which are exposed to the surroundings so that they remain at the lower temperatures required to maintain a good seal. The tubing between the compressor and the recuperator is not insulated because the coolant is at room temperature, or is being cooled back to room temperature, in this part of the loop.

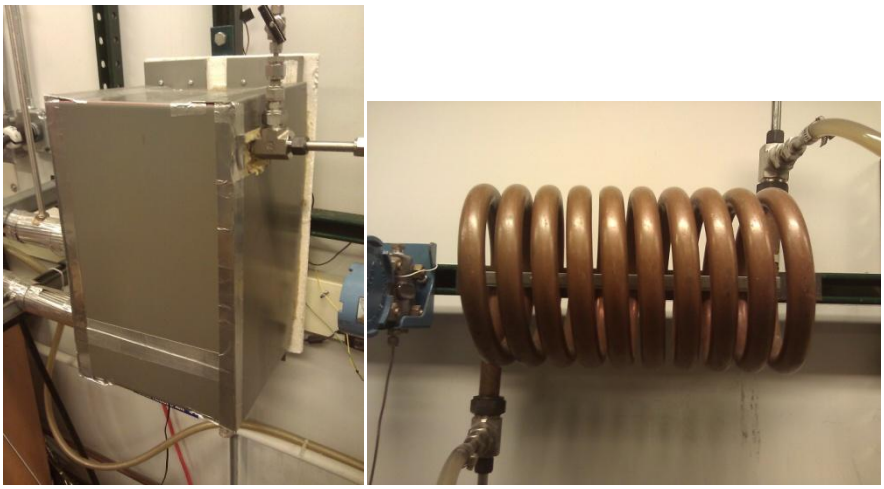

Figure 71. Photos of the recuperator (left) fully encased in insulation and the cooler (right). Both the recuperator and cooler are coil-in-coil heat exchangers

The compressor used for this loop, the Hydro-Pac® C01.5-05-450LX reciprocating compressor (Figure 72), is capable of providing mass flow rates for helium up to 10 g/s at pressures between 7.2 and 10.3 MPa. A reciprocating compressor was chosen for this loop because it was an economical choice for driving a flow with large pressure drops at high temperatures. This compressor uses a single-stage hydraulically driven intensifier with a stroke length of 102 mm and a frequency of ~ 1 Hz powered by a 5 hp motor. This leads to oscillations in the mass flow rate that are damped for steady-state experiments, as discussed in Section 6.2.1.

Figure 72. Hydro-Pac® C01.5-05-450LX reciprocating compressor shown from the front (left) and the back (right)

In practice, it is impractical to completely seal (*i.e.*, eliminate all leaks in) a helium loop. Nevertheless, the amount of leakage must be minimized, and the two buffer tanks in the loop ensure that the helium inventory is large enough that the total system pressure during an experimental run is not affected by leaks, which are estimated to be about 50 mg/h.

6.1.2 Test Section

The HEMJ divertor was selected for testing in the helium loop because it is the leading helium-cooled divertor design at present, and the only design (to our knowledge) that has been repeatably experimentally shown to accommodate incident heat fluxes of 10 MW/m^2 at prototypical conditions. A drawing of a cross-section of the HEMJ test section, and an image of the HEMJ outer shell, or thimble, are shown in Figure 73.

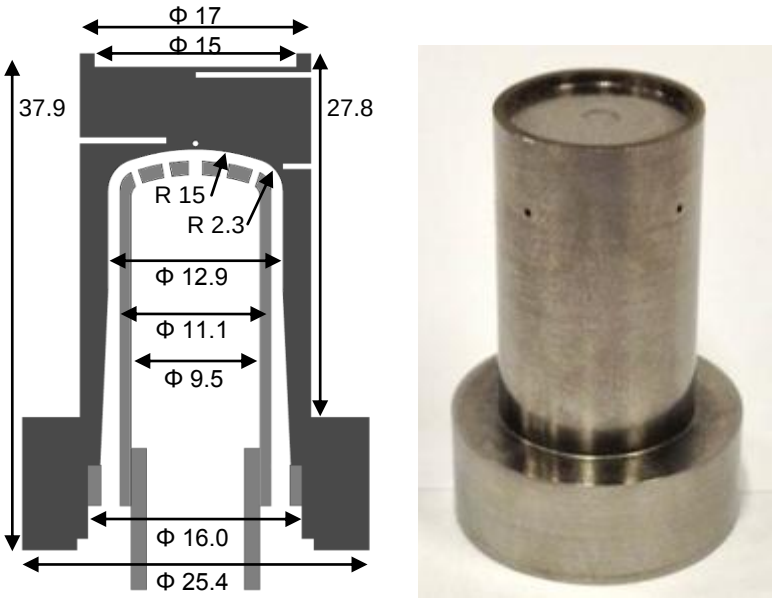

Figure 73. Cross-sectional drawing of the HEMJ test section thimble and jet cartridge (left) and an image of the complete test section thimble (right). The dimensions are given in mm

The thimble has an OD of 17 mm and a minimum ID of 12.9 mm; the inner radial dimension of the thimble gradually increases, reaching a maximum value of 16.0 mm at the bottom of the thimble. The 25.4 mm OD, 10.1 mm thick flange at the bottom of the thimble seals the test section to a manifold with a compression collar. The inside surface geometry is identical to that the of the HEMJ J1-c design, with radii of curvature of 2.3 mm at the corners and 15 mm in the center, resulting in a minimum thimble endcap thickness of 5 mm. The top heated surface of the thimble has an outer rim with a thickness (radial extent) of 1 mm and a height (axial extent) of 1 mm.

The thimble was constructed of tungsten alloy MT-185 (commonly referred to as ‘heavy tungsten’) consisting of 97% W, 1% Fe, and 2% Ni, which is similar to Densimet-185, because of its machinability (and commercial availability). Six type-K thermocouple (TC) probes with 0.5 mm OD sheaths were inserted into holes drilled into the side of the test section along two perpendicular planes. Four of the TCs were 0.5 mm away from

the cooled surface at radial distances of 0 mm, 2.1 mm, 4.3 mm, and 6.4 mm from the centerline; the temperatures measured by these TCs were used to estimate the temperature distribution over the cooled surface assuming an axisymmetric temperature field. The other two TCs were both on the centerline at axial distances of 0.5 mm and 2.9 mm from the heated surface; these TC readings were used to estimate the axial heat flux due to conduction and to determine the maximum temperature in the thimble.

Figure 74 shows the 302 stainless-steel inner jets cartridge, which is geometrically identical to the HEMJ J1-c design, used in these experiments. The cartridge has 25 jet holes: one 1.04 mm central hole and twenty-four 0.6 mm holes on a hexagonal grid. The three small flanges at the base of the cartridge ensure that the width of the gap between the end of the jet cartridge and the cooled surface is at least 0.74 mm. The jet cartridge is brazed onto a 0.375 in (9.53 mm) OD stainless steel tube with a threaded end so that, if desired, the gap width can be adjusted; in these experiments, however, the gap was always 0.9 ± 0.1 mm.

Figure 74. Isometric view (left) and top view (right) of the jet cartridge

The thimble is sealed to a stainless steel manifold with a custom machined copper gasket, as shown in Figure 75. A steel compression collar is bolted to the manifold to create the seal. Helium enters the bottom of the manifold, flows through the

holes in the cartridge forming an array of jets to cool the inner surface of the thimble, exits the thimble through the annulus between the jet cartridge and the thimble, and leaves the test section through a 0.5 in (12.7 mm) OD tube perpendicular to the axis of the manifold. The three other 0.25 in (6.4 mm) OD tubes in the manifold are instrumentation ports. The inlet and exit temperatures of the coolant, namely the temperatures when the coolant enters and exits the manifold, are measured by two 4-wire resistance temperature detectors (RTDs) (OMEGA P-L-A-1/8-6-0-TS-8). The outlet static pressure of the coolant is measured by a pressure transducer (OMEGA PX302-2KGV) at the exit of a ~12 in length of tubing attached to an instrumentation port in the manifold to ensure that the coolant is at room temperature (which protects the sensor and gives accurate measurements). Finally, the pressure drop across the test section is measured with a differential pressure transducer (Rosemount 1151 DP5S22) between an instrumentation port on the manifold and the inlet to the jet cartridge.

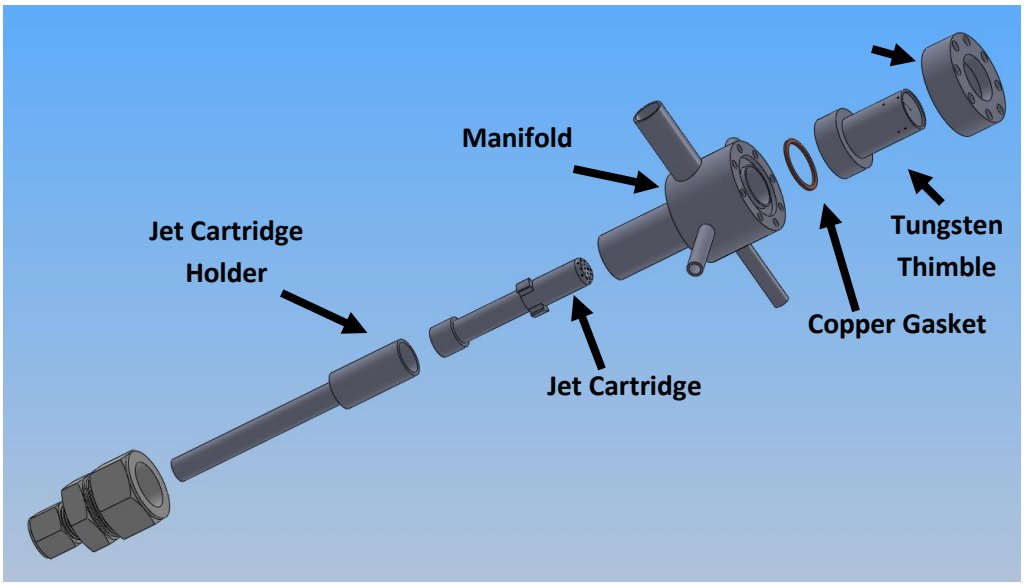

Figure 75. Exploded test section assembly

The manifold and test section are heavily insulated in layers of rock wool, and the manifold is bolted to a supporting 1 in thick Duraboard® plate, which, in turn, is bolted to

a Unistrut® support structure, to thermally isolate it from the surroundings. Most of the thimble is surrounded by a stack of Marinite® plates, but the last ~10 mm of the thimble is insulated instead in Marinite® powder to allow insertion of the TCs.

6.1.3 Heat source

The once-through experiments on the HEMP-like test section described in the previous chapters were performed at incident heat fluxes as great as 2 MW/m^2 with the oxy-acetylene torch, although Rader [42] achieved heat fluxes as great as 3 MW/m^2 using a brass HEMJ test section and an otherwise identical experimental setup. Higher heat fluxes could be achieved with the HEMJ test section because it has a larger cross sectional area, and hence the flame from the oxy-acetylene torch can impinge upon, and heat, a larger area. However, increasing the incident heat flux beyond 3 MW/m^2 is impractical, in part because this requires increasing the diameter of the flame from the torch, which damages the Duraboard® sleeve that protects the insulation and TCs. Despite the limitations on heat flux, the oxy-acetylene torch was used in several experiments, and a Duraboard® sleeve was machined to fit over the outer 1 mm of the thimble diameter to shield the TCs from the flame.

An induction heater was also used instead of the oxy-acetylene torch to achieve higher incident heat fluxes. A 10 kW induction heating system (Ambrell EasyHeat LI), on loan from the Safety and Tritium Applied Research (STAR) facility at Idaho National Laboratories (INL), was used in these experiments (Figure 76). This solid-state induction heating system converts three-phase electrical power into an oscillating magnetic field around a “workpiece,” inducing electrical eddy currents in, and heating, the workpiece. The magnetic field is generated by passing alternating current (AC) at frequencies as great as 480 kHz through a water-cooled copper coil.

Figure 76. 10 kW EasyHeat LI power supply used for induction heating

To inductively heat the surface of the test section, a workpiece consisting of a cylinder of extruded graphite with a 17 mm OD and 30 mm axial dimension is heated by a copper coil (Figure 77). The coil used in these experiments is a simple helical coil with four turns, a diameter of 38.1 mm, and a height of 30 mm. The coil is custom made using 0.25 in (6.35 mm) OD copper tubing. The graphite is thermally coupled to the heated tungsten surface of the test section by a 0.15 mm thick copper shim, which is first heated to its melting point using the oxy-acetylene torch, to ensure good contact between the graphite and tungsten surfaces.

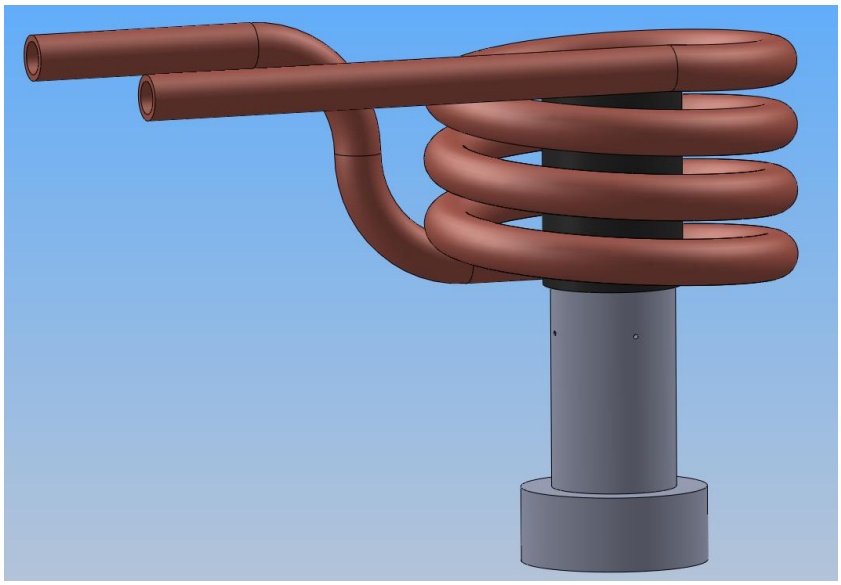

Figure 77. Solid model assembly of the induction heater copper coil, graphite workpiece, and HEMJ thimble

To reduce oxidation, and the resultant erosion, of the graphite workpiece during the experiment, argon is continuously injected to the top surface through six 0.125 in (3.18 mm) stainless steel tubes distributed circumferentially around the cylinder. An enclosure consisting of three side walls of 1 in (25.4 mm) thick Duraboard and a fourth side wall containing a window consisting of a 0.25 (6.35 mm) thick transparent pane of Pyroceram® contain the argon blanket and the workpiece. The floor of the enclosure consists of the Marinite® plates used to insulate the test section, and the ceiling consists of a 0.25 in (6.35 mm) aluminum plate. Compressed rock wool is used to fill voids in the enclosure, although there is significant leakage of argon from the enclosure. Nevertheless, a significant amount of the graphite is oxidized, and the graphite workpieces must be replaced every few experiments, where each experiment has a duration of at least 1 h. Despite oxidation and erosion of the workpiece, however, steady-state heat fluxes as great as 4.9 MW/m^2 were achieved with this induction heater setup.

6.2 Experimental Procedure

The procedure for experiments using the helium loop is similar to those for the single-pass experiments. Only steady-state experiments are performed. In all cases, the flow rate is set to achieve the desired Reynolds number, and the test section is heated until steady-state conditions, defined again to be when both the inlet temperature T_i and the outlet temperature T_o vary by less than 1 °C over a 5 min period, are achieved. In most cases, T_i and T_o vary by no more than 0.5 °C. Oscillations in the mass flow rate are kept below ±3% at flow rates greater than 3 g/s, as described later in this section. When heating with the oxy-acetylene torch, fluctuations as large as 5 °C in the readings from the embedded TC are also possible. When the induction heater is used instead, the output power can decrease slightly because of erosion and oxidation of the graphite workpiece during an experimental run. The current through the coil can be increased to maintain a constant power, but adjusting this current usually leads to small fluctuations in the incident heat flux. To minimize the effect of such fluctuations, steady-state temperature and pressure values were obtained by averaging the measurements over an interval of at least 150 s. Although temperatures in the following experiments were significantly higher than previous experiments on the HEMP-like divertor, simple calculations showed that, even in the best circumstances, contributions from radiative heat transfer from the cooled surface were minor compared to the total heat removed by convection and conduction. Therefore, radiative heat transfer is excluded from this analysis.

The coolant mass flow rate $\dot{m}$ is calculated from the pressure drop measurements through the Venturi meter as follows:

$$\dot{m} = CA_1\sqrt{\frac{2\rho_v \Delta P_v}{\left(A_1/A_2\right)^2 - 1}} \tag{75}$$

where ρ_v is the density of the coolant entering the Venturi meter, ΔP_v is the pressure drop between the throat and largest diameter of the Venturi meter, $A_1 = 196.0$ mm^2 is the large cross sectional area of the Venturi meter, $A_2 = 26.3$ mm^2 is throat cross sectional area of the Venturi meter, and $C = 0.8828$ is the flow coefficient provided by the manufacturer of the Venturi meter.

The mass flow rate is determined from the desired Reynolds number Re based on the diameter of the central port $D_o = 1.04$ mm:

$$Re = \frac{\rho V D_o}{\mu_i} = \frac{\dot{m} D_o}{A_j \mu_i} \tag{76}$$

where μ_i is the dynamic viscosity at the inlet, and $A_j =$ 7.64×10^{-6} m^2 is the total cross sectional area of the jets. The Reynolds number Re_p for the HEMJ at prototypical conditions of 6.8 g/s and $T_i = 637$ °C is ~2.14×10^4. However, experiments performed at the Efremov Institute have suggested that Re > 4×10^4 may be required to accommodate heat flux values of 10 MW/m^2. The range of Re that can be achieved in the helium loop, with a maximum mass flow rate of 10 g/s, of course depends on T_i. At room temperature (27 °C), $Re < 6.8\times10^4$ is feasible, while at $T_i = 300$ °C, only $Re < 4.4\times10^4$. As noted earlier, Re, and hence $\dot{m}$, are adjusted in the helium loop by using the bypass.

The thermal power incident on the test section is estimated from an energy balance applied to the coolant. This power is divided by the cross-sectional area of the test section $A_h = 227.0$ mm^2 to determine the average incident heat flux $\overline{q''}$ the test section:

$$\overline{q''} = \frac{\dot{m}\overline{c_p}\left(T_o - T_i\right)}{A_h} \tag{77}$$

where $\overline{c_p}$ is the specific heat evaluated at the average coolant temperature.

Using an energy balance to calculate the incident power to the test section assumes that losses from the test section are negligible. Although the test section is well-insulated in these experiments, these losses may not be negligible for higher operating temperatures. Eq. 77 also assumes a uniform incident heat flux. Although neither the oxy-acetylene torch nor the induction heater provide a uniform incident heat flux, the simulations by Rader [58] on the HEMP-like geometry using ANSYS FLUENT® 14.0 suggest that there is enough conduction between the heated and cooled surfaces of the thimble to "even out" the non-uniform incident heat flux profile.

The average cooled surface temperature $\overline{T_c}$ is an area-weighted average of the four local cooled surface temperatures T_{cr} (where r corresponds to the radial distance from the centerline in mm). First, T_{cr} is estimated by extrapolating the TC readings T_r to the cooled surface assuming one-dimensional conduction:

$$T_{cr} = \frac{\overline{q''}\delta_{TC}}{k_s} + T_r \tag{78}$$

where $\delta_{TC} = 0.5$ mm is the distance to the cooled surface and k_s is the thermal conductivity of the thimble evaluated at the average temperature between the two values (which requires iteration). $\overline{T_c}$ is then computed using the same equation used by Rader [58] where the area averaging is based on a 2-D projection of the curved surface:

$$\overline{T_c} = 0.026 \cdot T_{c0} + 0.218 \cdot T_{c2.1} + 0.314 \cdot T_{c4.3} + 0.442 \cdot T_{c6.4} \tag{79}$$

The average heat transfer coefficient $\overline{h}$ is then:

$$\overline{h} = \frac{\overline{q''}}{(\overline{T_c} - T_i)} \frac{A_h}{A_c} \tag{80}$$

where $A_c = 131.5$ mm^2. This area ratio assumes that all of the heat that is transferred through the heated surface is removed by convection at the cooled surface. Although this assumption is not exact for the HEMP-like and the HCFP-like designs, as discussed

in the previous chapters, we account for this by including the thermal conductivity ratio κ in the Nusselt number correlation.

The average Nusselt number $\overline{Nu}$ along the cooled surface is then:

$$\overline{Nu} = \frac{\bar{h} D_o}{k} \tag{81}$$

where k is the thermal conductivity of the coolant evaluated at the average coolant temperature $(T_i + T_o)/2$. Again, the correlation for $\overline{Nu}$ is assumed to be only a function of Re and κ, and we assume that Pr effects are negligible (*i.e.*, $\overline{Nu} = f(Re, \kappa)$).

Finally, loss coefficients K_L for each experiment are computed:

$$K_L = \frac{\Delta P}{\frac{1}{2}\rho_L \bar{V}^2} \tag{82}$$

where ΔP is the measured pressure drop, ρ_L is the coolant density, and $\bar{V}$ is the average coolant velocity at the jet. Again, ρ_L is evaluated using the outlet pressure and the inlet temperature because numerical simulations suggest that most of the pressure drop occurs across the jet holes before the coolant impinges on the cooled surface, and the properties at the outlet of these holes are well-approximated by the outlet pressure and inlet temperature. We again assume that K_L is only a function Re as has been shown in the HEMP-like geometry.

6.2.1 Mass Flow Rate Oscillations

The Hydro-Pac® C01.5-05-450LX reciprocating compressor used here can operate a flow loop with large pressure drops (exceeding 1.4 MPa) at 10 MPa, circulating helium by using a piston to compress helium at the desired pressure in one of two opposing cylinders. The downside to using a reciprocating compressor is the oscillations in the mass flow rate, which are as great as 8% of the average value.

This section describes the procedures used to reduce these oscillations to a maximum of 3% in these steady-state experiments. Although the two large buffer tanks downstream of the compressor should help to damp these oscillations, the maximum amplitude of the oscillations in the mass flow rate for an average $\dot{m} \approx 6.1$ g/s are about 5.7% of this value (Figure 78). Smaller secondary oscillations are also evident but of a negligible magnitude. The period of these oscillation are about 1 s, corresponding to the compressor frequency of ~1 Hz.

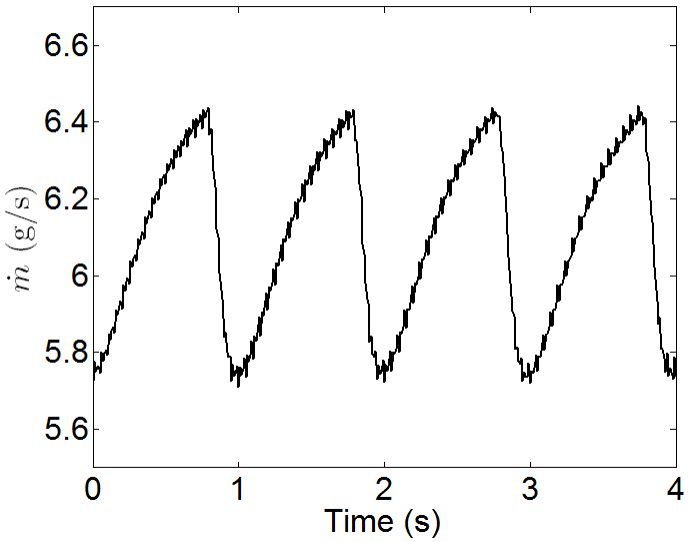

Figure 78. Measured mass flow rate as a function of time for an average $\dot{m} \approx$ 6.1 g/s

The overall pressure drop across the loop was therefore increased to reduce the magnitude of these oscillations. Additional pressure losses are “added” to the flow loop by using partially closed needle values on the bypass and main lines; these valves are adjusted to achieve the desired value of $\dot{m}$ through the test section with a total pressure drop of at least 1.1 MPa. The needle valve in the bypass line is shown in Figure 70, while the valve in the main line is located immediately downstream of the exit of the recuperator or, for experiments at room temperature, in the recuperator bypass line. The amplitude of the oscillations is less than 3% of the average value for these large

pressure drops (Figure 79). Increasing the pressure drop across the loop successfully reduces oscillations in the mass flow rate for average $\dot{m} =$ 3 g/s – 10 g/s. For $\dot{m} <$ 3 g/s, however, the maximum amplitude of the oscillations increases, and can be as great as 5%. These mass flow rates are not, however, of interest in these experiments.

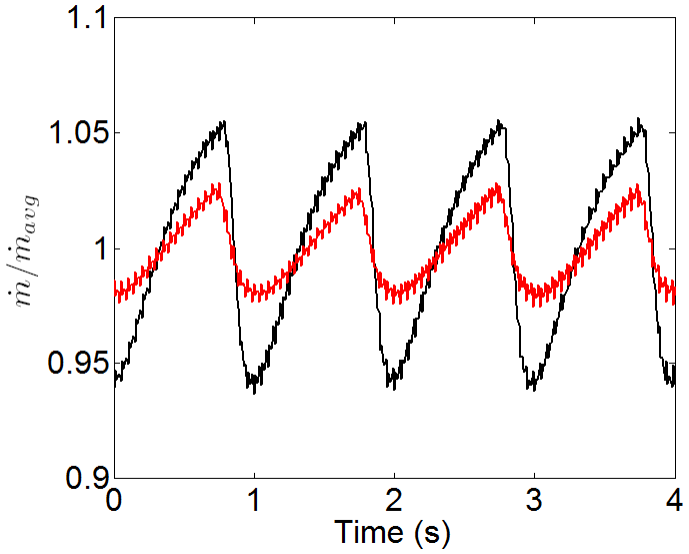

Figure 79. Comparison of mass flow rate as a function of time at $\dot{m} \approx 6$ g/s shown in the previous figure (black) and for an experiment where the pressure drop >1.1 MPa (red)

6.3 Experimental Results

A total of 24 steady-state experiments were performed at various inlet temperatures and mass flow rates using the oxy-acetylene torch as a heat source: 5 at $T_i = 27$ °C, 4 at $T_i = 100$ °C, 5 at $T_i = 200$ °C, 5 at $T_i = 250$ °C, and 5 at $T_i = 300$ °C. The Re in these experiments varied from 1.7×10^4 to 3.7×10^4, a range that brackets the prototypical value $Re_p = 21{,}400$ at $T_i = 637$ °C and $\dot{m} = 6.8$ g/s. The experiments performed at the Efremov Institute used mass flow rates up to 13 g/s and $T_i =$ 550-600 °C, corresponding to $Re \approx 4.2\times10^4$-4.4×10^4, slightly above in the values studied here. The experiments at $T_i = 300$ °C were only possible at $Re \approx 2.9\times10^4$ because the heaters were unable to achieve such high inlet temperatures at higher $\dot{m}$, suggesting that more

powerful, or additional heaters, will be required in future experiments. The incident heat flux varied from about 2.2 to 2.8 MW/m^2 for the experiments using the oxy-acetylene torch. Figure 80 shows the results for the average heat transfer coefficient $\bar{h}$ (details regarding the calculation of the experimental uncertainty are given in Appendix C).

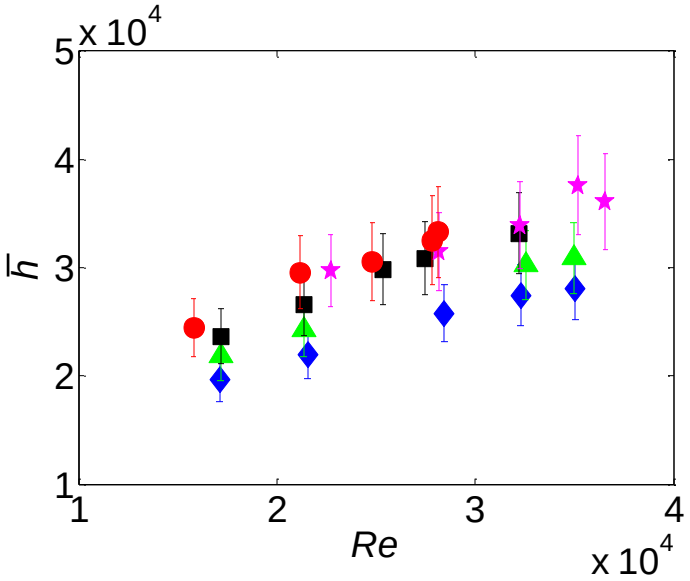

Figure 80. Average heat transfer coefficient $\bar{h}$ for $T_i = 27$ °C (♦), $T_i = 100$ °C (▲), $T_i = 200$ °C (■), $T_i = 250$ °C (★), and $T_i = 300$ °C (●)

These average heat transfer coefficients range from approximately 2×10^4 W/m^2·K at low Re to 3.7×10^4 W/m^2·K at the highest Re, and vary by as much as 20% at a given Re. Given that these experiments are all for the same geometry, the differences in $\bar{h}$ at a given Re are likely due to changes in the thermal conductivity of the coolant due to variations in T_i, variations in the amount of heat conducted through the walls of the divertor, and enhanced losses at high T_i. In addition, the values of $\bar{h}$ in Figure 80 are not the true average heat transfer coefficients of the cooled surface because they are based on A_h / A_c (*cf.* Eq. 80), and hence overestimate the average heat flux that is removed at the cooled surface. Figure 81 shows the corresponding average Nusselt number $\overline{Nu}$.

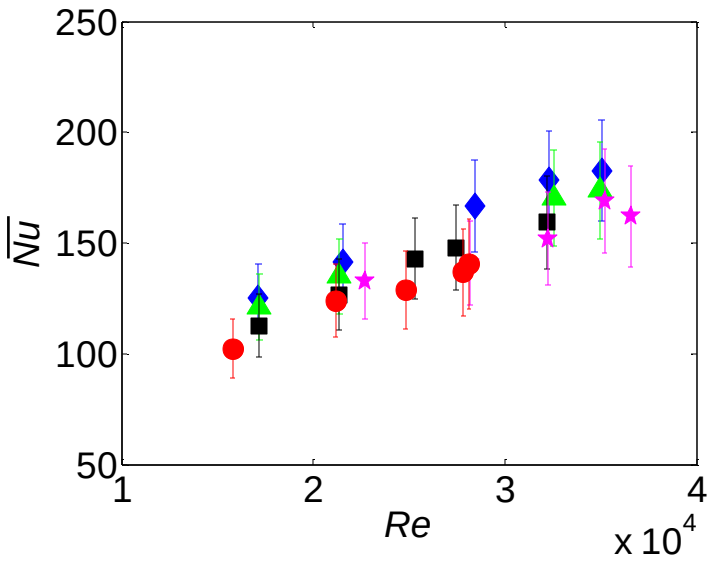

Figure 81. Average Nusselt number $\overline{Nu}$ for $T_i = 27$ °C (♦), $T_i = 100$ °C (▲), $T_i = 200$ °C (■), $T_i = 250$ °C (★), and $T_i = 300$ °C (●)

The variations in $\overline{Nu}$ at a given Re (but at different values of T_i) are greater than the experimental uncertainty. These variations are likely due in part to variations in the fraction of heat that is conducted through the walls of the divertor, *vs.* convected by the coolant at the cooled surface with T_i. Although the same coolant and thimble material are used for all experiments, the change in the respective thermal conductivities with temperature varies, and so the κ (as discussed in Chapter 5) varies from ~630 at $T_i = 27$ °C to ~460 at $T_i = 300$ °C. Based on previous experiments, these data are used to develop a correlation for $\overline{Nu}$ with a power law function of the form:

$$\overline{Nu} = C \cdot Re^a \cdot \kappa^b \tag{83}$$

The experiments of Rader [58] on an HEMJ module using room-temperature coolants at low pressures, gave a correlation of the form $\overline{Nu} \propto \kappa^{0.19}$ for $\kappa \approx 340$–7000. Since the range of κ in Rader's experiments is significantly larger than those tested here ($\kappa \approx 340$–7000 in Rader's experiments, *vs.* $\kappa \approx 460$–630 here), we assume here that $\overline{Nu}$ in these experiments is also proportional to $\kappa^{0.19}$. The HEMJ module used by

Rader was found to have a smaller gap width from the test section studied here (<0.6 mm). Therefore, Rader's correlation for $\overline{Nu}$ could not be directly compared with these data. However, this correlation for $\overline{Nu}$ did show an increase in performance compared with these data indicating that smaller gap widths may produce larger $\overline{Nu}$. This is left as an area of future study. A curve-fit of the data shown in Figure 80 with MATLAB 2008b then gives the following correlation:

$$\overline{Nu} = 0.196 \cdot Re^{0.537} \cdot \kappa^{0.19} \tag{84}$$

which is valid for:

$$\begin{bmatrix} 1.5\times10^4 \le Re \le 3.8\times10^4 \\ Pr \approx 0.7 \\ 460 \le \kappa \le 640 \end{bmatrix} \tag{85}$$

Although the $\kappa \approx 340$ under prototypical conditions, which is less than the values of κ given in Eq. 85, this correlation can likely be extended to lower values of κ, based on the range of validity for previous correlations for the HEMP-like geometry. Figure 82 compares this correlation with the experimental data.

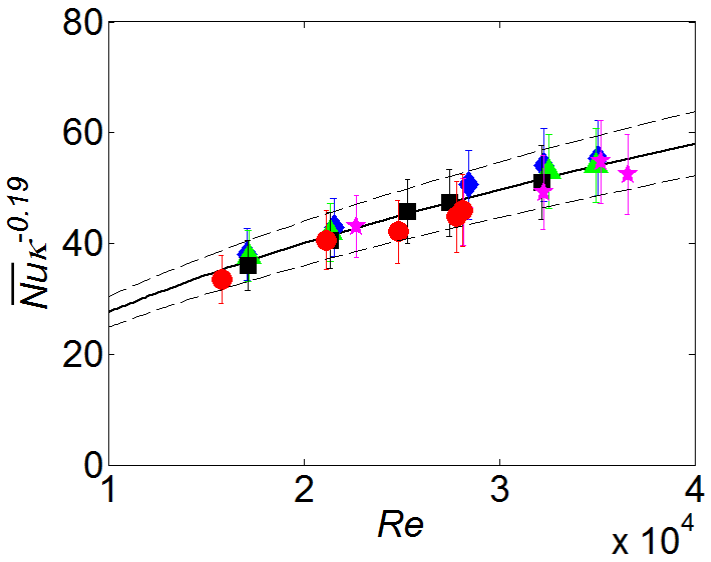

Figure 82. Based on the correlation of Eq. (76) $\overline{Nu}\kappa^{-0.19}$ as a function of Re for $T_i = 27$ °C (♦), $T_i = 100$ °C (▲), $T_i = 200$ °C (■), $T_i = 250$ °C (★), and $T_i = 300$ °C (●). The dashed lines denote a ±10% "error band" for the correlation

The experimental data are within 10% of the correlation (*i.e.*, within the dashed lines). Including the thermal conductivity ratio in the correlation for $\overline{Nu}$ decreases the variation in $\overline{Nu}$ at a given Re by about 6%, based on the values of κ at the highest and lowest T_i (*i.e.*, $(630/460)^{0.19} \approx 1.06$). The remaining variations in $\overline{Nu}$ at different T_i are likely due to losses, since the discrepancy between the true incident heat flux and that estimated from an energy balance of the coolant will change depending on T_i.

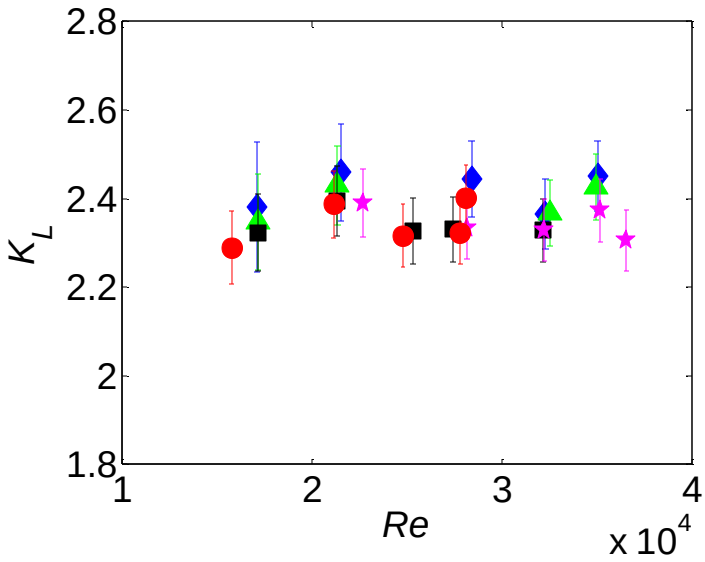

Figure 83. Loss Coefficient K_L for $T_i = 27$ °C (♦), $T_i = 100$ °C (▲), $T_i = 200$ °C (■), $T_i = 250$ °C (★), and $T_i = 300$ °C (●)

Finally, the loss coefficient results are shown in Figure 83 as a function of Re. K_L is almost constant, and has very little, if any, dependence on Re and T_i. This result is consistent with previous results on an HEMJ module [58] that gave K_L values ranging from 2.1 to 2.6 for the range of Re explored here. In this work, there was a weak dependence of K_L on Re, but the loss coefficients are simply assumed to be constant here, and the average value over these experiments:

$$K_L = 2.37 \tag{86}$$

All of these experiments were performed using the oxy-acetylene torch. The experiments thus far show that the correlation for $\overline{Nu}$ and K_L developed above using dynamically similar experiments are consistent for 27 °C $\leq T_i \leq$ 300 °C. This adds confidence that the correlations are capable of accurately predicting the thermal performance at prototypical conditions.

To extend the range of applicability of these correlations to higher heat fluxes, dynamically similar experiments were also performed at higher incident heat fluxes using

the induction heater. A total of 20 experiments were performed with the induction heater: 10 at $T_i = 27$ °C, 3 at $T_i = 100$ °C, 4 at $T_i = 200$ °C, and 3 at $T_i = 250$ °C. The Re in these experiments varied from 2.0×10^4 to 3.9×10^4, and the average incident heat fluxes ranged from 2.8 MW/m^2 (the highest value achieved with the torch) to 4.9 MW/m^2. Figure 84 shows the results for $\overline{Nu}\kappa^{-0.19}$ as a function of Re obtained for these experiments (filled symbols) as well as those shown in Figure 82 using the torch (open symbols).

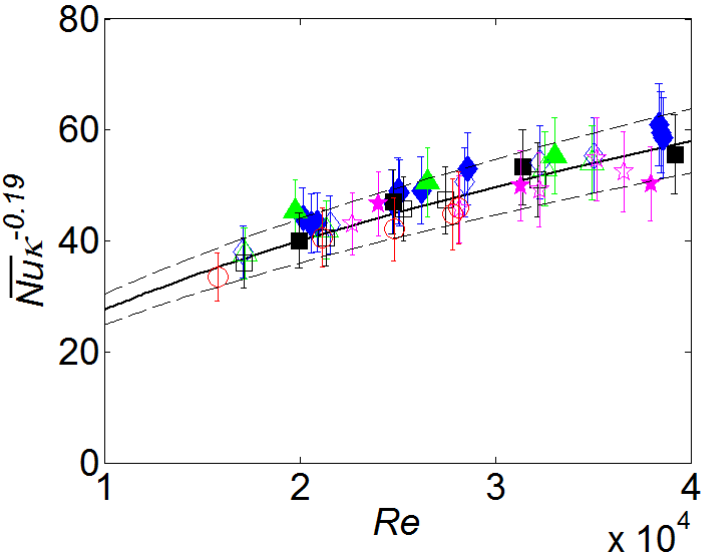

Figure 84. Average Nusselt number $\overline{Nu}$ including the thermal conductivity ratio κ for $T_i = 27$ °C (♦), $T_i = 100$ °C (▲), $T_i = 200$ °C (■), $T_i = 250$ °C (★), and $T_i = 300$ °C (●) using the oxy-acetylene torch (open symbols) and the induction heater (closed symbols)

The results obtained at higher incident heat flux values are in good agreement with the correlation developed for data at lower $\overline{q''}$, with only one data point (at the lowest Re studied) differing by more than 10% from the correlation. Table 9 summarizes the values of average incident heat flux $\overline{q''}$ for all experiments.

Table 9. Average incident heat flux for the induction heater experiments

Heat Source	Inlet Temperature (T_i)	Heat Flux ($\overline{q''}$) (MW/m^2)
Oxy-acetylene torch	27 °C	2.5 – 2.8
	100 °C	2.4 – 2.7
	200 °C	2.3 – 2.6
	250 °C	2.5 – 2.6
	300 °C	2.2 – 2.4
Induction Heater	27 °C	2.8 – 4.9
	100 °C	3.6 – 4.0
	200 °C	3.3 – 4.9
	250 °C	3.6 – 4.4

Figure 84 provides more confidence that this $\overline{Nu}$ correlation can therefore be extrapolated to prototypical conditions, although the maximum $\overline{q''}$ achieved here is still half that of the prototypical value.

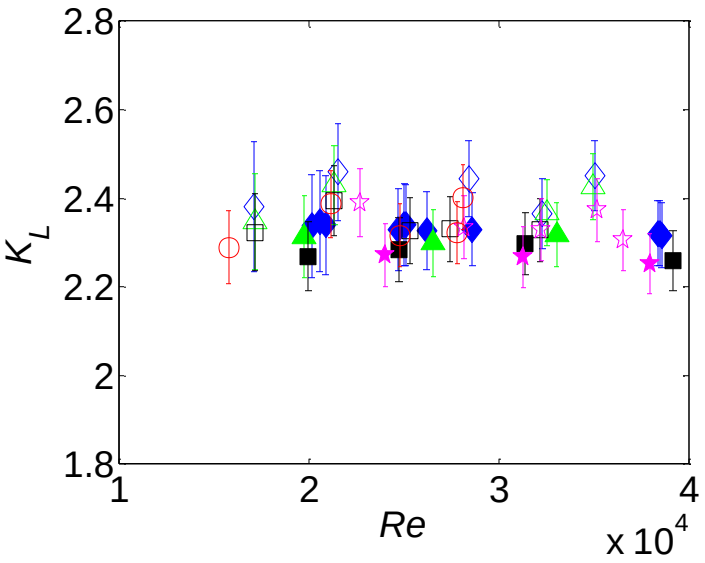

Figure 85. Loss Coefficient K_L for $T_i = 27$ °C (♦), $T_i = 100$ °C (▲), $T_i = 200$ °C (■), $T_i = 250$ °C (★), and $T_i = 300$ °C (●) using the oxy-acetylene torch (open symbols) and the induction heater (closed symbols)

Finally, Figure 8 shows the results for $K_L(Re)$ for all the experiments. As expected, K_L is nearly constant, with an average value of 2.34, for $1.7\times10^4 < Re < 3.9\times10^4$. The correlation for $\overline{Nu}$ and the estimate for K_L are therefore used to predict $\overline{q''}_{\max}$, the maximum heat flux the design can accommodate, and β, the pumping power as a fraction of incident power, at prototypical conditions, as detailed next.

6.4 Prototypical Performance

This procedure to estimate the thermal performance of the HEMJ divertor at prototypical operating conditions (Table 10) is similar to that described in Chapter 5 for the HEMP-like geometry. Two helium inlet temperatures ($T_i = 600$ °C and 700 °C) and three average pressure boundary/tile interface temperatures ($\overline{T_s} = 1100$ °C, 1200 °C and 1300 °C) were considered here, again because the material temperature limits remain unspecified.

Table 10. Prototypical operating conditions for the HEMJ divertor

Reynolds Number (Re_p)	2.14×10^4 (as high as 4×10^4 may be used)
Mass Flow Rate ($\dot{m}$)	6.8 g/s
Inlet Pressure (P_i)	10 MPa
Inlet Temperature (T_i)	600-700 ºC
Shell Material	WL10
Interface Temperature ($\overline{T_s}$)	1100-1300 ºC

For a given Re, $\overline{Nu}$ is calculated from Eq. 84 and used to calculate an average heat transfer coefficient $\bar{h}$ using Eq. 63. Then, $\overline{q''}_{\max}$ is calculated using Eqs. 64 and 65 where the thickness of the pressure boundary $\delta_s = 1$ mm. $\overline{T_c}$ and T_o are then calculated

using Eqs. 66 and 67 respectively and the procedure is iterated until $\overline{q''}_{\max}$, $\overline{T_c}$ and T_o all converge with an error of less than 0.01%.

Similarly, the maximum heat flux which can be accommodated at a given value of β is determined by a procedure similar to that used for the HEMP-like divertor. For a given Re, ΔP is computed using Eq. 68 and used to calculate the pumping power $\dot{W}$ from Eq. 69. Then $\overline{q''}_{\max}$ for a constant β can be determined using Eq. 70.

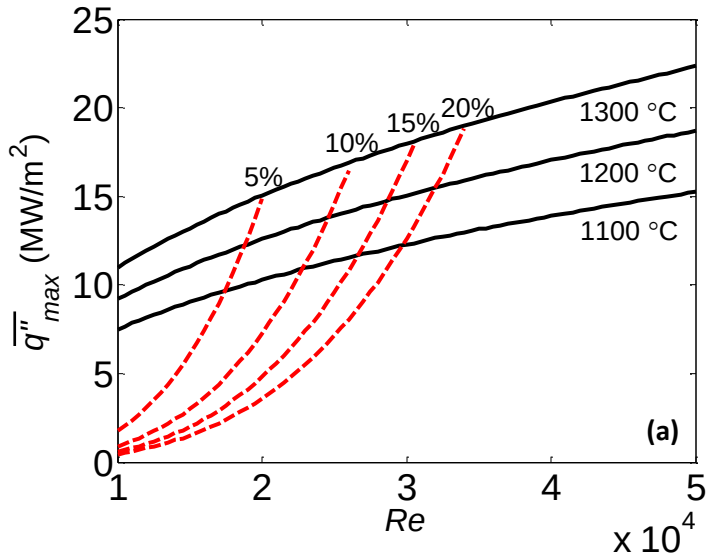

Figure 86. Maximum heat flux for the HEMJ divertor for $T_i = 600$ °C (a) and 700 °C (b) for $\overline{T_s} = 1100$, 1200, and 1300 °C (solid black lines) and $\beta = 5$, 10, 15, and 20% (red dashed lines)

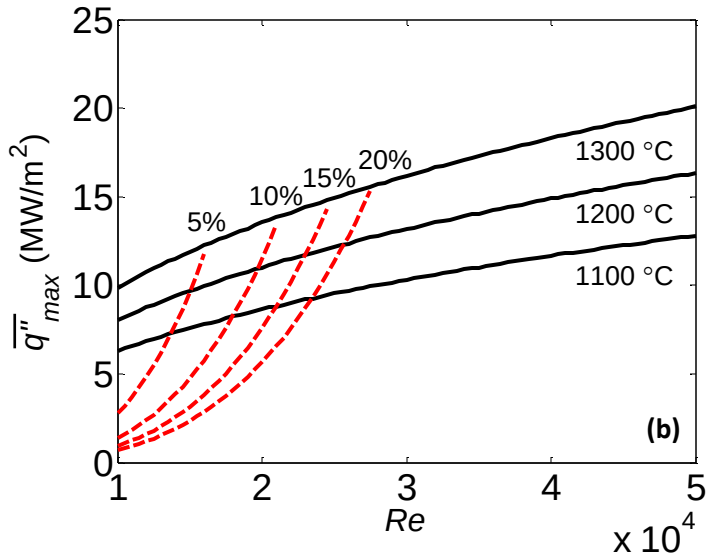

Figure 86 Continued. Maximum heat flux for the HEMJ divertor for $T_i = 600$ °C (a) and 700 °C (b) for $\overline{T_s} = 1100$, 1200, and 1300 °C (solid black lines) and $\beta = 5$, 10, 15, and 20% (red dashed lines)

Figure 86 gives $\overline{q''}_{\max}$ for the HEMJ divertor over a range of Re that span Re_p for inlet temperatures of (a) 600 °C and (b) 700 °C. The target plate for the HEMJ design is a hexagonal pure tungsten tile with a dimension (flat to flat) of 18 mm, which results in a ratio of heated surface to tile areas $A_h / A_t = 0.81$. Since $\overline{q''}_{\max}$ is the maximum heat flux on the pressure boundary A_h, $\overline{q''}_{\max}$ must be multiplied by this area ratio to determine the true maximum heat flux $\overline{q''}_{tile}$ that can be accommodated on the surface of the tile. At the expected prototypical conditions $Re_p = 2.14\times10^4$, $T_i = 600$ °C, and $\overline{T_s} = 1200$ °C, $\overline{q''}_{\max} = 13.0$ MW/m^2 and $\overline{q''}_{tile} = 10.5$ MW/m^2. Table 11 summarizes the maximum heat flux values at $Re_p = 2.14\times10^4$. Based on these results, the HEMJ divertor can accommodate incident heat fluxes on the tiles of 10 MW/m^2 at prototypical mass flow rates. However, if the inlet temperature of the coolant must be increased above 600 °C to avoid embrittlement issues with the tungsten alloy or the maximum allowable tungsten alloy temperature is less than 1200 °C, it may be necessary to increase the

mass flow rate. Finally, these are only steady-state heat flux values—and incident transient heat flux values due to ELMs, for example, may also require increasing Re.

Table 11. Thermal performance of the HEMJ divertor at $Re_p = 2.14\times10^4$

T_i (°C)	$\overline{T_s}$ (°C)	$\overline{q''}_{\max}$ (MW/m^2)	β (%)	$\overline{q''}_{tile}$ (MW/m^2)
600	1100	10.6	9	8.6
	1200	13.0	8	10.5
	1300	15.5	7	12.6
700	1100	8.9	16	7.2
	1200	11.4	13	9.2
	1300	13.9	11	11.3

CHAPTER 7: CONCLUSIONS AND RECOMMENDATIONS

This chapter summarizes the conclusions drawn from the previous chapters, discusses the contributions of this research to the MFE community, and makes recommendations for future work. Three modular helium-cooled divertor designs were studied in this work: a HEMP-like divertor with and without fins, the HCFP divertor, and the HEMJ divertor. The objectives of this research were to:

- perform dynamically similar experiments or numerical simulations to develop Nusselt number and loss coefficient correlations in order to evaluate the thermal-hydraulic performance of these designs at prototypical conditions
- develop charts from the correlations to determine how changes in operating conditions and material temperature constraints affect the maximum heat flux the designs can accommodate
- extend the range of experimental parameters to near prototypical conditions thereby enhancing confidence in the extrapolations based on dynamic similarity.

7.1 Research Findings:

7.1.1 The HEMP-like Divertor

A brass mockup of a HEMP-like divertor with and without fins was constructed and experimentally studied in four different flow configurations resulting from combining two different flow directions and a cooled surface with or without fins: forward flow without fins (BF), forward flow with fins (FF), reverse flow without fins (BR), and reverse flow with fins (FR). Dynamically similar experiments on each flow configuration were performed using helium or argon as a coolant. Compressibility effects were found to be

negligible in these experiments. Numerical simulations of the geometry without fins indicated that a significant fraction of the incident power was removed by conduction through the divertor walls as opposed to convection at the cooled surface that varied according to the coolant and test section material. A new dimensionless group, the thermal conductivity ratio κ, was introduced to account for this effect.

Correlations for the average Nusselt number $\overline{Nu}$ as a function of the Reynolds number Re and κ were developed for each flow configuration, and the experimental data fit within 10% of the resulting correlations given in Eq. 56. The range of validity for these correlations was found to encompass prototypical values of Re and κ. Correlations for the loss coefficient K_L as a function of only Re were also developed.

The correlations for $\overline{Nu}$ and K_L were used to generate generalized maximum heat flux charts for each flow configuration, given in Figure 63 and Figure 64, for inlet temperatures of 600 °C and 700 °C, respectively. Forward flow configurations were found to have the best thermal performance. At a prototypical Re of 7.6×10^4, inlet temperature of 600 °C, and a maximum alloy temperature of 1200 °C:

- the maximum heat flux the BF configuration can accommodate is 17.3 MW/m^2, based upon the heated surface (*vs.* tile) area, with a pumping power as a fraction of incident thermal power β of 13%
- the maximum heat flux the FF configuration can accommodate is 20.6 MW/m^2, based upon the heated surface (*vs.* tile) area, with a β value of 13%.

Finally, a significant increase in the pumping power was observed when increasing the inlet temperature from 600 °C and 700 °C.

7.1.2 The HCFP Divertor

Three-dimensional numerical simulations of the HCFP geometry were performed using ANSYS FLUENT® and validated against the earlier dynamically similar experiments using air performed by Hageman [45]. His experimentally derived $\overline{Nu}$ were within about 11% of the numerical predictions. More simulations were then performed with the same numerical model using different combinations of coolants and test section materials, and hence κ. An improved correlation for $\overline{Nu}$ as a function of Re and κ is given in Eq. 72; all of the numerical and experimental values are within 10% of this correlation. This revised $\overline{Nu}$ correlation, along with a correlation for K_L found using Hageman's experimental data, were used to generate generalized maximum heat flux charts, shown in Figure 66, for inlet temperatures of 600 °C and 700 °C. The maximum heat flux the divertor can accommodate for prototypical Re of 3.3×10^4, inlet temperature of 600 °C, and a maximum alloy temperature of 1300 °C is 7.0 MW/m^2 with a β value of 11%.

7.1.3 The HEMJ Divertor

Finally, a helium loop was constructed to perform dynamically similar experiments at near prototypical conditions to provide further confidence in the extrapolations to prototypical conditions and evaluate the HEMJ divertor. Dynamically similar experiments were performed on the HEMJ test section at inlet temperatures ranging from 27 °C to 300 °C using the oxy-acetylene torch as a heat source, and the correlation for $\overline{Nu}(Re,\kappa)$ given in Eq. 84 was developed from these data and found to be within 10% of the experimental measurements. The results from the helium loop experiments for pressure drop suggested that K_L correlation was essentially constant and independent of Re. More experiments at higher incident heat flux values were conducted at inlet temperatures ranging from 27 °C to 250 °C using the induction heater,

and these results were in good agreement with the correlations for $\overline{Nu}$ and K_L obtained using the oxy-acetylene torch at lower incident heat flux values. Based on the resulting generalized maximum heat flux charts, again for inlet temperatures of 600 °C and 700 °C (Figure 86), the maximum heat flux that can be accommodated by the divertor at a prototypical Re of 2.14×10^4, inlet temperature of 600 °C, and a maximum alloy temperature of 1200 °C is 13.0 MW/m^2, based on the heated surface (*vs.* tile) area, with a β value of 8%. Previous correlations for $\overline{Nu}$ derived from room temperature experiments performed by Rader [58] with a smaller gap width indicated that the HEMJ design could be improved by decreasing the gap width.

7.2 Contributions

The thermal performance of three leading modular helium-cooled tungsten divertor designs was experimentally investigated in this work. There are few such experiments because of the practical difficulties in achieving the very high prototypical temperatures and pressures required for prototypical conditions. These experiments are therefore valuable to the fusion community because they greatly expand the experimental thermal-hydraulics database for these configurations. The contributions of this work include:

- new experimentally and numerically based Nusselt number and loss coefficient correlations for the HEMP-like with and without fins, the HCFP, and the HEMJ divertor designs
- new generalized maximum heat flux charts that estimate the maximum heat flux each divertor design can accommodate under various temperature and coolant mass flow rate constraints.

These correlations can be used in system codes, for example, to optimize the overall performance of future commercial fusion reactor designs.

Although applied here to specific designs, the approach utilized here based on dynamically similar experiments to analyze the thermal performance was validated over a range of temperatures, pressures, coolants, heat fluxes, and materials. This study therefore suggests that results from properly conducted dynamically similar experiments at temperature and pressures lower than prototypical conditions, using alternative coolants, and at lower incident heat fluxes can be used with reasonable confidence to predict the thermal performance of future divertor designs at prototypical conditions. Experiments of this type require less effort both in terms of time and resources, which makes it more practical to experimentally investigate variants of the divertor designs. A helium loop was constructed as part of this research that enables dynamically similar experiments at near-prototypical conditions using tungsten-alloy test sections. This unique facility gives us the capability to study a wider range of modular divertor designs.

Finally, experimentally validated numerical simulations were used to extend the range of these studies as required. These simulations also evaluated the impact of using different turbulence models on the accuracy of the numerical predictions and investigated several key assumptions in the dimensional analysis.

7.3 Recommendations for Future Work

In terms of future work, the following suggestions would complement and extend this doctoral research.

- The $\overline{Nu}$ and K_L correlations presented here have been developed for three specific divertor designs. While there has been some research in the literature aimed at optimizing these designs, this work is limited, and there is little work to

date on optimizing the size(s) of the jet holes and the gap width between the jets and the cooled surfaces on the HEMJ divertor. Given that the current HEMJ test section used in the helium loop has an adjustable gap width, a combination of experiments and numerical simulations, should be performed to determine optimal geometries. Particular attention should be paid to the means by which coolant is exhausted from the jet array. A similar optimization should also be performed on the HEMP-like design in terms of gap width and jet diameter as indicated by the low fractions of incident heat removed by convection at the cooled surface of the divertor without fins in Figure 49.

- Given that the correlations developed in this work are only applicable for divertors of the same geometry, it is important to extend the validity of these correlations to cover relevant geometrical changes. For example, since the conduction through the walls of the divertor is significant, the effect of varying the thickness of the divertor walls should be investigated. This analysis could be performed numerically or experimentally.

- Again, given that conduction through the walls is significant, a new divertor test section for the helium loop should be constructed, preferably from the WL10 tungsten-alloy that is a leading candidate for future divertor designs, with thermocouples embedded in the walls at different axial locations to obtain wall temperature data that can be used to validate numerical simulations. Numerical simulations validated by these temperature data could then be used to more accurately quantify the fraction of heat removed through the walls of the divertor by conduction. Experiments using the helium loop indicate that heat losses increase, as expected, as the helium inlet temperature increases. These losses should be further quantified and these results should be used to improve the

estimates of the actual heat flux that is incident upon the test section. Temperatures measured by thermocouples attached to the outside of the insulation could be used to estimate the heat loss. An experimentally validated numerical model can also be used to estimate the magnitude of the losses by comparing simulations of room temperature experiments to those at high inlet temperatures.

- The current induction heater design should be modified to ensure more consistency at higher heat flux values. Using a workpiece made of a more oxidation-resistant graphite would also allow for longer run times, and increase the number steady-state experiments that can be performed with a given workpiece. The possibility of using a tungsten-alloy workpiece should also be considered, since such a workpiece would undergo less oxidation and have better thermal contact with the test section. Finally, a new test section should be constructed that integrates the workpiece with the thimble to eliminate contact issues altogether.

- Dynamically similar experiments on a HCFP test section made from a low thermal conductivity material should be performed using air as a coolant to validate the simulations performed here to obtain experimental data at thermal conductivity ratios closer to prototypical values. In addition, experiments should be performed on a HCFP test section similar to the design described in Tillack et al. [36].

- The effect of surface roughness on the cooled surface of each divertor module should be investigated. By increasing the surface roughness, the thermal performance could be enhanced but at a cost of increased pressure drop. The magnitude of this tradeoff is important for optimizing each design. Careful

measurements of the existing test sections should also be made to determine if surface roughness is a factor in the existing experimental data.

- While the numerical model for the HEMP-like module without fins showed reasonable agreement with the experimental data in forward flow, there is considerable room for improvement. Ideally, the same turbulence model should be applicable for both forward and reverse flows, but this may require that a different mesh is used for each flow direction. Other commercial CFD packages should be explored for these geometries, and a model for the HEMP-like divertor with fins and the HEMJ model should be created and validated using the experimental data contained within this work.

APPENDIX A: EXPERIMENTAL DATA

This appendix includes the measured time-averaged data for all steady-state experiments that appear in this work. Each row corresponds to a single steady-state experiment. All variables are defined in the Nomenclature. Tables A.1 through A.20 include data for the HEMP-like divertor experiments. Table A.21 includes data for the HCFP experiments. Tables A.22 through A.23 include data for the HEMJ divertor experiments with the helium loop. Finally, Tables A.24 and A.25 include the reference cases for the HEMP-like geometry and the HCFP geometry.

A.1 Bare Forward Data with Air [59]

P_R (Pa)	ΔP (Pa)	P_i (Pa)	T_{c6} (°C)	T_{c5} (°C)	T_{c4} (°C)	T_{c3} (°C)	T_i (°C)	T_o (°C)	Q (cm^3/s)
417966	137598	413656	83.2	81.7	81.8	81.2	20.9	31.5	1216.2
348066	118387	344059	88.3	86.8	87.2	86.5	20.9	33.4	1132.2
282441	99814	278846	95.1	93.6	94.0	93.4	21.1	36.0	1038.3
215010	79797	211955	104.2	102.7	103.0	102.5	21.3	39.6	934.6
145849	57740	143479	117.8	116.3	116.5	115.9	21.6	44.8	806.2
106365	44220	104459	129.3	127.8	128.0	127.4	21.9	49.5	707.4
71156	31047	69752	144.0	142.5	142.5	141.9	22.1	54.9	598.7
49156	22041	48129	159.0	157.5	157.4	156.8	22.3	61.2	514.7
35650	16205	34906	173.6	172.1	171.8	171.2	22.6	68.1	440.6
20831	9546	20423	197.5	195.9	195.5	194.9	22.9	78.5	336.9
6954	3294	6940	249.0	247.3	246.2	245.8	23.6	100.4	178.8
415530	130439	411819	205.6	201.6	201.6	197.8	21.9	55.8	1191.5
348387	112281	344978	220.8	216.8	217.0	213.1	22.1	61.6	1107.5
277220	92594	274247	240.6	236.5	236.8	232.8	22.3	68.9	1018.6
210001	73139	207566	265.8	261.7	261.9	257.8	22.5	78.7	905.0
140743	51937	138974	304.5	300.2	300.1	295.8	22.8	94.6	766.6
107647	41176	106259	333.1	328.7	328.3	323.9	23.0	106.5	677.7
69512	28188	68618	348.9	344.8	344.3	340.4	23.3	117.6	564.1
49362	20706	48779	345.7	342.0	341.3	338.1	23.6	120.8	485.1
35965	15438	35601	338.9	335.5	334.9	332.2	23.7	122.0	420.9
20245	8945	20180	310.0	307.3	306.6	305.1	24.0	117.9	317.1

A.2 Fins Forward Data with Air [59]

P_R (Pa)	ΔP (Pa)	P_i (Pa)	T_{c6} (°C)	T_{c5} (°C)	T_{c4} (°C)	T_{c3} (°C)	T_i (°C)	T_o (°C)	Q (cm^3/s)
418004	150890	413884	64.4	62.8	64.1	66.0	21.7	34.0	1181.6
348102	129777	344285	69.4	67.9	69.2	71.2	21.8	36.5	1097.6
281912	109412	278390	70.1	68.7	70.0	72.1	22.0	37.8	1008.7
210358	85848	207392	77.7	76.3	77.6	79.7	22.2	41.7	895.1
141424	61786	139110	88.5	87.2	88.4	90.5	22.5	47.0	761.7
100817	46276	98980	99.7	98.4	99.5	101.6	22.7	52.7	658.0
69924	33383	68519	111.2	110.0	111.0	113.1	23.0	58.9	569.1

A.2 Fins Forward Data with Air Continued [59]

P_R (Pa)	ΔP (Pa)	P_i (Pa)	T_{c6} (°C)	T_{c5} (°C)	T_{c4} (°C)	T_{c3} (°C)	T_i (°C)	T_o (°C)	Q (cm^3/s)
48807	23859	47754	125.0	123.8	124.6	126.7	23.2	66.1	480.1
34712	17255	33928	138.3	137.3	138.0	140.0	23.5	73.2	406.0
20656	10463	20165	161.3	160.3	160.7	162.8	23.8	84.7	312.2
7161	3861	7027	214.4	213.5	213.3	215.1	24.6	107.1	168.9
419135	145038	415652	136.4	131.7	134.7	134.7	21.7	54.9	1151.9
346794	123349	343730	147.6	143.0	145.9	146.2	21.9	60.6	1063.0
278600	102196	275668	161.9	157.5	160.2	160.7	22.1	67.7	969.2
211619	80851	209159	181.8	177.5	180.0	180.6	22.4	77.8	870.4
139998	56877	138147	213.5	209.4	211.6	212.2	22.6	93.7	727.1
104989	44337	103536	238.3	234.2	236.2	236.8	23.0	106.6	638.2
70116	30980	69096	276.7	272.7	274.4	274.9	23.4	127.6	534.5
49572	22828	48824	266.0	262.7	264.0	264.7	23.6	127.3	460.4
35086	16671	34560	257.6	254.8	255.9	256.8	23.8	126.4	391.2
21470	10570	21166	257.2	255.0	255.7	256.6	24.1	128.0	302.3

A.3 Bare Reverse Data with Air [59]

P_R (Pa)	ΔP (Pa)	P_i (Pa)	T_{c6} (°C)	T_{c5} (°C)	T_{c4} (°C)	T_{c3} (°C)	T_i (°C)	T_o (°C)	Q (cm^3/s)
415634	179849	410095	121.0	120.2	119.0	118.8	23.9	31.7	1300.1
349237	154196	344224	128.8	128.0	126.9	126.8	23.8	33.2	1196.4
274102	124403	269829	141.3	140.6	139.1	139.1	23.8	35.7	1087.7
208304	97504	204791	151.2	150.6	149.0	149.0	23.8	38.5	974.1
142657	69779	140012	164.7	164.2	162.5	162.5	24.0	42.9	840.7
107156	53770	105047	174.6	174.2	172.3	172.4	24.1	46.6	741.9
70392	36027	68921	190.0	189.6	187.4	187.6	24.2	52.6	618.5
48030	24716	47018	211.2	210.8	208.3	208.3	24.4	60.8	519.7
35618	18338	34540	229.1	228.6	225.8	225.4	24.1	67.2	450.5
21836	11234	21055	244.5	244.0	241.1	240.8	24.5	78.3	346.8
7087	3745	6445	283.1	282.4	279.5	278.8	26.0	106.9	178.8
417008	175510	411010	272.5	270.8	267.7	267.2	23.8	46.1	1260.6
351943	151041	346479	294.3	292.6	289.3	288.4	23.8	50.3	1166.8
284747	125280	279987	310.4	308.9	305.2	304.6	23.9	54.9	1063.0
208548	93967	205054	338.4	337.1	333.1	332.0	24.5	63.1	929.7
135232	63862	132539	373.9	372.7	368.4	367.9	24.6	76.0	771.6
105706	51340	103355	332.4	331.5	328.1	328.6	24.7	74.2	702.4
70154	34992	68281	356.4	355.7	351.8	352.5	25.0	85.9	578.9
51224	25816	49580	325.5	325.0	321.8	322.8	25.3	86.6	509.8
36105	18393	34751	339.3	338.7	335.3	336.4	25.6	95.9	430.7
22828	11659	21529	362.9	362.3	358.7	359.7	26.2	112.5	331.9

A.4 Fins Reverse Data with Air [59]

P_R (Pa)	ΔP (Pa)	P_i (Pa)	T_{c6} (°C)	T_{c5} (°C)	T_{c4} (°C)	T_{c3} (°C)	T_i (°C)	T_o (°C)	Q (cm^3/s)
202356	97649	200244	103.9	104.0	102.0	105.2	24.1	52.3	835.8
140885	72377	139363	117.4	117.5	115.5	118.7	24.2	60.7	707.4
105792	56723	104661	129.7	129.8	127.7	131.0	24.3	68.5	618.5
68465	38591	67754	150.3	150.4	148.0	151.4	24.6	81.8	504.8
49077	28479	48590	165.9	166.0	163.3	166.8	24.8	92.4	425.8
34399	20509	34211	178.0	177.8	175.4	178.5	24.0	100.7	356.6
20176	12429	19756	206.3	206.2	203.6	206.9	24.9	119.1	262.8
7816	4962	7505	148.1	148.3	147.2	150.4	25.5	90.0	159.1

A.4 Fins Reverse Data with Air Continued [59]

P_R (Pa)	ΔP (Pa)	P_i (Pa)	T_{c6} (°C)	T_{c5} (°C)	T_{c4} (°C)	T_{c3} (°C)	T_i (°C)	T_o (°C)	Q (cm^3/s)
272602	122491	269198	98.7	98.8	97.4	101.3	23.8	48.6	939.5
346500	149126	342566	90.5	90.6	89.2	93.3	23.6	44.0	1043.3
416416	178775	412139	85.0	85.1	83.6	87.6	23.6	40.9	1142.1
413913	174871	410371	181.3	179.0	176.7	180.6	24.1	70.0	1077.9
349537	149498	346439	198.1	196.1	193.6	197.5	24.1	78.8	988.9
279442	124424	276771	217.3	215.5	213.0	216.8	24.1	90.0	885.2
214041	100626	211807	241.2	239.4	236.9	240.5	24.2	104.9	776.5
146306	74785	144511	278.9	277.1	274.4	277.4	24.4	128.9	643.2
110324	59370	108524	313.7	312.1	309.2	312.0	24.7	151.3	564.1

A.5 Bare Forward Data with Air at High Pressure [59]

P_R (Pa)	ΔP (Pa)	P_i (Pa)	T_{c6} (°C)	T_{c5} (°C)	T_{c4} (°C)	T_{c3} (°C)	T_i (°C)	T_o (°C)	Q (cm^3/s)
618878	186357	611419	196.1	195.6	189.7	187.6	24.4	51.5	1413.3
624458	130169	619440	209.0	208.5	202.7	200.6	24.5	55.8	1268.1
626537	110546	622919	215.1	214.6	208.9	206.6	24.7	58.3	1189.7
627923	94029	625152	221.8	221.3	215.6	213.3	24.9	60.8	1109.2
631634	69770	630007	239.5	238.8	231.5	227.9	25.1	66.6	962.1
634942	48216	634559	260.5	259.9	252.4	247.8	25.5	74.6	797.3
636723	34021	637642	284.9	284.3	276.5	273.1	26.0	84.4	656.0
640393	20853	641581	330.3	329.5	321.5	318.4	26.5	103.7	467.6
645468	9914	647537	313.1	312.5	306.7	305.1	27.1	115.8	238.1

A.6 Fins Forward Data with Air at High Pressure [59]

P_R (Pa)	ΔP (Pa)	P_i (Pa)	T_{c6} (°C)	T_{c5} (°C)	T_{c4} (°C)	T_{c3} (°C)	T_i (°C)	T_o (°C)	Q (cm^3/s)
623970	202956	616244	164.7	158.6	161.3	160.6	24.6	60.6	1370.2
633562	136942	628060	176.2	170.0	172.6	171.8	24.7	66.2	1201.4
644780	88312	641283	193.9	187.9	190.2	189.4	25.0	75.3	989.5
652453	61198	649482	212.6	206.5	208.8	208.1	25.6	84.0	828.6
647092	46875	645870	228.7	222.4	225.2	224.1	25.8	93.2	718.8
655121	30990	655131	259.3	253.2	255.7	254.7	26.2	109.2	559.9
673550	13967	673225	249.3	245.3	246.8	246.7	26.8	117.6	304.8

A.7 Bare Reverse Data with Air at High Pressure [59]

P_R (Pa)	ΔP (Pa)	P_i (Pa)	T_{c6} (°C)	T_{c5} (°C)	T_{c4} (°C)	T_{c3} (°C)	T_i (°C)	T_o (°C)	Q (cm^3/s)
666430	213420	661438	353.4	352.0	343.8	342.2	23.3	49.5	1462.4
671771	139918	668367	327.9	326.7	319.5	318.3	23.3	49.5	1272.1
677353	105648	674711	342.7	341.5	334.3	333.2	23.4	52.9	1124.9
684200	75714	683812	333.2	331.9	325.4	324.5	23.5	54.6	962.1
687168	54909	687203	346.8	345.3	338.6	337.2	23.7	59.2	814.9
690413	41601	691898	319.3	318.0	312.2	311.2	23.7	58.9	699.2
692502	27566	695026	345.1	343.7	337.8	336.8	24.0	67.8	534.3
700911	13995	703559	372.2	370.8	364.9	364.3	24.5	86.5	304.8

A.8 Fins Reverse Data with Air at High Pressure [59]

P_R (Pa)	ΔP (Pa)	P_i (Pa)	T_{c6} (°C)	T_{c5} (°C)	T_{c4} (°C)	T_{c3} (°C)	T_i (°C)	T_o (°C)	Q (cm^3/s)
666279	244680	664245	164.9	160.6	162.6	164.1	23.9	56.6	1370.2
671218	158259	672266	178.0	173.5	175.7	177.2	24.1	62.9	1172.0

A.8 Fins Reverse Data with Air at High Pressure Continued [59]

P_R (Pa)	ΔP (Pa)	P_i (Pa)	T_{c6} (°C)	T_{c5} (°C)	T_{c4} (°C)	T_{c3} (°C)	T_i (°C)	T_o (°C)	Q (cm^3/s)
675800	123339	677172	187.7	183.2	185.5	186.9	24.2	67.9	1048.4
680005	88143	682965	202.6	198.0	200.2	201.4	24.3	75.9	887.5
685041	60784	688467	222.9	218.4	220.3	221.3	24.5	87.7	720.7
690182	38823	693951	254.1	249.6	251.1	251.8	24.8	107.1	542.2
694857	19970	699147	225.2	222.0	223.0	223.4	25.1	110.1	348.0

A.9 Bare Forward Data with Helium

P_R (Pa)	ΔP (Pa)	P_i (Pa)	T_{c6} (°C)	T_{c5} (°C)	T_{c4} (°C)	T_{c3} (°C)	T_i (°C)	T_o (°C)	Q (cm^3/s)
129760	50286	126937	216.0	218.5	209.5	211.7	26.1	80.7	732.1
186003	69454	182715	184.0	185.8	177.8	179.9	25.4	66.5	860.5
312534	108928	307922	158.9	161.0	153.6	155.0	26.7	55.7	1172.2
624700	198174	612856	134.9	131.8	128.3	131.8	27.1	45.0	1448.6
1349135	400165	1323938	96.9	95.7	92.9	93.4	24.5	33.1	2060.8
1058651	319528	1038029	104.0	102.5	99.7	99.4	28.3	38.1	1854.8

A.10 Fins Forward Data with Helium

P_R (Pa)	ΔP (Pa)	P_i (Pa)	T_{c6} (°C)	T_{c5} (°C)	T_{c4} (°C)	T_{c3} (°C)	T_i (°C)	T_o (°C)	Q (cm^3/s)
153329	64798	152625	167.6	162.5	164.9	166.7	25.6	82.3	775.7
348026	133822	347809	122.7	116.8	119.9	120.4	25.5	55.1	1091.6
206700	83678	202723	146.6	140.1	144.6	144.0	25.5	69.9	865.9
1114294	371109	1091288	83.8	78.0	81.5	81.0	27.4	37.4	1825.4
668915	233354	656101	100.6	94.5	97.5	96.8	25.7	42.9	1438.8
1369349	448083	1346506	78.8	73.2	77.0	76.5	27.7	35.7	2033.3

A.11 Bare Forward Data with Argon

P_R (Pa)	ΔP (Pa)	P_i (Pa)	T_{c6} (°C)	T_{c5} (°C)	T_{c4} (°C)	T_{c3} (°C)	T_i (°C)	T_o (°C)	Q (cm^3/s)
213670	75988	215074	322.1	321.9	312.8	312.8	22.4	97.9	913.0
342935	108448	335725	343.2	342.1	331.5	329.9	22.3	94.6	1095.5
85265	34662	81906	285.0	284.3	279.0	278.6	23.1	102.1	624.6
467383	148183	480073	318.7	317.7	306.1	303.7	21.9	81.4	1276.0

A.12 Fins Forward Data with Argon

P_R (Pa)	ΔP (Pa)	P_i (Pa)	T_{c6} (°C)	T_{c5} (°C)	T_{c4} (°C)	T_{c3} (°C)	T_i (°C)	T_o (°C)	Q (cm^3/s)
217574	83736	211890	208.2	204.7	212.0	207.8	22.4	93.9	867.9
493441	164832	485897	212.1	206.1	217.5	209.8	22.2	84.3	1232.8
376237	132412	368736	194.8	190.1	200.4	193.4	22.3	82.3	1101.4
113813	50371	108550	173.6	171.8	177.8	174.4	22.9	85.5	669.7

A.13 Bare Forward Data with Argon at High Pressure

P_R (Pa)	ΔP (Pa)	P_i (Pa)	T_{c6} (°C)	T_{c5} (°C)	T_{c4} (°C)	T_{c3} (°C)	T_i (°C)	T_o (°C)	Q (cm^3/s)
1355005	26151	1351963	321.4	321.5	312.0	312.7	22.9	96.4	461.7
1345285	55109	1349893	304.0	303.2	293.1	291.4	22.9	79.6	824.7
1344510	40053	1353662	331.3	330.5	319.8	318.2	23.1	90.8	661.9
1347534	19121	1356405	302.1	302.6	294.2	295.4	23.5	100.1	316.6

A.14 Fins Forward Data with Argon at High Pressure

P_R (Pa)	ΔP (Pa)	P_i (Pa)	T_{c6} (°C)	T_{c5} (°C)	T_{c4} (°C)	T_{c3} (°C)	T_i (°C)	T_o (°C)	Q (cm^3/s)
1360325	30979	1353518	215.7	211.5	217.2	214.0	22.5	94.6	485.3
1352208	48446	1344673	205.9	199.9	210.0	203.0	22.2	84.6	683.5
1355190	65977	1345788	211.1	204.2	216.0	207.8	21.4	82.4	854.2
1352806	22515	1342578	194.1	190.4	197.9	193.4	22.9	89.7	349.9

A.15 Bare Reverse Data with Helium

P_R (Pa)	ΔP (Pa)	P_i (Pa)	T_{c6} (°C)	T_{c5} (°C)	T_{c4} (°C)	T_{c3} (°C)	T_i (°C)	T_o (°C)	Q (cm^3/s)
149677	60558	140669	336.1	333.8	324.4	323.4	24.4	75.8	773.7
206948	81148	200496	304.7	301.9	293.5	292.3	24.5	64.0	897.3
348718	124626	338094	255.4	252.9	245.1	243.6	25.5	51.1	1123.0
641980	208522	624928	212.8	210.3	204.3	202.7	25.5	40.9	1468.3
1065365	332588	1058206	169.2	166.6	161.9	160.3	21.7	30.8	1872.4
1287210	392996	1270890	163.9	161.4	156.8	154.8	26.8	34.5	2060.8

A.16 Fins Reverse Data with Helium

P_R (Pa)	ΔP (Pa)	P_i (Pa)	T_{c6} (°C)	T_{c5} (°C)	T_{c4} (°C)	T_{c3} (°C)	T_i (°C)	T_o (°C)	Q (cm^3/s)
158083	82140	162738	170.4	165.6	166.4	168.1	25.1	87.2	734.5
248935	116110	251735	145.4	140.6	142.4	144.9	25.3	69.0	895.4
380192	160308	375860	122.3	117.5	120.1	122.5	24.4	54.1	1075.9
775777	293281	777293	101.8	97.0	99.9	102.0	25.0	41.1	1509.5
1122394	400174	1103355	91.2	88.8	89.6	91.7	28.1	39.0	1782.2
1394344	487098	1370401	84.1	80.0	82.6	84.7	26.4	35.2	1962.7

A.17 Bare Reverse Data with Argon

P_R (Pa)	ΔP (Pa)	P_i (Pa)	T_{c6} (°C)	T_{c5} (°C)	T_{c4} (°C)	T_{c3} (°C)	T_i (°C)	T_o (°C)	Q (cm^3/s)
152427	63334	148290	306.8	305.9	301.4	301.6	24.5	73.9	783.5
276039	105025	276131	271.8	270.8	266.9	266.8	24.0	57.9	1028.8
458418	159060	456835	305.3	304.0	299.2	298.4	23.6	55.0	1268.1
56616	26346	52363	305.9	305.2	301.2	301.8	26.0	92.9	516.7

A.18 Fins Reverse Data with Argon

P_R (Pa)	ΔP (Pa)	P_i (Pa)	T_{c6} (°C)	T_{c5} (°C)	T_{c4} (°C)	T_{c3} (°C)	T_i (°C)	T_o (°C)	Q (cm^3/s)
219891	103123	220649	258.0	255.0	255.2	255.2	25.0	118.8	799.2
555384	216178	555573	237.5	233.6	234.4	235.4	21.1	85.0	1219.1
328754	141582	328604	223.2	220.4	220.5	221.1	24.2	94.7	969.9
80296	45022	81369	181.7	180.2	180.3	180.7	25.7	103.2	546.1

A.19 Bare Reverse Data with Argon at High Pressure

P_R (Pa)	ΔP (Pa)	P_i (Pa)	T_{c6} (°C)	T_{c5} (°C)	T_{c4} (°C)	T_{c3} (°C)	T_i (°C)	T_o (°C)	Q (cm^3/s)
1370834	21296	1373270	296.9	296.0	291.7	292.0	24.4	70.2	346.0
1346243	30209	1345373	274.7	273.8	269.3	269.2	22.1	57.3	508.8
1351218	61288	1350072	316.0	314.8	309.1	308.4	21.7	53.6	848.3
1348211	43322	1339507	245.4	244.6	240.6	240.6	22.2	49.1	681.5

A.20 Fins Reverse Data with Argon at High Pressure

P_R (Pa)	ΔP (Pa)	P_i (Pa)	T_{c6} (°C)	T_{c5} (°C)	T_{c4} (°C)	T_{c3} (°C)	T_i (°C)	T_o (°C)	Q (cm^3/s)
1359135	38429	1352281	227.3	225.0	224.6	226.2	24.7	98.5	503.0
1366279	56843	1361754	197.0	194.4	194.8	196.4	23.9	79.6	685.4
1355410	81500	1349634	231.6	228.5	228.9	231.3	23.0	85.4	840.4
1363343	26206	1359218	131.2	129.8	130.5	131.6	23.9	67.6	371.5

A.21 HCFP Data with Air [45]

$\dot{m}$ (g/s)	ΔP (Pa)	P_o (Pa)	T_{c0} (°C)	T_{c4} (°C)	T_{c4} (°C)	T_{c8} (°C)	T_{c8} (°C)	T_i (°C)	T_o (°C)
21.7	55296	151685	221.9	223.2	222.8	216.5	218.3	22.0	55.1
8.8	1999	330948	183.1	183.2	183.2	179.9	180.9	22.7	63.0
32.5	86736	275790	259.1	258.2	257.9	243.7	244.3	19.8	51.9

A.22 HEMJ Experiments on the Helium Loop with the Oxy-Acetylene Torch

P_v (Pa)	ΔP (Pa)	P_o (Pa)	T_{c8} (K)	T_{c6} (K)	T_{c4} (K)	T_{c2} (K)	T_i (K)	T_o (K)	T_v (K)	ΔP_v (Pa)
9978567	102779	9828747	727.6	719.9	694.7	687.3	573.5	588.3	300.1	2334
9984519	12913	9948200	543.9	531.4	509.5	503.6	299.1	334.4	299.0	554
1000564	21436	9945653	597.2	584.5	563.0	559.9	374.8	404.9	299.3	741
1003260	36858	9928638	675.5	663.8	647.5	640.2	473.1	498.6	298.7	1018
9728412	59197	9613695	755.1	745.5	727.6	709.2	573.9	595.3	298.6	1350
9910125	34430	9834626	509.9	504.1	481.2	469.2	299.0	322.4	298.9	1475
9908580	57811	9784144	565.2	560.2	537.4	523.0	373.5	393.2	298.8	1992
9951785	22463	9888293	538.2	533.4	495.2	482.3	299.0	328.1	298.9	967
9881462	53707	9760751	721.5	717.0	679.7	659.2	522.8	545.2	298.1	1340
9989591	128049	9741741	689.7	685.5	650.7	633.7	522.1	536.9	298.4	3184
9917703	7947	9866387	566.3	552.0	530.5	515.1	298.8	342.2	297.8	350
9905958	13413	9858941	613.3	599.8	579.2	563.2	373.7	410.0	297.8	480
9985226	23116	9948244	682.7	667.8	658.6	638.4	473.4	502.7	297.4	659
9986007	30749	9898046	766.5	753.2	745.2	724.8	574.0	600.4	297.2	730
9986664	97949	9832994	725.2	713.9	707.2	688.1	575.3	590.2	297.3	2272
9982100	27770	9921173	514.1	502.8	480.5	462.8	298.2	322.8	297.9	1234
1001124	47800	9988994	565.2	552.2	536.1	519.7	373.2	393.6	298.3	1704
1004293	81720	9882967	645.8	633.3	617.5	601.0	473.0	489.9	298.5	2308
1001083	79562	9916526	699.2	687.2	676.7	657.5	522.8	540.8	298.1	2038
1001001	104991	9882109	691.6	680.2	669.6	650.8	524.1	540.0	298.1	2680
1003289	134363	9824458	684.9	674.0	663.7	645.0	524.1	538.3	298.5	3441
9879938	77535	9736510	750.5	740.0	724.0	701.9	572.5	590.9	297.5	1814
9884544	50965	9777705	666.7	655.0	638.9	618.2	472.4	494.7	297.6	1445
9874238	60359	9746097	660.7	649.1	633.6	612.8	473.0	493.4	297.2	1701

A.23 HEMJ Experiments on the Helium Loop with the Induction Heater

P_v (Pa)	ΔP (Pa)	P_o (Pa)	T_{c8} (K)	T_{c6} (K)	T_{c4} (K)	T_{c2} (K)	T_i (K)	T_o (K)	T_v (K)	ΔP_v (Pa)
9862351	15757	9854213	542.611	541.372	554.754	511.851	295.201	333.483	294.393	714
9879137	38069	9824207	473.723	468.580	497.199	457.796	294.427	316.714	294.027	1728
9910615	38350	9860821	479.310	474.653	500.283	464.505	296.289	319.341	295.653	1737
9909881	11356	9889357	530.951	524.798	550.071	514.988	296.226	337.093	295.376	511
9756258	21257	9754338	576.693	572.784	569.160	523.797	294.816	334.489	294.242	964
9756002	10594	9768501	598.752	593.708	588.606	546.674	294.986	346.934	294.308	479
9807200	17938	9773701	626.179	623.798	632.806	569.953	295.811	345.005	294.975	811
9821345	11103	9818969	659.911	657.533	662.373	600.686	295.720	357.408	295.081	499
9843161	16501	9833954	652.311	646.975	663.642	601.054	296.312	352.236	295.816	745

A.23 HEMJ Experiments on the Helium Loop with the Induction Heater Continued

P_v (Pa)	ΔP (Pa)	P_o (Pa)	T_{c8} (K)	T_{c6} (K)	T_{c4} (K)	T_{c2} (K)	T_i (K)	T_o (K)	T_v (K)	ΔP_v (Pa)
9840362	16443	9830026	666.260	660.626	679.908	616.714	296.441	355.631	295.902	742
9893773	48974	9895835	594.021	618.861	610.111	546.386	374.131	402.338	296.046	1770
9873118	17530	9893803	631.336	656.079	645.382	582.708	374.277	420.810	296.082	636
9850675	31305	9834119	633.472	633.805	649.349	596.846	372.871	411.332	296.003	1143
9940803	120082	9778007	643.627	638.157	669.879	640.981	475.189	493.757	297.714	3469
9945854	76977	9896869	673.428	663.984	690.437	669.705	473.696	499.390	297.917	2219
9995570	30654	9951374	761.352	767.602	793.229	759.810	474.116	520.814	297.524	894
9984224	47521	9911051	758.571	759.781	783.736	760.564	473.742	516.506	297.263	1372
9963832	139791	9787075	684.001	697.474	741.771	702.794	520.842	539.954	297.013	3681
9963822	96561	9801727	742.518	754.071	793.024	747.487	522.929	551.699	297.049	2519
9816600	57401	9737149	750.433	762.305	770.399	739.695	522.759	556.661	296.865	1507

A.24 Reference Cases for the HEMP-like Simulations

Case	P_R (Pa)	ΔP (Pa)	P_i (Pa)	T_{c6} (°C)	T_{c5} (°C)	T_{c4} (°C)	T_{c3} (°C)	T_i (°C)	T_o (°C)	Q (cm^3/s)
RC1	624700	198174	612856	134.9	131.8	128.3	131.8	27.1	45.0	1448.6
RC2	145849	57740	143479	117.8	116.3	116.5	115.9	21.6	44.8	816.5
RC3	640393	20853	641581	330.3	329.5	321.5	318.4	26.5	103.7	359.9
RC4	1347534	19121	1356405	302.1	302.6	294.2	295.4	23.5	100.1	316.6

A.25 Reference Cases for the HCFP Simulations

Case	$\dot{m}$ (g/s)	ΔP (Pa)	P_o (Pa)	T_{c0} (°C)	T_{c4} (°C)	T_{c4} (°C)	T_{c8} (°C)	T_{c8} (°C)	T_i (°C)	T_o (°C)
RC5	21.7	55296	151685	221.9	223.2	222.8	216.5	218.3	22.0	55.1

APPENDIX B: MATERIAL PROPERTIES

Many of the materials in this work are evaluated over a wide range of temperatures. As such, it is imperative to include temperature dependent properties in the calculations. The properties for the coolants and the solid materials used in this work were compiled from a number of different sources in the literature and are summarized below.

B.1 Coolant Properties

Three coolants were used in the experiments: air, helium, and argon. For the once-through experiments, pressure was limited to <1.4 MPa therefore effects in the properties from varying pressure were negligible. Experiments using the helium loop were conducted at pressures up to 10 MPa, but the variation in helium's properties between atmospheric pressure and 10 MPa is also negligible. Therefore, properties were only evaluated based on their temperature.

The properties for air, helium and argon were evaluated from Table 12, Table 13, and Table 14, respectively. Linear interpolation was utilized for temperature values that fall between available temperatures in the tables.

Table 12. Temperature dependent properties for air [15]

T (°C)	c_P (J/kg·K)	μ (μPa·s)	k (W/m·K)
250	1006	16	0.0223
300	1007	18.5	0.0263
350	1009	20.8	0.03
400	1014	23	0.0338
450	1021	25.1	0.0373
500	1030	27	0.0407

Table 13. Temperature dependent properties for helium [76]

T (°C)	c_P (J/kg·K)	μ (μPa·s)	k (W/m·K)
275	5193.00	18.78	0.147
300	5192.99	19.93	0.156

Table 13 Continued. Temperature dependent properties for helium [76]

T (°C)	c_P (J/kg·K)	μ (μPa·s)	k (W/m·K)
325	5192.98	21.05	0.165
350	5192.98	22.15	0.174
375	5192.98	23.23	0.182
400	5192.98	24.29	0.190
425	5192.98	25.33	0.199
450	5192.98	26.36	0.207
475	5192.98	27.37	0.215
500	5192.98	28.36	0.222
525	5192.99	29.34	0.230
550	5192.99	30.31	0.238
575	5192.99	31.27	0.245
600	5192.99	32.22	0.252
625	5192.99	33.15	0.260
650	5193.00	34.07	0.267
675	5193.00	34.99	0.274
700	5193.00	35.89	0.281
725	5193.00	36.79	0.288
750	5193.00	37.68	0.295
775	5193.01	38.56	0.302
800	5193.01	39.43	0.309
825	5193.01	40.30	0.315
850	5193.01	41.15	0.322
875	5193.01	42.00	0.328
900	5193.02	42.85	0.335
925	5193.02	43.68	0.341
950	5193.02	44.52	0.348
975	5193.02	45.34	0.354
1000	5193.02	46.16	0.361
1025	5193.02	46.97	0.367
1050	5193.02	47.78	0.373
1075	5193.02	48.58	0.379
1100	5193.03	49.38	0.385

Table 14. Temperature dependent properties for argon [76]

T (°C)	c_P (J/kg·K)	μ (μPa·s)	k (W/m·K)
280	521.76	21.40	0.0167
300	521.54	22.70	0.0177
320	521.36	23.90	0.0187
340	521.22	25.10	0.0196
360	521.11	26.30	0.0206
380	521.02	27.50	0.0215
400	520.94	28.60	0.0224
420	520.87	29.70	0.0232
440	520.82	30.80	0.0241
460	520.77	31.90	0.0249

Table 14 Continued. Temperature dependent properties for argon [76]

T (°C)	c_P (J/kg·K)	μ (μPa·s)	k (W/m·K)
480	520.73	33.00	0.0257
500	520.69	34.00	0.0265

The specific ideal gas constant for each of the three coolants is given in Table 15.

Table 15. Specific ideal gas constants for air, helium, and argon

Coolant	$\Re$ (J/kg·K)
air	287.0
He	2077.1
Ar	208.2

B.2 Test Section Material Properties

Four test section materials were included in this work: C36000 brass, AISI 1018 carbon steel, the tungsten alloy WL10, and the tungsten alloy MT-185. Since only steady-state experiments and simulations were performed, the only relevant property for each test section was the thermal conductivity. For C36000 brass, AISI 1018 carbon steel, and WL10, discrete thermal conductivity data were gathered from the literature and fit using a polynomial or a power law.

The brass alloy, C36000, was fit to the data plotted in Figure 87 with the following equation:

$$k_s(T) = 11.661 \cdot T^{0.4006} \tag{87}$$

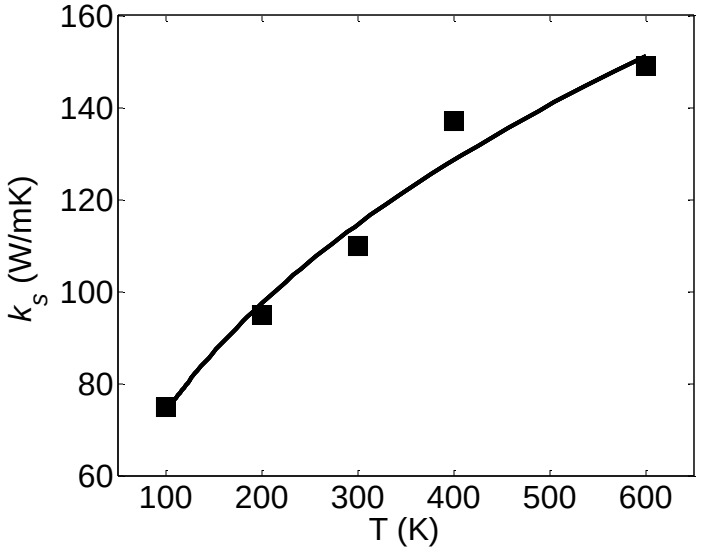

Figure 87. Thermal conductivity data with varying temperature for brass alloy [15] and power law fit

The steel alloy, AISI 1018, was fit to the data plotted in Figure 88 with the following linear equation:

$$k_s(T) = -0.0496 \cdot T + 77.47 \tag{88}$$

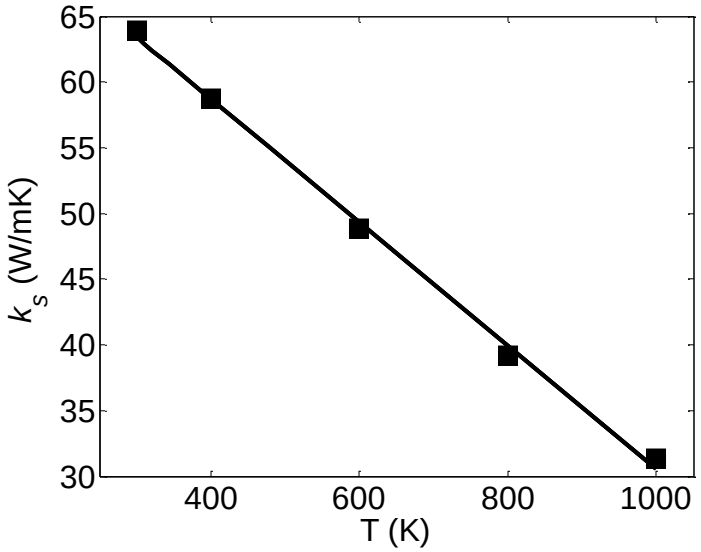

Figure 88. Thermal conductivity data with varying temperature for steel alloy [15] and a linear fit

The tungsten alloy, WL10, was fit to the data plotted in Figure 89 with the following second order polynomial:

$$k_s(T) = -3.372 \times 10^{-5} \cdot T^2 - 0.1143 \cdot T + 206.8 \tag{89}$$

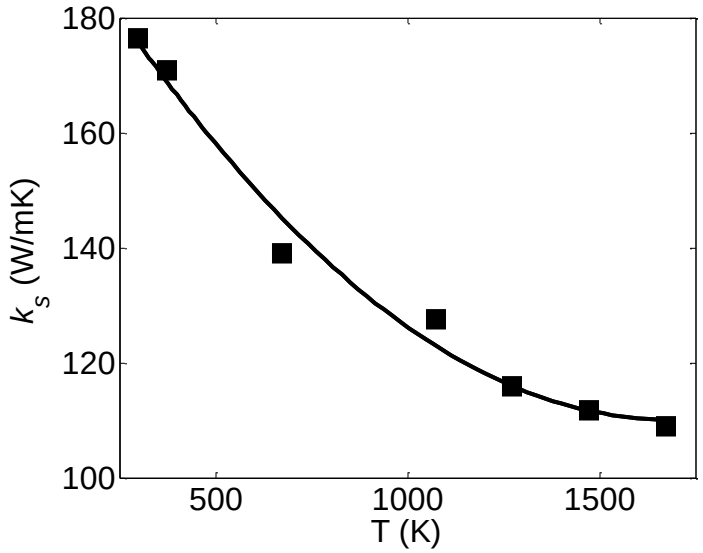

Figure 89. Thermal conductivity data with varying temperature for WL10 [77] and a second order polynomial fit

Measurements for the thermal conductivity of the tungsten alloy, MT-185, were taken at Oak Ridge National Laboratory using the laser-flash method. Small thin samples from the MT-185 rod used to construct the test sections were cut using wire EDM for the measurements. The specific heat c_P and the thermal diffusivity α were each measured separately with respect to temperature. For each discrete temperature in which α was measured, the c_P at a corresponding temperature was selected from the measured data and k_s was calculated with the following equation:

$$k_s = \alpha \rho c_P \tag{90}$$

where $\rho =$ 18.5 g/cm^3 was the density of MT-185 (changes in volume with temperature were deemed negligible). The calculated data for k_s is plotted in Figure 90 with the following third order polynomial:

$$k_s(T) = 5.325\text{e-}8 \cdot T^3 - 1.261\text{e-}4 \cdot T^2 + 0.105 \cdot T + 58.36 \quad (91)$$

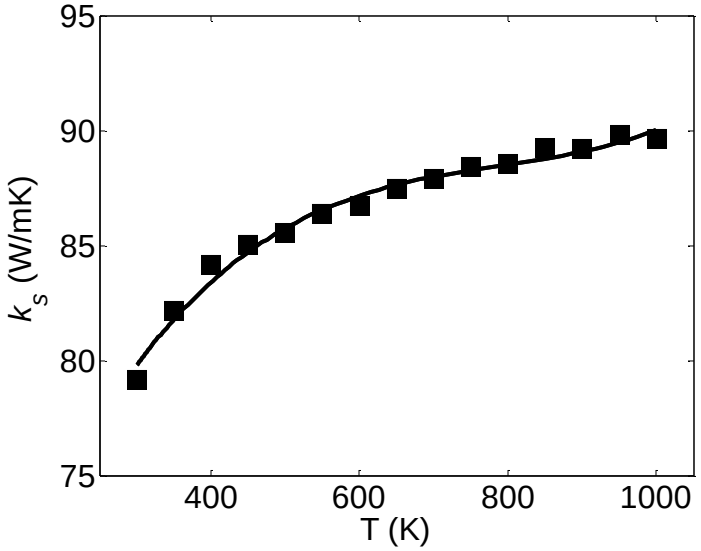

Figure 90. Thermal conductivity data measured at ORNL with varying temperature for MT-185 and a third order polynomial fit

APPENDIX C: UNCERTAINTY ANALYSIS

As with all experimental analysis, it is imperative to estimate the uncertainty in each measurement and propagate that uncertainty through the calculations. This appendix summarizes the uncertainty in the instruments, the material properties, and the dimensions used in these experiments. Then, the method for propagating the uncertainty through to the Nusselt number and loss coefficient correlations is explained in accordance with the procedure described in the references [78,79]. An example is also provided.

C.1 Uncertainty in the Instruments

Table 16 lists the instruments used in this experiment and their corresponding uncertainty. The uncertainty in analog instruments is half of the resolution of the instrument, and the uncertainty in the digital instruments is specified by the manufacturer.

Table 16. Experimental uncertainty in the instruments used in all experiments

Instrument	Uncertainty	Units
Omega Type-E TC Probe	1.0 (≤250°C) $0.004 \cdot T$ (<250°C)	°C
Brooks 1110 Rotameter	1.180×10^{-5}	m^3/s
Omega PX302-2KGV	34474	Pa
Omega PX302-300AV	5170	Pa
Omega PX180-060DV	1241	Pa
Omega PX26-100DV	1723	Pa
Omega PX26-30DV	517	Pa
Omega Type-K TC Probe	1.1 (≤275°C) $0.004 \cdot T$ (<275°C)	°C
Omega PX309-2KGI	34474	Pa
Rosemount 1151DP3E22	12	Pa
Rosemount 1151 DP5S22	329	Pa
Omega P-L-A-1/8-6-0-TS-8 RTD	$0.15+0.002 \cdot T$	°C

C.2 Uncertainty in the Material Properties

The uncertainty in the material properties was either specified in the source or approximated with a conservative assumption. The uncertainties used in the calculations here are summarized in Table 17.

Table 17. Uncertainty in the material properties used in the calculations

Material/Coolant	Property	Uncertainty (%)
Air	μ	5
	$\overline{c_p}$	5
	k	5
Helium [76]	μ	10
	$\overline{c_p}$	5
	k	5
Argon [76]	μ	2

Table 17 Continued. Uncertainty in the material properties used in the calculations

Material/Coolant	Property	Uncertainty (%)
Argon [76]	$\overline{c_P}$	0.3
	k	2.2
C36000 Brass	k_s	5
AISI 1018 Steel	k_s	5
MT-185	k_s	5

C.3 Uncertainty in the Dimensions

The uncertainty in the dimensions used in the calculations is summarized in Table 18. The geometrical uncertainty is the smallest contribution to the overall uncertainty in the experimental results.

Table 18. Uncertainty in the dimensions

Dimension	Uncertainty	Units
A_c (HEMP)	0.7	mm^2
A_h (HEMP)	1.0	mm^2
A_c (HEMJ)	1.3	mm^2
A_h (HEMJ)	2	mm^2
D_j	0.05	mm
D_o	0.05	mm
δ_{TC}	0.1	mm

C.4 Propagation of Uncertainty

For a value $R = f(x_1, x_2, ..., x_L)$, the most probable estimate of the uncertainty U_R is generally accepted to be root squared sum of the uncertainty for each

independent variable multiplied by a sensitivity index [79]. The sensitivity index in this case is simply $\partial R/\partial x_i$ where $i = 1, 2, \ldots, L$. That is:

$$U_R(x_1, x_2, ..., x_L) = \pm\sqrt{\sum_{i=1}^{L}\left(U_{x_i}\frac{\partial R}{\partial x_i}\right)^2} \tag{92}$$

where U_{x_i} is the uncertainty in the independent variable x_i. It is important to emphasize this is only an estimate of the uncertainty derived from truncated Taylor series expansion of $R = f(x_1, x_2, ..., x_L)$. This also ignores any covariant variables, but these do not appear in this analysis.

As an example, the uncertainty in the Reynolds number Re, U_{Re}, is calculated for Reference Case #1 (Appendix A). First, the density at the exit of the Rotameter ρ_R is calculated using the ideal gas law. For brevity, $\rho_R =$ 1.16 kg/m^3 and $U_{\rho_R} =$ ± 0.055 kg/m^3. Then, the mass flow rate $\dot{m}$ is computed as follows (see Appendix D, $\rho_c =$ 1.20 kg/m^3):

$$\dot{m} = Q\sqrt{\rho_c \rho_R} \tag{93}$$

$$U_{\dot{m}} = \sqrt{\left(U_Q\left(\sqrt{\rho_c \rho_R}\right)\right)^2 + \left(U_{\rho_R}\left(\frac{Q\rho_c}{2\sqrt{\rho_c \rho_R}}\right)\right)^2} \tag{94}$$

$$\dot{m} = 1.71 \text{ g/s}$$

$$U_{\dot{m}} = \pm 0.043 \text{ g/s}$$

Now, the Reynolds number Re is calculated using Eq. 27 where the uncertainty in the port diameter $U_{D_j} =$ ± 0.05 mm and an uncertainty of 10% is assumed for the viscosity U_μ:

$$Re = \frac{4\dot{m}}{\pi D_j \mu} \tag{95}$$

$$U_{Re} = \sqrt{\left(U_{\dot{m}}\left(\frac{4}{\pi D_j \mu}\right)\right)^2 + \left(U_{D_j}\left(\frac{4\dot{m}}{\pi {D_j}^2 \mu}\right)\right)^2 + \left(U_\mu\left(\frac{4\dot{m}}{\pi D_j \mu^2}\right)\right)^2} \tag{96}$$

$$Re = 54704$$

$$U_{Re} = \pm 5804$$

APPENDIX D: MASS FLOW RATE MEASUREMENTS USING A ROTAMETER

For the HEMP-like experiments conducted in this work, a variable area Rotameter (Brooks 1110) was used to measure the volumetric flow rate. In its simplest form, a Rotameter is a tube, usually transparent, with a increasing cross sectional area from the bottom to the top. A float inside the tube indicates the volumetric flow rate versus a calibrated linear scale printed on the tube. The density of the coolant is then measured at the exit of the Rotameter, and the mass flow rate is calculated. The advantages of a Rotameter are its simplicity and low cost, but it must be oriented vertically and is sensitive to the temperature of the coolant (since the viscosity of the coolant changes with temperature). The scale is typically calibrated for a single temperature. For the experiments conducted in this work, the inlet temperatures did not significantly vary from the calibrated temperature.

To accurately measure the mass flow rate of different coolants at a variety of pressures using a variable area Rotameter requires that minor corrections are made to its calibrated scale. The volumetric flow rate through a Rotameter can be calculated from a force balance on the float itself. The resulting equation is as follows [58]:

$$Q = CA_T \sqrt{\frac{2g\left(m_F - \rho V_F\right)}{A_F \rho}} \tag{97}$$

where C is a discharge coefficient specified for the Rotameter, A_T is the annular cross sectional area between the float and the tube, V_F, m_F, A_F are the volume, mass and cross sectional area of the float, respectively, and ρ is the coolant density. It is assumed that the steel float is significantly more dense than the gas coolant (not necessarily the case for liquids) and therefore the contribution of ρV_F is negligible. The equation then simplifies to:

$$Q = CA_T \sqrt{\frac{2gm_F}{\rho A_F}} \tag{98}$$

The actual volumetric flow rate Q_a is then calculated using a Rotameter scale that is calibrated for a volumetric flow rate Q_c at a specific pressure. Based upon the above equation, the volumetric flow rate is inversely proportional to the square root of the density of the gas. As a result, the following equality can be formed for a given float position:

$$Q_a \sqrt{\rho_a} = Q_c \sqrt{\rho_c} \tag{99}$$

$$Q_a = Q_c \frac{\sqrt{\rho_c}}{\sqrt{\rho_a}} = Q_c \frac{\sqrt{\rho_c}}{\sqrt{\rho_R}} \tag{100}$$

where $\rho_c = 1.20$ kg/m^3 is the calibrated density for this Rotameter using air at 101.3 kPa and 21.1 °C, and $\rho_a = \rho_R$ is the actual measured density at the exit of the Rotameter. Finally, the mass flow rate is calculated as follows:

$$\dot{m} = \rho_R Q_a = Q_c \sqrt{\rho_R \rho_c} \tag{101}$$

APPENDIX E: PEER-REVIEWED PUBLICATIONS

A large portion of this work has resulted in peer-reviewed publications as conference papers and journal articles. Two peer-reviewed conference papers were featured at the Technology on Fusion Energy (TOFE) conference in 2010 and 2012 as oral presentations, and the conference paper presented in 2010 earned the Best Student Paper Award. A journal article was published in 2012 in Fusion Science and Technology. The publications are included in this appendix as they appeared in the journals. This author also contributed to other closely related publications as a co-author and they are also listed below (but not included).

E.1 Peer-Reviewed Publications as First Author

- B. H. Mills, J. D. Rader, D. L. Sadowski, M. Yoda, and S. I. Abdel-Khalik, "Experimental Investigation of Fin Enhancement for Gas-Cooled Divertor Concepts," in *Technology of Fusion Energy*, vol. 60, Las Vegas, 2011, pp. 191-195.
- B. H. Mills, J. D. Rader, D. L. Sadowski, M. Yoda, and S. I. Abdel-Khalik, "Dynamically Similar Studies of the Thermal Performance of Helium-Cooled Finger-Type Divertors With and Without Fins," *Fusion Science and Technology*, vol. 62, pp. 379-388, Nov 2012.
- B. H. Mills, Rader J. D., D. L. Sadowski, M. Yoda, and S. I. Abdel-Khalik, "An Experimental Study of the Effects of the Solid-to-Coolant Thermal Conductivity Ratio in Helium-Cooled Divertor Modules," *Fusion Science and Technology*, vol. 64, pp. 670-674, September 2013.

E.2 Co-Authored Peer-Reviewed Publications

- J. D. Rader, B. H. Mills, D. L. Sadowski, M. Yoda, and S. I. Abdel-Khalik, "Experimental and Numerical Investigation of Thermal Performance of Gas-cooled Jet-Impingment Finger-type Divertor Concept," *Fusion Science and Technology*, vol. 60, pp. 223-227, July 2011.
- J. D. Rader, B. H. Mills, D. L. Sadowski, M. Yoda, and S. I. Abdel-Khalik, "Optimization of Pin-fin Arrays for Helium-cooled Finger-type Divertor," *Fusion Science and Technology*, vol. 64, pp. 315-319, August 2013.
- J. D. Rader, B. H. Mills, D. L. Sadowski, M. Yoda, and S. I. Abdel-Khalik, "Verification of thermal performance predictions of prototypical multi-jet impingement helium-cooled divertor module," *Fusion Science and Technology*, vol. 64, pp. 282-287, August 2013.

EXPERIMENTAL INVESTIGATION OF FIN ENHANCEMENT FOR GAS-COOLED DIVERTOR CONCEPTS

B. H. Mills, J. D. Rader, D. L. Sadowski, S. I. Abdel-Khalik and M. Yoda

G. W. Woodruff School of Mechanical Engineering, Georgia Institute of Technology, Atlanta, GA 30332–0405 USA
bmills@gatech.edu

The addition of fins to the cooled surface of gas-cooled divertor modules has been proposed as a means to enhance their thermal performance, in the HEMP concept, for example. Such fins enhance heat transfer by significantly increasing the surface area over which convection occurs. However, adding fins also increases pressure losses and manufacturing costs and can adversely affect coolant flow over the cooled surface. More importantly, the high heat transfer coefficients expected with helium (He) cooling may significantly lower the fin efficiency, thereby limiting the extent of heat transfer enhancement to values well below the increase in the area ratio. An experimental investigation was undertaken to quantify the extent of heat transfer enhancement and corresponding pressure loss increase associated with the addition of pin fins to the cooled surface of a modular, helium-cooled, finger-type divertor. Four test cases, including configurations similar to the HEMP and HEMJ concepts, were studied. The results show that the addition of fins to helium jet-cooled finger divertors may not provide enough heat transfer enhancement to justify the associated increases in design complexity and pressure loss. Generalized charts for the thermal performance of helium-cooled divertors have been developed; these allow the designers to estimate the maximum allowable heat flux and corresponding pressure drop for a specified set of operating conditions and maximum operating temperature.

I. INTRODUCTION

The thermal-hydraulic and thermo-mechanical performance of a number of helium-cooled divertor designs, including the T-Tube,[1] the HEMJ (Refs. 1-4), the He-cooled flat plate (HCFP) (Refs. 5-7), and the He-cooled modular design with integrated pin array (HEMP) (Refs. 8,9) have been investigated as part of the ARIES research program and other fusion studies. Except for the HEMP design, these divertor module designs rely on jet impingement to safely accommodate the high heat fluxes (~10 MW/m^2) expected in a magnetic fusion energy reactor.

For the HEMP concept, heat transfer is enhanced by passing He across an array of pin fins. Design studies[8] and material analyses[9] suggest that the HEMP design can withstand up to 15 MW/m^2 on its plasma-facing surface, although the results have not been experimentally validated. Recent experiments[6] have verified that the addition of pin fins improves the thermal performance of the jet-cooled HCFP design.[7] However, the fins also increase manufacturing complexity and pressure drop.

The objective of this paper is to experimentally evaluate how the addition of pin fins affects the thermal-hydraulic performance of modular finger-type divertor designs similar to HEMP and the HEMJ. To quantify these effects, baseline geometries without pin fins were also experimentally studied.

Prototypes of finger-type modules with and without pin fins were designed and instrumented. Experiments were conducted using air over a wide range of parameters that span the expected non-dimensional parameters at prototypical operating conditions. The thermal performance was quantified in terms of the heat transfer coefficients (HTC), estimates of the maximum heat flux q''_{max} that can be accommodated by the various geometries when helium is used as the coolant, the corresponding pressure loss coefficients, and the fraction of total incident power required for pumping the coolant.

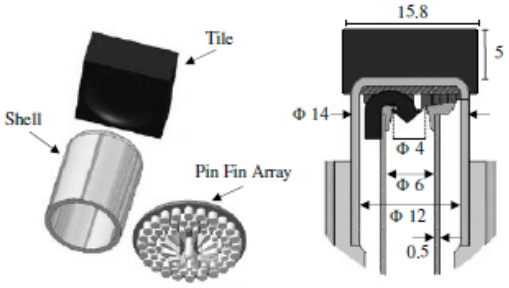

Fig. 1. Sketch[9] (left) and a radial cross-section[8] (right) of the HEMP divertor. All dimensions are in mm.

II. THE HEMP AND HEMJ DIVERTORS

The HEMP finger-type divertor module (Fig. 1) (Refs. 8,9) consists of a plasma-facing surface comprised of a 5 mm thick 15.8 mm square tungsten (W) tile brazed to a W-1%La_2O_3 shell. Helium at 600 °C and 10 MPa flows through a 2.5 mm wide annular gap inside the shell, turns 90° and flows radially through an array of pin fins of varying geometry, then again turns 90° and exits at the center of the module at ~700 °C. The initial design studies showed that the pumping power required to overcome the pressure drop across the module was less than 5% of the total incident power. In addition, HEMP was shown to withstand heat fluxes up to 15 MW/m^2 without exceeding the maximum recommended operating temperature of W-1%La_2O_3, 1200 °C (Ref. 9).

The HEMJ concept[4] also uses a finger-type configuration similar to that of HEMP, but uses instead the impingement of an array of 25 jets to cool the plasma-facing surface. Helium enters the inner tube at 634 °C and 10 MPa, then exits through an array of round holes impinging onto the inner surface of a hexagonal W tile 20.6 mm across brazed onto a W alloy endcap. After impingement, the He turns 90° and exits through the 0.9 mm gap between the inner tube and endcap. HEMJ can accommodate heat fluxes of 10 MW/m^2, without exceeding the maximum recommended temperature for the endcap of 1300 °C. Although both the HEMP and HEMJ concepts can accommodate high heat fluxes of at least 10 MW/m^2, they have the disadvantage that a large number (~10^5) of modules are required to cover a divertor area of O(100 m^2).

III. EXPERIMENT

The test section used to simulate the modular finger divertor (Fig. 2) consists of an inner tube of OD 8 mm and ID 5.8 mm centered within a cylindrical outer shell of OD 12 mm and ID 10 mm by an insulating polyetherimide ring, and a manifold that supplies the coolant. The inner tube had an endcap 1 mm thick with a D_o = 2 mm diameter port in the center, while the outer shell had a 6 mm thick endcap. The radial gap between the inner tube and outer shell was 1 mm, while the axial gap between their endcaps was 2 mm. Two different outer shells, one where the inner surface of the shell endcap was covered with a hexagonal array of 48 cylindrical pin fins and one with no fins, were fabricated. The pin fins had a diameter and length of 1 mm and 2 mm, respectively with a pitch of 1.2 mm and were formed by electro-discharge machining. For the surface with the fin array, the fins contacted the inner tube, but machining imperfections and misalignment prevented perfect contact between the fin tips and the inner tube endcap. Unless otherwise specified, all components were made from brass C36000 alloy, which has a thermal conductivity under experimental conditions nearly equal to that for W-1%La_2O_3 at prototypical conditions. The brass finger was then insulated with Marinite blocks and fitted with a ceramic sleeve to protect instrumentation.

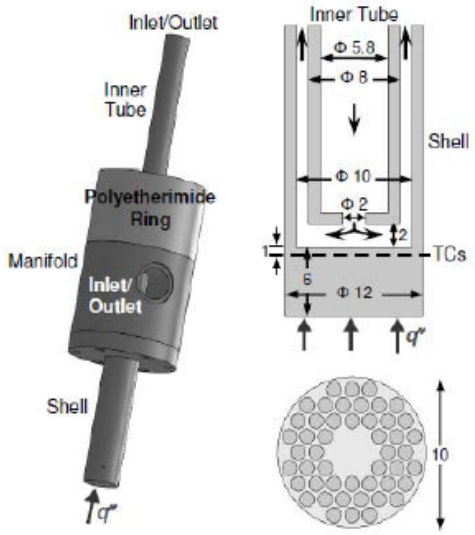

Fig. 2. Sketch (left), radial cross section with arrows indicating the flow direction for the forward flow case (upper right), and top view of the pin fin array covering the inside of the cooled surface (lower right). All dimensions are in mm.

Air supplied by a compressed air-line flows through the test section, and is then discharged into a fume hood. Two different flow types were studied, namely "forward flow" and "reverse flow." In forward flow, jet impingement cooling is utilized where the coolant flows out the 2 mm diameter port in the inner tube endcap at average speeds $\overline{V}_o$ = 75-175 m/s, impinges upon the inner surface of the outer shell endcap, flows radially outwards and exits along the annular gap between the sides of the inner tube and the outer shell. In reverse flow, air flows through the annular gap first, flows radially inwards along the inner surface of the outer shell endcap and exits through the port in the center of the inner tube. These two different flows through the two different test sections (with and without the pin fins) gave four different experimental cases: 1) forward flow without fins; 2) forward flow with fins; 3) reverse flow without fins; and 4) reverse flow with fins. In terms of the cooling approaches used, the last configuration is similar to HEMP, while the first configuration is similar to the HEMJ design, albeit with only one central jet (*vs.* an array of jets) and more than twice the gap width. We refer to

these two configurations, for lack of better terms, as "HEMP-like" and "HEMJ-like."

The flame from an oxy-acetylene torch was used to simulate the incident heat flux on the divertor module by impinging directly on the outside of the outer shell endcap. The temperature distributions near the cooled inner surface of the shell endcap were measured by four type-E thermocouples (TCs) embedded 1 mm from the cooled surface at radial distances of 0, 1, 2, and 3 mm from the shell axis (azimuthally spaced by 90°).

The test conditions studied here were chosen to span the most important thermal-hydraulic dimensionless group, namely the Reynolds number Re, for prototypical conditions. Here, $Re = 4\dot{m}/(\pi D_o \mu_o)$ where $\dot{m}$ is the coolant mass flow rate, and μ_o is the coolant dynamic viscosity at the central port in the inner tube endcap. For the forward flow cases, μ_o was taken to be the viscosity at inlet conditions; for the reverse flow cases, it was taken to be that at exit conditions. Based on the operating conditions for HEMP with an incident heat flux of 10 MW/m^2 and a He temperature rise from 600 °C at the inlet to 700 °C at the outlet, an energy balance gives a nominal coolant mass flow rate $\dot{m}_{He}$ = 4.81 g/s per module; the corresponding Re for the reverse flow (with or without pins) cases is 7.0×10^4. For the forward flow cases, however, the nominal Re = 7.6×10^4 because μ is based on the (cooler) conditions at the central port. The experiments conducted in this investigation covered the range $Re = 8\times10^3$–1.1×10^5, thereby spanning the expected nominal conditions.

The coolant mass flow rate through the test section was measured by a Rotameter (Brooks R8M-25-4) upstream of the test section. The pressure at the Rotameter and the test section inlet were measured by pressure gauges (Omega PX180-060DV); the pressure drop across the test section was measured by a differential pressure transducer (Omega PX26-030DV). Coolant temperatures at the inlet and exit of the test section T_i and T_e, respectively, were measured by two type-E TCs.

The heat transfer rate from the flame to the test section was determined using a control-volume energy balance and the coolant enthalpies at the test section inlet and exit. The average heat flux incident upon the test section $\overline{q}''$ was calculated by dividing this heat transfer rate by the heated area of the outer surface of the shell endcap A = 113 mm^2. Although steady-state heat fluxes as high as 2 MW/m^2 were achieved with the torch, most of the experiments were performed at $\overline{q}'' \le 1.3$ MW/m^2 to limit damage to the test section.

IV. EXPERIMENTAL RESULTS

The area-averaged temperature of the cooled surface T_c was calculated from the four TC measurements extrapolated to temperatures on the cooled surface assuming conduction through 1 mm of brass alloy. In all cases, the standard deviation in the surface temperature values was no more than 3.8 °C. The *effective* HTC is then:

$$h_{eff} \equiv \frac{\overline{q}''}{T_c - T_i}\frac{A}{A_c} \qquad (1)$$

where A_c = 78.5 mm^2 is the area of the (cooled) inner surface of the shell endcap.

Strictly speaking, h_{eff} is the HTC required for a surface without fins to have the same T_c when subject to $\overline{q}''$. So for the test section without fins, the *actual* HTC $h_{act} = h_{eff}$. However, for the test section with fins, h_{eff} must be corrected for the nonuniform temperatures over the surface of the pin fins by an average fin efficiency η.

$$h_{eff} A_c = h_{act}(A_p + \eta A_f) \qquad (2)$$

where A_p = 40.8 mm^2 is the area of the cooled base surface between the fins, and A_f = 314 mm^2 is the surface area of the fins exposed to coolant.

To determine η, an adiabatic boundary condition was assumed over the fin tip because of the presence of a small air gap between the fin and the inner tube endcap and the fact that air is a relatively poor thermal conductor. The average fin efficiency was then taken to be:

$$\eta = \frac{\tanh(\alpha)}{\alpha} \quad \text{where} \quad \alpha \equiv L_f\sqrt{\frac{4h_{act}}{k_f D_f}} \qquad (3)$$

Here, L_f, D_f and k_f are the fin length, diameter, and thermal conductivity, respectively.[10] Note that η decreases as h_{act} increases. Since η depends upon h_{act}, determining the actual HTC and fin efficiency required an iterative solution.

Figure 3 presents h_{eff} and h_{act} as a function of Re with air as the coolant for the four configurations tested. Results are presented for each configuration at $\overline{q}''$ = 0.3 and 1.3 MW/m^2; the HTC values appear to be essentially independent of incident heat flux within this range. The maximum uncertainties in Re and h_{eff} based on measurement errors were 6% and 15%, respectively. For a given flow direction, the cases with fins have significantly larger h_{eff} than the cases without fins. However, the fin cases have a significantly lower h_{act} than the cases without fins. This result suggests that the improvement in effective HTC is due to the fins increasing the cooled surface area (the total area of the surface with fins is 355 mm^2, or ~4.5 A_c). Overall, the HEMP-like case (▲) has the largest h_{eff}, while the HEMJ-like case (■) has the largest h_{act}. The decrease in h_{act} for surfaces with fins compared to surfaces without fins was very large for forward flow, suggesting that the benefits of jet impingement are reduced due to the presence of the fins.

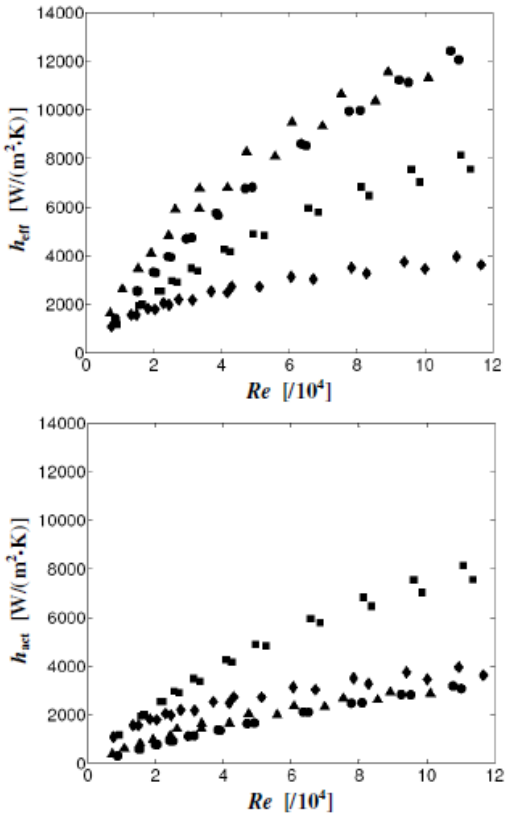

Fig. 3. Effective (top) and actual HTCs (bottom) as a function of *Re* for forward flow without fins (■), forward flow with fins (●), reverse flow without fins (◆), and reverse flow with fins (▲).

The measured pressure drops across the test section Δp were used to determine loss coefficients:

$$K_L = \frac{\Delta p}{\rho_o \bar{V}_o^2 / 2} \qquad (4)$$

based on the density ρ_o and average speed $\bar{V}_o$ of the air at the central port in the inner tube. Figure 4 shows K_L as a function of *Re* for all four tested configurations. Over the range of prototypical *Re*, the forward flow cases have the highest K_L, and fins, as expected, increase the loss coefficient for a given flow direction. For the HEMP-like case (▲), K_L decreases as *Re* increases, presumably due to changes in the flow between the fins. Numerical simulations of the flow through the fin array to understand this unusual behavior are underway.

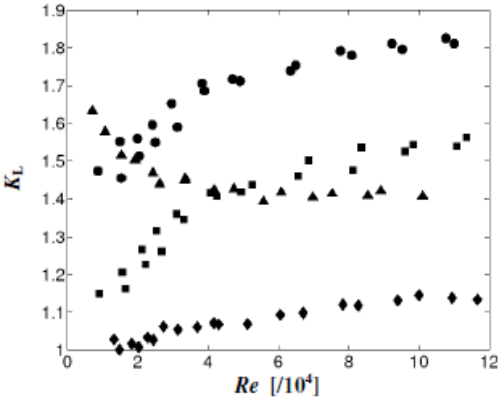

Fig. 4. Loss coefficient as a function of *Re*. The symbols are the same as those for the previous Figure.

V. PROTOTYPICAL CONDITIONS

Using dynamic similarity, the data obtained for air at near-room temperatures, can be extrapolated to prototypical conditions for He at 600 °C and 10 MPa at $\overline{q''}$ = 10 MW/m^2. Determining the actual HTC for He h_{act}^{He} for all cases simply entails correcting for the different thermal conductivities k of the two coolants, since the Nusselt number is expected to be the same for dynamically-similar conditions: $h_{act}^{He} = (k_{He} / k_{air}) h_{act}$. To determine h_{eff}^{He} for the cases with fins, Eqs. (2) and (3) were solved iteratively (since the thermal conductivity of W-1%La_2O_3 varies with *T*).

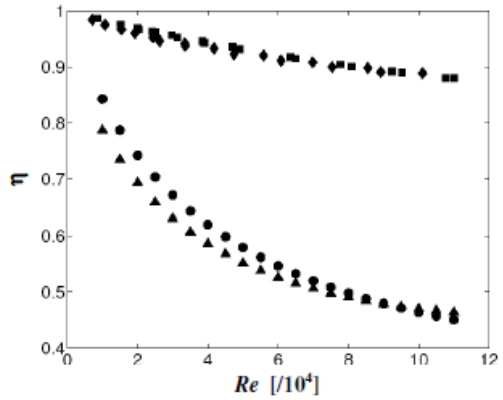

Fig. 5. Average fin efficiency η as a function of *Re* for air in forward flow (■) and reverse flow (◆) and He in forward flow (●) and reverse flow (▲).

Figure 5 shows η for air and He as a function of *Re* for forward and reverse flows. As expected, at a given *Re*, the fin efficiency for He is less than that for air. At $Re = 7.0\times10^4 - 7.6\times10^4$, $\eta = 50-55\%$ for He, *vs.* >90% for air because of the higher HTC in the He cases (*cf.* Eq. 3). This result suggests that pin fins could potentially reduce, *vs.* enhance, thermal performance when compared with their bare counterpart if the increase in cooled area was not sufficient to overcome the detriment in performance from the presence of the fins (h_{act}^{He} with fins < h_{act}^{He} without fins for a given flow direction).

For a given value of the maximum allowable temperature, the values for h_{eff}^{He} and η at prototypical conditions can be used to estimate the maximum heat flux q''_{max} that can be accommodated by the four flow/divertor configurations:

$$q''_{max} = \frac{T_s - T_{in}}{R_T} \qquad (5)$$

where T_{in} = 600 °C. The total thermal resistance due to convection to the cooled surface and conduction through the pressure boundary

$$R_T = \frac{A}{h_{eff}^{He} A_c} + \frac{\delta_p}{k_p} \qquad (6)$$

where δ_p = 1 mm and k_P were the thickness and thermal conductivity of the W-1%La_2O_3 pressure boundary.

The loss coefficient was used to estimate the fraction of the total power β required to pump the He and hence cool the divertor. For dynamically similar conditions, the loss coefficient should be the same for both air and helium, *i.e.*, the loss coefficient should be a function of only the geometry and *Re*. The pressure drop for He under prototypical conditions Δp_{He} was first determined from K_L using the density and average speed of the He (600 °C, 10 MPa) at the central port in the inner tube. The corresponding pumping power was then determined: $\dot{W}_{He} = \dot{m}_{He}\,\Delta p_{He} / \overline{\rho}_{He}$, where $\overline{\rho}_{He}$ is the average of the He densities at the test section inlet and outlet. Finally, the pumping power as a fraction of the total thermal power incident on the divertor:

$$\beta = \frac{\dot{W}_{He}}{q'' A} \qquad (7)$$

Figure 6 shows q''_{max}, the maximum heat flux that can be accommodated by the four divertor/flow configurations, extrapolated to He at a surface temperature T_s = 1200 °C as a function of *Re* for all four configurations. At prototypical *Re*, all four configurations can accommodate at least 13 MW/m^2, although the reverse flow without fins case (◆) has the worst thermal performance. The remaining three configurations can all accommodate approximately 22 MW/m^2. The HEMJ-like case (■) has a slightly better thermal performance than either the HEMP-like case (▲) or the forward flow case with fins (●). Given the high pressure drops associated with the forward flow with fins case (*cf.* Fig. 4), this divertor/flow configuration, as well as the reverse flow without fins case, were both eliminated from further consideration.

It should be noted that the heat flux values shown in Figure 6 correspond to those incident on the finger module itself (based on the area of the outer surface of the shell endcap A = 113 mm^2), rather than that incident on the W tile facing the plasma. The values shown in the Figure should be reduced by the area ratio (typically a factor of two; *cf.* Fig. 7) between the tile and the finger to determine the maximum allowable heat flux on the plasma-facing surface.

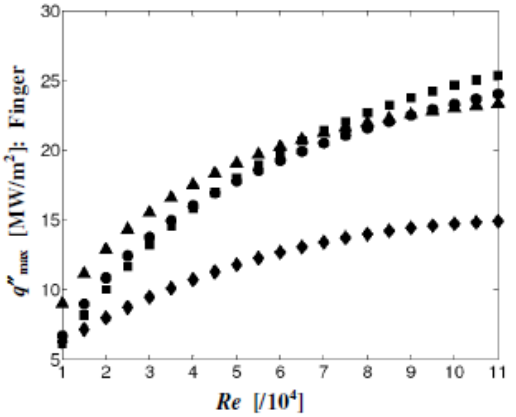

Fig. 6. Maximum heat flux incident on the outer surface of the finger module for He at T_s = 1200 °C as a function of *Re* for forward flow without fins (■), forward flow with fins (●), reverse flow without fins (◆), and reverse flow with fins (▲).

For reverse flow with no jet impingement cooling, pins greatly enhance thermal performance, as expected (▲ *vs.* ◆). For forward flow, pins actually reduce the thermal performance of the design for $Re > 4.7\times10^4$ (● *vs.* ■), suggesting that fins offer little, if any, additional benefit over jet impingement at higher coolant flow rates. This observation is consistent with experimental studies showing that the thermal performance of a plate-type divertor was significantly improved by adding an array of pin at lower *Re*, where $Re = 1\times10^4$ to 4.5×10^4, with an increase in q''_{max} as great as 34%.[6] Doubtless differences in the characteristics of the fin array and the geometry of divertor also determine the effectiveness of pin fins; the pin fin design used here, which was based on that used in our previous studies of the HCFP, may well be unsuitable for the finger-type modules studied here. Further

investigation of these effects is the subject of ongoing work.

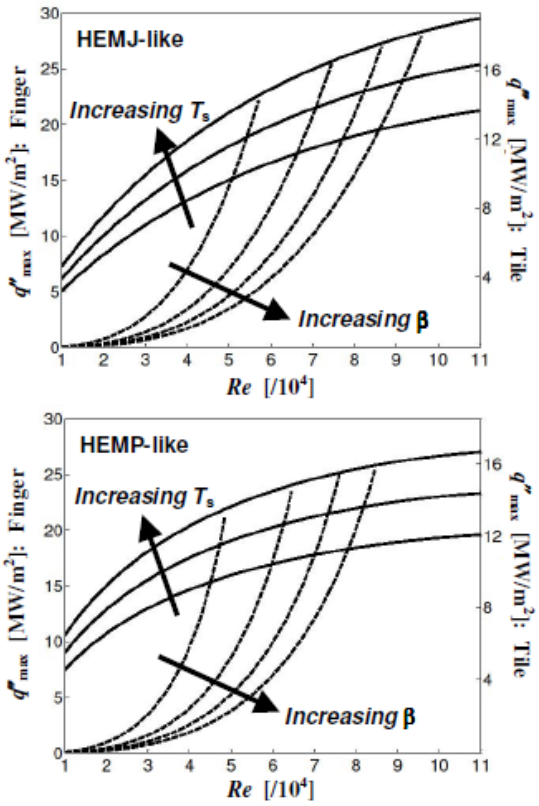

Fig. 7. Parametric design curves showing the maximum heat flux that can be accommodated by the HEMJ-like (top) and HEMP-like (bottom) configuration as a function of *Re* for T_s = 1100 °C, 1200 °C and 1300 °C (solid lines) and for β = 5%, 10% 15% and 20% (dashed lines). The values given on the left vertical axis are based on the area of the finger module, while those given on the right vertical axis are based on the area of the tile as detailed in Section II.

Figure 7 shows parametric design curves for the HEMJ-like (forward flow without fins) and HEMP-like (reverse flow with fins), respectively. These figures show the maximum heat flux $q''_{max}(Re)$ that can be accommodated by these two divertor designs at constant T_s = 1100 °C, 1200 °C and 1300 °C (solid lines), corresponding to the maximum surface temperature at the pressure boundary, as well as curves of $q'_{max}(Re)$ at constant β = 5%, 10% 15% and 20% (dashed lines).

The generalized charts shown in Figure 7 assume a helium inlet temperature of 600 °C, and an inlet pressure of 10 MPa. The maximum recommended operating temperature of W-1%La_2O_3 is 1200 °C, and most divertor designs specify that coolant pumping power should be less than 10% of the total power. At prototypical *Re*, the HEMJ-like divertor configuration requires more than 10% of the pumping power, while the HEMP-like divertor requires more than 15% of the total power. This suggests that both divertor configurations, which can accommodate heat fluxes well in excess of 10 MW/m^2, could be operated at significantly lower flow rates (*i.e.*, *Re*) to reduce pumping power requirements, albeit at the cost of lower q'_{max}. At T_s = 1200 °C, these figures suggest that the HEMJ-like divertor design should be operated with He at $Re < 7.5\times10^4$ to ensure that β <10%, and will still accommodate heat fluxes as great as 22 MW/m^2 at these conditions. Similarly, the HEMP-like design should be operated at $Re < 6.5\times10^4$ to ensure that β <10%, and $q''_{max} < 21$ MW/m^2 under these conditions.

VI. CONCLUSIONS

The thermal performance of four finger-type modular divertor designs, including configurations similar to the HEMP and HEMJ designs originally proposed by FZK, were experimentally investigated to evaluate whether an array of pin fins enhances the thermal performance of these helium-cooled divertor concepts. Dynamically similar experiments were performed on a test module heated by an oxy-acetylene torch to achieve heat fluxes exceeding 2 MW/m^2 using air as the coolant. The range of Reynolds numbers *Re* studied spanned prototypical operating conditions based on the expected He mass flow rate for HEMP of 4.81 g/s, which gave prototypical $Re = 7.0\times10^4$–7.6×10^4.

The experimentally measured heat transfer coefficients and pressure drops were used to determine the corresponding values for helium at prototypical conditions. Based on these results, the pin fins, as expected, greatly increase the thermal performance of modular divertor designs in the absence of jet impingement. However, the fins, at least in the configuration studied here, actually decrease the thermal performance of the HEMJ-like design at higher coolant flow rates or *Re* exceeding 4.7×10^4, and increase the pressure drop or loss across the divertor. This result suggests that the pin fins provide little if any additional cooling beyond that provided by jet impingement for the configurations studied here.

The extrapolated data can be plotted on parametric design curves giving the maximum heat flux that can be accommodated as a function of the coolant flow rate, given here in non-dimensional form in terms of the coolant *Re*, at constant pumping power as a fraction of the total power and at constant maximum temperature of the pressure boundary. These curves will be invaluable to

designers to estimate the maximum heat fluxes that can be accommodated by various divertor designs within the temperature limits imposed by thermal stresses and material properties without exceeding the limits placed upon the fraction of the total power required to pump coolant.

ACKNOWLEDGMENTS

This work was performed as a part of the ARIES study. We thank the U.S. DOE Office of Fusion Energy Sciences for their support through contract number DE-FG02-01ER54656.

REFERENCES

1. L. CROSATTI, "Experimental and Numerical Investigation of the Thermal Performance of the Gas-Cooled Divertor Modules," *Ph.D. Thesis,* Georgia Institute of Technology (2008).
2. J. B. WEATHERS, "Thermal Performance of Helium Cooled Divertors for Magnetic Fusion Applications," *M.S. Thesis,* Georgia Institute of Technology (2007).
3. P. NORAJITRA, ET AL., "Status of He-cooled divertor development for DEMO," *Fusion Engineering and Design*, **75-79**, 307 (2005).
4. V. WIDAK and P. NORAJITRA, "Optimization of He-cooled divertor cooling fingers using CAD-FEM method," *Fusion Engineering and Design*, **84**, 1973 (2009).
5. E. GAYTON, ET AL., "Experimental and Numerical Investigation of the Thermal Performance of the Gas-Cooled Divertor Plate Concept," *Fusion Science and Technology*, **56**, 75 (2009).
6. M. HAGEMAN, "Experimental Studies of the Thermal Performance of Gas-Cooled Plate-Type Divertors," to appear in *Fusion Sci. Technology*. (2011).
7. S. HERMSMEYER and S. MALANG, "Gas-cooled high performance divertor for a power plant," *Fusion Engineering and Design*, **61-62**, 197-202 (2002).
8. E. DIEGELE, ET AL., "Modular He-cooled divertor for power plant application," *Fusion Engineering and Design*, **66-68**, 383 (2003).
9. P. NORAJITRA, ET AL., "Development of a helium-cooled divertor concept: design-related requirements on materials and fabrication technology," *Journal of Nuclear Materials*, **329–333**, 1594 (2004).
10. F. INCROPERA and D. P. DEWITT, *Fundamentals of Heat and Mass Transfer*, pp. 144-149, 6th Ed., John Wiley, Hoboken, New Jersey (2007).

DYNAMICALLY SIMILAR STUDIES OF THE THERMAL PERFORMANCE OF HELIUM-COOLED FINGER-TYPE DIVERTORS WITH AND WITHOUT FINS

B. H. MILLS,* J. D. RADER, D. L. SADOWSKI, M. YODA, and S. I. ABDEL-KHALIK

Georgia Institute of Technology, G. W. Woodruff School of Mechanical Engineering
Atlanta, Georgia 30332-0405

Received May 28, 2012
Accepted for Publication July 14, 2012

Experimental studies based upon dynamic similarity have been used to evaluate the thermal performance of several modular helium-cooled tungsten divertor designs, including a configuration similar to the helium-cooled modular divertor with multiple jets (HEMJ). Until recently, all of these experiments used air, instead of helium, as the coolant. The average Nusselt number and loss coefficient were determined from cooled surface temperature and pressure drop data. Correlations were developed for the Nusselt number and loss coefficient as a function of the Reynolds number then used to predict the thermal performance of the divertor under prototypical conditions when cooled with high-temperature, high-pressure helium. Recently, experiments were performed using helium and argon to confirm the dynamic similarity assumption. The results indicated that the previous experiments with air, which were performed at the prototypical nondimensional coolant mass flow rate, or Reynolds number, did not account for the differences in the fraction of the incident power conducted through the walls of the divertor versus that convected, i.e., removed, by the coolant.

Dimensional analysis and numerical simulations suggest that for a given divertor geometry this fraction can be characterized by the ratio of the thermal conductivities of the divertor material and the coolant. Nusselt number correlations were developed to include the effect of the thermal conductivity ratio. Based on these correlations, the predicted maximum heat flux values that can be accommodated by the HEMJ-like configuration are reduced by ~20% from previous estimates. The results also suggest that the maximum heat flux that can be accommodated by this design can be increased by as much as 19% by adding an array of cylindrical pin fins on the cooled pressure boundary. However, as expected, adding the fins increases the pumping power for the coolant by ~16%. As a fraction of maximum total incident thermal power, however, the pumping power decreases by 2% when the fins are added due to the significant increase in the maximum heat flux.

KEYWORDS: *divertor, HEMJ, HEMP*

I. INTRODUCTION

The divertor is a critical component in commercial magnetic fusion reactors, helping to remove impurities and fusion by-products from the plasma. The plasma-facing surface of the divertor is subjected to extremely high steady-state heat fluxes of at least 10 MW/m^2 (Refs. 1 through 5). A variety of different modular helium-cooled tungsten divertor designs have been proposed, which typically employ cooling techniques such as jet impingement, cooling fins, or a combination of the two to cool the divertor surface and accommodate such high heat fluxes. Various research groups, including the ARIES team and the Karlsruhe Research Center (FZK) have evaluated the thermal performance of these modular divertor designs.

Earlier work has relied primarily on numerical simulations to evaluate the divertor thermal performance, in part because of the difficulties and expense involved in performing experimental studies with helium at the high

*E-mail: bmills@gatech.edu

pressures (typically 10 MPa) and temperatures (typically 600°C to 700°C) typical of prototypical divertor operating conditions. Experimental studies of mock-ups of the helium-cooled modular divertor with multiple jets (HEMJ) design[4,6] were nevertheless conducted at prototypical conditions by FZK using a helium loop at the Efremov Institute in Russia.[7] These experiments, which used ~10-MPa, 500°C to 600°C helium at a mass flow rate $\dot{m} \approx 5$ to 15 g/s to cool the HEMJ mock-up heated by an electron beam at incident heat fluxes up to 14 MW/m^2, demonstrated that the HEMJ design could accommodate heat fluxes of at least 10 MW/m^2.

An alternative, more economical approach to experimental studies of divertor thermal performance is to exploit dynamic similarity and use coolants at lower temperatures and pressures.[8–10] To that end, experimental studies have been performed as part of the ARIES study of several different divertor geometries using air instead of helium. In these studies, test modules or test sections of a geometry that closely simulate the proposed divertor geometry are constructed of materials such as brass that have thermal conductivities similar to the tungsten and tungsten alloys of the actual divertor at prototypical temperatures. Steady-state experiments are then conducted where air, typically at much lower temperatures and nearly ambient pressures, cools the test section, heated either electrically or with an oxyacetylene flame at incident heat fluxes up to 2 MW/m^2, at nondimensional coolant flow rates, or at Reynolds numbers Re that span the prototypical value. Temperatures measured with thermocouples (TCs) embedded slightly below the cooled surface are used to calculate nondimensional average heat transfer coefficients, or Nusselt numbers Nu, as a function of Re. The effects of the small difference in the Prandtl numbers Pr between air and He at appropriate temperatures of 0.71 and 0.66, respectively, are assumed to be small because of the expected $\mathrm{Pr}^{0.4}$ dependence of Nu. The experimental results are used to obtain correlations for Nu(Re), which are then used to predict the heat transfer coefficient at prototypical conditions for a helium-cooled tungsten divertor. These are in turn used to predict the maximum heat flux that can be accommodated by that particular divertor design for a given range of operating temperatures and maximum allowable temperature for the pressure boundary. Finally, nondimensional loss coefficients K_L, which are calculated from the pressure drop measured across the divertor test section in the dynamically similar experiments with air, are correlated to Re and extrapolated to the protoypical value of Re to determine the pressure drop expected for the helium-cooled divertor at prototypical operating conditions.

This simpler experimental approach has made it possible to evaluate a variety of divertor designs in a relatively short period of time. However, there have been a number of questions regarding the assumptions required to apply the results, i.e., the correlations, obtained with air to He at prototypical conditions. As described here, experiments were therefore performed using He, as well as argon, at near-ambient temperatures and pressures to cool a test section with a geometry similar to the HEMJ design to help resolve some of these questions, i.e., confirm the assumed dynamic similarity. The results of these experiments are presented here. The finger-type divertor test section with and without pin fins used in the study by Mills et al.,[10] with only a single impinging jet issuing from a central port similar to that in the helium-cooled modular divertor with integrated pin array[1,2] (HEMP), was used in these experiments. As detailed in Sec. II, experiments were performed with three different gaseous coolants—namely, air, He, and Ar—at Re ranging from $\sim 2 \times 10^4$ to 1.2×10^5, versus the prototypical Re of $\sim 7 \times 10^4$.

II. EXPERIMENTS

The two test sections studied in this work, namely, without fins and with fins, both consisted of two concentric cylindrical shells, with an inner shell of 8-mm outer diameter and 5.8-mm inner diameter centered inside an outer shell with 10-mm inner diameter and 12-mm outer diameter (Fig. 1a). The inner shell was sealed by a brazed cap with a 2-mm-diam circular port in the center. The spacing between the cap and the cooled surface on the inside of the outer shell was 2 mm. Both shells and the cap were made of C36000 brass, which has a thermal conductivity k_s at room temperature similar to that of the tungsten alloy W-1%La_2O_3 (~115 W/m·K) at prototypical temperatures of ~1000°C. The test section dimensions were comparable to those proposed for the HEMP

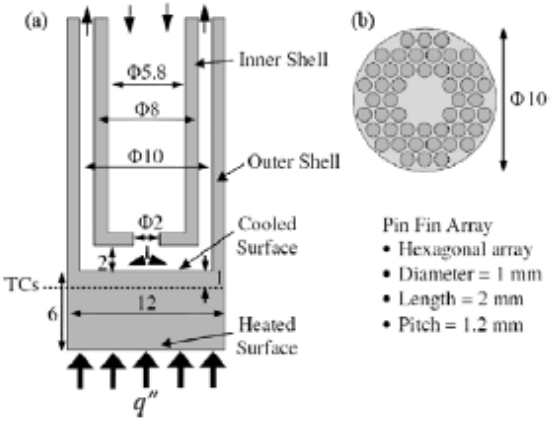

Fig. 1. (a) A cross section of the test section (without fins) indicating the coolant flow direction and (b) a top view of the pin-fin array. All dimensions are given in units of millimeters.

design.[1,2] The test section with fins included a hexagonal array of cylindrical pin fins that were an integral part of the cooled surface on the inside of the outer shell. The pin fins, which were fabricated using electrodischarge machining, were 2 mm in length, 1 mm in diameter, and spaced 1.2 mm apart (Fig. 1b). Note that the tips of the fins touch the cap of the inner shell, since the pin fins span the entire 2-mm gap between the cap and the (base of the) cooled surface.

The 6-mm-thick tip of the outer shell was heated on its outer surface by the flame from an oxyacetylene torch at incident heat fluxes $q'' = 0.2$ to 1.5 MW/m^2, and the test section was insulated to minimize heat loss to the surroundings. The heat flux was controlled by adjusting the fuel and oxidant flow rates provided to the torch. All of the experiments reported here were obtained with the same two (i.e., without fins and with fins) test sections, which were subjected multiple times to heat fluxes as large as 2 MW/m^2. Although the test sections maintained their physical dimensions through these experiments, they became discolored in the regions where the flame impinged on the brass, and soot due to the flame was wiped off from the test sections periodically.

Helium from five interconnected 300-scf (standard cubic foot) compressed-gas cylinders was supplied to the test section, entering the inner shell and exiting through the central port as a turbulent jet, which impinges upon the cooled surface on the inside of the outer shell before being discharged into a fume hood. Another set of experiments was also performed using argon, supplied by two interconnected 300-scf compressed-gas cylinders.

In both cases, the coolant volume flow rate through the test section Q was measured by a variable-area rotameter[a] upstream of the test section. The coolant pressures at the rotameter and at the test section inlet were measured by pressure transducers,[b] and the pressure drop across the test section Δp was measured by a differential pressure transducer.[c] The coolant temperatures at the inlet T_i and exit T_e of the test section were measured by two type-E TCs. The temperature distribution over the cooled surface was determined using four type-E TCs embedded 1 mm from the cooled surface in the brass at radial distances measured from the center of 0, 1, 2, and 3 mm spaced 90 deg apart (Fig. 2).

Each experiment was considered to have achieved a thermal steady state once the coolant temperatures T_i and T_e both varied by <1°C over a 5-min period and no consistent heating or cooling trends were observed over this interval. The typical time required to reach steady-state conditions from startup was ~15 min. Since fluctuations in the heat flux delivered by the oxyacetylene torch caused variations in the temperature readings from the embedded TCs as great as ~3°C, the temperature and pressure measurements were averaged over a 200-s interval.

[a]Brooks 1110.
[b]Keyence AP-15SK and Omega PX302-300AV, respectively.
[c]Omega PX26-030DV/100DV.

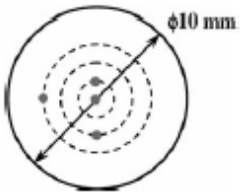

Fig. 2. Schematic of the cooled surface showing the positions of the four TC beads (gray circles) embedded 1 mm below the cooled surface. The three concentric dashed circles denote radial distances of 1, 2, and 3 mm from the center.

III. RESULTS

For each steady-state experiment, the mass flow rate of the coolant $\dot{m} = \rho Q$, where Q is the coolant volume flow rate and ρ is the density of the coolant at the exit of the rotameter, was set to the desired value by adjusting the pressure p_i at the test section inlet. The Reynolds number Re, corresponding to the nondimensional mass flow rate, at the central port in the inner shell (i.e., at the jet exit) was calculated as follows:

$$\mathrm{Re} = \frac{4\dot{m}}{\pi D \mu_i} , \tag{1}$$

where $D = 2$ mm is the port diameter and μ_i is the dynamic (or absolute) viscosity of the coolant evaluated at T_i. The uncertainty in the mass flow rate (estimated from the measurements of Q and the value of ρ calculated from the pressure and temperature at the exit of the rotameter), which is the dominant component of the uncertainty in Re, was estimated (using the standard error propagation technique described in Ref. 11) to be $<3.3\%$ for $\mathrm{Re} > 3 \times 10^4$.

The thermal power incident upon the outer surface of the test section was estimated using an energy balance approach under the assumption that heat losses to the surroundings are negligible. The average incident heat flux is

$$\bar{q}'' = \frac{\dot{m}\bar{c}_p(T_e - T_i)}{A_h} , \tag{2}$$

where $\bar{c}_p$ is the constant-pressure specific heat evaluated at the average coolant temperature $(T_i + T_e)/2$ and A_h is the area of the heated surface (a circle 12 mm in diameter).

The temperature at the cooled surface itself was estimated by extrapolating the temperature readings from

the embedded TCs assuming one-dimensional conduction through the 1 mm of brass alloy; an iterative procedure was used to account for the temperature dependence of the thermal conductivity. An area-weighted average temperature over the cooled surface $\bar{T}_c$ was calculated from the extrapolated surface temperature values assuming an axisymmetric temperature profile over the cooled surface. The average heat transfer coefficient for the test section without fins was then calculated using the relation

$$\bar{h} = \frac{\bar{q}''}{(\bar{T}_c - T_i)} \frac{A_h}{A_c} , \tag{3}$$

where A_c is the area of the cooled surface, a circle 10 mm in diameter. The equation for the average heat transfer coefficient [Eq. (3)] assumes that most of the heat incident on the test section is transferred by convection to the coolant at the cooled surface. It should be noted, however, that heat is also transferred by conduction through the side walls of the shell and removed at the side walls by convection to the coolant. The average Nusselt number over the cooled surface is calculated using the relation

$$\overline{\mathrm{Nu}} = \frac{\bar{h}D}{k} , \tag{4}$$

where k is the thermal conductivity of the coolant evaluated at the average coolant temperature $(T_i + T_e)/2$.

To calculate the average Nusselt number for the test section with fins requires accounting for the increase in cooled surface area created by the presence of the fins. However, the average heat transfer coefficient cannot simply be rescaled to the larger exposed area of the finned surface because the surface temperature of the fin is spatially nonuniform. This nonuniform temperature distribution is typically accounted for by the fin efficiency η. The actual spatially averaged heat transfer coefficient for the test section with fins is therefore

$$\bar{h} = \frac{A_h}{(A_p + \eta A_f)} \frac{\bar{q}''}{(\bar{T}_c - T_i)} , \tag{5}$$

where $A_p = 40.8\ \mathrm{mm}^2$ is the area of the cooled surface uncovered by the fins and $A_f = 302\ \mathrm{mm}^2$ is the area of the fins not including the fin tips. The fin efficiency, derived using a one-dimensional model that assumes that the temperature varies only along the length of the fin,[12] is taken to be that for an adiabatic boundary condition at the fin tip because the fin tips do not make perfect contact with the cap, and the nearly stagnant coolant in the resulting small gap between the cap and the fin tip is a poor conductor:

$$\eta = \frac{\tanh(\alpha)}{\alpha} \quad \text{where} \quad \alpha = L_f \sqrt{\frac{4\bar{h}}{k_f D_f}} , \tag{6}$$

and where L_f, D_f, and k_f are the length, diameter, and thermal conductivity, respectively, of the fins.

Figure 3 compares the average Nusselt numbers obtained for the air experiments of Mills et al.[10] at $\mathrm{Re} \approx 8 \times 10^3$ to 1.1×10^5 with those obtained for He and Ar for the test sections with and without fins over a similar range of Reynolds numbers. For the test section without fins, the $\overline{\mathrm{Nu}}$ results for argon are similar to those for air, but the results from the helium experiments are well below those for the two other gases, suggesting that our previous experiments with air at the same Re are not dynamically similar to those with He. However, the average Nusselt numbers obtained for the test section with fins are similar for all three coolants. The uncertainty in $\overline{\mathrm{Nu}}$ was, on average, 5.1% for the divertor without and with fins; the maximum uncertainty in $\overline{\mathrm{Nu}}$, for experiments with air at low $\bar{q}''$ and experiments with He at high Re with small increase in coolant temperature $(T_e - T_i)$, were 16.8% and 19.3% for the divertor without fins and with fins, respectively.

To explain the discrepancy in $\overline{\mathrm{Nu}}$ versus Re without fins, we examined whether compressibility effects were significant, since the inlet pressures, and hence volume flow rates, for each coolant at a given Re varied significantly among the three gases. A second series of experiments was therefore performed on the test section without fins with air and Ar at fixed inlet pressures $p_i = 0.7$ and 1.4 MPa, respectively, where Q was controlled by adjusting Δp. For the original series of experiments, the coolant flow rate Q was adjusted by varying p_i from ~10 to 415 kPa. No experiments at a fixed p_i were performed with He because the required inlet pressures exceeded

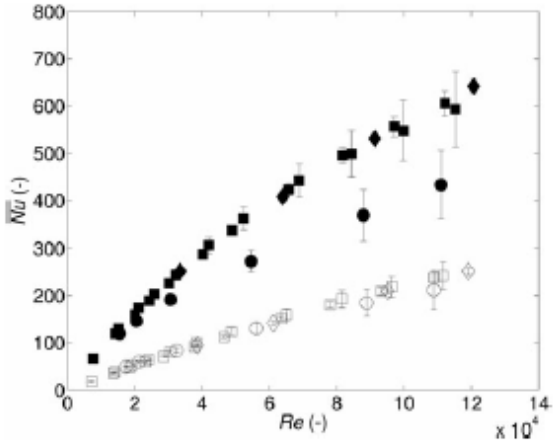

Fig. 3. Average Nusselt number $\overline{\mathrm{Nu}}$ as a function of Reynolds number Re for air[10] (■), helium (●), and argon (♦). The filled symbols are results for the test section without fins; the open symbols are results for the test section with fins.

the 1.4-MPa limit of the test loop. Figure 4a compares $\overline{\mathrm{Nu}}$ as a function of Re for the fixed inlet pressure experiments for air and Ar, as well as with the results for the variable p_i experiments shown in Fig. 3.

The average Mach number for the jet flowing through the central part is calculated as follows:

$$\mathrm{M} = \frac{1}{\sqrt{\gamma \mathcal{R} T_i}} \frac{4\dot{m}}{\rho \pi D^2} \quad , \tag{7}$$

where γ is the ratio of specific heats and $\mathcal{R}$ is the specific ideal-gas constant. Figure 4b shows variation of the Mach number for each coolant as a function of Re for all the experimental cases shown in Fig. 4a. The results for $\overline{\mathrm{Nu}}$ are identical for the variable and the fixed inlet pressure experiments at a given Re, demonstrating that compressibility effects are negligible in these studies, even at Mach numbers exceeding 0.6.

The nondimensionalized pressure drop across the test section, or the loss coefficient K_L, based on the coolant properties at the central port in the inner shell was determined as follows:

$$K_L = \frac{\Delta p}{\rho \overline{V}^2/2} \quad , \tag{8}$$

where Δp is the pressure drop measured across the test section and $\overline{V} = 4Q/(\pi D^2)$ is the average speed across the port. Figure 5 shows K_L as a function of Re for the test sections with and without fins. These data were curve fit to power laws:

$$K_L = (8.495 \times 10^4)\mathrm{Re}^{-1.337} + 1.056 \quad \text{without fins} \tag{9}$$

and

$$K_L = (6.965 \times 10^4)\mathrm{Re}^{-1.268} + 1.208 \quad \text{with fins} \quad , \tag{10}$$

with coefficients of determination $R^2 = 0.893$ and 0.887, respectively. As expected, the loss coefficients for the

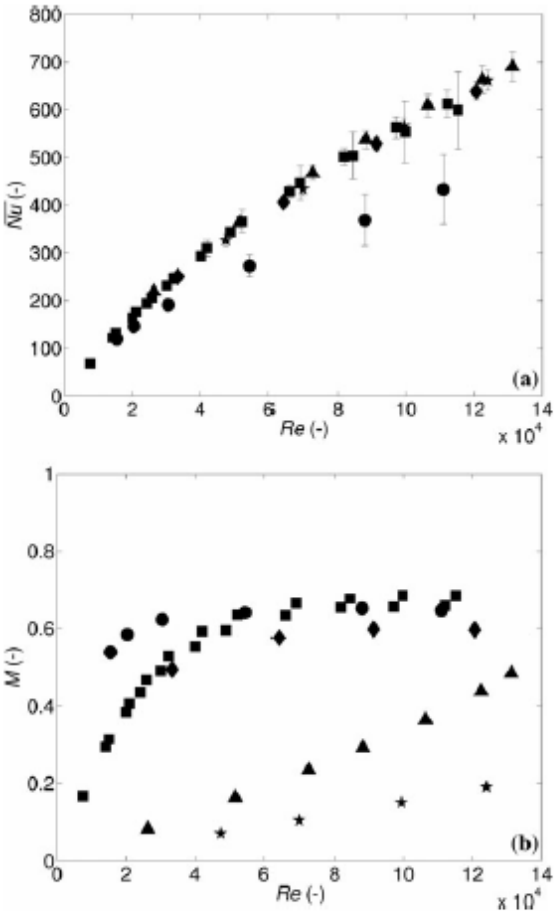

Fig. 4. (a) Average Nusselt number $\overline{\mathrm{Nu}}$ as a function of Reynolds number Re for the test section without fins at fixed inlet pressure $p_i = 0.7$ MPa for air (▲) and at $p_i = 1.4$ MPa for Ar (⋆), as well as the previous experiments at variable p_i for air (■), He (●), and Ar (♦), and (b) the corresponding M as a function of Re for these experiments.

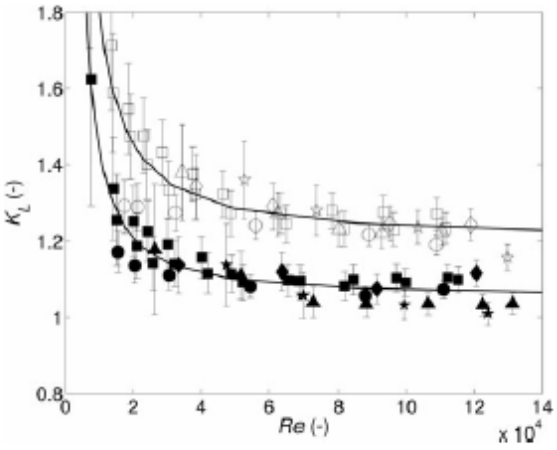

Fig. 5. Loss coefficient K as a function of Reynolds number Re for the experimental cases with air (■), He (●), Ar (♦), high-pressure air (▲), and high-pressure Ar (⋆). The filled symbols are results for the test section without fins; the open symbols are results for the test section with fins. Lines correspond to fits given in Eqs. (9) and (10).

test section with fins are 15% to 25% higher than the corresponding values for the test section without fins at a given Re because of the additional flow resistance by the fins for flow through the gap between the cap and the cooled surface. At the prototypical Re $= 7.6 \times 10^4$, the addition of fins increases the loss coefficient by ~16%. The average uncertainty in the loss coefficient was 3.8% for Re $> 6 \times 10^4$ (versus the prototypical Re of $\sim 7 \times 10^4$), while the maximum uncertainty in K_L was 9.5% for Re $> 3 \times 10^4$.

IV. DISCUSSION

To further explore the differences in $\overline{\text{Nu}}$ shown in Fig. 4a between experiments with air, He, and Ar with the test section without fins, computational fluid dynamics (CFD) simulations were performed using the commercial software package ANSYS FLUENT 13. The numerical model consisted of a two-dimensional axisymmetric model of the 50-mm section nearest the heated outer surface of the test section without fins. The mesh was composed of ~480 000 uniform quadrilateral cells with dimensions of 25 μm on a side. To ensure that the simulations were directly comparable to the experiments, the simulations were performed at the mass flow rate measured in the corresponding experiment at the measured T_i. The outlet pressure was set at a value equal to $p_i + \Delta p$ as measured in that experiment, while the heated surface was subjected to a uniform heat flux of $\bar{q}''$ [Eq. (2)] calculated for that experiment. With the exception of the heated surface, all boundaries were assumed to be adiabatic, and the material properties were identical to the temperature-dependent values used in the experimental calculations.

A comparison of otherwise identical numerical results obtained using both the realizable k-ε and the Spalart-Allmaras turbulence models showed that the temperatures predicted with the Spalart-Allmaras model gave $\overline{\text{Nu}}$ that were on average 4.4% different from experimental values of $\overline{\text{Nu}}$ for Re $> 3 \times 10^4$. As shown in Fig. 6, the $\overline{\text{Nu}}$ values as a function of Re calculated from these numerical predictions using Eq. (4) (open symbols) for all the air, helium, and argon experiments are in good agreement with the experimental values shown in Fig. 3 (closed symbols).

These experimentally validated simulations were used to determine radial profiles of the local Nusselt number at the cooled surface for the air, He, and Ar experiments from the radial heat flux and cooled surface temperature profiles $q''(r)$ and $T_c(r)$, respectively:

$$\text{Nu}(r) = \frac{q''(r)D}{[T_c(r) - T_i]k} \quad . \tag{11}$$

Figure 7 plots Nu(r) for three representative simulations of the test section without fins for air, He, and Ar at similar Re values of 5.88×10^4, 5.28×10^4, and 5.78×10^4, respectively. Interestingly, the radial profiles of the local Nu for these three coolants are similar, even though Fig. 3 suggests that the Nusselt number averaged over the cooled surface is much lower for He at a given Re. Given that the $\overline{\text{Nu}}$ values predicted by the simulations and calculated in the experiments are in good agreement (Fig. 6), this result suggests that the assumption made in the experimental calculations of

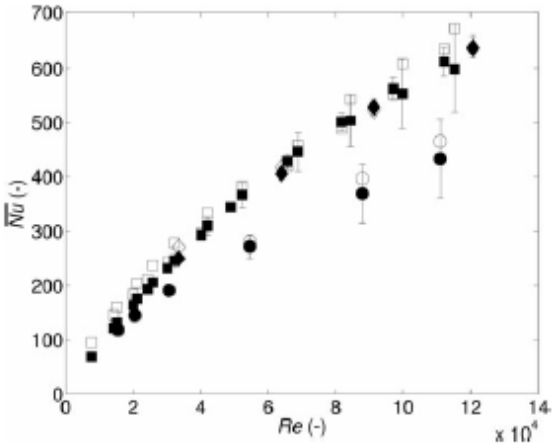

Fig. 6. Average Nusselt number $\overline{\text{Nu}}$ of each CFD simulation (open symbols) compared against experimental results without fins (closed symbols) for air[10] (■), helium (●), and argon (♦).

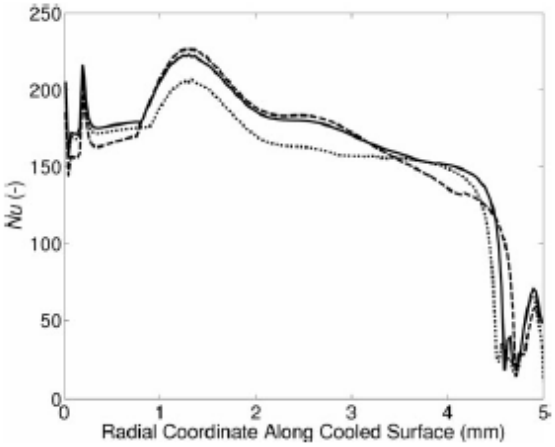

Fig. 7. Radial profiles of local Nu along the cooled surface predicted by the numerical simulations at Re ≈ 5×10^4 for air (solid line), helium (dashed line), and argon (dotted line).

$\overline{\text{Nu}}$—namely, that nearly all of the heat is removed by convection at the cooled surface [see Eq. (3)]—is not valid, and that a significant fraction of heat is conducted through the shell walls (and eventually removed by convection farther downstream). The fraction of heat transferred by conduction through the shell walls is expected to increase as the convection heat transfer coefficient for the cooled surface decreases.

Figure 8 shows the fraction of the total heat incident upon the heated surface removed by convection at the cooled surface (with a smaller area) determined from the numerical simulations as a function of Re for all three coolants. To obtain this fraction, the local heat flux predicted by the simulations was integrated over the cooled surface area, and the result was divided by the total incident thermal power $\bar{q}''A_h$. These results clearly show that less than two-thirds of the heat is removed by convection at the cooled surface in all cases, and that helium removes much more of the heat by convection at the cooled surface than air and argon. Based on this result and the results of Fig. 3, this is not the case for the test section with fins, where all three coolants convectively remove the same fraction of the power input at the cooled surface.

In summary, the above results suggest that matching the prototypical Reynolds number is not sufficient to ensure the dynamic similarity of the experiments for the test section without fins. Achieving dynamic similarity—and using the results from experiments with coolants at lower temperatures and pressures to predict the maximum heat flux that can be accommodated by this divertor design—also requires considering the relative amount of the incident heat flux removed by convection at the cooled surface versus that conducted through the shell walls. In our initial dimensional analysis, the heat transfer coefficient averaged over the cooled surface $\bar{h}$ was originally considered to be a function of D, ρ, $\bar{V}$, μ_i, c_p, and k. By the Buckingham pi theorem, this problem involves a total of seven parameters and four basic dimensions, and hence the problem is completely specified by three dimensionless groups, namely, $\overline{\text{Nu}}$, Re, and Pr. In the revised dimensional analysis, however, since the geometry is fixed, $\bar{h}$ is also a function of the thermal conductivity of the shell k_s, and so the problem is now described by four dimensionless groups, where the new dimensionless group is the ratio of the thermal conductivities of the shell and the coolant:

$$\overline{\text{Nu}} = f\left(\frac{\rho \bar{V} D}{\mu}, \frac{\mu c_p}{k}, \frac{k_s}{k}\right) = f\left(\text{Re}, \text{Pr}, \frac{k_s}{k}\right) . \quad (12)$$

Assuming that the functional form of the independent variables in Eq. (12) is a power law and that Pr effects are still negligible, the average Nusselt number can be correlated as follows:

$$\overline{\text{Nu}} = C\text{Re}^a \left(\frac{k_s}{k}\right)^b , \quad (13)$$

where a, b, and C are all constants determined from the experimental data. Using MATLAB 2008b, multiple linear regression of the experimental results for the test section without fins where k_s was evaluated at $\bar{T}_c$ and k was evaluated at the average coolant temperature $(T_i + T_e)/2$ gave the following correlation for the average Nusselt number:

$$\overline{\text{Nu}} = 0.0348\text{Re}^{0.753} \left(\frac{k_s}{k}\right)^{0.118} , \quad (14)$$

where $R^2 = 0.991$ for data obtained for $1 \times 10^4 < \text{Re} < 1.2 \times 10^5$, $900 < k_s/k < 7000$, and $\text{Pr} \approx 0.7$. Given that the results for the test section with fins were in good agreement for all three coolants, it was assumed that $\overline{\text{Nu}}$ was a power law function only of Re for this case. This essentially means that nearly all the heat incident on the test section is removed by convection at the finned cooled surface and that conduction through the shell walls is negligible. A power law fit over all the data with fins shown in Fig. 3 gave the following correlation:

$$\overline{\text{Nu}} = 0.0113\text{Re}^{0.857} , \quad (15)$$

where $R^2 = 0.995$.

Figures 9a and 9b show the data (points) for the test sections without fins and with fins, respectively, as well as Eqs. (14) and (15) (solid lines), respectively, along with ±10% uncertainty bands (dashed lines). By including the fraction of heat removed by convection at the cooled surface, characterized by the thermal conductivity ratio, the results for the test section for all three coolants are in

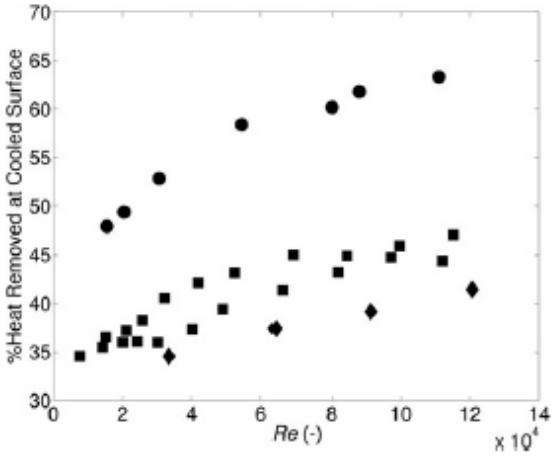

Fig. 8. Percentage of total heat removed by convection at the cooled surface for air (■), helium (●), and argon (♦) coolants calculated from the numerical simulations.

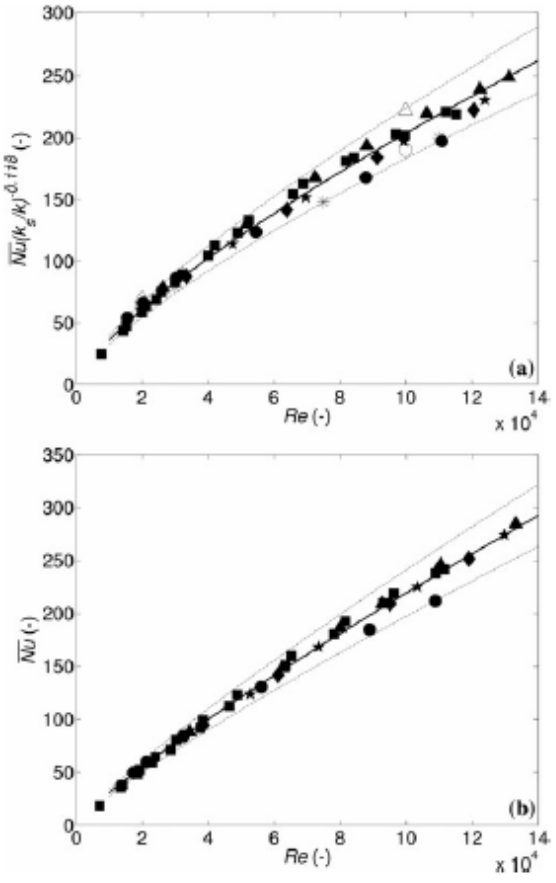

Fig. 9. Experimental data for air (■), helium (●), argon (♦), high-pressure air (▲), and high-pressure argon (★) experiments (a) without fins and (b) with fins after applying fit given in Eqs. (14) and (15), respectively. Open symbols in (a) represent simulations performed with air as a coolant for $k_s/k = 900$ and 7000 (○ and ◇, respectively) and with He as a coolant for $k_s/k = 340$ (*). Dashed lines indicate deviation of ±10% from fit.

good agreement and are well approximated by Eq. (14). To further test this correlation, which was obtained by a curve fit to data at only three values of k_s/k (namely, 900, 5000, and 7000 for He, air, and Ar, respectively) and one approximate value of k_s [namely, ~125 to 150 W/(m·K) for the brass alloy at temperatures of 100°C to 300°C], further numerical simulations were performed for the test section without fins and with air for $\mathrm{Re} \approx 2 \times 10^4$ and $\mathrm{Re} \approx 10^5$ at an incident heat flux $\bar{q}'' = 0.35$ MW/m^2 and $k_s/k = 900$ and 7000, where the thermal conductivity of the shell k_s was adjusted to achieve these thermal conductivity ratio values. Given that the prototypical value of $k_s/k \approx 340$ for W-1%La_2O_3 at 1200°C and He at 700°C, a value beyond the bounds of the curve fits of Eqs. (14) and (15), numerical simulations with He were also performed for the test section without fins at $k_s/k \approx 340$ and $\mathrm{Re} = 3 \times 10^4$, 7.5×10^4, and 1.1×10^5. The results for these simulations, which are all in good agreement with Eq. (14), are also shown in Fig 9a.

The $\overline{\mathrm{Nu}}$ correlations given in Eqs. (14) and (15) can be used to predict the maximum heat flux that can be accommodated by the divertor subject to material temperature limits. As detailed in Ref. 10 and summarized here, these correlations are used to calculate $\overline{\mathrm{Nu}}$ for the appropriate test section. Next, the maximum heat flux that can be accommodated by the divertor $\bar{q}''_{\max}$ at a given maximum pressure boundary surface temperature T_s was determined as follows:

$$\bar{q}''_{\max} = \frac{T_s - T_i}{R_T} \quad , \tag{16}$$

where the thermal resistance

$$R_T = \frac{A_h}{A_c h_{eff}} + \frac{\delta_s}{k_s} \quad , \tag{17}$$

where $\delta_s = 1$ mm was the thickness of the pressure boundary in the actual divertor design. An iterative solution was required because the thermal conductivity of the shell k_s depends upon temperature. The pressure boundary in the HEMP design was made from the tungsten alloy W-1%La_2O_3, and the typical maximum temperatures recommended for this alloy are $T_s = 1100$°C to 1300°C (Refs. 2, 13, and 14). Figures 10a and 10b show curves for $q''_{\max}$ as a function of Re for the test sections without fins and with fins, respectively, obtained at coolant inlet conditions $T_i = 600$°C and $p_i = 10$ MPa for $T_s =$ 1100°C, 1200°C, and 1300°C.

These $\bar{q}''_{\max}(\mathrm{Re})$ curves give values for the maximum heat flux that can be accommodated by the test section without fins that are ~22% less at a given Reynolds number than the values given by the analogous parametric design curves of Mills et al.,[10] which did not account for the thermal conductivity ratio. At prototypical helium mass flow rates of 4.8 g/s ($\mathrm{Re} \approx 7.6 \times 10^4$), $\bar{q}''_{\max} = 17.3$ MW/m^2 at $T_s = 1200$°C, versus ~22 MW/m^2 from Mills et al. Adding the cylindrical pin-fin array increases $\bar{q}''_{\max}$ to 20.6 MW/m^2, or by 19%, under otherwise identical conditions, as shown in Fig. 10b (and Ref. 10). Assuming the $\overline{\mathrm{Nu}}$ correlations have an uncertainty of 10% (see Fig. 9) and other uncertainties are negligible in comparison, the uncertainty in $\bar{q}''_{\max}$ is 1.3 and 1.5 MW/m^2 at the prototypical $\mathrm{Re} = 7.6 \times 10^4$ for the divertor without fins and with fins, respectively.

The experimental results were also used to predict β, the pumping power as a fraction of the total incident thermal power, at a given Re. The pressure drop for He Δp_{He} was calculated from the loss coefficient correlations given in Eqs. (9) and (10) for the test sections without

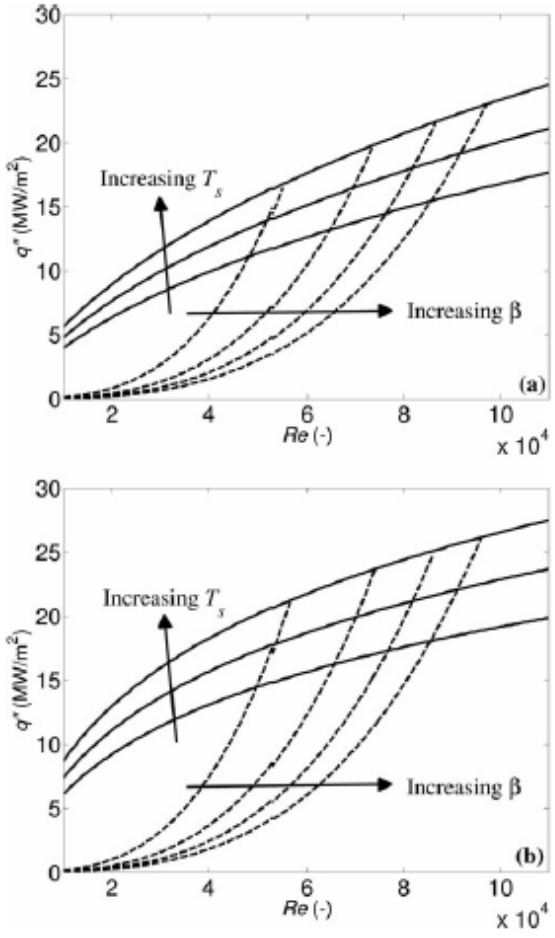

Fig. 10. Parametric design curves showing the maximum heat flux that can be accommodated by the divertor as a function of Re for $T_s = 1100$°C, 1200°C, and 1300°C (solid lines) and for $\beta = 5\%$, 10%, 15%, and 20% (dashed lines) (a) without fins and (b) with fins.

fins and with fins, respectively. The pumping power for helium at a given mass flow rate $\dot{m}_{He}$ is then

$$\dot{W}_{He} = \frac{\dot{m}_{He}\Delta p_{He}}{\bar{\rho}_{He}} , \quad (18)$$

where $\bar{\rho}_{He}$ is the average of the inlet and outlet coolant densities. This pumping power, as a fraction of the maximum total thermal power incident upon the heated outer surface of the shell, is then

$$\beta = \frac{\dot{W}_{He}}{\bar{q}''_{max} A_h} . \quad (19)$$

For the geometry without fins at the prototypical Re $= 7.6 \times 10^4$ and $T_s = 1200$°C, $\beta = 0.125$. For the geometry with fins at the same conditions, the pumping power as a fraction of the total incident thermal power is less, with $\beta = 0.123$. As noted in the discussion of Fig. 5, the K_L, and hence the $\dot{W}_{He}$, required to overcome this pressure drop are ~16% higher for the test section with fins. However, this increase in pumping power is outweighed by the increase in the maximum heat flux due to the addition of the fins, resulting in a 2% decrease in β compared with the case without fins.

Figure 10 provides generalized charts, which can be used to predict the performance of the examined finger-type divertor geometry (with and without fins) over a wide range of operating conditions. These charts can be integrated within system design codes to allow designers to select the optimum operating condition with the allowable range of material properties. These results are of course specific to this particular geometry and do not consider the effects of varying the divertor dimensions. We also emphasize that the maximum heat flux values are obtained based solely on thermal-hydraulic (versus thermal stress) considerations.

In summary, experiments using helium and argon have shown that matching the nondimensional coolant mass flow rate, or Reynolds number, is not sufficient to ensure dynamic similarity, and that the fraction of heat removed by the coolant at the cooled surface, characterized by the ratio of the thermal conductivities of the divertor and the coolant, must also be matched to achieve dynamic similarity. Given that all of the experimental results to date are at thermal conductivity ratios that are much higher than the prototypical value $k_s/k \approx 340$, current efforts focus on experimental studies using helium, albeit at near-ambient temperatures, at lower values of k_s/k. Nevertheless, the numerical simulations at the prototypical values of k_s/k provide confidence in the applicability of Eq. (14), and hence the generalized charts in Fig. 10, over the entire range of operating conditions.

V. CONCLUSION

The thermal performance of a modular helium-cooled tungsten finger-type divertor similar to the HEMJ design with and without a cylindrical pin-fin array was experimentally evaluated in experiments using three different coolants—namely, air, helium, and argon. The results for different coolants show that the average Nusselt number obtained from the experiments for the test section without fins depends on the coolant, even at a given nondimensional coolant mass flow rate, or Reynolds number, suggesting that the experiments with air reported in Mills et al. are not dynamically similar to the thermal hydraulics of the divertor under prototypical conditions.

Although further experiments performed over a wide range of Mach numbers demonstrated that compressibility effects were negligible, numerical simulations showed that there were significant differences in how much of the heat incident upon the plasma-facing surface of the divertor was removed at the cooled surface by the three different coolants. Indeed, even helium, which transfers much more heat by convection than air and argon, only removes two-thirds of the heat at the cooled surface; the remainder is conducted through the shell walls. Given that the average heat transfer coefficient and Nusselt number over the cooled surface were calculated under the assumption that most of the heat is transferred by convection to the coolant at the cooled surface [Eq. (3)], this result suggests that the previous correlations developed by Mills et al. must be modified to account for this effect.

To account for variations in the fraction of incident thermal power removed at the cooled surface, the $\overline{\mathrm{Nu}}$ correlations were revised to include the ratio of the thermal conductivities of the divertor material and the coolant. The revised correlations for $\overline{\mathrm{Nu}}$ as a function of Re for the divertor designs without fins and with fins [Eqs. (14) and (15), respectively] are consistent over all the experimental data for the three coolants, and with numerical simulations that vary the thermal conductivity of the divertor material. These revised correlations were then used at prototypical conditions to estimate the maximum heat flux $\bar{q}''_{\max}$ that could be accommodated by the divertor at a given maximum temperature for the surface of the pressure boundary. The revised correlations predict $\bar{q}''_{\max}$ values that are 21% less than previous estimates at a maximum pressure boundary surface temperature of 1200°C.

Adding the fin array to the cooled surface increases the maximum heat flux that can be accommodated by the divertor by 19%. Although the addition of the fin array increases the pressure drop across the divertor, and hence the coolant pumping power, by 16%, this increase in pumping power is more than offset by the increase in maximum heat flux. In fact, the pumping power as a fraction of total incident thermal power is reduced by 2% compared with the case without fins.

REFERENCES

1. E. DIEGELE et al., "Modular He-Cooled Divertor for Power Plant Application," *Fusion Eng. Des.*, **66–68**, 383 (2003).

2. P. NORAJITRA et al., "Development of a Helium-Cooled Divertor Concept: Design-Related Requirements on Materials and Fabrication Technology," *J. Nucl. Mater.*, **329–333**, 1594 (2004).

3. S. HERMSMEYER and S. MALANG, "Gas-Cooled High Performance Divertor for a Power Plant," *Fusion Eng. Des.*, **61–62**, 197 (2002).

4. P. NORAJITRA et al., "Status of He-Cooled Divertor Development for DEMO," *Fusion Eng. Des.*, **75–79**, 307 (2005).

5. T. IHLI et al., "An Advanced He-Cooled Divertor Concept: Design, Cooling Technology, and Thermohydraulic Analyses with CFD," *Fusion Eng. Des.*, **75–79**, 371 (2005).

6. V. WIDAK and P. NORAJITRA, "Optimization of He-Cooled Divertor Cooling Fingers Using CAD-FEM Method," *Fusion Eng. Des.*, **84**, 1973 (2009).

7. P. NORAJITRA et al., "He-Cooled Divertor Development Towards DEMO," *Fusion Sci. Technol.*, **56**, 1013 (2009).

8. E. GAYTON et al., "Experimental and Numerical Investigation of the Thermal Performance of the Gas-Cooled Divertor Plate Concept," *Fusion Sci. Technol.*, **56**, 75 (2009).

9. M. HAGEMAN et al., "Experimental Studies of the Thermal Performance of Gas-Cooled Plate-Type Divertors," *Fusion Sci. Technol.*, **60**, 228 (2011).

10. B. H. MILLS et al., "Experimental Investigation of Fin Enhancement for Gas-Cooled Divertor Concepts," *Fusion Sci. Technol.*, **60**, 190 (2011).

11. S. KLINE and F. McCLINTOCK, "Describing the Uncertainties in Single Sample Experiments," *Mech. Eng.*, **75**, 3 (1953).

12. F. INCROPERA and D. P. DEWITT, *Fundamentals of Heat and Mass Transfer*, 6th ed., pp. 144–149, John Wiley, Hoboken, New Jersey (2007).

13. P. NORAJITRA et al., "He-Cooled Divertor for DEMO: Experimental Verification of the Conceptual Modular Design," *Fusion Eng. Des.*, **81**, 341 (2006).

14. P. NORAJITRA et al., "Progress of He-Cooled Divertor Development for DEMO," *Fusion Eng. Des.*, **86**, 1656 (2011).

AN EXPERIMENTAL STUDY OF THE EFFECTS OF SOLID-TO-COOLANT THERMAL CONDUCTIVITY RATIO IN HELIUM-COOLED DIVERTOR MODULES

B. H. Mills, J. D. Rader, D. L. Sadowski, M. Yoda, S. I. Abdel-Khalik

G. W. Woodruff School of Mechanical Engineering, Georgia Institute of Technology, Atlanta, GA 30332–0405 USA
bmills@gatech.edu

As part of the ARIES study, the Georgia Tech group has experimentally studied the thermal performance of a helium-cooled 'finger-type' tungsten divertor design that uses jet impingement and a fin array to cool the plasma-facing surface. These studies were performed using air at Reynolds numbers Re, spanning those for prototypical operating conditions. A brass test section heated with an oxy-acetylene torch at incident heat fluxes up to 2 MW/m^2 was used. Recently, data obtained with room-temperature helium suggests that dynamic similarity between the air and helium experiments cannot be achieved by only matching Re because of the difference in the relative contributions of convection and conduction through the annular side walls of the divertor. Numerical simulations suggest that achieving dynamic similarity requires matching the ratio of the thermal conductivity of the divertor module material to that of the coolant under operating conditions, as well as Re.

Studies were performed to verify that experiments at the prototypical Re and thermal conductivity ratio using helium at room temperature give Nusselt numbers Nu that are dynamically similar to those at prototypical operating conditions. Given that the thermal conductivity of helium decreases as temperature decreases, matching of the thermal conductivity ratio required a carbon steel test section with a thermal conductivity much lower than that of the brass alloy previously used. The resulting ratio of the test section to coolant thermal conductivities is similar to that of the tungsten alloy and helium at prototypical conditions. The data were used to verify generalized correlations for Nu, as a function of Re and the thermal conductivity ratio. The correlations can be used to determine the maximum heat flux that can be accommodated by the divertor at prototypical conditions.

I. INTRODUCTION

Several modular tungsten He-cooled divertor designs have been proposed to cool the 10 MW/m^2 heat fluxes (Ref. 1-3) expected on the divertor surface inside a fusion reactor. Designs that have been studied as part of the ARIES research program include the T-Tube (Ref. 4), the He-cooled multi-jet HEMJ (Ref. 5), the He-cooled flat plate (HCFP) (Ref. 6-7), and the He-cooled modular divertor with integrated pin array (HEMP) (Ref. 8-9). These designs rely on jet impingement, flow through a fin array, or a combination of the two using helium (He) at 10 MPa to remove this heat.

Experiments to evaluate the thermal-hydraulic performance of each design with actual materials at prototypical operating conditions are difficult and expensive due to the high temperatures and pressures required. Experiments on the HEMJ design were performed at prototypical conditions by the Karlsruhe Institute of Technology (KIT) and the Efremov Institute. These experiments focused on developing methods to fabricate the HEMJ design from the proposed materials and verifying that the design could accommodate heat fluxes of 10 MW/m^2.

Over the last several years, a number of studies to quantify and improve the thermal performance of various He-cooled divertor designs have been performed at Georgia Tech using dynamically similar experiments on brass test sections with dimensions similar to those of the actual design cooled by air at nearly ambient temperatures and pressures. The experiments were performed over a range of nondimensionalized coolant mass flow rates, or Reynolds numbers Re, that span the expected value at prototypical operating conditions. The outer surface of the pressure boundary of the test section was heated by an oxy-acetylene torch at heat fluxes $q'' \leq 2$ MW/m^2.

The temperature distribution over the cooled inner surface of the pressure boundary was measured by thermocouples embedded in the test section and used to estimate nondimensional average heat transfer coefficients, or Nusselt numbers $\overline{Nu}$. The experimental data were used to develop correlations for $\overline{Nu}\,(Re)$ (assuming that the effect of Prandtl number Pr is minimal because the Pr of air and He are of the same order of magnitude). These correlations were in turn extrapolated to predict the maximum heat flux q''_{max} the design can endure without exceeding temperature limits dictated by material properties.

The pressure drop across the test section Δp was also measured, and converted to nondimensional loss

coefficients K_L, which were in turn, extrapolated to prototypical conditions to predict the prototypical pressure drop, and hence the pumping power as a fraction of the incident thermal power β. Finally, these results are summarized in generalized design charts that present q''_{max} as a function of Re for a given maximum pressure boundary surface temperature T_s and a given β that can be used to predict how the design will perform at different operating conditions.

Recent experiments by Mills *et al.*[10] using He in a single-pass system on a modular finger-type divertor test section with dimensions similar to HEMP have shown that the $\overline{Nu}$ values determined with He are different from those obtained with air at the same Re. This result implied that dynamic similarity could not be achieved by only matching Re. Numerical simulations using ANSYS FLUENT® 13 revealed that a significant portion of the heat was being conducted through the divertor annular side walls as opposed to being removed by convection at the cooled surface. The simulations also showed that the relative contributions of convection and conduction differ significantly between the He and air-cooled experiments.

By dimensional analysis, accounting for this effect introduces a new nondimensional parameter, the ratio of the thermal conductivities of the divertor module k_s and the coolant k. Re-analyzing the He and air data, as well as results from experiments performed with a third coolant, argon (Ar), to obtain correlations for $\overline{Nu}\left(Re, k_s/k\right)$ assuming a power-law dependence on both independent variables, yielded:

$$\overline{Nu} = 0.0348 Re^{0.753}\left(\frac{k_s}{k}\right)^{0.118} \quad (1)$$

The thermal conductivity ratios used to generate Eq. (1) were based on one value of k_s, namely that for brass, with $k_s/k \approx$ 900-7000. However, the thermal conductivity ratio of a W-1%La_2O_3 (WL-10) ($k_s \approx$ 116 W/(m·K) at 1000 °C) test section cooled by He ($k \approx$ 0.34 W/(m·K) at 650 °C) is much lower: $k_s/k \approx$ 340.

Numerical simulations for different values of k_s and k over a range of k_s/k suggest that Eq. (1) can be extrapolated to the prototypical thermal conductivity ratio. The objective of this study was to experimentally validate Eq. (1) at near-prototypical values of k_s/k.

Experimentally achieving $k_s/k \approx$ 340 in the single-pass system using He at near-ambient temperature, and hence a value of k less than the prototypical value, requires a test section fabricated of a material with $k_s <$ 116 W/(m·K). The pressure boundary portion of the test section was therefore fabricated from AISI 1010 carbon steel, which has a thermal conductivity that varies over the range of temperatures observed in the experiments from ~63 W/(m·K) at 20 °C to ~41 W/(m·K) at 500 °C, and cooled by He, air and Ar. This variation in thermal conductivity gives a range of thermal conductivity ratios that will give values of k_s/k for experiments with helium that bracket the prototypical value of ~340.

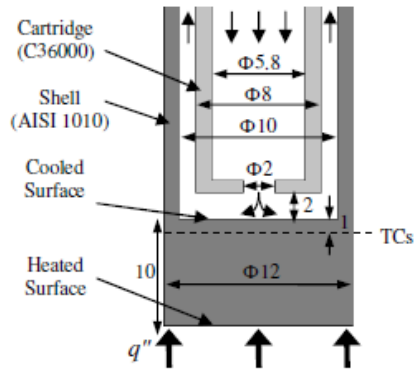

Fig. 1. A cross section of the test section. Arrows indicate coolant flow direction. All dimensions are in mm.

The remainder of this paper is organized as follows. Section II details the experiments, while Section III presents results for $\overline{Nu}$ and K_L. Section IV discusses these results, and compares them to our previous results for the brass test section, as well as the correlation given in Eq. (1). Section V then summarizes our conclusions.

II. EXPERIMENT

The test section used in the experiments (Fig. 1) consisted of a cylindrical steel shell with an OD of 12 mm, ID of 10 mm, and a 10 mm thick solid tip (*i.e.*, the distance between the inner cooled and outer heated surfaces of the pressure boundary). A brass inner cylindrical cartridge with an OD of 8 mm, ID of 5.8 mm and a 3 mm thick endcap with a 2 mm diameter circular port in the center was inserted concentrically inside the steel shell; the gap between the cartridge endcap and the inner surface of the shell was 2 mm. These dimensions were similar to those of the HEMP module. Although the shell was fabricated from AISI 1010 carbon steel, the other components, including the inner cartridge, were constructed of C36000 brass alloy.

The steel shell was heated by the flame from an oxy-acetylene torch that directly impinged on the outer surface of the shell tip, or the "heated surface," at heat fluxes up to 2 MW/m^2. For the air-cooled experiments, air was supplied from the building compressed-air line at pressures up to ~0.7 MPa. The He experiments used five interconnected 300 SCF compressed-He cylinders at pressures up to ~1.4 MPa with two pressure regulators in series, while the Ar experiments used two interconnected 300 SCF compressed-Ar cylinders connected in the same manner. In all cases, the coolant entered the test section through the inner cartridge, accelerated through the

central port forming a turbulent jet that impinged on the cooled surface of the steel shell before exiting via the annular gap between the cartridge and the shell. The test section was insulated within Marinite® blocks; all other piping was insulated using pipe foam and rock wool.

The coolant volumetric flow rate Q through the test section was measured using a variable-area flow meter (Brooks 1110) upstream of the test section. The coolant pressures at the flow meter and the test section inlet p_i were measured by pressure transducers (Omega PX302-2KGV and Omega PX302-300AV, respectively), and the pressure drop across the test section Δp was measured by a differential pressure transducer (Omega PX26-100DV). The coolant temperatures at the inlet and outlet of the test section T_i and T_e, respectively, were measured using Type-E thermocouple (TC) probes. Four Type-E TCs were also embedded in the steel shell tip 1 mm from the cooled surface at radial distances of 0, 1, 2, and 3 mm from the center and spaced 90° apart. Each experiment was performed at steady-state conditions, defined to be the condition where T_i and T_e varied by at most 1°C over 5 min and no heating or cooling trends were observed. All the temperatures from the embedded TCs were averaged over 200 s intervals because fluctuations in the torch flame resulted in variations as great as ~3°C.

III. RESULTS

The mass flow rate of the coolant $\dot{m} = \rho Q$ was set by adjusting p_i, where ρ is the coolant density at the exit of the Rotameter. The non-dimensional mass flow rate $Re = 4\dot{m}/(\pi D \mu_i)$ where $D = 2$ mm is the diameter of the center port and μ_i is the dynamic viscosity evaluated at T_i. Note that the prototypical Re is 7.6×10^4 (Ref. 9-10).

The average heat flux $\overline{q''}$ incident on the test section is calculated using an energy balance assuming that heat losses to the surroundings are negligible:

$$\overline{q''} = \frac{\dot{m}\overline{c}_p (T_e - T_i)}{A_h} \tag{2}$$

where $\overline{c}_p$ is the constant-pressure specific heat evaluated at the average coolant temperature $T_{av} = (T_i + T_e)/2$ and $A_h = 113.1$ mm^2 is the area of the heated surface.

The embedded TC readings were extrapolated assuming 1D conduction through 1 mm of steel to estimate the temperature at the cooled surface, and these extrapolated temperatures were then averaged using an area-weighted average assuming an axisymmetric temperature distribution to determine the average cooled surface temperature $\overline{T_c}$. The average heat transfer coefficient (HTC) $\overline{h}$ over the cooled surface is then:

$$\overline{h} = \frac{\overline{q''}}{(\overline{T_c} - T_i)} \frac{A_h}{A_c} \tag{3}$$

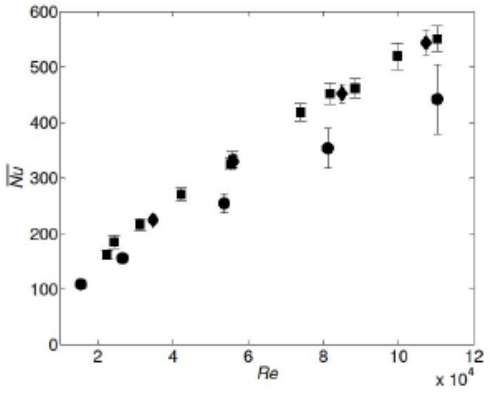

Fig. 2. $\overline{Nu}$ as a function of Re for the experiments performed with air (■), He (●), and Ar (♦) with the steel finger-type divertor test section. Error bars denote the experimental uncertainty.

where $A_c = 78.5$ mm^2 is the area of the cooled surface.

Including of the ratio between the heated and cooled surface areas in Eq. (3) assumes that all of the incident power is convected away at the cooled surface. As discussed in Mills *et al.*,[10] conduction through the annular side wall of the divertor can remove a significant portion of the incident heat, and this heat is ultimately convected to the coolant from the surface of the divertor annular side walls, and hence included in the measured average heat flux value. Finally, the nondimensional HTC, or $\overline{Nu}$ over the cooled surface is defined as follows:

$$\overline{Nu} = \frac{\overline{h}D}{k} \tag{4}$$

where k is the coolant thermal conductivity at T_{av}.

Fig. 2 summarizes the $\overline{Nu}$ results for twenty steady-state experiments: eleven with air, five with He, and four with Ar. As seen in Mills *et al.*,[10] the $\overline{Nu}$ values obtained with He are significantly different from those for air and Ar. This discrepancy can be directly attributed to different fractions of the total incident power being removed at the cooled surface, as characterized by the different thermal conductivity ratios, with k_s/k = 1900–2200 for air, 2900–3000 for Ar, and 350–380 for He.

The measured pressure drops Δp were nondimensionalized to loss coefficients K_L:

$$K_L = \frac{\Delta p}{\rho \overline{V}^2/2} \tag{5}$$

where $\overline{V} = 4Q/(\pi D^2)$ is the average speed across the center port. Since K_L is a "hydraulic" parameter that depends upon Re and the flow geometry, it should be independent of the material of the test section (and hence the thermal conductivity k_s). Since the flow geometry for the steel and brass test sections is identical, the correlation

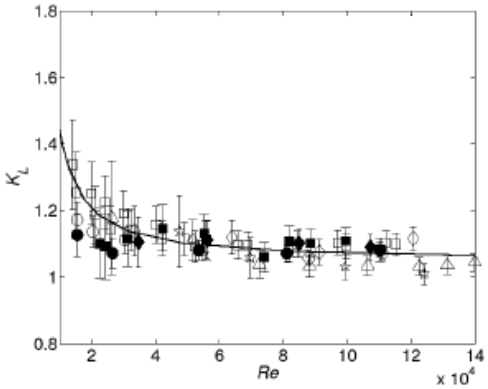

Fig. 3. K_L as a function of Re for the experiments performed with air (■), He (●), and Ar (♦). The new results are compared with previous results from Mills *et al.*[10] (open symbols) and correlation given by Eq. (6). Error bars denote the experimental uncertainty.

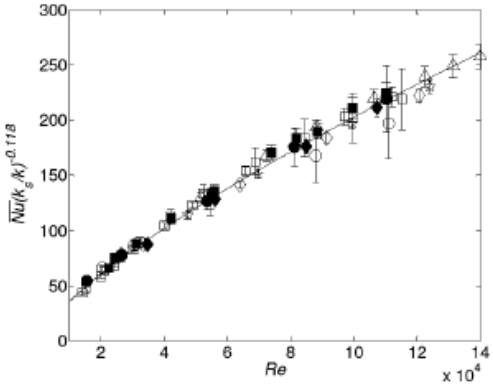

Fig. 4. Experimental data with the steel test section for air (■), He (●), and Ar (♦) compared with the correlation of Eq. (1) (line). Both are compared with the data obtained with the brass test section from Mills *et al.*[10] (open symbols). Error bars denote the experimental uncertainty.

for $K_L(Re)$ determined from the earlier air, He and Ar results with the brass test section[10] should still be valid:

$$K_L = 8.495\times10^4 Re^{-1.337} + 1.056 \quad (6)$$

Figure 3 summarizes the results of the air, He and Ar experiments with the steel test section (points), and compares them with the correlation given in Eq. (6) (line). As expected, the correlation developed for the brass test section can also be applied to these data. Although the agreement between the data and Eq. (6) is much worse at $Re < 3\times10^4$, we suspect that most of this is due to large uncertainties in the data because the uncertainty in the Δp measurements are a significant fraction of these relatively low pressure drop values. Given that this range of Re is significantly below prototypical values, Eq. (6) should still be useful for design purposes.

IV. DISCUSSION

Figure 4 compares the experimental results shown in Figure 2 (points) with the correlation given in Eq. (1) (line) by plotting $\overline{Nu}(k_s/k)^{-0.118}$ as a function of Re. The experimental data obtained with the steel are in good agreement with the correlation, confirming that Eq. (1) is valid for $1\times10^4 < Re < 1.2\times10^5$, $350 < k_s/k < 7000$, and $0.66 < Pr < 0.72$. This correlation can therefore be used to predict the performance of He-cooled tungsten-alloy finger-type divertor modules at prototypical conditions.

Building upon previous numerical simulations,[10] the commercial software package ANSYS FLUENT® 14 was used to analyze the experiments with the steel test section. An already existing 2D axisymmetric numerical model of a 54 mm long (axial dimension) section of the shell and tube was updated from brass to steel, with a distance of 10 mm (*vs.* 6 mm) between the cooled inner and heated outer surfaces of the shell, giving a mesh consisting of approximately 5×10^6 uniform quadrilateral cells 25 μm across. The incident heat flux was assumed to be uniform over the heated surface, and all other boundaries were assumed to be adiabatic. A Spalart-Allmaras turbulence model was used since previous studies[10] suggested that this turbulence model gave the most accurate results.

Using experimental data measured in each steady-state experiment to define the coolant boundary conditions and the incident heat flux ($\dot{m}$, T_i, p_e and $\overline{q''}$), the HTC $\overline{h}$ and $\overline{Nu}$ were calculated from the cooled surface temperatures from the simulations with Eqs. (3) and (4), respectively. Fig. 5 then compares these numerical predictions with the correlation of Eq. (1) and the experimental results for the steel test section. The simulation results are in good agreement with the experiments and the correlation.

Finally, as detailed in Mills *et al.*,[10] the simulations can also be used to estimate the fraction of the incident power removed by the coolant at the cooled surface by convection (*vs.* conducted through the annular side walls of the divertor). Figure 6 shows this fraction, which is simply the ratio of the local heat flux integrated over the area of the cooled surface to the total thermal power incident on the heated surface $\overline{q''}A_h$, as a function of Re, and compares the values for the steel test section with those for the brass test section.[10]

The fraction of heat removed by convection at the cooled surface varies from ~34% to ~70% over the range of Re and k_s/k studied. The highest fraction of heat removed by convection was observed for the He-cooled steel test section, with the lowest $k_s/k \approx 360$ (similar to the prototypical value), while the lowest fraction was

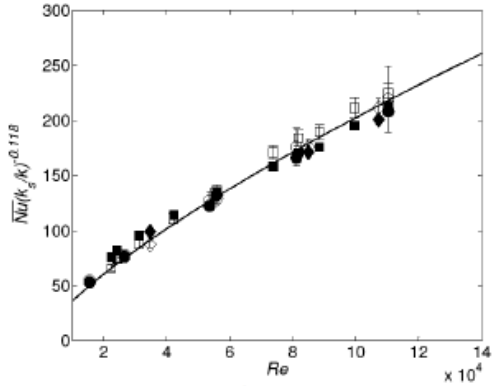

Fig. 5. Simulation results for steel test sections with air (■), He (●), and Ar (♦) compared with Eq. (1) (line) and the corresponding experimental results (open symbols). Error bars denote the experimental uncertainty.

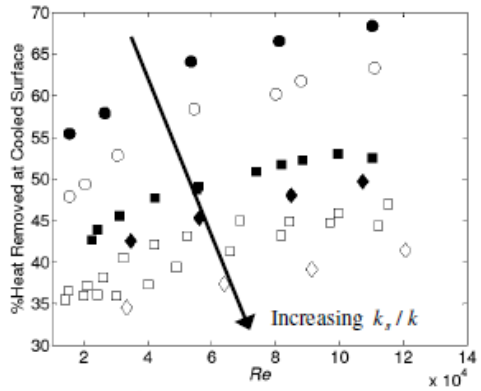

Fig. 6. Percent of incident heat removed by convection at the cooled surface found by CFD simulations for air (■), He (●), and Ar (♦). The filled and open symbols represent results for the steel and brass test sections,[10] respectively. The arrow indicates increasing thermal conductivity ratio.

observed for the Ar-cooled brass test section with the highest $k_s/k \approx 7000$. As expected, an increase in k_s/k is associated with a decrease in the fraction of heat removed by convection at the cooled surface, confirming that the thermal conductivity ratio can be used to characterize the relative importance of convection at the cooled surface, *vs.* conduction through the divertor walls, and that k_s/k must be included in the correlation for $\overline{Nu}$.

V. CONCLUSIONS

The effect of the ratio of the divertor and coolant thermal conductivities k_s/k on $\overline{Nu}$ at nearly prototypical values was investigated experimentally. Previous experiments using a HEMP-like divertor module fabricated in brass had developed a correlation for $\overline{Nu}$ as a function of Re and k_s/k, Eq. (1), for thermal conductivity ratios $900 < k_s/k < 7000$. These experiments used a nearly identical divertor module fabricated in steel cooled with helium at near-ambient temperatures to achieve the prototypical value of the thermal conductivity ratio $k_s/k = 340$. These dynamically similar experiments, as well as experiments using air and argon, confirmed that this correlation is valid at the prototypical thermal conductivity ratio and expanded the range. Numerical simulations of these experiments confirmed that the fraction of heat that was removed by convection at the cooled surface (*vs.* conduction through the walls of the divertor) increased as the solid-to-coolant thermal conductivity ratio decreased.

REFERENCES

1. E. DIEGELE, ET AL., "Modular He-cooled divertor for power plant application," *Fusion Engineering and Design*, **66-68**, 383 (2003).
2. P. NORAJITRA, ET AL., "Development of a helium-cooled divertor concept: design-related requirements on materials and fabrication technology," *Journal of Nuclear Materials*, **329–333**, 1594 (2004).
3. S. HERMSMEYER and S. MALANG, "Gas-cooled high performance divertor for a power plant," *Fusion Engineering and Design*, **61-62**, 197-202 (2002).
4. T. IHLI, ET AL., "Design and performance study of the helium-cooled T-Tube divertor concept," *Fusion Engineering and Design*, **82**, 249 (2007)
5. J. B. WEATHERS, ET AL., "Development of modular helium-cooled divertor for DEMO based on the multi-jet impingement (HEMJ) concept: experimental validation of thermal performance," *Fusion Engineering and Design*, **83**, 1120 (2008)
6. E. GAYTON, ET AL., "Experimental and Numerical Investigation of the Thermal Performance of the Gas-Cooled Divertor Plate Concept," *Fusion Science and Technology*, **56**, 75 (2009).
7. M. HAGEMAN, "Experimental Studies of the Thermal Performance of Gas-Cooled Plate-Type Divertors," *Fusion Sci. Technology*, **60**, 228 (2011).
8. J. D. RADER, ET AL., "Experimental and numerical investigation of thermal performance of gas-cooled jet-impingement finger-type divertor concept," *Fusion Science and Technology*, **60**, 223 (2011)
9. B. MILLS, ET Al., "Experimental investigation of fin enhancement for gas-cooled divertor concepts," *Fusion Science and Technology*, **60**, 190 (2011)
10. B. MILLS, ET AL., "Dynamically similar studies of the thermal performance of helium-cooled finger-type divertors with and without fins," *Fusion Science and Technology*, **62**, 379 (2012)

REFERENCES

[1] (2013, July) International Energy Outlook 2013. [Online]. http://www.eia.gov/forecasts/ieo/

[2] R Nave. HyperPhysics. [Online]. http://hyperphysics.phy-astr.gsu.edu/hbase/nucene/nucbin.html#c2

[3] Prachai Norajitra, *Divertor Development for a Future Fusion Power Plant*. Karlsruhe, Germany: KIT Scientific Publishing, 2011.

[4] R Nave. HyperPhysics. [Online]. http://hyperphysics.phy-astr.gsu.edu/hbase/astro/procyc.html

[5] Garry McCracken and Peter Stott, *Fusion: The Energy of the Universe*, 2nd ed. Saint Louis, USA: Academic Press, 2012.

[6] ITER Organization. (2013) ITER.org. [Online]. http://www.iter.org

[7] (2013) European Fusion Development Agreement. [Online]. http://www.efda.org/fusion/focus-on/limiters-and-divertors/

[8] M. Rieth, D. Armstrong, B. Dafferner, S. Heger, and A. Hoffmann, "Tungsten as a Structual Material," *Advances in Science and Technology*, vol. 73, pp. 11-21, 2010.

[9] A. Loarte et al., "Chapter 4: Power and particle control," *Nuclear Fusion*, vol. 47, pp. S203-S263, 2007.

[10] P Norajitra, R Giniyatulin, N Holstein, T Ihli, and W Krauss, "Status of He-cooled divertor development for DEMO," *Fusion Engineering and Design*, vol. 75-79, pp. 307-311, 2005.

[11] T. Ihli et al., "An advanced He-cooled divertor concept: Design, cooling technology, and thermohydraulic analyses with CFD," *Fusion Engineering and Design*, vol. 75-79, pp. 371-375, 2005.

[12] S. Hermsmeyer and K. Kleefeldt, "Review and comparative assessment of helium-cooled divertor concepts," Forchungszentrum Karlsruhe, 2001.

[13] Yunus A. Cengel, *Heat Transfer: A Practical Approach*, 2nd ed. United States of America: Mcgraw-Hill, 2002.

[14] Adrian Bejan and Allan D. Kraus, *Heat Transfer Handbook*. Hoboken, United States of America: John Wiley & Sons, 2003.

[15] Frank P. Incropera, David P. DeWitt, Theodore L. Bergman, and Adrienne S. Lavine, *Fundamentals of Heat and Mass Transfer*, 6th ed. United States of America: John Wiley & Sons, 2007.

[16] H. A. El-Sheikh and S. V. Garimella, "Enhancement of Air Jet Impingement Heat Transfer Using Pin-Fin Heat Sinks," *IEEE Transactions on Components and Packaging Technology*, vol. 23, no. 2, pp. 300-308, June 2000.

[17] S. Hermsmeyer and S. Malang, "Gas-cooled high performance divertor for a power plant," *Fusion Engineering and Design*, vol. 61-62, pp. 197-202, 2002.

[18] E. Diegele, R. Kruessmann, S. Malang, P. Norajitra, and G. Rizzi, "Modular He-cooled divertor for power plant application," *Fusion Engineering and Design*, vol. 66-68, pp. 383-387, 2003.

[19] Holger Martin, "Heat and Mass Transfer between Impinging Gas Jets and Solid Surfaces," *Advances in Heat Transfer*, vol. 13, pp. 1-60, 1977.

[20] D. Lytle and B. W. Webb, "Air jet impingement heat transfer at low nozzle-plate spacings," *Int. J. Heat and Mass Transfer*, vol. 37, no. 12, pp. 1687-1697, January 1994.

[21] Jung-Yang San and Wen-Zheng Shiao, "Effects of jet plate size and plate spacing on the stagnation Nusselt number for a confined circular air jet impinging on a flat surface," *International Journal of Heat and Mass Transfer*, vol. 49, no. 19-20, pp. 3477-3486, February 2006.

[22] S. V. Garimella and R. A. Rice, "Confined and submerged liquid jet impingement heat transfer," *Journal of Heat Transfer*, vol. 117, no. 4, pp. 871-877, 1995.

[23] Jung-Yang San and Mao-De Lai, "Optimum jet-to-jet spacing of heat transfer for staggered arrays of impinging air jets," *International Journal of Heat and Mass Transfer*, vol. 44, pp. 3997-4007, January 2001.

[24] S. A. Salamah and D. A. Kaminshi, "Modeling of Turbulent Heat Transfer from an Array of Submerged Jets Impinging on a Solid Surface," *Numerical Heat Transfer*, vol. 48, pp. 315-337, 2005.

[25] K. R. Saripalli, "Visualization of Multijet Impingement Flow," *AIAA Journal*, vol. 21, no. 4, pp. 483-484, April 1983.

[26] C. Cornaro, A. S. Fleischer, and R. J. Goldstein, "Flow visualization of a round jet impinging on cylindrical surfaces," *Experimental Thermal and Fluid Science*, vol. 20, pp. 66-78, July 1999.

[27] K. Kleefeldt and S. Gordeev, "Performance Limits of a Helium-Cooled Divertor (Unconventional Design)," Forschungszentrum Karlsruhe GmbH, Karlsruhe, Final Report on Subtask PPA 1.3.2 on the Preparation of a Power Plant Conceptual Study on Plant Availability 2000.

[28] (2012, December) Sandia National Laboratories. [Online]. http://energy.sandia.gov/?page_id=1498

[29] E. Gayton et al., "Experimental and numerical investigation of the thermal performance of the gas-cooled divertor plate concept," *Fusion Science and Technology*, vol. 56, pp. 75-79, July 2009.

[30] P. Norajitra et al., "He-cooled divertor for DEMO: Experimental verification of the conceptual modular design," *Fusion Engineering and Design*, vol. 81, pp. 341-346, 2006.

[31] P Norajitra, R. Giniyatulin, T. Ihli, and G. Janeschitz, "European development of He-cooled divertors for fusion power plants," *Nuclear Fusion*, vol. 25, pp. 1271-1276, 2005.

[32] P. Norajitra et al., "Progress of He-cooled divertor development for DEMO," *Fusion Engineering and Design*, vol. 86, pp. 1656-1659, 2011.

[33] T. Ihli, "He-cooled Divertor Development in the EU: The Helium Jet cooled Divertor HEMJ," in *ARIES Meeting*, San Diego, CA, 2005.

[34] P Norajitra, S. I. Abdel-Khalik, L. M. Giancarli, Ihli T., and G. Janeschitz, "Divertor conceptual designs for a fusion power plant," *Fusion Engineering and Design*, vol. 83, pp. 893-902, 2008.

[35] X. R. Wang, S. Malang, A. R. Raffray, and the ARIES Team, "Design Optimization of the High Performance Helium-cooled Divertor Plate Concepot," *Fusion Science and Technology*, vol. 56, pp. 1023-1027, 2009.

[36] M. S. Tillack et al., "Recent US Activities on Advanced He-cooled W-alloy Divertor Concepts for Fusion Power Plants," *Fusion Engineering and Design*, vol. 86, no. 1, pp. 71-98, 2011.

[37] A. R. Raffray, S. Malang, and X. Wang, "Optimizing the overall configuration of a He-cooled W-alloy divertor for a power plant," *Fusion Engineering and Design*, vol. 84, pp. 1553-1557, 2009.

[38] I. Ovchinnikov et al., "Experimental study of DEMO helium cooled divertor target mock-ups to estimate their thermal and pumping efficiencies," *Fusion Engineering*

and Design, vol. 73, pp. 181-186, 2005.

[39] P. Norajitra et al., "He-Cooled Divertor Development Towards DEMO," *Fusion Science and Technology*, vol. 56, pp. 1013-1017, 2009.

[40] P. Norajitra et al., "He-cooled divertor development for DEMO," *Fusion Engineering and Design*, vol. 82, pp. 2740-2744, 2007.

[41] L. Crosatti, J. B. Weathers, D. L. Sadowski, and S. I. Abdel-Khalik, "Experimental and numerical investigation of prototypical multi-het impingement (HEMJ) helium-cooled divertor modules," *Fusion Science and Technology*, vol. 56, pp. 70-74, July 2009.

[42] J. D. Rader, B. H. Mills, D. L. Sadowski, M. Yoda, and S. I. Abdel-Khalik, "Verification of thermal performance predictions of prototypical multi-jet impingement helium-cooled divertor module," *Fusion Science and Technology*, vol. 64, pp. 282-287, August 2013.

[43] P. Norajitra et al., "Development of a helium-cooled divertor concept: design-related requirements on materials and fabrication technology," *Journal of Nuclear Materials*, vol. 329-333, pp. 1594-1598, 2004.

[44] P. Norajitra, T. Chehtov, A. Gervash, R. Giniyatulin, and T. Ihli, "Status of He-cooled Divertor Development," Forschungszentrum Karlsruhe in der Helmholtz-Gemeinschaft, Annual Report 2005.

[45] M. D. Hageman, D. L. Sadowski, M. Yoda, and S. I. Abdel-Khalik, "Experimental studies of the thermal performance of gas-cooled plate-type divertors," *Fusion Science and Technology*, vol. 60, pp. 228-232, July 2011.

[46] A. R. Raffray, S. Malang, L. El-Guebaly, and T. Ihli, "Major integration issues in evolving the configuration design space for the AREIS-CS compact sellarator power plant," *Fusion Engineering and Design*, vol. 81, pp. 1159-1168, 2006.

[47] T. Ihli, A. R. Raffray, S. I. Abdel-Khalik, and S. Shin, "Design and performance study of the helium-cooled T-tube divertor concept," *Fusion Engineering and Design*, vol. 82, pp. 249-264, 2007.

[48] L. Crosatti, D. L. Sadowski, J. B. Weathers, S. I. Abdel-Khalik, and M. Yoda, "Experimental and numerical investigation of the thermal performance of gas-cooled T-Tube divertor modules," *Fusion Science and Technology*, vol. 52, pp. 531-538, Oct. 2007.

[49] L. Crosatti, D. L. Sadowski, S. I. Abdel-Khalik, M. Yoda, and ARIES Team, "Thermal perforamnce of a prototypical gas-cooled T-Tube divertor module with single sided

heating," *Fusion Science and Technology*, vol. 56, pp. 96-100, July 2009.

[50] D. L. Youchison, B. E. Williams, S. O'Dell, and S. Sharafat, Testing of Helium-Cooled PFCs in the PMTF, 2008, Presentation.

[51] D. L. Youchison, M. T. North, J. E. Lindemuth, J. M. McDonald, and T. J. Lutz, "Thermal performance and flow instabilities in a multi-channel, helium-cooled, porous metal divertor module," *Fusion Engineering and Design*, vol. 49-50, pp. 407-415, 2000.

[52] P. Norajitra, Development of He-cooled Divertors for Fusion Power Plants, July 5-7, 2005, IAEA-TM-1.

[53] Lorenzo Crosatti, "Experimental and Numerical Investigation of the Thermal Performance of Gas-Cooled Divertor Modules," *Ph. D. Thesis, Georgia Institute of Technology*, 2008.

[54] J. B. Weathers, L. Crosatti, R. Kruessmann, D. L. Sadowski, and S. I. Abdel-Khalik, "Development of modular helium-cooled divertor for DEMO based on the multi-jet impingement (HEMJ) concept: Experimental validation of thermal performance," *Fusion Engineering and Design*, vol. 83, pp. 1120-1125, 2008.

[55] Koncar, B., P. Norajitra, and K. Oblak, "Efect of nozzle sizes on jet impingement heat transfer in He-cooled divertor," *Applied Thermal Engineering*, vol. 30, pp. 697-705, November 2010.

[56] B. Koncar, S. Kosmrlj, and P. Norajitra, "On the accuracy of CFD modeling of cyclic high heat flux divertor experiment," *Fusion Engineering and Design*, vol. 87, pp. 1621-1627, June 2012.

[57] Elisabeth Gayton, "Experimental and Numerical investingation of the thermal performance of the gas-cooled divertor plate concept," Georgia Institute of Technology, Atlanta, PhD Thesis 2008.

[58] J. Rader, "Thermal Performance of Finger-Type Gas-Cooled Divertors," Georgia Institute of Technology, Atlanta, PhD Thesis 2013.

[59] B. H. Mills, J. D. Rader, D. L. Sadowski, M. Yoda, and S. I. Abdel-Khalik, "Dynamically Similar Studies of the Thermal Performance of Helium-Cooled Finger-Type Divertors With and Without Fins," *Fusion Science and Technology*, vol. 62, pp. 379-388, Nov 2012.

[60] J. O. Hinze, *Turbulence*. New York, United States of America: McGraw-Hill Publishing Company, 1975.

[61] (2014, January) FLUENT Theory Guide - 4. Turbulence. ANSYS 14.0 Help.

[62] P. R. Spalart and S. R. Allmaras, "A One-Equation Turbulence Model for Aerodynamic Flows," in *AIAA-92-0439*, Reno, NV, 1992.

[63] B. E. Launder and D. B. Spalding, *Lecures in Mathematical Models of Turbulence*. London, England: Academic Press, 1972.

[64] V. Yakhot and S. A. Orszag, "Renormalization Group Analysis of Turbulence. I. Basic Theory," *Journal of Scientific Computing*, vol. 1, no. 1, pp. 3-51, May 1986.

[65] T-H. Shih, W. W. Liou, A. Shabbir, Z. Yang, and J. Zhu, "A new k-epsilon eddy viscosity model for high Reynolds number turbulent flows," *Computers Fluids*, vol. 24, pp. 227-238, 1995.

[66] S. Sarkar and B. Lakshmanan, "Application of a Reynolds Stress Turbulence Model to the Compressible Shear Layer," *AIAA Journal*, vol. 29, no. 5, pp. 743-749, May 1991.

[67] B. E. Spalding, D. B. Launder, "The Numerical Computation of Turbulent Flows," *Computer Methods in Applied Mechanics and Engineering*, vol. 3, pp. 269-289, August 1974.

[68] M. Wolfshtein, "The Velocity and Temperature Distribution of one=Dimensional Flow with Turbulence Augementation and Pressure Gradient," *International Journal of Heat and Mass transfer*, vol. 12, pp. 301-318, 1969.

[69] T. Jongen, "Simulation and Modeling of Turbulent Incompressible Flows," EPF Lausanne, Lausanne, PhD Thesis 1992.

[70] H. C. Chen and V. C. Patel, "Near-Wall Turbulence Models for Complex Flows Including Separation," *AIAA Journal*, vol. 26, pp. 641-648, 1988.

[71] B. Kader, "Temperature and Concentration Profiles in Fully Turbulent Boundary Layers," *Internation Journal of Heat and Mass Transfer*, vol. 24, pp. 1541-1544, 1981.

[72] F. White and G. Christoph, "A Simple New Analysis of Compressible Turbulent Skin Friction Under Arbitrary Conditions," Technical Report AFFDL-TR-70-133 1971.

[73] P. Huang, P. Bradshaw, and T Coakley, "Skin Friction and Velocity Profile Family for Compressible Turbulent Boundary Layers," *AIAA Journal*, vol. 31, pp. 1600-1604, 1993.

[74] B. H. Mills, J. D. Rader, D. L. Sadowski, M. Yoda, and S. I. Abdel-Khalik, "Experimental Investigation of Fin Enhancement for Gas-Cooled Divertor Concepts," in *Technology of Fusion Energy*, vol. 60, Las Vegas, 2011, pp. 191-195.

[75] James Brandon Weathers, "Thermal Performance of Helium-Cooled Divertors for Magnetic Fusion Applications," *M. Sc. Thesis, Georgia Institute of Technology*, 2007.

[76] Thermophysical Properties of Fluid Systems. (2011) National Institute of Standards and Technology. [Online]. http://webbook.nist.gov/chemistry/fluid/

[77] M. Roedig et al., "Post irradiation testing of samples from the irradiation experiments PARIDE 3 and PARIDE 4," *Journal of Nuclear Materials*, vol. 329-333, pp. 766-770, 2004.

[78] S. J. Kline and F. A. McClintock, "Describing the uncertainties in single sample experiments," *Mechanical Engineering*, pp. 3-8, 1953.

[79] R. S. Figliola and D. E. Beasley, *Theory and Design for Mechanical Measurements*, 4th ed. Hoboken, United States of America: John Wiley & Sons, Inc., 2006.

[80] B. H. Mills, Rader J. D., D. L. Sadowski, M. Yoda, and S. I. Abdel-Khalik, "An Experimental Study of the Effects of the Solid-to-Coolant Thermal Conductivity Ratio in Helium-Cooled Divertor Modules," *Fusion Science and Technology*, vol. 64, pp. 670-674, September 2013.

[81] J. D. Rader, B. H. Mills, D. L. Sadowski, M. Yoda, and S. I. Abdel-Khalik, "Experimental and Numerical Investigation of Thermal Performance of Gas-cooled Jet-Impingment Finger-type Divertor Concept," *Fusion Science and Technology*, vol. 60, pp. 223-227, July 2011.

[82] J. D. Rader, B. H. Mills, D. L. Sadowski, M. Yoda, and S. I. Abdel-Khalik, "Optimization of Pin-fin Arrays for Helium-cooled Finger-type Divertor," *Fusion Science and Technology*, vol. 64, pp. 315-319, August 2013.

VITA

Brantley H. Mills was born in La Grange, GA on July 22, 1986 to Lisa Head and Jeff Mills. After graduating from J. L. Mann High School in 2005, he attended Clemson University and graduated in 2009 with Bachelor of Science degree in Mechanical Engineering (magna cum laude). He then attended Georgia Institute of Technology in 2009, where he began pursuing a doctoral degree in Nuclear Engineering.

This thesis was typed by Brantley H. Mills